Formulation of Instrument Noise Analysis Techniques and Their Use in the Commissioning of the Gravitational Wave Observatory, GEO 600

Von der Fakultät für Mathematik und Physik
der Gottfried Wilhelm Leibniz Universität Hannover
zur Erlangung des Grades

Doktor der Naturwissenschaften
– Dr. rer. nat. –

genehmigte Dissertation von

B.Sc. Joshua Ryan Smith

geboren am 26. August 1980 in Glens Falls, NY, USA.

2006

Zusammenfassung

In der allgemeinen Relativitätstheorie hat Albert Einstein die Existenz von sich in der Raum-Zeit ausbreitenden Störungen vorausgesagt, die als Gravitationswellen bezeichnet werden. Wegen ihrer äußerst geringen wahrnehmbaren Auswirkungen, nahm Einstein nicht an, dass sie jemals direkt meßbar wären. Fast ein Jahrhundert später haben Fortschritte in dem Bereich der Laser-Interferometrie die Detektion von Gravitationswellen zu einem realisierbarem Ziel gemacht. Der Nachweis solcher Wellen wäre ein Meilenstein für die Relativitätstheorie und in der Bereitstellung von astrophysischen Informationen, welche elektromagnetischen Beobachtungen unzugänglich sind.

Es wurde ein internationales Netzwerk von sechs laserinterferometrischen Gravitationswellendetektoren errichtet. Diese Instrumente befinden sich im Übergang zwichen Aufbau und langfristiger Datenaufnahme bei Zielempfindlichkeit.

Der deutsch-britische Gravitationswellendetektor ist ein sogenannter Michelson-Interferometer, mit 600 m langen Meßstrecken. Er befindet sich in Deutschland, ungefähr 20 km südlich von Hannover. Die ambitionierte Gestaltung des GEO 600 Detektors vereinigt verschiedene Arten von fortschrittlichen Technologien, die ihn konkurrenzfähig zu den größten gegenwärtigen Detektoren und darüberhinaus zu einem Prototypen für die geplanten Detektoren der nächsten Generation machen. Diese Arbeit beschreibt wesentliche Aspekte des Aufbaus und Verbesserung von GEO 600. Das erste Kapitel gibt einen Überblick über den GEO 600 Detektor, sowie seine wichtigsten Teilsysteme, und stellt seine aktuelle Leistungsfähigkeit.

In den anschließenden Kapiteln wird detailiert auf Aspekte der Rauschanalyse engegangen, die zur Identifikation und Eliminierung empfindligkeitsbegrenzender Rauschquellen dient. Während des Aufbaus von GEO 600 wurde eine Technik zur Rauschanalyse entwickelt, "noise projection" genannt, um systematisch zu ermitteln in welchem Grad die verschiedenen Rauschquellen in den Ausgang des Detektors koppeln.

In Kapitel 2 werden die Prinzipien der *noise projection* beschrieben. Es wird das Verfahren erläutert und es werden verschiedene Kategorien von *noise projections* dargestellt, sowie durch Beispiele an vereinfachte Regelungssystemen demonstriert.

Die an GEO ausgeführten *noise projections* werden im 3. Kapitel erläutert. Jedes Teilsystem, das mit wichtigen Rauschquellen zusammen hängt, wird kurz beschrieben. Ebenfalls wird eine Zusammenfassung dieser Rauschbeiträge mit der erzielten Empfindligkeit des Detektors und dessen Zielempflindlichkeit verglichen.

Zum Abschluss werden in Kapitel 4 die Erweiterungen dieser Technik diskutiert, welche die Automation, das Substrahieren von technisches Rauschbeiträge und das Erstellen von Vetos beinhalten.

Stichworte: Gravitationswellen, Regelungssysteme, Rauschanalyse

Summary

In his theory of general relativity, Albert Einstein predicted the existence of traveling disturbances in space-time called gravitational waves. Because of the exceedingly small observable effects of these waves, he did not think that they would ever be directly measured. Almost a century later, advances in the field of laser interferometry have made the detection of gravitational waves a realizable goal. The direct detection of gravitational waves would be a scientific milestone strongly supporting the general theory of relativity and providing astrophysical information that is inaccessible to electromagnetic observations.

An international network of six long-baseline laser-interferometric gravitational-wave detectors has now been constructed. These instruments are in transition from intense commissioning, focused on bringing the interferometers to stable operation at their target sensitivity, to long term data collecting.

The German-British GEO 600 gravitational-wave detector is a Michelson-type interferometer, with a baseline of 600 m, that is located about 20 km south of Hannover, Germany. The ambitious design of GEO 600 incorporates various types of advanced technologies that make it both competitive with the largest of current detectors, and in some ways prototypical of the planned advanced detectors of the next generation. This thesis describes important aspects related to the commissioning of GEO 600. The first chapter will introduce the GEO 600 detector and its most important subsystems, and briefly describe the performance of this instrument to date.

The following chapters will focus on aspects of noise analysis that aid identification and elimination of technical noise that contributes to limiting the detector sensitivity. During the commissioning of GEO 600, a technique called *noise projection* was developed to systematically determine the level with which various noise sources couple to the detector output. This has played a key role in expediting the GEO 600 commissioning process.

In chapter 2, the principles of noise projections are described. A procedure is given, and several categories of noise projections are described, and demonstrated though examples on simplified control loops.

Noise projections performed on GEO 600 are described in chapter 3. A brief description of each subsystem that relates to an important noise source is given, and the sum of the noise from these is compared to the detector output and the target sensitivity.

Finally, chapter 4 discusses extensions of the technique. These include automation, technical noise subtraction, and vetoes against false gravitational-wave signals.

Keywords: gravitational-wave detection, control systems, noise analysis

iv

Contents

List of figures

List of tables

Glossary

B	a bias voltage
ϵ_0	electric permeability of vacuum
f	an audio-band frequency
F	an RF-band frequency
F_{MI}	the (de)modulation frequency used for control of the Michelson interferometer
F_{SR}	the (de)modulation frequency used for control of the signal-recycling cavity
F_{PR}	the (de)modulation frequency used for control of the power-recycling cavity
h	gravitational wave strain amplitude
H	the detector output channel
$\hbar$	$h/2\pi$ Planck's constant
I	a current
L	a length
m	a mass, *e.g.*, of a mirror
M	a noise projection
N	a noise channel
P	a light power
T	a mirror transmission coefficient
T,α	a transfer function
U	a voltage signal

AA	automatic alignment
AS	amplitude spectrum
ASD	amplitude spectral density
BS	the main GEO 600 beamsplitter
DARM	differential arm-length (fluctuations)
DC	average of a fluctuating signal or the limit of some signal towards low frequencies
DFT	discrete Fourier transform
DRMI	dual-recyled Michelson interferometer
EOM	electro-optic modulator
ESD	electro-static drive
GW	gravitational wave
HVA	high-voltage amplifier
LIF	linear inverting feedback
LIN	laser intensity (power) noise
LO	local oscillator
MC1	mode cleaner 1
MC2	mode cleaner 2
MCe	mirror central east
MCn	mirror central north
MFe	mirror far east
MFn	mirror far north
MI	Michelson interferometer
MID	Michelson differential
OAN	oscillator amplitude noise
OMC	output modecleaner
OPN	oscillator phase noise
PDO	output single-element photodiode
PDPR	single-element photodiode that generates the errorsignal for the PR loop.
PDSR	single-element photodiode that generates the errorsignal for the PR loop.
PR	power-recycling
PRC	power-recycling cavity
PRMI	power-recyled Michelson interferometer

Q	mechanical quality factor
QMTPS	quasi-monolithic triple-pendulum suspension
QPDO	output quadrant photodiode
RF	radio frequency
SNR	signal-to-noise ratio
SRC	signal-recycling cavity
TEM	transverse electromagnetic modes
UGF	unity gain frequency

Chapter 1.

The gravitational-wave detector, GEO 600

1.1. The current gravitational-wave detector network

1.1.1. Gravitational waves

Gravitational waves (GWs) are distortions of the space-time continuum that travel outward from their sources at the speed of light. Their associated particle, the graviton, has spin two, giving gravitational radiation its two polarizations, known as plus "+" and cross "×". In the far-field, the crest of one such wave will cause an apparent stretching of the distance between freely falling masses in one spatial direction orthogonal to the direction of travel of the wave, and a simultaneous shrinking of the distance between such masses along the mutually orthogonal axis. However, because space-time acts as an extraordinarily stiff medium, the apparent strain between two test objects in the far-field will be exceedingly small. Astrophysical systems are the most realistic candidates for producing measurable space-time distortions on Earth. The gravitational waves emitted from, *e.g.,* a supernova explosion within our galaxy would create a strain amplitude of order $h \sim 10^{-18}$.

Gravitational radiation was first proposed by Albert Einstein in his General Theory of Relativity in 1918. Nearly a century later, they have not yet been directly observed. The best indirect evidence supporting their existence resulted from careful analysis of radio observations of the loss of kinetic energy of a rotating binary neutron star system [Taylor79], for which Taylor and Hulse were awarded the 1993 Nobel Prize in physics. Direct detection of GWs would be a scientific milestone providing a strong check on General Relativity and disclosing astronomical information that is inaccessible to electromagnetic radiation.

The current network of GW detectors are searching for GWs from sources such as supernovae [LSC05], spinning neutron stars [LSC05e], in-spiraling binary systems of neutron stars and/or black holes [LSC05b, LSC05c], and the aftermath of the big bang [LSC05d]. Although no positive results have yet been found, there is a reasonable possibility that the data being taken by the international GW detector network as this thesis is being written may contain the first detectable traces of gravitational waves.

1.1.2. The detectors

Over the past few decades, considerable progress has been made in the development of *gravitational-wave detectors*, or transducers to convert the energy carried by gravitational waves into another more easily measurable quantity, such as voltage. Two

main types of detectors have been built: resonant-mass and laser-interferometric. The former are designed to detect tiny vibrations of large test bodies when their internal resonances are excited by passing gravitational waves. The latter are to measure the influence of passing gravitational waves on the distances between test masses with large separations using a laser-interferometric readout. The work pertaining to this thesis was undertaken at an interferometric GW detector, and will therefore focus on that technology. However, brief descriptions of the resonant detectors are also given below.

The following is intended to give a snapshot of the current status of the international network of gravitational wave detectors that is in operation in early 2006. The geographic location of these detectors is shown in Figure 1.1.
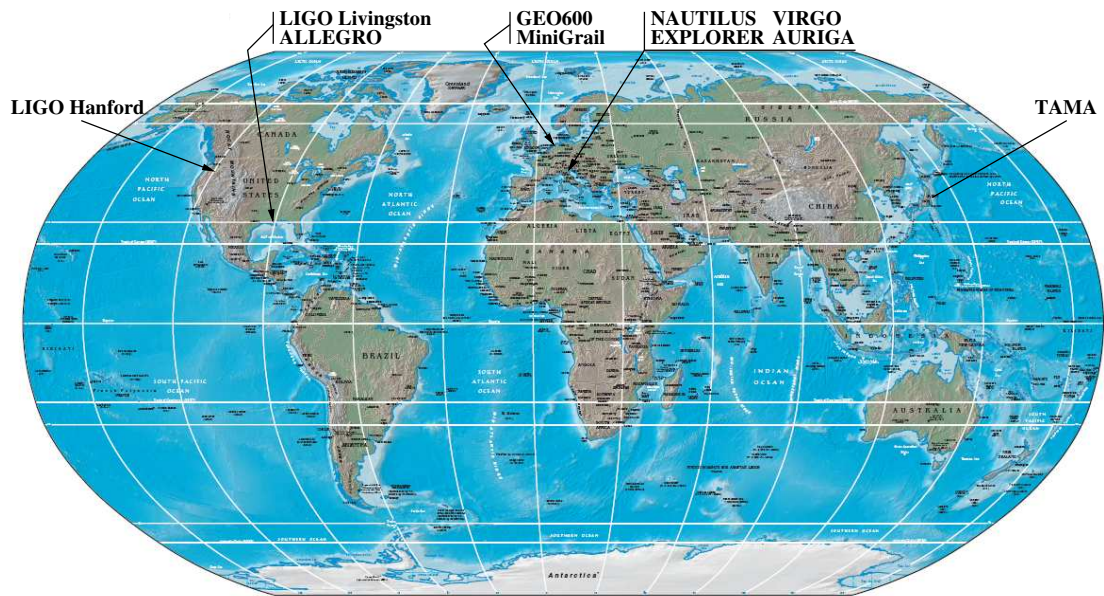
Figure 1.1.: Approximate geographical locations of the gravitational-wave detectors currently in operation.

The resonant-masses: The current generation of resonant-mass GW detectors achieve their sensitivities by operating at cryogenic temperatures and transforming the vibrations of the resonant masses to voltage signals using superconducting inductive transducers and SQUID amplifiers. These detectors can roughly be characterized as having a relatively narrow sensitive frequency bandwidth compared with the interferometers, and peak sensitivities that are close to or above $1\,\mathrm{kHz}$.

ALLEGRO: Cylindrical bar detector located on the campus of Louisiana State University in Baton Rouge, Louisiana, USA. The bar is made of aluminum alloy 5056 (AL5056), is 60 cm in diameter and 300 cm in length, and has a mass of 2296 kg. Its resonance frequencies are around 895 and 920 Hz. See [ALLEGRO, Heng].

NAUTILUS: Cylindrical bar detector at the National Institute of Nuclear Physics (INFN) Frascati National laboratory in Frascati, Italy. The bar is made of AL5056, is 60 cm in diameter and 300 cm in length, and has a mass of 2300 kg. Its resonance frequencies are around 908 and 924 Hz. See [NAUTILUS, Astone].

AURIGA: Cylindrical bar detector at the National Institute of Nuclear Physics (INFN) Legnaro National laboratory in Padova Italy. It was designed to be similar to NAUTILUS. The bar is made of AL5056, is 60 cm in diameter and 300 cm in length, and has a mass of 2330 kg. Its resonance frequencies are around 913 and 931 Hz. See [AURIGA, Cerdonio].

EXPLORER: Cylindrical bar detector located at the European Organization for Nuclear Research (CERN) in Geneva, Switzerland. The bar is made of AL5056, is 60 cm in diameter and 300 cm in length, and has a mass of 2300 kg. Its resonance frequencies are around 906 and 923 Hz. See [EXPLORER, Astone].

MiniGRAIL: Spherical detector located at the Kamerlingh Onnes Laboratory of Leiden University in the Netherlands. The sphere is made of CUAL16% with diameter 68 cm and mass of about 1300 kg. Its resonant frequencies are around 2930 and 3030 Hz. See [MiniGRAIL, DeWaard].

The laser-interferometers: The interferometric gravitational wave detectors currently in operation are all based on the Michelson interferometer, which will be discussed in 1.2.1. However, none of these devices is a simple Michelson interferometer. Each incorporates a number of enhancements aimed at improving the sensitivity. Describing each interferometer in detail is well beyond the scope of this work. The following gives some information that the author considers interesting, and references for further reading about each of the detectors.

LIGO: A project consisting of three interferometers in the USA. Two of these are collocated in Hanford, Washington, with 4 and 2 km baselines. The third is located in Livingston, Louisiana, and has a 4 km baseline. The detectors are configured as power-recycled Michelson interferometers (see below) with Fabry-Perot arm cavities. All three are run by LIGO Lab, an American
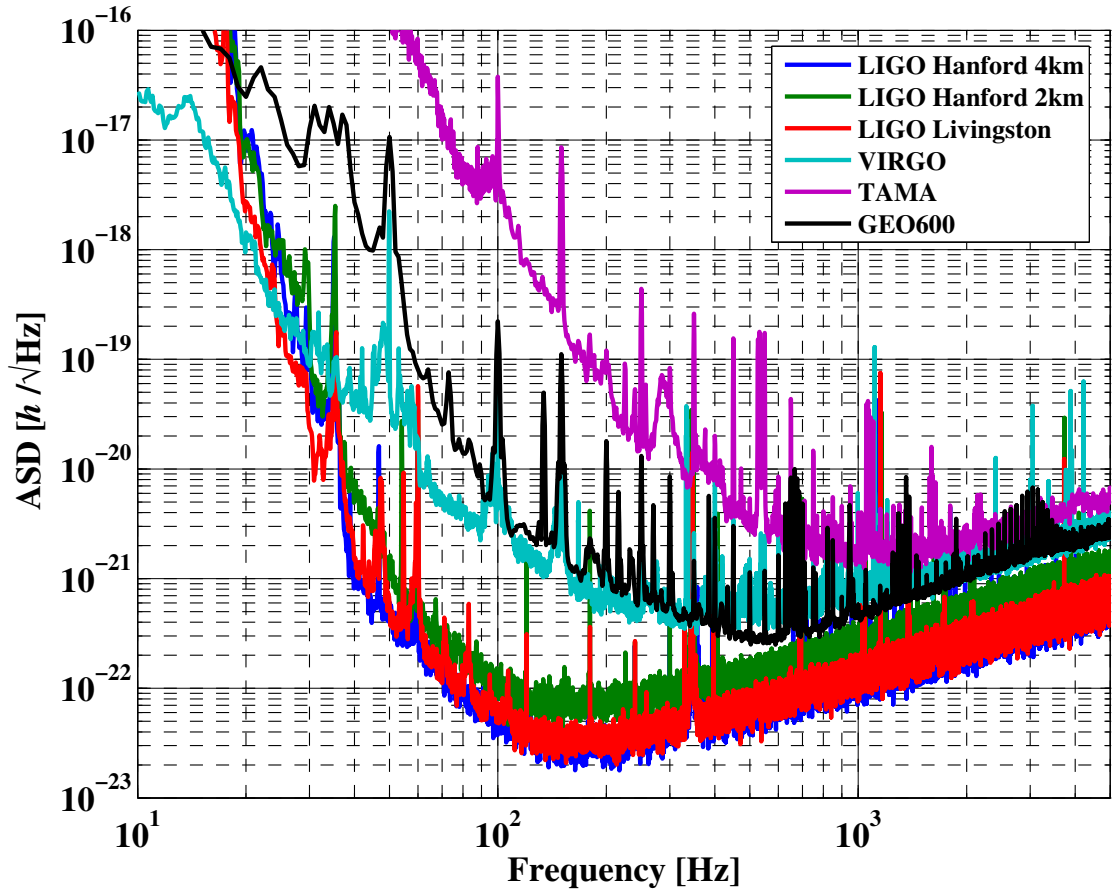
Figure 1.2.: Approximate sensitivity of the first generation of long baseline interferometric GW detectors to gravitational waves circa 2006.

collaboration. At the time of writing, the 4 km LIGO Hanford detector has the highest strain sensitivity of any gravitational wave detector. See [LIGO, Sigg].

VIRGO: A 3 km baseline interferometer in Cascina, Italy. Its optical configuration is similar to that of LIGO. The most well-known feature of the VIRGO detector is its aggressive seismic isolation system of so-called *superattenuators*. It is run by a French-Italian collaboration. See [VIRGO, Acernese].

TAMA: A 300 m baseline interferometer close to Tokyo, Japan. Its optical configuration is close to that of LIGO and VIRGO. It is run by a Japanese collaboration. See [TAMA, Ando].

GEO 600: A 600 m baseline interferometer close to Hannover, Germany, run by the British-German GEO collaboration. Unlike LIGO, VIRGO, and TAMA, GEO 600 does not use Fabry-Perot arm cavities, but rather a combination of folded arms and dual-recycling. These techniques will be discussed in more detail in the following sections. See [GEO 600, Lück06] and below.

The sensitivities[1] of the interferometric GW detectors to gravitational waves around the time of writing are shown in figure 1.2. It should be emphasized that this represents a snapshot only. The detectors are all at various stages of commissioning, and improvement in their sensitivity, especially that of the VIRGO detector, is expected over the coming months and years.

1.2. Introduction to GEO 600
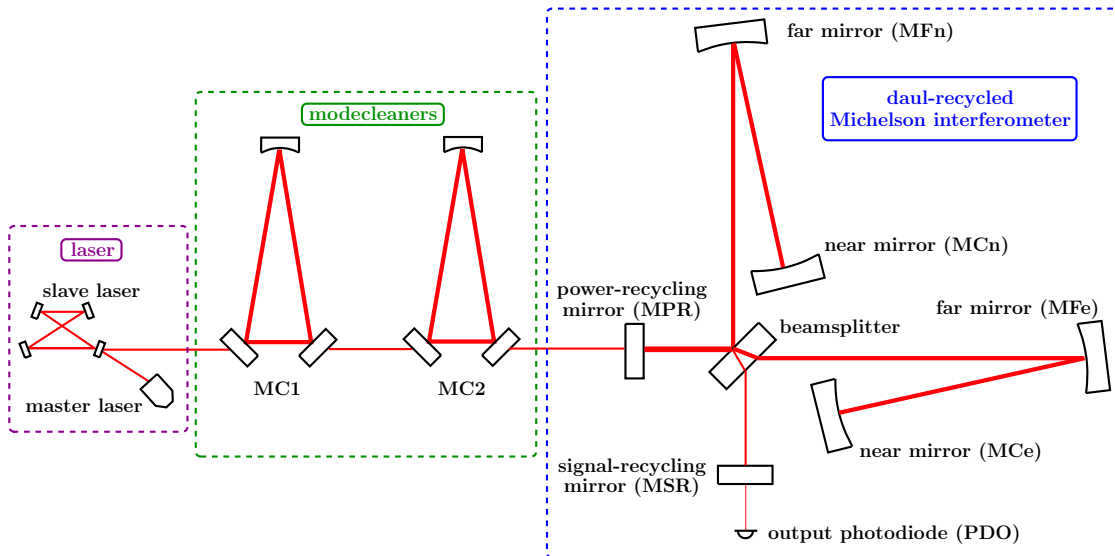
Figure 1.3.: A simplified diagram of the GEO 600 optical layout.

The GEO 600 GW detector is located in the village of Ruthe, about 20 km south of Hannover, Germany. An aerial photograph of its location is shown on the first page of this chapter. In contrast to its larger cousins, LIGO and VIRGO, GEO 600 is rather indistinct with respect to its surroundings. It is therefore shown highlighted

---

[1]The sensitivity of a GW detector is typically given in units of amplitude (or linear) spectral density (ASD). This normalization, the most common among experimental physicists in the gravitational-wave detection field, will be used throughout this work unless explicitly stated otherwise. For more information about spectral normalization see [Heinzel02].

against the rural background. Construction of the site began in 1995, and the first official data-taking commenced in 2002. Since that time, the GEO 600 team has been alternating between data-taking and commissioning the detector to improve its stability and sensitivity. Much of the work presented in this thesis was done to expedite the commissioning process.

Figure 1.3 shows a simplified diagram of the optical layout of GEO 600. A more detailed layout can be found in Appendix A. This section will introduce the optical layout of the dual-recycled Michelson interferometer that forms the heart of GEO 600. Several of the key subsystems, such as the laser and modecleaners will be discussed in Section 1.3. GEO 600 is nominally sensitive to GWs at audio frequencies, with a measurement band spanning from roughly 50 to 5000 Hz.

1.2.1. The Michelson interferometer

The historical origin of the Michelson interferometer is the famous Michelson and Morley experiment. This was designed to measure the effects of the purported ether on the differential travel time of light in two perpendicular arms which could be rotated with respect to the direction of motion of the Earth[2].

A simplified layout of the GEO 600 Michelson interferometer (MI) is shown in Figure 1.4. The laser light enters from the West, is phase modulated by an electro-optic modulator (EOM) to produce control sidebands, and is split into two beams of approximately equal intensity by the beamsplitter, **BS**. These traverse the North and East arms, which are singly folded delay lines comprising the far mirrors, **MFe** and **MFn**, and the near mirrors, **MCe** and **MCn**. The near mirror positions are adjusted such that the carrier light, upon returning to the beamsplitter, interferes destructively to give an intensity minimum, or *dark fringe*, at the output port. Differential length fluctuations between the two arms of the MI that are small with respect to the laser wavelength, $\lambda_\mathrm{L} = 1064\,\mathrm{nm}$, will cause amplitude fluctuations of the light field present at the output port. These are the so called *signal sidebands* that contain the gravitational wave information. By detecting these fields using a photodiode, PDO, a differential strain, caused *e.g.,* by a GW, is transformed into a voltage.

The dark fringe operating point gives cancellation of any common-mode effects on the incident laser light, or imparted on the light from common-mode motion of the arms. However, it also minimizes the amplitude of the signal sidebands,

---

[2]Michelson and Merely ultimately failed to detect the effects of an ether. Whether gravitational waves will be detected remains to be seen.
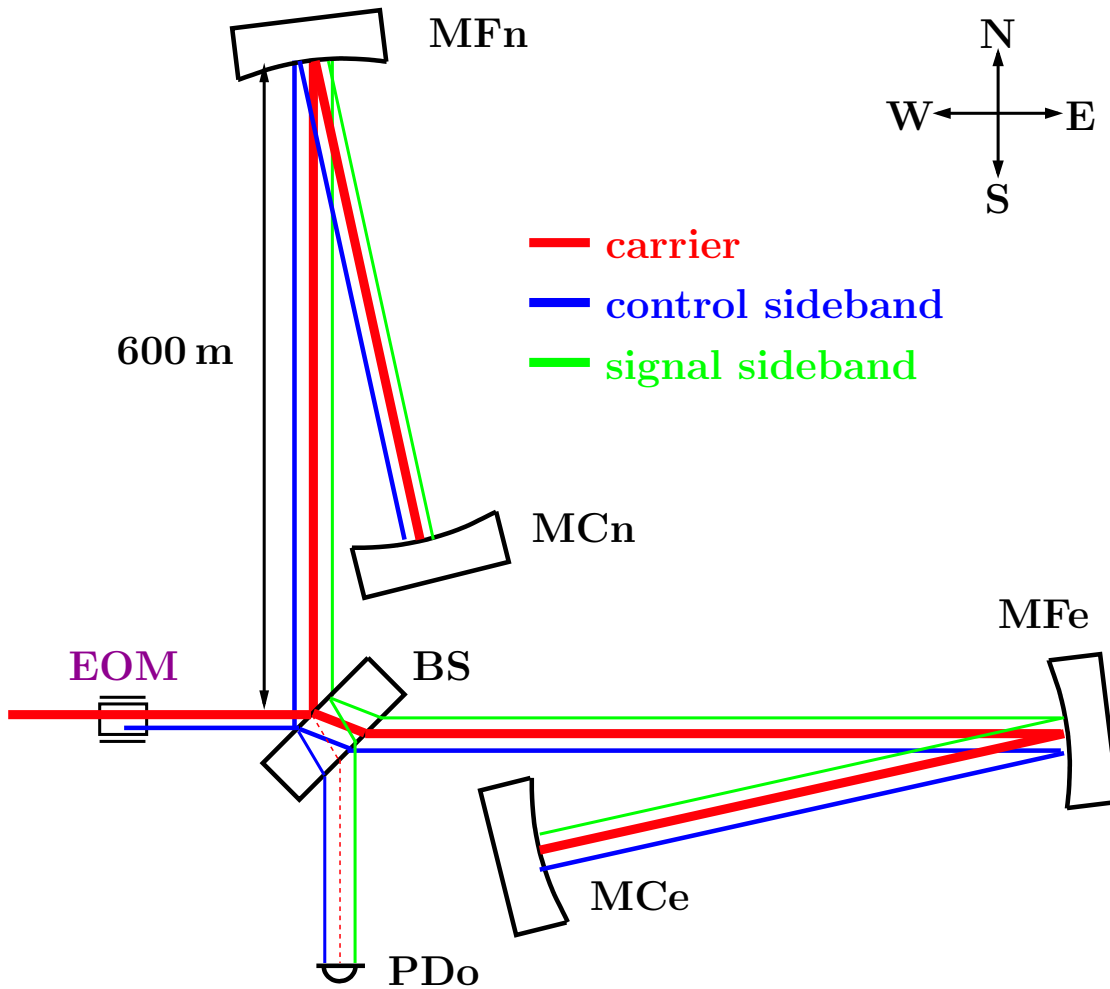
Figure 1.4.: A simplified diagram of the GEO 600 Michelson interferometer, with and idealized distribution of light fields. The sideband and carrier beams overlap in reality. Here a spatial separation is introduced to allow better visualization of the different fields.

which makes detection of any GW signal difficult in the presence of technical noise. For this reason, a technique known as *frontal* or *Schnupp modulation* is employed at GEO 600. The incoming light is phase modulated at a significantly high frequency that the laser is quantum noise limited (a so called radio frequency (RF)). In addition, the two MI arms are made to be of slightly different lengths. In this situation, when the MI is adjusted to the dark fringe, it provides a (nearly) perfect destructive interference of the carrier light, but other frequencies experience imperfect cancellation. Modulation sidebands that are incident on PDO due to this

Schnupp asymmetry beat with the signal sidebands and the resulting photo-current is then demodulated at the modulation frequency. The resulting signal is called the Michelson differential (MID) longitudinal error-signal. For more information about the extraction of the MID error-signal, see [Freise, Grote03, Malec05]. This signal is eventually calibrated to strain to become the main detector output, H, as will be described in 3.2.

Folded arms (DL4)

Since the shot-noise limited sensitivity (see section 1.4.1) of a Michelson interferometer to strain scales with the round-trip travel time that the light takes in the arms, it is desirable to either have very long arms, or to reflect the light in the arms many times before allowing it to interfere. The limit to this is when the storage time in an arm is as long as the period of the gravitational waves being searched for, such that the light has no net phase shift upon interference. For gravitational waves of around 100 Hz, this sets an arm length limit of about 3000 km, with an optimal length about half that. For a terrestrial gravitational wave detector, the arm lengths are practically limited to less than about 10 km by the curvature of the earth (or more realistically, by the project's budget and the geometry of the affordable land, as in the case of GEO 600). Thus to achieve the best possible sensitivity requires implementing extra reflections in the arms. Prior to the construction of GEO 600, scientists at the 30 m Garching prototype interferometer experimented with so called delay lines, which had many beams ($\approx$90) in each arm. The Garching team found realizing the sensitivity enhancement from this technique to be technically difficult due to additional noise caused by scattered light in the delay line [Shoemaker, Winkler]. For that reason, a more conservative delay line was chosen for GEO 600.

As shown in Figure 1.4 the GEO 600 MI utilizes a single extra mirror in each arm to double the path length from 600 m to 1200 m. This is referred to as a four-beam delay line, or 'DL4'. Here we investigate what effect this has on the theoretical sensitivity of the MI by comparing the coupling level of different types of noise to the detector output for folded and unfolded configurations[3].

Test mass motion noise There are many noise sources in GEO 600 that manifest themselves by moving the test masses longitudinally, and thereby coupling into the

---

[3]The garching delay line was plagued by scattered light. However, to date there has been no evidence that light scattered directly back from the far mirrors causes any additional noise in GEO 600. Therefore, scattered light is neglected in the following.

detector output. Two examples of these are thermal noise of the mirrors and seismic noise (see 1.4). These can cause differential changes in the lengths of the arms of the MI, creating a strain signal,

$$h = \frac{2\delta l}{L},$$
(1.1)

where δl is the length change in one arm (for a differential arm-length change there is also a δl length change in the other arm, thus the factor 2) and L is one-half the optical path length of one arm of the IFO ($L = 1200\,\text{m}$ for GEO 600)[4]. This shows up as a noise in the detector output signal, and is indistinguishable from a GW signal.

Now, let us work in the frequency domain with amplitude spectral densities. If we assume that the motions of the mirrors of the MI are statistically independent (uncorrelated)[5], we can add their contributions in quadrature. In this case, the contribution of the longitudinal motion of each mirror in GEO 600 to the strain measured in the detector output is[6],

$$\hat{h}_{\text{folded}} = \frac{2\sqrt{\frac{1}{2}\hat{X}_{\text{BS}}^2 + \hat{X}_{\text{MFn}}^2 + \hat{X}_{\text{MFe}}^2 + \frac{1}{4}\hat{X}_{\text{MCn}}^2 + \frac{1}{4}\hat{X}_{\text{MCe}}^2}}{L}$$
(1.2)

where $\hat{X}_y$ is the ASD of the longitudinal motion of mirror y [Smith04, Crooks][7].

Assuming that all mirrors have the same level of longitudinal mirror motion noise[8], $\hat{X}$, simplifies the equation,

$$\hat{h}_{\text{folded}} = \frac{2\sqrt{3}\hat{X}}{L}.$$
(1.3)

If the interferometer did not have folded arms, it would have only a single mirror in each arm, *e.g.,* **Me** and **Mn**, and the contribution to the detector output would be,

$$h = \frac{2\sqrt{\frac{1}{2}X_{\text{BS}}^2 + \frac{1}{4}X_{\text{Mn}}^2 + \frac{1}{4}X_{\text{Me}}^2}}{L_{\text{unfolded}}} = \frac{2X}{L_{\text{unfolded}}}.$$
(1.4)

---

[4]For a description of the way that the GW strain predicted by general relativity relates to differential arm-length fluctuations in a MI, see *e.g.,* the Introduction in [Hewitson04].

[5]This is a good assumption for random thermal noise and seismic noise of mirrors separated by large distances, etc.

[6]Here explicit frequency dependence is left away for simplicity. In reality this equation has to be carried out for each frequency bin, however that does not effect the following analysis.

[7]Equation 1.2 is equivalent to Equation 2.57 of [Crooks], since the latter uses $L = 600\,\text{m}$.

[8]This assumption is appropriate for *e.g.,* suspension thermal noise and seismic noise, since the main test masses are all nearly identical suspensions, in similar environments.

where L_{unfolded} is 600 m, since there is no longer an extra beam path per arm.

Comparing the two cases shows that,

$$\frac{h_{\text{folded}}}{h_{\text{unfolded}}} = \frac{2\sqrt{3}X}{2X}\frac{600}{1200} = \frac{\sqrt{3}}{2} = 0.866. \tag{1.5}$$

So uncorrelated longitudinal test mass motion noise of a DL4 produces about 13% less apparent strain than it would in an unfolded configuration.

Noise not related to test mass motion   There are also many noise sources that do not manifest themselves through test mass motion. Some examples of these are shot noise of the light at the detector output, electronic noise added during the detection process and amplitude noise of the laser. As long as these noise sources do not couple to differential arm-length changes (*e.g.*, via radiation pressure), their influence will halved by the presence of folded arms. This is because the noise sources themselves will typically not be influenced by the additional mirrors and beams, while the strain sensitivity of the detector will be doubled due to the doubled effective arm-lengths. Thus the ratio of the strain signal to noise of this type in the detector output is doubled for the case of folded arms, resulting in a factor of two less apparent strain for such noise sources. This makes the use of folded arms particularly important for the sensitivity of GEO 600, since shot noise is expected to be one of the limiting noise sources over much of the measurement band.

1.2.2. The Power-recycled Michelson interferometer

When the MI is held to a dark fringe, conservation of energy requires that the incident light power is either lost in the cavity, or reflected back towards the laser. High quality MI optics ensure small losses, and thus the MI acts effectively as a highly-reflective mirror for the incident laser light. *power-recycling* is the term describing the insertion of an extra mirror, the *power-recycling mirror* (**MPR**), between the laser and the MI to form a coupled cavity. The power-recycled Michelson interferometer (PRMI) has an additional buildup of power that depends on the reflectivity of **MPR** and the losses within the MI. This technique was first suggested by Drever [Drever] and Schilling, and demonstrated in a suspended Michelson interferometer in Garching [Schnier]. It is now implemented on all first generation interferometric GW detectors.

The GEO 600 PRMI is shown in figure 1.5. The power-recycling mirror has a transmittance of 0.1%, allowing for a theoretical power buildup factor of 1000
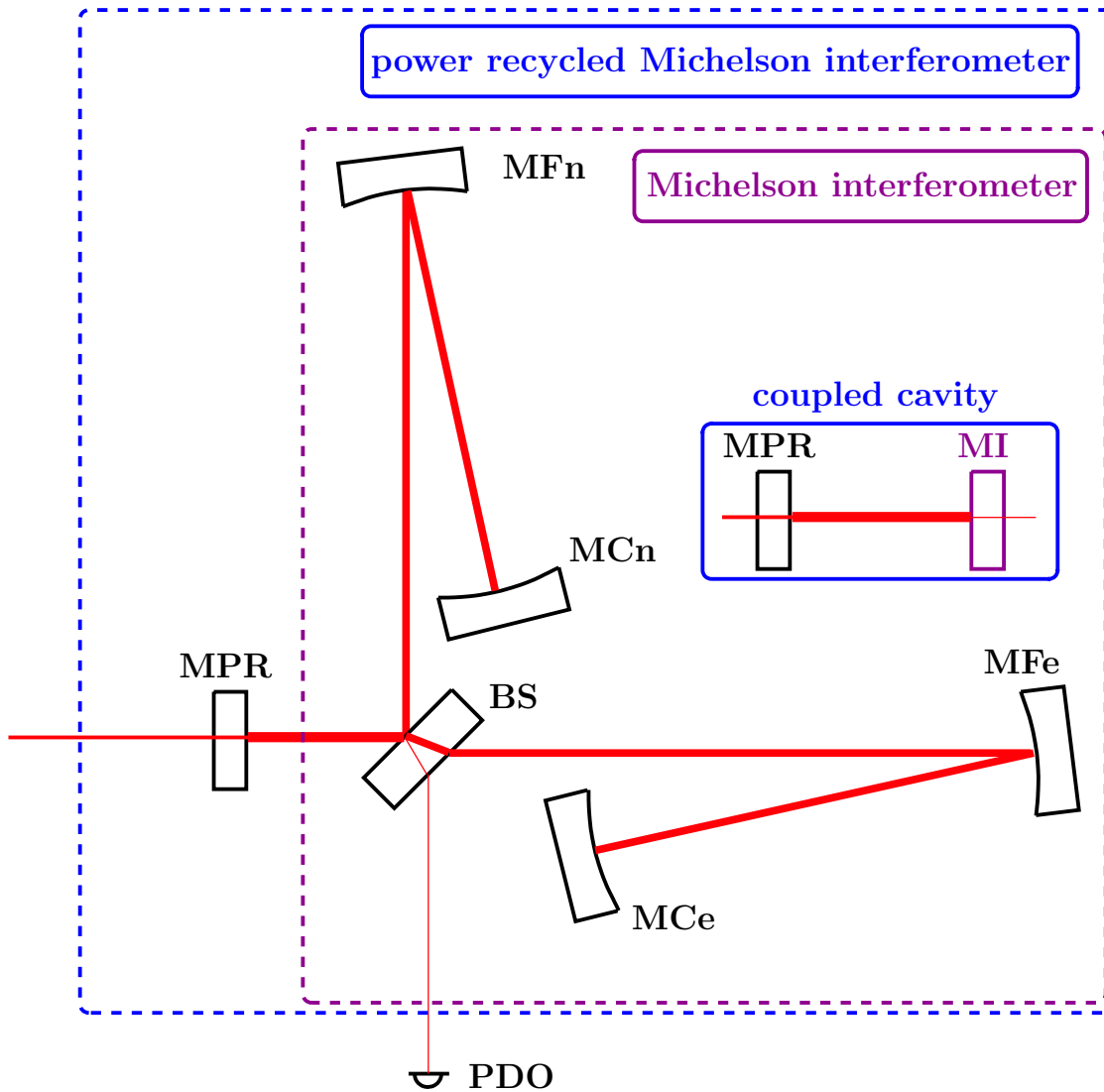
Figure 1.5.: A simplified diagram of the GEO 600 power recycled Michelson inter-
ferometer.

assuming that the transmittance roughly matches the losses in the MI, following equations 26 and 27 in [Mizuno]. In the current GEO 600, a PR factor of roughly 800 is achieved[9]. This may be limited by extra losses within the MI, perhaps due to beam clipping. The storage time of the light within the PRMI results in a cavity pole of around 15Hz, above which amplitude noise of the laser is passively filtered.

---

[9]This is for 5.2 W injected to the modecleaners, of which 2.6 W is incident on **MPR** and 2100 W incident on the **BS** [Hild06c].

The power-recycling cavity also serves another important role. Since it is formed by suspended mirrors separated by large distances, it is an exceptionally quiet length (and thus frequency) reference to which the laser frequency can be locked. This is done using a standard Pound-Drever-Hall locking technique, and forms the final stage of laser frequency stabilization [Freise, Grote03].

1.2.3. The dual-recycled Michelson interferometer

As was shown in Figure 1.4, signal sidebands created within the MI exit the output port. In 1988 Meers [Meers] suggested inserting a so-called *signal-recycling mirror* **MSR** between the beamsplitter and the detector output to form a coupled cavity. In such a *signal-recycling cavity* (SRC), the signal sidebands experience a larger buildup than the carrier light. Since the resonantly enhanced signal sidebands contribute negligibly to the total light power at the detector output, the GW signal increases with respect to the shot noise. Another benefit of a signal-recycling cavity is that it converts a certain amount of of light in the form of higher order spatial modes back into the TEM00 mode, through a process known as *mode healing*. This not only increases the light power level in the interferometer, but also reduces the level of shot noise and other technical noise at the detector output. Considering both effects, a sizable increase in the shot-noise limited sensitivity can be achieved with signal-recycling.

The combination of signal-recycling and power-recycling is known as *dual-recycling*. GEO 600 is the first large baseline interferometric gravitational wave detector to incorporate dual-recycling. However, the technique will be used in most of the next generation of interferometric detectors. The GEO 600 dual-recycled Michelson interferometer (DRMI) is shown in Figure 1.6.

The bandwidth of the signal-recycling resonance is determined largely by the reflectivity of **MSR**. The currently-installed **MSR** has a transitivity of roughly 2%, giving a resonance with a full-width at half-maximum of approximately 700 Hz. In addition, by microscopic adjustment of the position of **MSR**, the frequency of the signal-recycling resonance can be shifted with respect to the carrier (about which are the signal sidebands). If **MSR** is adjusted such that the resonance is centered about the carrier, the SRC is said to be *tuned*. If it is instead adjusted to enhance signal sidebands that are separated from the carrier by a given Fourier frequency, f_{sig}, the SRC is said to be *detuned* to that frequency. The optical transfer function of differential arm-length (DARM) fluctuations to the detector output for several different detuning frequencies of the SRC is shown in Figure 1.7.
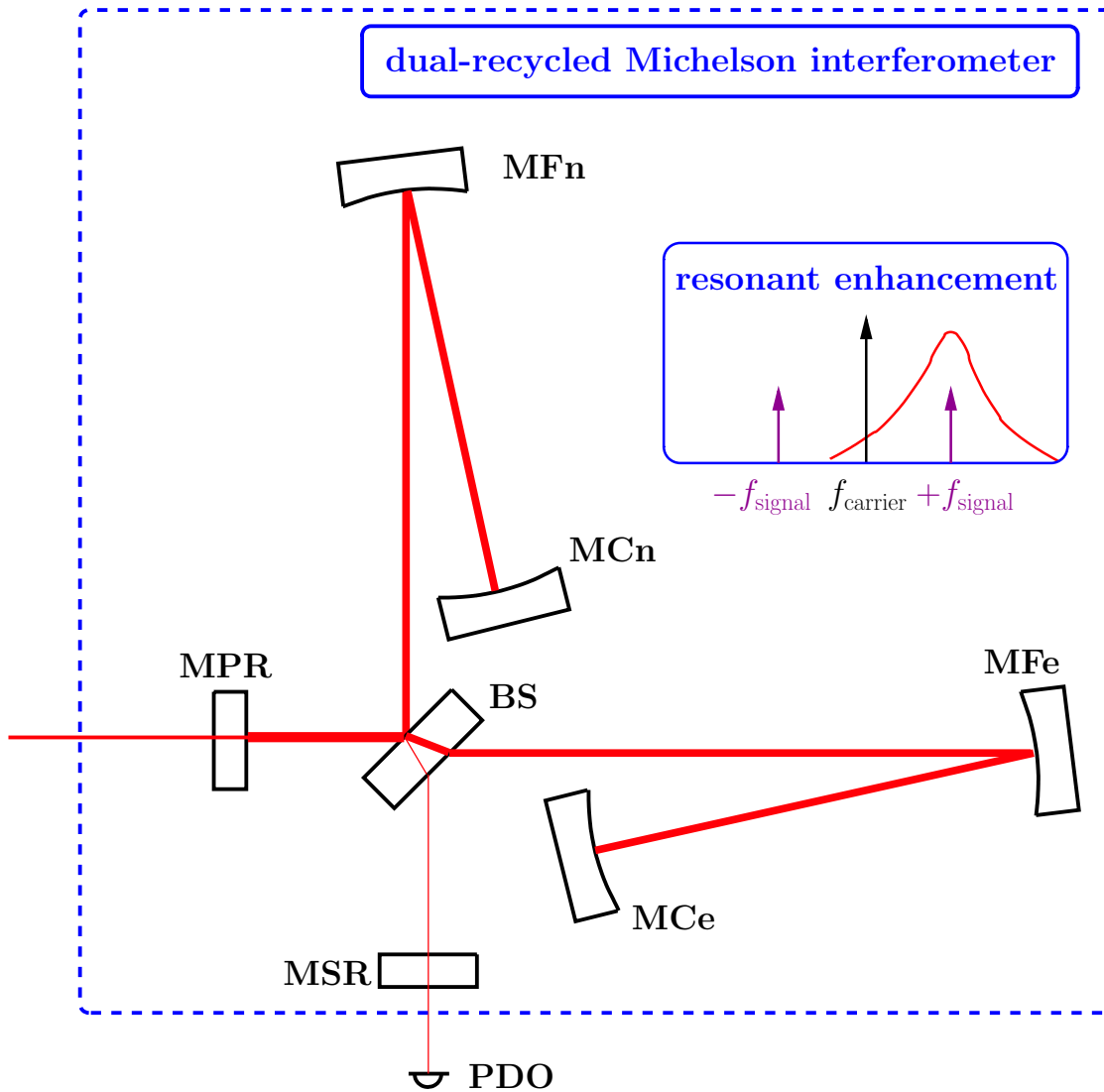
Figure 1.6.: The GEO 600 dual-recycled Michelson interferometer. Also shown is a simplified diagram of the resonant enhancement of the signal sidebands due to signal-recycling.

Power- and signal-recycling improve the shot-noise limited sensitivity of the detector (and the limits imposed by other non-mirror-motion noise). However, mirror-motion type noise that is indistinguishable from gravitational-wave strain are also enhanced by the optical transfer function of the DRMI, resulting in no improvement in detected SNR. For very high recycling factors and input powers, the fluctuating pressure of the light on the test masses, known as *radiation pressure noise*,
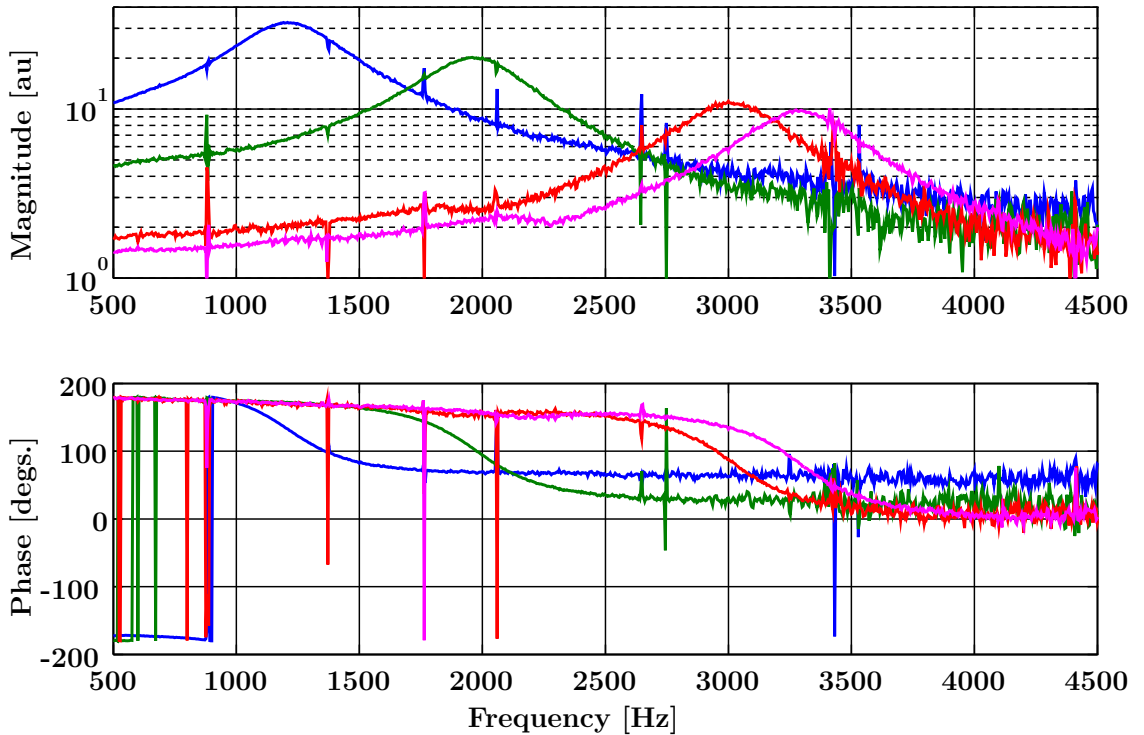
Figure 1.7.: The optical transfer function of the GEO 600 DRMI for several detuning frequencies of the signal-recycling cavity.

begins to play a role. The combination of shot noise and radiation pressure sets a limit on the detector sensitivity known as the standard quantum limit[10]. This limit can be overcome by the use of non-classical techniques, such as squeezed light [Caves, Schnabel], as is planned for the successor of GEO 600, GEO HF [GEO HF].

1.3. Key subsystems

In order to achieve a sensitivity comparable to that of the interferometers with longer baselines, *i.e.,* LIGO and VIRGO, GEO 600 incorporated several advanced techniques in its first generation design. In addition, several of its more typical subsystems have more stringent requirements to ensure the lower absolute noise

---

[10]The standard quantum limit is given by $\hat{h}_{\mathrm{SQL}} = \sqrt{8\hbar/(m2\pi f^2 L^2)}$, where $\hbar$ is Planck's constant, m is the mass of a test mass, and L is the arm length [Buonanno]. For GEO 600 this gives a value of $8.14 \times 10^{-23} (f/100\mathrm{Hz})^2 \, \mathrm{Hz}^{-1}$.

needed to give similar sensitivity performance as the larger detectors. This section is intended to provide some information about the characteristics and motivations for several of the key subsystems. Particular attention is given to those that are known to be important with respect to noise coupling to the detector output, the subject of the following chapters.

1.3.1. The laser system

For GEO 600 to reach its commissioning goals, it is crucial that its main laser light source[11] meet its stability, reliability and noise performance requirements. The GEO 600 laser was chosen to be an all-solid state Nd:YAG (Neodymium-doped Yttrium-Aluminum-Garnet) injection locked master-slave system, with output wavelength 1064 nm. This system is a natural choice because it is stable and well tested, and because high-quality optics for the same wavelength are readily available. For more information about the GEO 600 laser system, see [Heurs]. Here we focus on the aspects of the laser that will directly effect the noise performance of GEO 600.

Shot noise is one of the most important limits to the sensitivity of the current generation of gravitational wave detectors (see Section 1.4.1 for its contribution to the theoretical sensitivity limit of GEO 600). Since for a set interferometer configuration, the amplitude spectral density of shot noise increases with the square root of the light power, and since gravitational wave signal gain increases proportionally to the laser power, the signal-to-shot-noise ratio increases with the square-root of the laser power [Mizuno]. Limits to this are set by absorption of optical components, and the SQL. Thus it is desirable to have a high input laser power. The GEO 600 laser system outputs about 12 W of single-mode light.

Intensity fluctuations of the laser light within the MI cause radiation-pressure fluctuations on the surfaces of the MI mirrors and beamsplitter, and thus differential arm-length fluctuations that are indistinguishable from gravitational wave signals at the detector output. This coupling mechanism sets a relative intensity noise fluctuation requirement of RIN $= 5 \times 10^{-8}/\sqrt{\text{Hz}}$ over the GEO 600 measurement band [Winkler02]. In order to achieve this, an active stabilization of the intensity noise is required. In chapter 3 we will briefly describe the stabilization systems used. The achieved RIN of the GEO 600 laser system is given in [Heurs]. In addition, intensity noise creates amplitude modulation sidebands on the carrier and control sidebands that beat at the dark port. The coupling of these amplitude

---

[11]The main laser system is not the only laser used at GEO 600. A diode laser is located in the North building to provide photon pressure on **MFn** for a calibration reference. See, [Mossavi].

sidebands into H is determined by many parameters, including the fringe contrast, which may be worsened by, for example, asymmetries between the arms, deviations of the MI from the dark fringe, and thermal lensing in the beamsplitter.

As mentioned earlier, the two arms of the MI have a small but macroscopic length difference (roughly 7 cm [Malec05]) to allow Schnupp modulation. Frequency fluctuations of the laser, when injected into this slightly asymmetric MI can also cause signals indistinguishable from GWs. This sets the requirement that the frequency of the laser light be stabilized to within $\delta f = 2 \times 10^{-4}\,\mathrm{Hz}/\sqrt{\mathrm{Hz}}$ over the measurement band. However, poor fringe contrast, parasitic cavities, and/or scattered light may increase the coupling of frequency noise to H. The frequency stabilization scheme for GEO 600 is described in [Freise].

Besides these, other important laser properties that must be optimized include beam jitter, polarization, and mode shape. Because of the filtering properties of the two modecleaners, these effects are transformed into additional frequency and intensity observables at the input to DRMI. The requirements of the GEO 600 laser system are summarized in Table 1.1.

Output Power	10 W
Intensity Noise	$\mathrm{RIN} = 5 \times 10^{-8}/\sqrt{\mathrm{Hz}}$
Frequency Noise	$\delta f = 2 \times 10^{-4}\mathrm{Hz}/\sqrt{\mathrm{Hz}}$
Beam Mode	$95\%\ TEM_{00}$

Table 1.1.: Requirements of the main GEO 600 laser system.

1.3.2. Modecleaners

Input modecleaners

After exiting the laser system, the light is filtered by two sequential triangular ring cavities called *modecleaners*, as was shown in Figure 1.3. modecleaners earn their name by being resonant for only one transverse spatial mode, the TEM00. Higher order spatial modes experience a larger phase shift (with respect to the TEM00) for each round trip, and fall out of the small linewidth of the cavity resonance [Adhikari]. The two GEO 600 modecleaners, MC1 and MC2, have round trip lengths of about 8 and 8.1 m, and finesses of 2700 and 1900, respectively. This allows for a separation of higher order spatial modes and multiple free spectral ranges between the two modecleaners, to ensure sufficient suppression of the

unwanted light fields. Since angular fluctuations of the input beam manifest themselves as higher order spatial modes, the modecleaners provide passive filtering of beam jitter. In addition, laser frequency and amplitude noise are filtered with a single pole per modecleaner, the *cavity pole*, which is around 8 kHz for MC1 and MC2.

The modecleaners (and the rest of GEO 600) are operated with s-polarized light[12]. The fact that s- and p-polarized light have different resonant frequencies, and that the modecleaners include polarizing optics, means that the Finesses of the modecleaner cavities for p-polarized light are less[13]. Thus polarization noise in the modecleaners, which could couple to intensity noise via the polarizing optics between the modecleaners and power-recycling mirror, is filtered. Besides these roles, the modecleaners serve as quiet frequency references for intermediate stages of the frequency stabilization [Freise]. One significant drawback of many of these features of the modecleaners is that by filtering away higher order modes, polarization noise, *etc.*, they introduce additional intensity noise on the laser light. For this reason, the laser intensity must be stabilized to a reference after the modecleaners, as described in section 3.3.4. For more information about the GEO 600 modecleaners, see [Freise, Goßler04].

Output modecleaner

Higher order spatial modes on the light exiting the dark port of the interferometer do not carry any GW signal, but do contribute to the shot noise and other noise. Therefore, it is desirable to filter these higher order modes out, with as little loss for the TEM00 mode as possible. For this purpose, a small triangular *output modecleaner* (OMC) was designed and built for GEO 600. This device was foreseen to be suspended in vacuum at the output port of the interferometer. A description of the OMC and its suspension can be found in [Goßler].

Tests of an identical modecleaner, without suspension and in air, were performed using the output beam at LIGO [Kawabe]. Under these conditions, the system resulted in excess noise in the detector output. This was likely due to jitter of the incoming beam, which coupled to the detecor output via insufficient filtering

---

[12]A common convention for referring to the polarization of light fields is in relation to the plane made by the propagation direction and a normal to the plane of a reflecting surface. Polarization parallel and perpendicular to this plane are referred to as p- and s-polarized (from *senkrecht*, which means "perpendicular" in German), respectively.

[13]The lower Finesse of p-polarized light could also serve as an advantage. A possible plan for improving the throughput of the modecleaners (currently about 50%) in the future is to operate them with p-polarization (after the necessary adjustment of polarizing optics) [Lück, Grote].

of higher order modes, or a DC offset in the OMC. Suspension within vacuum, and a redesign of the OMC incorporating four mirrors would largely alleviate this problem. Currently there is no OMC installed in GEO 600.

1.3.3. Test mass suspensions
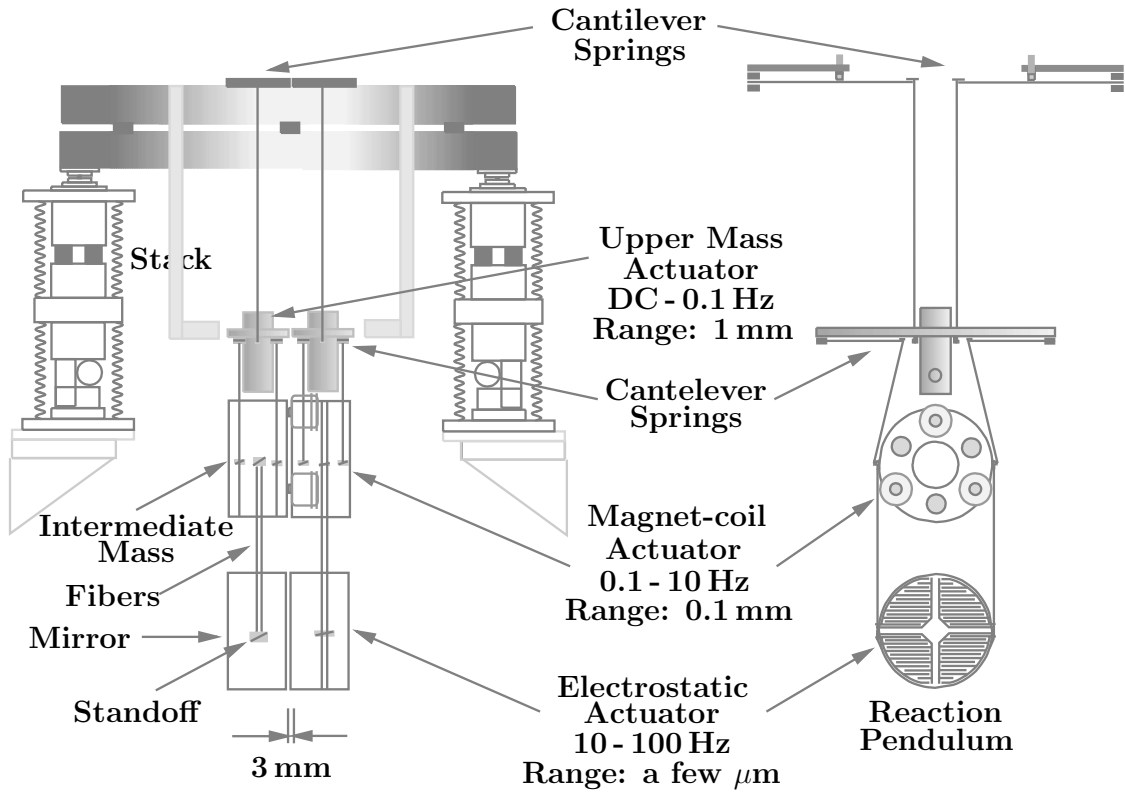
Figure 1.8.: The GEO 600 quasi-monolithic triple pendulum suspension and reference pendulum. The three pendulum actuators and their respective frequency and actuation ranges are also shown.

One of the advanced techniques used by GEO 600 is that of quasi-monolithic triple-pendulum suspensions (QMTPS). A diagram of a near mirror QMTPS and reaction pendulum suspension is shown in Figure 1.8. For detailed information about many aspects of these pendulums, see [Goßler]. The three pendulum stages provide effectively f^{-6} filtering of vibrations from the upper stage to the mirror level for frequencies well above the main pendulum resonances. This is one of the most important factors that help determine the low-frequency limit to GEO 600 sensitivity, as will be discussed in 1.4.4. In addition, for the near mirrors a reference triple

pendulum is suspended behind the main QMTPS to provide a quiet actuation reference. This system allows a three-level split-feedback system with high dynamic range (~ 15 orders of magnitude[14]). Large and thus relatively noisy feedback is applied to the upper and intermediate stages, and only fine actuation is applied at the mirror level. The approximate frequency and actuation ranges of the MID longitudinal feedback applied to these actuators is also shown in Figure 1.8.

The pendulums are referred to as 'quasi-monolithic' because the lower two stages are made from high-quality fused parts that have been joined together by flame welding and hydroxy-catalysis bonding [Gwo, Smith, Sneddon]. This is done for two reasons, both concerning thermal noise, which will be discussed below in 1.4.2. The first is to preserve the high *mechanical quality factor*, or Q, of the test mass in order to reduce its off-resonance internal thermal noise level (see below). The second is to ensure that only materials with high Q are located close to the test mass stage to ensure the lowest possible test mass motion due to pendulum thermal noise[15]. For more information about the characteristics and expected noise performance of the quasi-monolithic stages, see [Goßler, Goßler04b, Smith04], and the following section.

Electro-static drives

The actuators used for the upper two levels of the QMTPSs are straightforward magnet-coil actuators that produce a force proportional to the voltage input to their current drivers [Grote03]. The electro-static drives, however are more complicated. They were chosen as actuators because unlike magnet-coil actuators, they require no additional materials to be attached to the test masses. The ESDs for **MCe** and **MCn** each consist of four quadrants of combs of adjacent gold electrodes deposited onto the surface of the respective reaction masses. When a voltage is applied to the electrodes, the drive exerts a pulling force on the dielectric test mass. Since both the polarization of the dielectric material and the force applied to the induced dipoles are proportional to the applied voltage, the total force on the test mass is proportional to the voltage squared,

$$F_{\text{ESD}} \sim U^2, \tag{1.6}$$

---

[14]This is calculated as the difference between the order of magnitude of displacement of the largest signals applied to the actuators on the upper stage, and that of the signals applied to the ESD actuators at the unity gain frequency of the MID longitudinal control loop.

[15]Pendulum thermal noise of the upper and intermediate stages experience the filtering of the respective pendulum stages before reaching the test mass. Therefore, the test mass stage is most important.

where U is the applied voltage [Grote03, Strain02]. In order to produce bipolar forces on the test mass, a large DC bias voltage is added to U. A discussion of additional noise that could be caused by this nonlinear actuator will be given in Chapter 3.

1.3.4. Automatic beam alignment

As discussed above, GEO 600 consists of multiple optical cavities formed by suspended optics, many of which are separated by large distances. For the interferometer to maintain longitudinal lock and produce sensitive output signals, the alignment and overlap of many of the beams associated with these cavities must be controlled. This is the task of the automatic-alignment system, called *autoalignment* or *AA* for short. This system senses positions of beams at various points in the interferometer using position sensitive devices, such as quadrant photodiodes. In addition, it measures the degree of overlap of the beams using differential wavefront sensing. Both of these types of degrees of freedom are controlled by applying feedback to the corresponding degrees of freedom of the suspended optics. The full AA system is described in detail in [Grote03, Grote04]. The most crucial degrees of freedom concerning the stability of the detector and its sensitivity, are the alignment and overlap of the beams of the Michelson interferometer. The noise performance of the Michelson differential autoalignment system is described later in 3.3.5.

1.4. Theoretical limit to sensitivity

Figure 1.9 shows the theoretical limit to the sensitivity of GEO 600 for a signal-recycling cavity detuning of 550 Hz (the effects that different detunings have on this curve will be discussed further in 1.4.1). This comprises the uncorrelated sum of the calculated apparent strain amplitude spectral density produced by the various 'fundamental'[16] noise sources considered to be inherent in the instrumental design. This section will introduce the few theoretical noise sources that are expected to limit the final sensitivity of GEO 600.

---

[16]This nomenclature is appropriate for all of the GEO 600 theoretical noise sources shown here, except seismic noise, which can be measured by seismometers, and in principle, subtracted away from the detector output. The other noise contributions cannot be subtracted. They originate from random processes, and the DRMI provides the most sensitive measure of their effects, which are indistinguishable from gravitational waves.
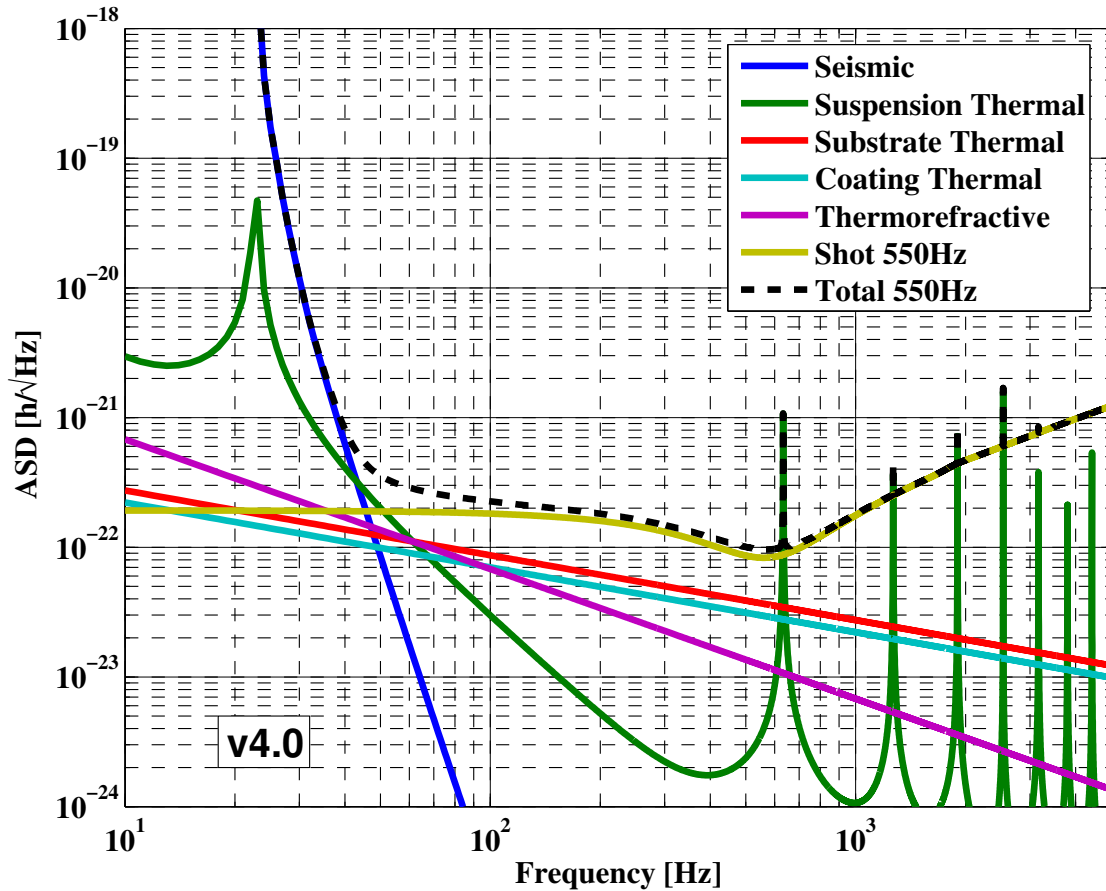
Figure 1.9.: Theoretical sensitivity limit for GEO 600 with a signal-recycling cavity detuning frequency of 550 Hz.

1.4.1. Shot noise

Shot noise is the quantum-limited intensity noise of light, which, as already mentioned, sets a limit on the sensitivity of an interferometric GW detector [Mizuno, Buonanno]. It may be interpreted as arising from random photon detection events in a given photodetector due to the discreteness of light, or as a property of the light field itself. Recently, *squeezed light* [Caves] has been shown to exhibit intensity noise below the shot noise limit (also in dual-recycled interferometers [Valbruch], and in the measurement band of GEO 600 [Vahlbruch06]), which makes it an exciting option for improving the shot-noise limited sensitivity of GW detectors [Schnabel]. Squeezed light will not be used in GEO 600, but it is planned to be implemented in the upgrade, GEO HF [GEO HF].

The ASD of shot noise for a given average light power, $\bar{P}$ is

$$\tilde{S}(f) = \sqrt{2hf_{\mathrm{L}}\bar{P}}, \tag{1.7}$$

where f_{L} is the frequency of the light and h is Planck's constant. This white noise limits the sensitivity of the signal detected at the output photodetector of GEO 600. In addition, the heterodyne detection scheme used by GEO 600 leads to an increase in the detected shot noise in the demodulated output signal of about 20-40% [Meers88], depending on several parameters associated with the (de)modulation signals and the detuning frequency of the SRC. The demodulated signal is divided by the optical transfer function of the DRMI, to give the strain limit to sensitivity. The determination of this transfer function is complicated, depending on many of the optical properties of GEO 600 such as mirror reactivities, losses, cavity lengths and control sideband modulation depths. For this reason, the shot-noise limited sensitivity for GEO 600 is calculated using FINESSE [FINESSE, Freise], a powerful frequency-domain simulation tool developed within our group. For a discussion concerning the calculation of the optical transfer function of GEO 600 see [Malec05].

signal-recycling is a unique feature of GEO 600 with respect to other GW detectors. This is immediately apparent in the shot-noise limited sensitivity. Since the resonance frequency of the SRC can be detuned to enhance signal sidebands at a given Fourier frequency by minute adjustments of the signal-recycling mirror position, it is possible to shape the shot-noise curve. Simulated shot-noise limited sensitivity spectra for various tunings and the corresponding total theoretical sensitivity limits are shown in Figure 1.10.

Since for a given MID control sideband modulation depth, the strain signal at the detector output increases proportionally to the power in the interferometer, while the shot noise increases with the square-root of this, it is optimal to have the highest laser power that the interferometer can accommodate. For the current configuration of GEO 600 a limit to intra-cavity power of around 40 kW is set by thermal lensing due to absorption of the beamsplitter [Winkler06], which was derived to be less than 0.25 ppm/cm, representing the lowest value measured in fused silica [Hild06b]. However, reaching this power would require a higher-power laser system, or larger power-recycling factor, neither of which will be installed before GEO 600 becomes GEO HF. A power of 10 kW incident on the BS was assumed for the curves shown in Figure 1.10.

It should be noted that while the modeled shot-noise limited sensitivity spectra presented here are approximately correct, they are not perfect. Several effects, such as the optical spring resonance [Harms, Miyakawa], have not yet been taken
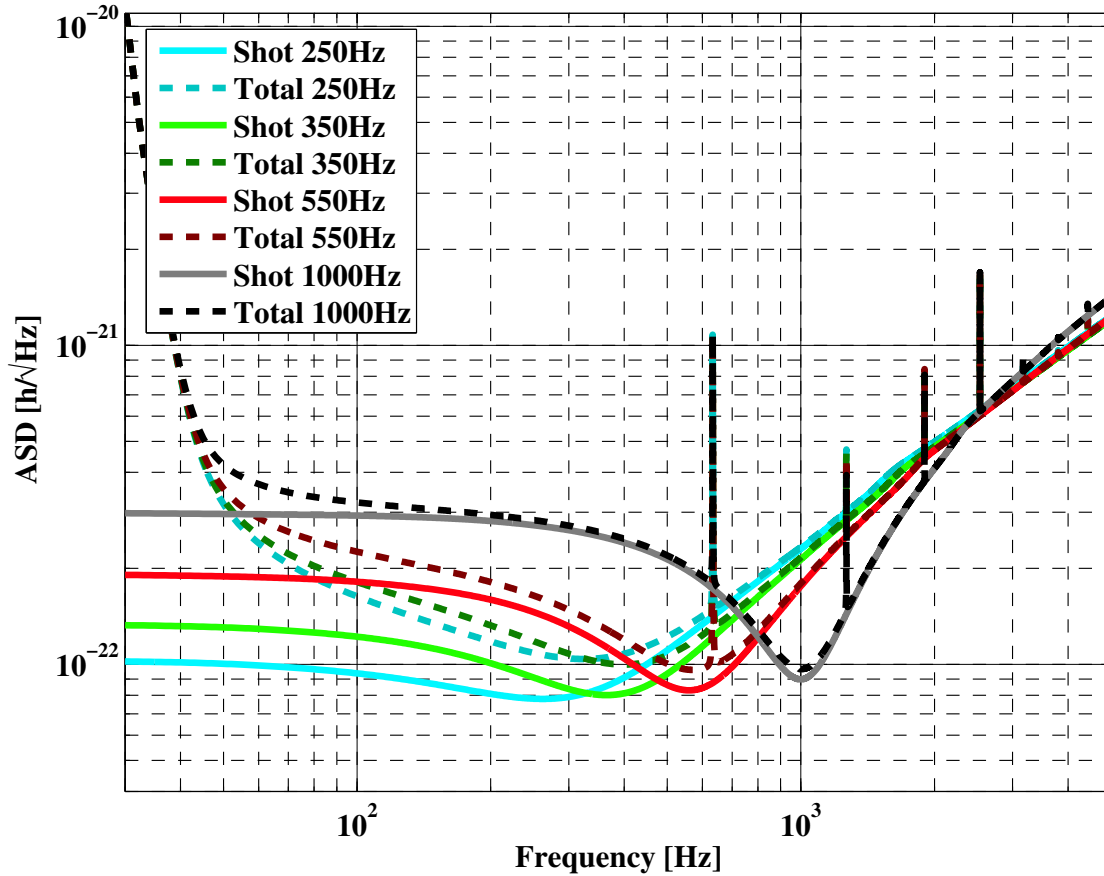
Figure 1.10.: Modeled shot noise limited sensitivity curves for GEO 600 for a power of 10 kW incident on the beamsplitter and four different detunings of the signal-recycling cavity. The total limits resulting from uncorrelated sums of all other theoretical noise sources and the shot noise are also shown.

into account. The continual improvement of the shot noise model accuracy is a work in progress within the GEO 600 group that extends beyond the scope of this thesis.

1.4.2. Thermal noise

Mechanical thermal noise consists of fluctuations of the position of an object arising from temperature-driven Brownian motion of the molecules within a material. The most troubling manifestations of thermal noise in GW detectors are those associ-

ated with the materials of the test masses and their suspensions[17]. The frequency-dependent thermal noise motion spectrum of a given object is directly related to its mechanical energy dissipation by the fluctuation-dissipation theorem [Callen]. The integral over this spectrum is constant, depending only on temperature. Therefore, the less dissipation a material has, *i.e.,* the higher its Q, the more of its thermal motion will be confined at its resonance frequencies, and the lower the off-resonance thermal noise [Saulson]. For these reasons, the materials for the optics and suspensions of GW detectors are designed to have as high Q as possible, and geometries that give resonance frequencies that lie outside of the measurement band. In addition, future GW detectors will be operated at cryogenic temperatures to reduce the thermal noise.

Internal thermal noise

Thermal noise originating from fluctuations in the substrate material of the test masses is known as *internal thermal noise.* Components of this along the longitudinal axis of the MI produce random differential arm-length fluctuations that cannot be distinguished from GWs and that significantly contribute to the theoretical sensitivity limit of GEO 600. These thermal motions are sensed and averaged over by the Gaussian profile of the laser beam on each mirror surface, as described in [Levin]. To minimize the level of internal thermal noise over the measurement band, GEO 600 mirrors are made of very high quality fused silica, and their geometries were chosen to have the lowest internal resonance frequencies above the measurement band of the instrument (the first is above 11 kHz [Smith04]). In addition, as described in Section 1.3.3, in order to preserve the high quality factors of the MI mirrors, they are suspended quasi-monolithically. This reduces any dissipation of the mirror substrate related to rubbing at the interfaces between different materials such as occurs in clamps or wire slings.

In order to determine the level of internal thermal noise in GEO 600, the quality factors of the test masses were measured. The thermal noise motion associated with the MI mirrors that was calculated based on these measurements is [Smith04],

$$\hat{X}_{\mathrm{substr}}(f) = \frac{9.40 \times 10^{-20}}{\sqrt{f}} \qquad \left[\frac{\mathrm{m}}{\sqrt{Hz}}\right]. \tag{1.8}$$

However, recent research concerning the thermal noise properties of fused silica indicate that the above equation may be an overestimate. A compilation of measure-

---

[17]Electrical thermal noise due to temperature-driven motions of electrons in conductors is also an important noise source for GEO 600, especially for the main output photodiode [Grote06]. However, this is considered to be a sort of 'technical noise' (see below).

ments from around the world [Penn05] indicates that the intrinsic loss of fused silica may be more than an order of magnitude lower than that measured in [Smith04], and may also be frequency dependent[18].

Coating thermal noise

In order to minimize optical losses and allow high power buildup in the DRMI, the main optics of GEO 600[Winkler06] are coated with highly reflective coatings. Such (Bragg) coatings are produced by stacking alternating quarter-wavelength optical path-length layers of materials of differing indexes of refraction such that all reflections constructively interfere. The MI mirrors are coated with 32 alternating layers of silica and tantala. The thermal noise of the coating material can be estimated from its quality factor and its thickness, again following Levin's approach [Levin]. These have been measured to be 2.7×10^{-4} and 4.27μm, respectively [Crooks04, Penn]. The expected level of coating thermal noise is shown in Figure 1.9. Coating thermal noise is expected to be one of the limiting noise sources in several of the next generation interferometric GW detectors. Therefore, research on reducing the thermal noise of mirror coatings is currently very active.

Suspension thermal noise

Thermal noise of the various components of the suspensions of the MI optics also causes longitudinal motions of the MI, and thus contributes noise to the detector output. Within the GEO 600 measurement band, the importance of the thermal noise of the suspension components increases with the proximity of the component to the test mass. This is because the thermal motions of the components of the upper and intermediate stages are filtered by the transfer functions of the pendulum stages when they reach the test mass. In particular, the fused-silica fibers used to suspend the main optics play a key role. For details about these fibers and in particular, measurements of their Qs and discussion of their role in GEO 600 pendulum thermal noise, see [Goßler, Goßler04b]. The estimated pendulum thermal noise limit to sensitivity is shown in Figure 1.9, with the main visible features belonging to thermal noise of the bounce mode (longitudinal elongation mode of the fibers) at 22Hz, and the fundamental and harmonics of the fiber violin modes at multiples of roughly 600 Hz.

---

[18]The discrepancies between these measurements are likely due to additional energy loss through the suspension fibers for the measurements of the GEO 600 mirrors, as explained in [Smith04]

1.4.3. Thermorefractive noise

Because GEO 600 does not use Fabry-perot arm cavities, the full power of the laser light within the DRMI is present at the beamsplitter. This means that (apparent) differential length fluctuations imparted on the beams due to noise at the beamsplitter will experience roughly the same transfer function to the detector output as those of the other mirrors of the MI (as was explained in 1.2.1). Besides the longitudinal motions of the mirrored surface that contribute to the thermal noise estimates given above, the beamsplitter can also contribute noise to the detector output via path length changes of the beam transmitted through its substrate. Of this class of noise, the most important for GEO 600 is thermorefractive noise. This arises when random temperature variations translate, via a nonzero dependence of the index of refraction on temperature, into microscopic variations of the index of refraction of the beamsplitter substrate material. For a more detailed description of this effect, see [Braginsky]. The estimated sensitivity limit due to thermorefractive noise is shown in Figure 1.9.

1.4.4. Seismic noise

Finally, the limit to sensitivity at lower Fourier frequencies (below about 50 Hz) is determined by the local motions of the ground on which GEO 600 rests and the attenuation systems used to filter these motions on the path from the ground to the test masses. These include a layer of passive rubber in the stacks supporting the suspensions, and the triple pendulum suspensions, as shown in figure 1.8. This gives roughly a f^{-8} attenuation[19] from 30 to 50 Hz, which when combined with the roughly f^{-2} decrease in the seismic motions over the same range, gives the f^{-10} shown in Figure 1.9.

Seismic noise is not a fundamental noise source. It is distinguishable from a GW in that it can be measured using seismometers that have utterly negligible sensitivity to GWs. Given a sensitive array of seismometers, and a well-understood transfer function from seismic motion to longitudinal motion of the test masses, seismic noise could be fed-forward to the actuators or subtracted from the detector outputs. In practice, however, this may be very difficult.

---

[19]A single pendulum has response f^{-2} above $f_0 = \sqrt{g/L}/2\pi$, where g is the acceleration due to gravity and L is the length of the pendulum. The individual pendulum stages of the main optics of GEO 600 have a length of about 0.28m, giving a resonance frequency just below one Hertz. GEO 600 triple pendulums are very complex, involving multiple cross couplings, that can complicate the response of the transfer function. For more information about this see [Goßler, Smith05].

1.4.5. Comparison with other interferometric GW-detectors
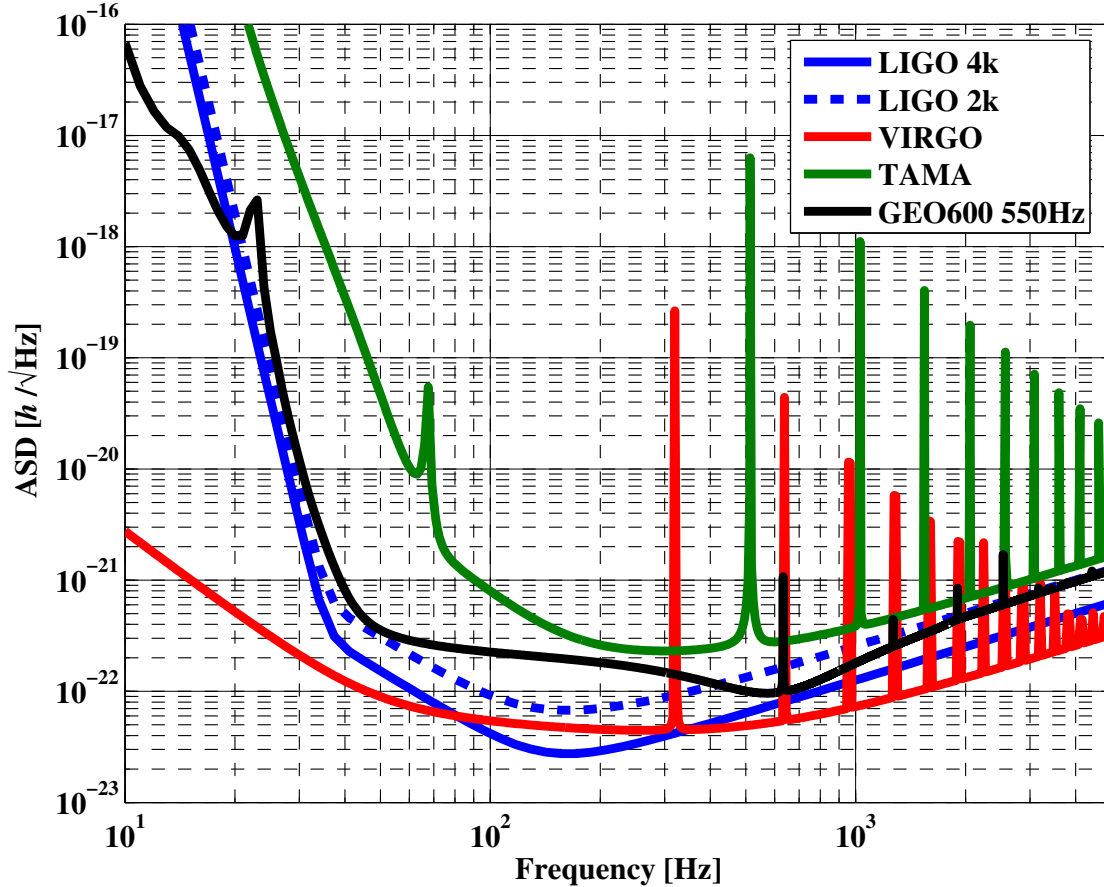
Figure 1.11.: Theoretical sensitivity limits for GEO 600, with a signal-recycling cavity tuning of 550 Hz, the 4-kilometer and 2-kilometer LIGO detectors, TAMA, and VIRGO.

The theoretical sensitivity limits for all of the first generation of long baseline interferometric GW detectors are shown in Figure 1.11. The LIGO 4 Km interferometers are expected to achieve the beast peak sensitivity, in part due to their longer baseline. VIRGO is expected to have the best sensitivity below 80 Hz due to the aforementioned aggressive seismic attenuation strategy. The GEO 600 sensitivity shown is for a tuning of 550 Hz, which gives a sensitivity limit comparable to that of the much larger LIGO and VIRGO detectors, particularly from 500 to 1000 Hz.

1.4.6. Technical noise

In addition to the theoretical noise sources described in this section, there exists a variety of expected but not insurmountable so called *technical noise* sources. These include, *e.g.,* electronics noise of the various control servos, scattered light, and laser amplitude and frequency noise. These typically limit the sensitivity of interferometric GW detectors during the commissioning phase, and it is the identification and removal of these that makes up the bulk of noise hunting. A brief overview of the development of the primarily technical-noise limited sensitivity of GEO 600 over the past few years is given in the next section. Work undertaken to identify and quantify the level of coupling of these noise sources to the detector output will be the main subject of the rest of this work.

1.5. Short history of the performance of GEO 600

Two of the most important measures of the performance of a GW detector are its sensitivity to GW strain, and the percentage of time the detector is operating in a well-understood way and with a good sensitivity, its so called *duty cycle*. The sensitivity is typically quantified, as in this work, by an ASD of the detector output calibrated to apparent strain. Other measures exist however, that may be more relevant for a particular GW signal search (*e.g.,* the so-called *inspiral range*).

The following subsections describe the configuration and performance of GEO 600 during each of the data-taking runs it has taken part in. These so called *science runs*, are periods of time in which GEO 600 ran in coincidence with LIGO and other GW detectors of the LIGO Scientific Collaboration (LSC). These represent the longest periods of data-taking for which the GEO 600 detector was well-understood, undergoing as few as possible hardware changes, and accurately calibrated.

1.5.1. S1

The first official scientific data recorded by GEO 600 was during the inaugural LSC science run, S1, between August 23 and Sept 9, 2002. The detector was operated as a PRMI (*i.e.,* without signal-recycling). In addition, the main optics of the MI were test mirrors suspended from test triple-pendulum suspensions using steel wires and clamps instead of fused silica fibers and silicate bonds. Some of the configuration parameters for this run are summarized in Table 1.2. For more information about

the configuration of GEO 600 during S1 see [LSC04, Willke].

Optical Configuration	PRMI
T of MSR	MSR not installed
MSR tuning	MSR not installed
T of MPR	1.35%
Power into MC1	2 W
Intra-cavity Power	300 W
MI mirrors	Test mirrors and suspensions

Table 1.2.: Configuration parameters for GEO 600 during S1.

The typical sensitivity during S1 is shown in Figure 1.12. Also shown are the *calibration lines* that are used to calibrate the coupling of different observables into the detector output. For information about the calibration of the data recorded by the GEO 600 PRMI during S1, see [Hewitson03]. The sensitivity from about 300 Hz to 2 kHz was limited by scattered light. This was determined by both the shape of the noise, a characteristic *scattering shoulder*, and its non stationarity. A duty cycle of 98.5% was achieved over S1.

1.5.2. S2

After S1, the final MI optics were suspended quasi-monolithically, and the signal-recycling mirror was installed. GEO 600 did not take part in the S2 science run, but rather allocated this time to incorporate the changes, and in particular, to commission the control of the signal-recycling cavity. For details about the commissioning work undertaken during this period, see [Willke, Grote04b, Smith05].

1.5.3. S3

The third LSC science run, S3, was performed between November 1st, 2003 and January 13th, 2004. The commissioning work mentioned above produced a stably-locking DRMI only about two weeks before the start of S3, leaving little time for testing and sensitivity optimization. Therefore it was decided that GEO 600 would run for about one week, near the start of S3, then go offline to allow time to improve the sensitivity and stability of the detector, and finally rejoin for the remainder of the run. Thus, GEO 600 participation in the S3 science run was divided into two separate periods of time, having somewhat different interferometer configurations
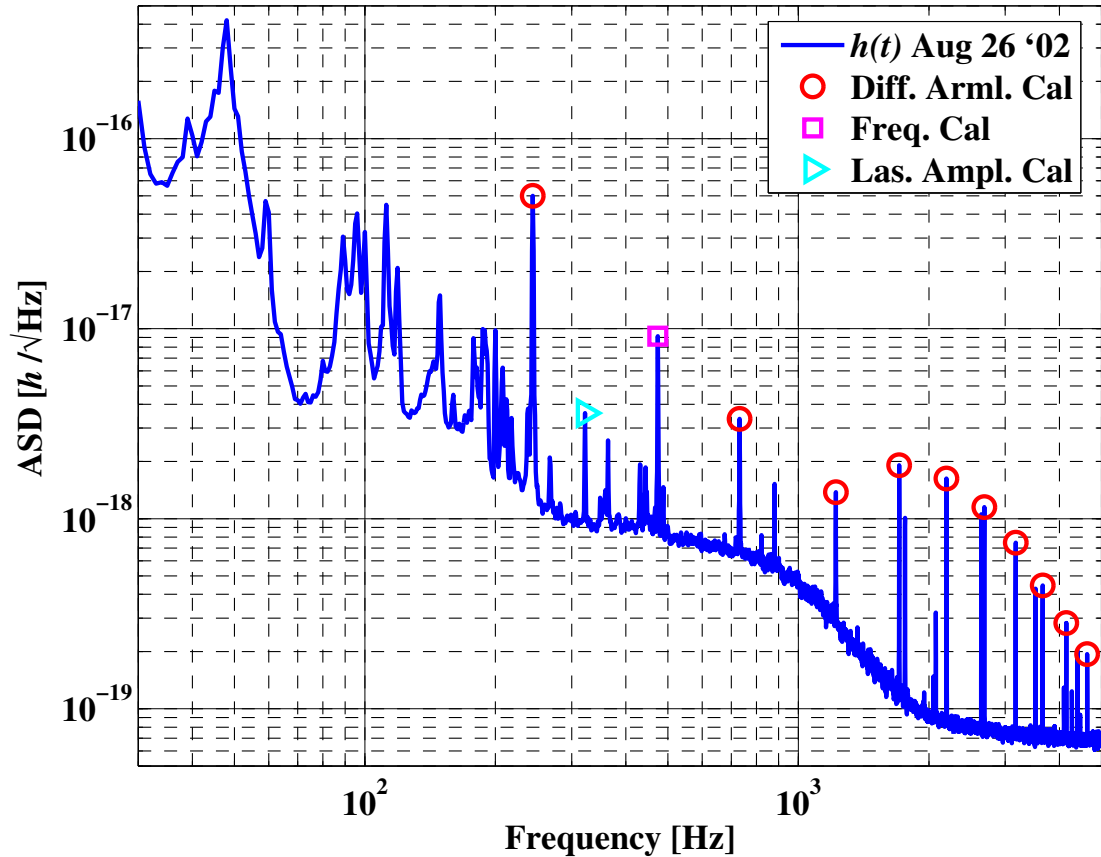
Figure 1.12.: Typical sensitivity during S1, with continuously injected calibration lines marked.

and sensitivities. The first, referred to here as S3 I, ran from November 5th through 12th. The second, S3 II, ran from December 30th to January 13th. During both periods GEO 600 was operated as a dual-recycled Michelson interferometer with an SRC detuning close to 1 kHz. Table 1.3 summarizes the configuration parameters during S3[20]. The following gives an overview of the status of GEO 600 during S3 I and S3 II, as well as a description of the work undertaken during the period between them. For more information about the configuration and performance during S3 see [Smith04b].

---

[20]The intra-cavity power was roughly the same for S1 and S3, despite the mode-healing effect of the signal-recycling cavity. This is because the relatively high transmission power-recycling mirror used for these runs (and S4) made the losses due to higher order modes less critical. For times after the installation of a more highly reflective power-recycling mirror (see below), the mode-healing effect resulted in a roughly 50% increase in the intra-cavity light power.

Optical Configuration	DRMI
T of MSR	2.3%
MSR tuning	1.3 kHz for S3 I, 1 kHz for S3 II
T of MPR	1.35%
Power into MC1	2 W
Intra-cavity Power	300 W
MI mirrors	Final mirrors and suspensions

Table 1.3.: Configuration parameters for GEO 600 during S3.

S3 I

GEO 600 participation in S3 I provided the first ever scientific data recorded by a long-baseline dual-recycled Michelson interferometer. For this period, the SRC detuning was set to 1.3 kHz to give the best peak sensitivity with regard to the technical noise that were present. The sensitivity for S3 I is shown in Figure 1.13. The calibration of the detector outputs of the GEO 600 DRMI are more complicated than for the PRMI case, as described in [Hewitson04, Hewitson04c, Hewitson04b]. The duty cycle for this run was 95.2%, very high considering the relatively immature status of the dual-recycled lock.

S3 engineering period

The period following S3 I was used to improve the lock stability and sensitivity of the detector. The causes for most of the losses of lock were identified, and when possible, fixed. Noise analysis performed during this period indicated that the limiting noise sources during S3 I were: noise introduced by the servo used to control the longitudinal degree of freedom of the SRC; electronic noise of the photodiode used to measure the MID longitudinal error-point; and phase noise of the function generator that supplied the (de)modulation frequency signal for the MI. The noise level introduced by the SRC servo was reduced by changing the gain distribution within the servo electronics. The MI function generator and high power photodiode were replaced with models with lower phase and electronic noise, respectively. These changes led to the improved sensitivity during S3 II.
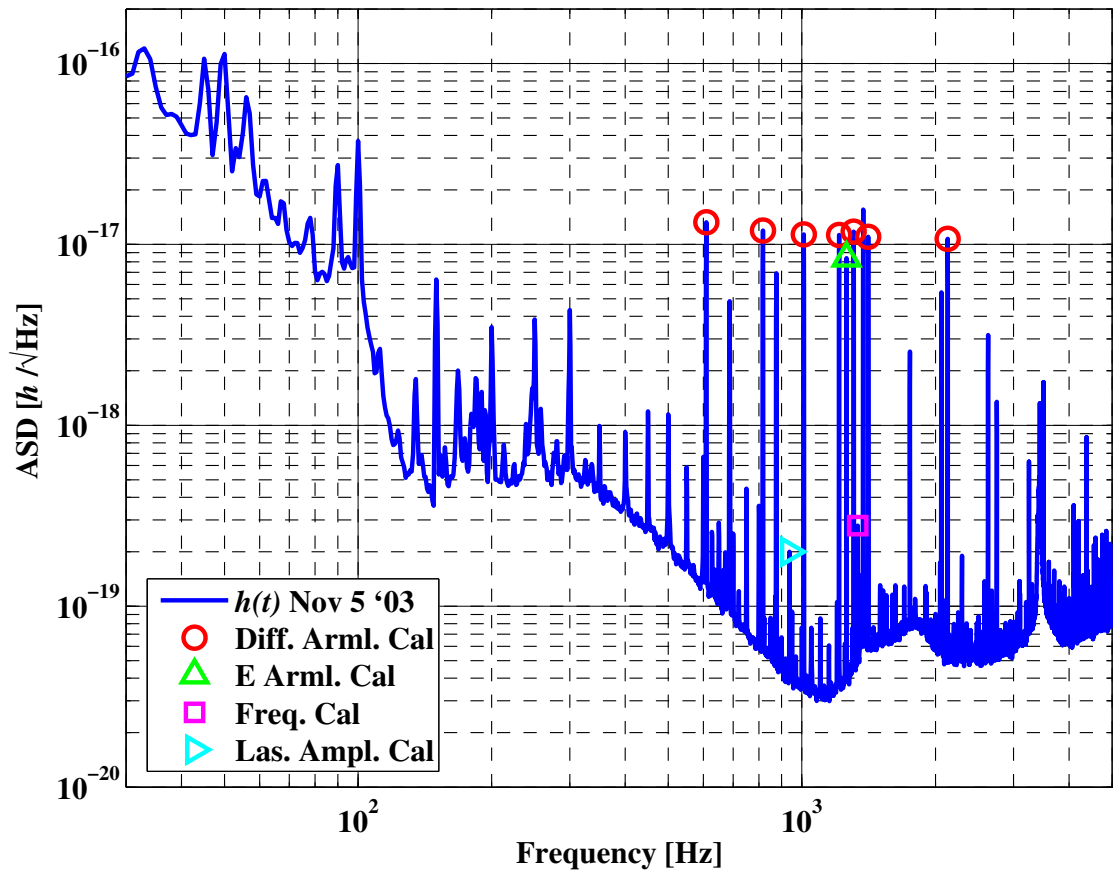
Figure 1.13.: Typical sensitivity during S3 I, with calibration lines marked.

S3 II

The configuration of GEO 600 during S3 II was basically the same as that for S3 I, except for the improvements of lock stability and noise coupling discussed above. In addition, the SRC detuning frequency was reduced to 1 kHz. The influence of these changes on the sensitivity can be seen in figure 1.14. An order of magnitude peak sensitivity improvement was made during the 47 day engineering period, the fastest such improvement in GEO 600 history. The duty cycle of this period was also improved, with respect to S3 I, to 98.7%, with 5 locks lasting longer than 24 hours, and one longer than 95 hours.
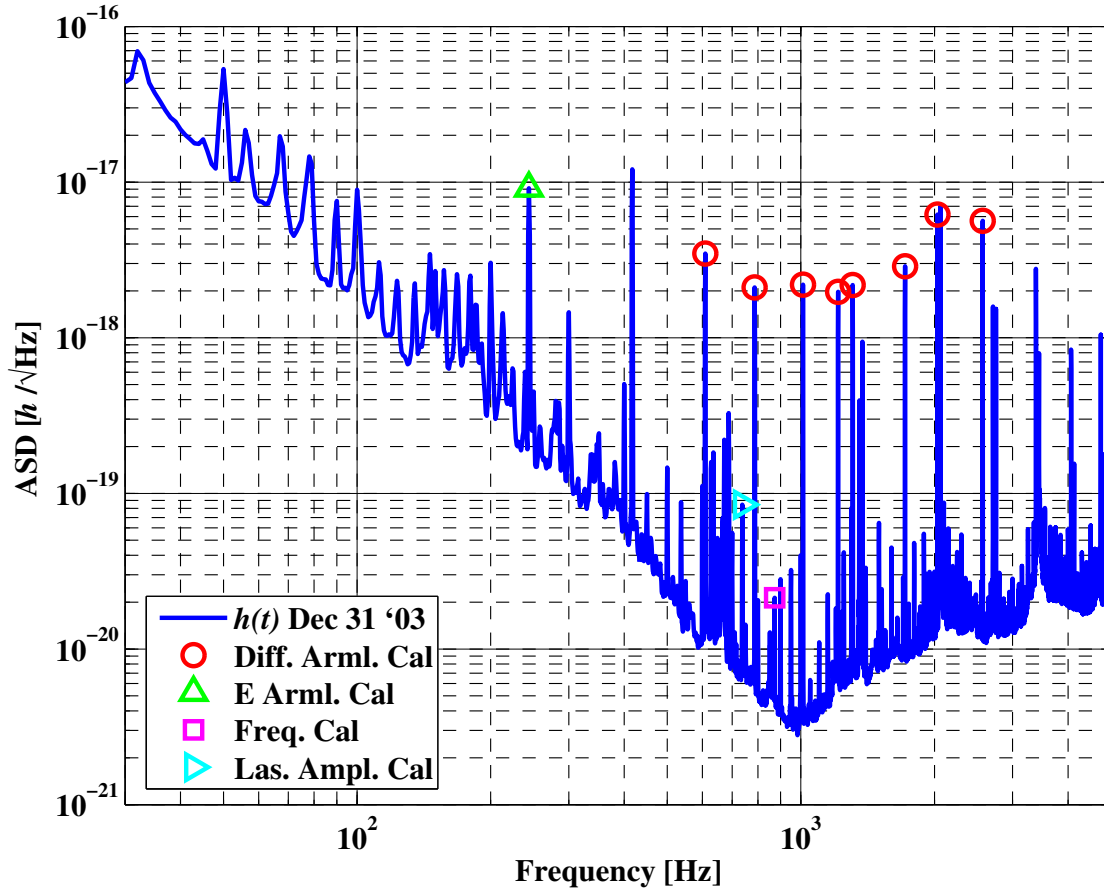
Figure 1.14.: Typical sensitivity during S3 II.

Optical Configuration	DRMI
T of MSR	2.3%
MSR tuning	1 kHz
T of MPR	1.35%
Power into MC1	5 W
Intra-cavity Power	500 W
MI mirrors	Final mirrors and suspensions

Table 1.4.: Configuration parameters for GEO 600 during S4.

1.5.4. S4

The period after S3 was followed by nearly a year of commissioning that resulted in a broadband improvement in sensitivity, highlighted by close to two orders of
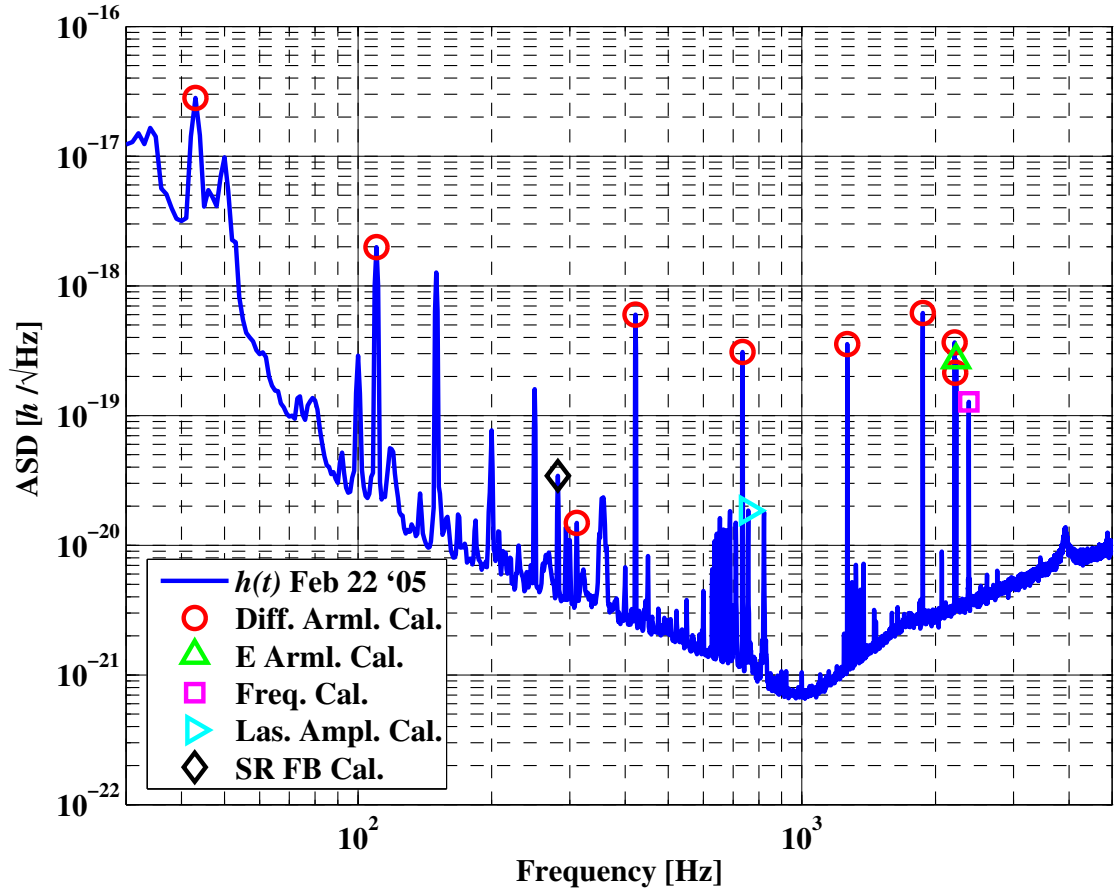
Figure 1.15.: Typical sensitivity during S4.

magnitude less noise around 100 Hz. After this, between February 22 and March 24 2005, GEO 600 took part in S4. The detector was again operated as a DRMI tuned to close to 1 kHz. To maximize the sensitivity, the input laser power used was roughly double that used in S3 II. The configuration parameters for S4 are shown in Table 1.4, and the sensitivity is shown in Figure 1.15. Several of the contributing noise sources during S4 were measured using the methods described in this work, see [Smith06]. Prior to the S4 run, the calibration method was improved yet again to include an optimal combination of two GEO 600 detector output signals to produce a single single signal with a better (optimal) strain signal to noise ratio. For more details see [Hewitson05]. The duty cycle for S4 was 96.6%, and the longest lock lasted more than 52 hours. For more information about the S4 run, see [Lück06, Hild06].

1.5.5. S5

Directly following S4, the 1.35% transmission MPR that had been used since S1 was replaced with a 0.09% mirror. This resulted in a larger power-recycling factor, and thus a larger circulating light power in the interferometer. The following months were devoted largely to stabilizing the detector with the higher power-recycling factor, improving the infrastructure of GEO 600, and noise hunting. Extensive work on reducing scattered light [Hild06] and servo control noise was undertaken. Much of the noise reduction effort was focused on the several hundred Hz region. To accommodate this, the SR tuning frequency was reduced from 1 kHz to lower frequencies, with several months spent at 350 Hz, and a final value of 550 Hz chosen.

Starting in late 2005, the detectors of the LSC began joining the S5 run. On the weekend of January 21, GEO 600 began taking science data during nighttime and weekends, when no commissioning work was being done on the instrument. The commencement of full-time GEO 600 participation in S5 was May 1st (which is, not coincidentally, concurrent with the writing of this thesis). A sensitivity spectrum measured close to the start of the GEO 600 participation in the S5 run is shown in Figure 1.16. The noise sources that contribute to limiting the sensitivity at this time will be discussed in Chapter 3. Approximate values for the configuration parameters at the start of GEO 600 full-time participation[21] in S5 are given in Table 1.5.

Optical Configuration	DRMI
T of MSR	2.3%
MSR tuning	550 Hz
T of MPR	0.09%
Power into MC1	5 W
Intra-cavity Power	2.1 kW
MI mirrors	Final mirrors and suspensions

Table 1.5.: Approximate configuration parameters for GEO 600 during S5.

The S5 run is foreseen to be the longest uninterrupted data taking period for all of the LSC detectors by far. GEO 600 will likely participate in data-taking for of order one year. The author and reader will have to wait to see what the duty cycle and other performance measures will be for GEO 600 during S5. However, with a peak sensitivity of $2.8 \times 10^{-22}\,\mathrm{Hz}^{-1/2}$, and running simultaneously with three even

---

[21]These parameters were not static with time during the night and weekend participation due to commissioning work.
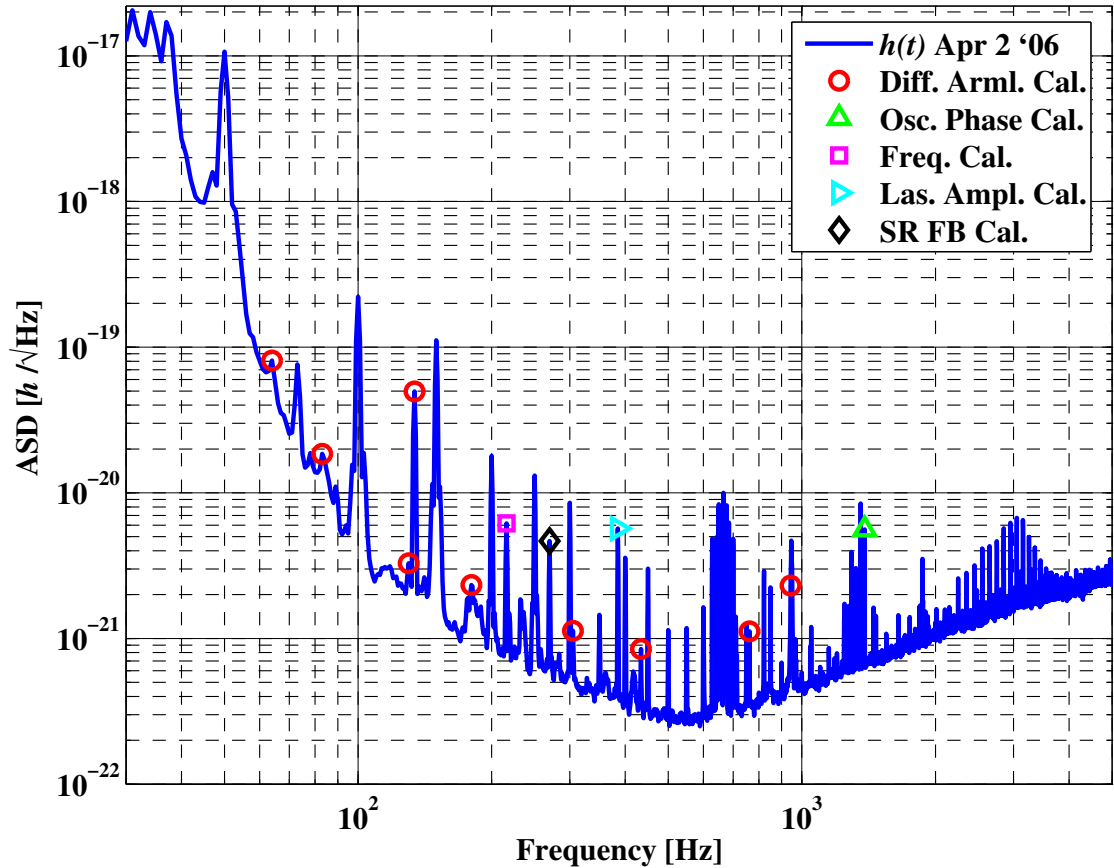
Figure 1.16.: Typical sensitivity close to the start of GEO 600 participation in S5.

more sensitive LIGO detectors, the data produced during S5 promises to be very interesting for gravitational-wave astrophysics.

1.5.6. Evolution of the Performance

One would hope that the result of the past several years of commissioning would be improvement in both key measures of interferometer performance described here. However, the evolution of the duty cycle of GEO 600 for the runs it has completed thus far, shown in Figure 1.17, shows no clear trend.

When compared to the other interferometric GW detectors in the world, these values, which are all not far from 100% are outstanding. However, during none of these runs was the duty cycle limited by unavoidable events, such as large earthquakes, which indicates that an even higher duty cycle is achievable. One possible
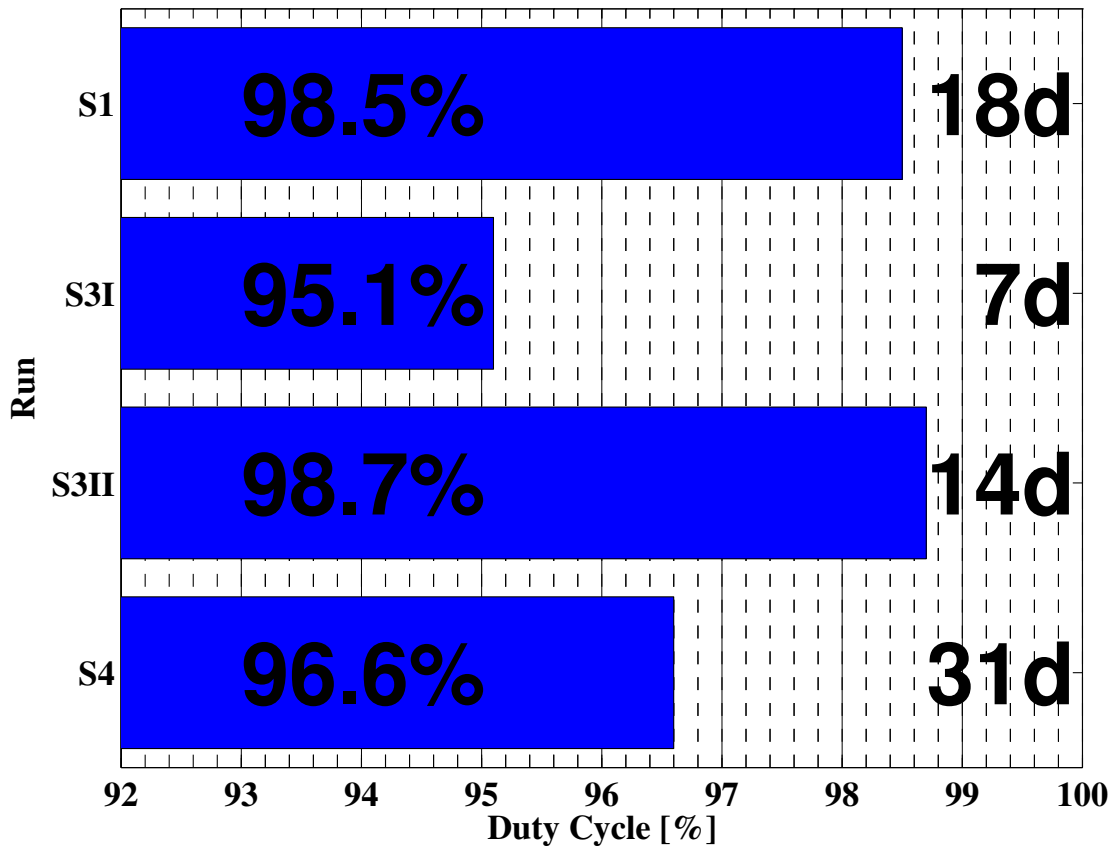
Figure 1.17.: Duty cycle percentages and run lengths in days for the GEO 600 science data-taking runs.

reason that the duty cycle has not tended to improve could be that a sort of equilibrium exists between the rate of identification and removal of causes of losses of lock (this makes up a large part of the commissioning effort), and the introduction of possible failure points through the increase in complexity caused by the addition of ever more control loops and switches to switch to lower-noise signals, *etc.*

The typical sensitivity for all GEO 600 science runs to date are shown in Figure 1.18 with respect to the theoretical noise limit for detunings of 1 kHz (close to that used in S3 and S4) and 550 Hz (that used in S5). Over the past four years, several orders of magnitude of noise have been removed from the detector output. The noise analysis techniques that are described in the following three chapters were essential for the identification of many of the limiting noise sources that have been removed to date. However, GEO 600 has not yet reached its theoretical sensitivity limit. Further commissioning is required to remove the last technical noise from

the detector output, especially below 100 Hz, to allow GEO 600 to reach its full potential.
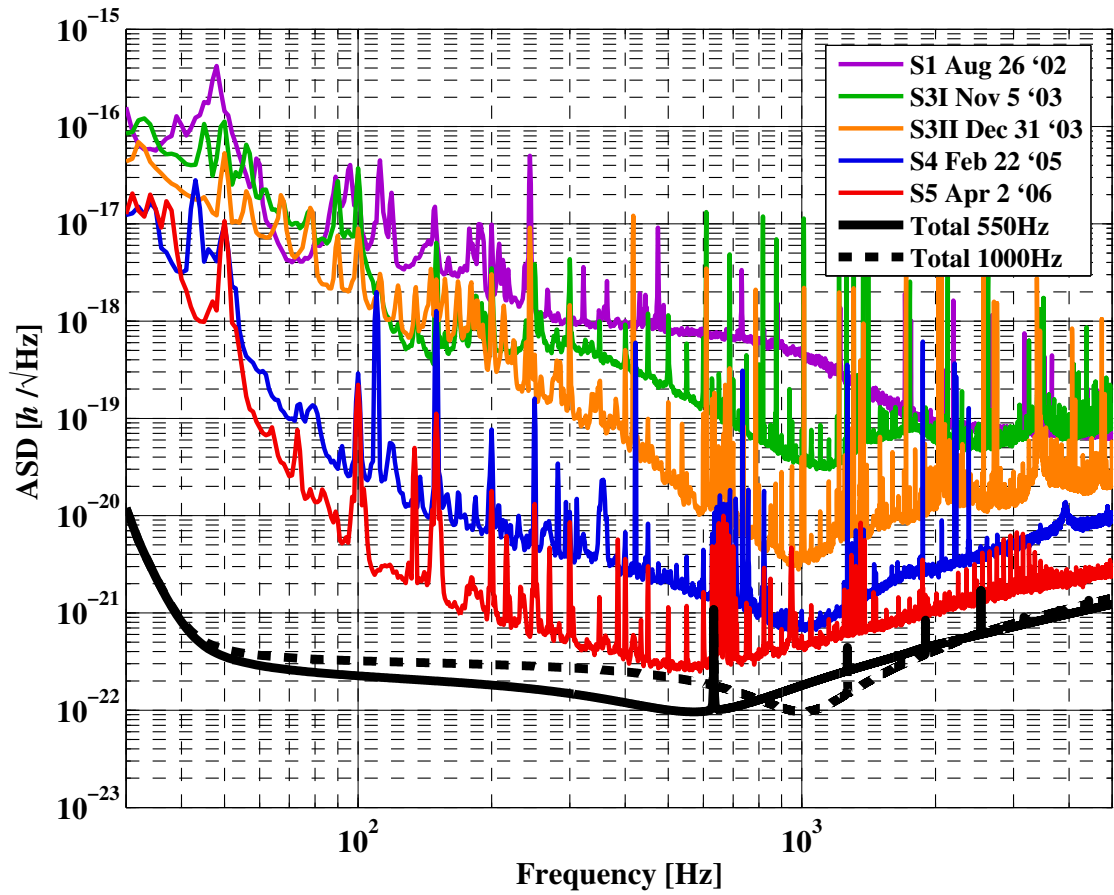
Figure 1.18.: Typical strain sensitivity of the GEO 600 detector output during the science data-taking runs to date. The theoretical sensitivity limits for 1 kHz and 550 Hz tunings are also shown for reference.

Chapter 2.

Principles of noise projections
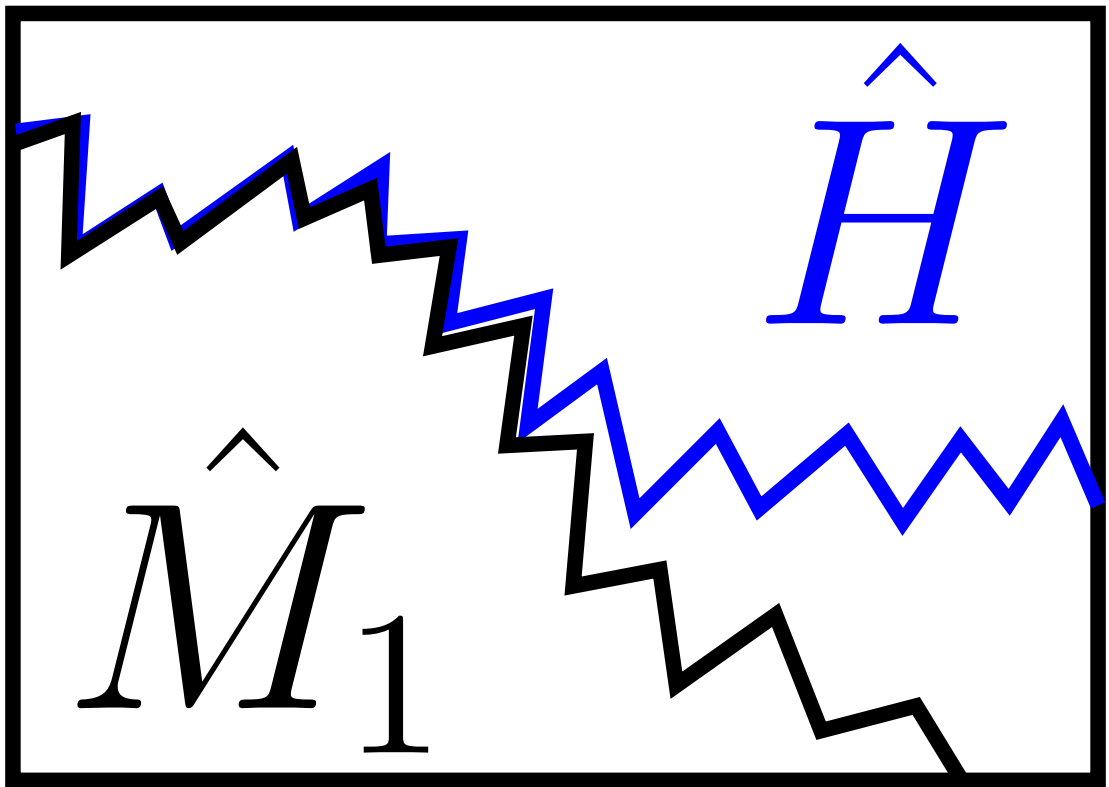
2.1. Introduction

As mentioned in Chapter 1, the scientific teams responsible for the current generation of interferometric GW detectors have spent much of the past few years commissioning these instruments to maximize their potential science output. The goals of this commissioning effort are essentially twofold: the first is to bring the detectors to robust states, allowing them to operate stably, with high duty cycles, over long periods of time (many months); the second involves identification and elimination of any technical noise that couples significantly to the detector outputs (often referred to as *noise hunting*). To help accomplish this second goal, noise analysis techniques have been developed that allow estimation of the levels with which various sorts of technical noise couple into the detector output signals [Allen, Adhikari, Flaminio, Tatsumi]. This chapter describes the principles of *noise projection*[1], the technique most often used to do this by the GEO 600 comissioners.

As was discussed in the previous chapter, GEO 600 is designed to have a peak equivalent strain amplitude spectral density sensitivity on the order of $10^{-22}\,\mathrm{Hz}^{-1/2}$. To achieve this goal, the influence of disturbances, caused by external sources and detector subsystems, on the detector output must be minimized. More than 200 control loops are needed to keep the interferometer and all of its subsystems (laser frequency and power, beam alignment, *etc.*) at their nominal operating points. Although many of these loops are designed to ensure that the observable that they control does not negatively influence the detector outputs, it is often the case that noise sources associated with these loops introduce additional noise to the detector output, reducing its sensitivity to gravitational waves. The combination of these insturmental noise sources and the various sourts of external disturbances, such as seismic or acoustic noise, can couple into the system through a variety of paths. Thus, the number of different noise sources that can contribute to limiting the detector sensitivity, and the number of paths through which they may couple, is very large.

One very effective way to expedite commissioning, is to determine which of the myriad of noise sources contributes most to the current limit to the detector sensitivity, such that the attention of the commissioners can be focused on it. While intuition and simple experiments are often sufficient to achieve this for projects of smaller scale, experience with commissioning at GEO 600 has shown that it is invaluable to systematically determine and track the level with which technical noise

---

[1]To the best of my knowledge, Benno Willke coined this name, and first suggested that we do something like it in a systematic way at GEO 600.

couples to the detector output. The noise projection technique described below is effective at doing this for noise sources that couple in a primarily linear fashion.

2.2. Detector output and noise channels

In the following it is assumed that time-domain signals originate in systems as voltages, and are recorded as *channels*, with a fixed discrete sampling rate using a digital data acquisition system like the one used in GEO 600 [Hewitson04, Kötter, Kötter02]. These channels will be denoted by uppercase italic letters, *e.g.*, X, and indicated in figures with red boxed outputs. For simplicity, the following analysis will be done entirely in the frequency domain. The frequency content of a given channel over a length of time will be described by a discrete Fourier transform $(DFT)^2$ of the time-domain signal over that time. The DFT of the signal recorded in a given channel will be denoted by the same uppercase italic letter as the channel, but with an additional tilde, *e.g.*, $\tilde{X}$. Each of the variables in the equations of this chapter are assumed to be frequency dependent. Thus, for clarity, explicit denotation of frequency dependence is not given.
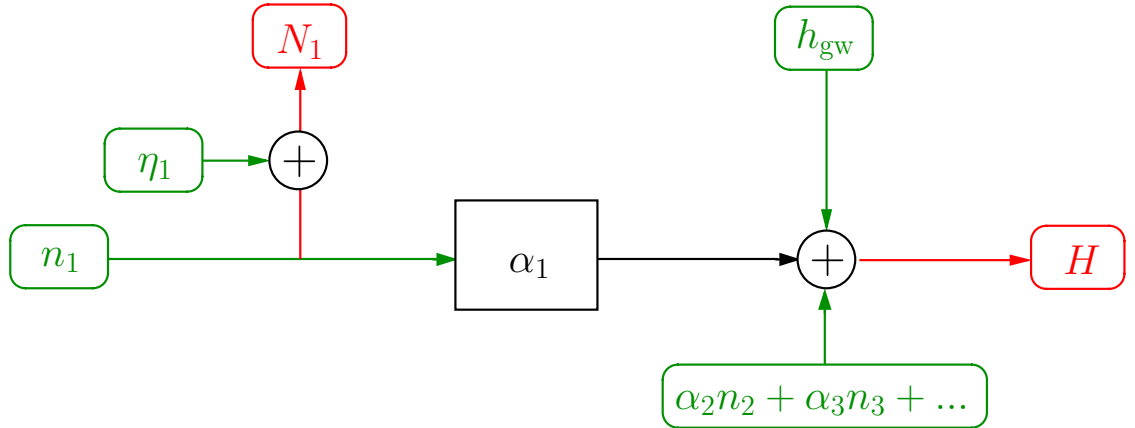
Figure 2.1.: The channels H and N_1 and their constituent signals and noise.

Consider the main detector output channel, H. This is composed of strain from gravitational waves, h_{gw} (at some level), and instrumental and environmental noise that can be decomposed to various noise sources, n_i,

$$\tilde{H} = \tilde{h}_{\mathrm{gw}} + \sum_i \alpha_i \tilde{n}_i, \tag{2.1}$$

---

[2]The DFTs are assumed to be computed using standard techniques, including windowing, as described in [Heinzel02].

where α_i is the complex response of the transfer function relating n_i to H. Now consider that a subset of these noise sources, $n_j \subset n_i$, are measured by dedicated instrumental or environmental devices, along with some additional noise, η_j, and negligible gravitational wave strain. The outputs of these devices are recorded as *noise channels*, N_j, with DFTs given by,

$$\tilde{N}_j = \tilde{n}_j + \tilde{\eta}_j. \tag{2.2}$$

The relationship of a given channel N_1 to H is shown in Figure 2.1. In realistic situations, measurements are only possible through channels, *i.e.*, N_j is measurable, while n_j is not. For that reason it is desirable to have sensitive devices that are well decoupled from other noise sources, such that the additional noise contribution can be reduced to a level low enough that the noise channel is an accurate representation of the noise source in question[3],

$$\tilde{N}_j \simeq \tilde{n}_j. \tag{2.3}$$

If Equation 2.3 holds, the contribution of each n_j to H can be determined by measuring α_j, and forming the product,

$$\tilde{M}_j = \alpha_j \tilde{N}_j. \tag{2.4}$$

This is the noise projection[4] of channel N_j to channel H. A practical procedure for measuring noise projections is given in the following section.

The sum of all noise projections,

$$\tilde{M} = \sum_j \alpha_j \tilde{N}_j, \tag{2.5}$$

is called a *noise budget*[5]. This represents the total amount of the noise present in H that, based on noise projections and the above assumptions, can be considered not to be caused by gravitational waves, but rather by instrumental or environmental noise sources.

In addition to providing information about the level with which various noise sources couple to the detector output, noise projections can be used to improve

---

[3]One may assume that all channels are calibrated, *i.e.,* that H is in units of strain and that each N_j is in the natural units that correspond to the noise source, n_j. However, it is not necessary to do so for the following.

[4]Here we see that a noise projection is not mathematically a projection, but rather a mapping of a given signal using a transfer function.

[5]A term taken from LIGO.

the sensitivity of the detector. A more sensitive detector output signal can be obtained by subtracting the noise budget (or individual noise projections) from H,

$$\tilde{H}' = \tilde{h}_{\text{gw}} + \sum_i \alpha_i \tilde{n}_i - \sum_j \alpha_j \tilde{N}_j. \tag{2.6}$$

The amount by which the noise in the detector output can be reduced depends on the level with which the subset of noise sources that are measured, n_j, couples to H, the degree to which the noise channels represent the noise in question (*i.e.,* Equation 2.3), and the accuracy of the measured transfer functions. Thus the more complete the subset n_j is with respect to the n_i noise sources, the better. Noise subtraction will be described in more detail in Chapter 4.

Allen *et al* [Allen] suggest a similar procedure to estimate and subtract instrumental and environmental noise from the detector output during nominal operating conditions of the detector, using the ambient correlations between H and N_j. However, their method has several drawbacks. First, the correlation of noise channels and the detector output for noise sources that are not completely dominant will be small, resulting in poor (not well-determined) estimates of the transfer functions. Second, since Equation 2.3 is only ever approximately true, in the situation where both N_j and H sense another noise source, n_k, the transfer function estimated will be erroneous; It will not represent the transfer function between two points separated by a causal path. The procedure given in the following section is more robust concerning both of these points.

2.3. Noise projection procedure

A practical procedure for computing the noise projection of N_j to H is as follows: (A diagram of the process, with corresponding steps numbered, is shown in Figure 2.2).

1. **Compute the average transfer function, α_j:**
   In order to ensure an accurate and correct estimate of the transfer function from N_j to H, it is necessary to increase the magnitude of the noise source in question, n_j, enough that it is the dominating noise source in both channels over the frequency range of interest[6]. In this state, the level of correlation

---

[6]This is normally achieved by use of an actuator. For example, if one wished to increase the amount of laser intensity noise in both a laser signal and H, one could add a current noise to the slave laser pump diodes. For most of the measurements done to date at GEO 600, the actuator was driven by a band-limited random noise provided by a spectrum analyzer.
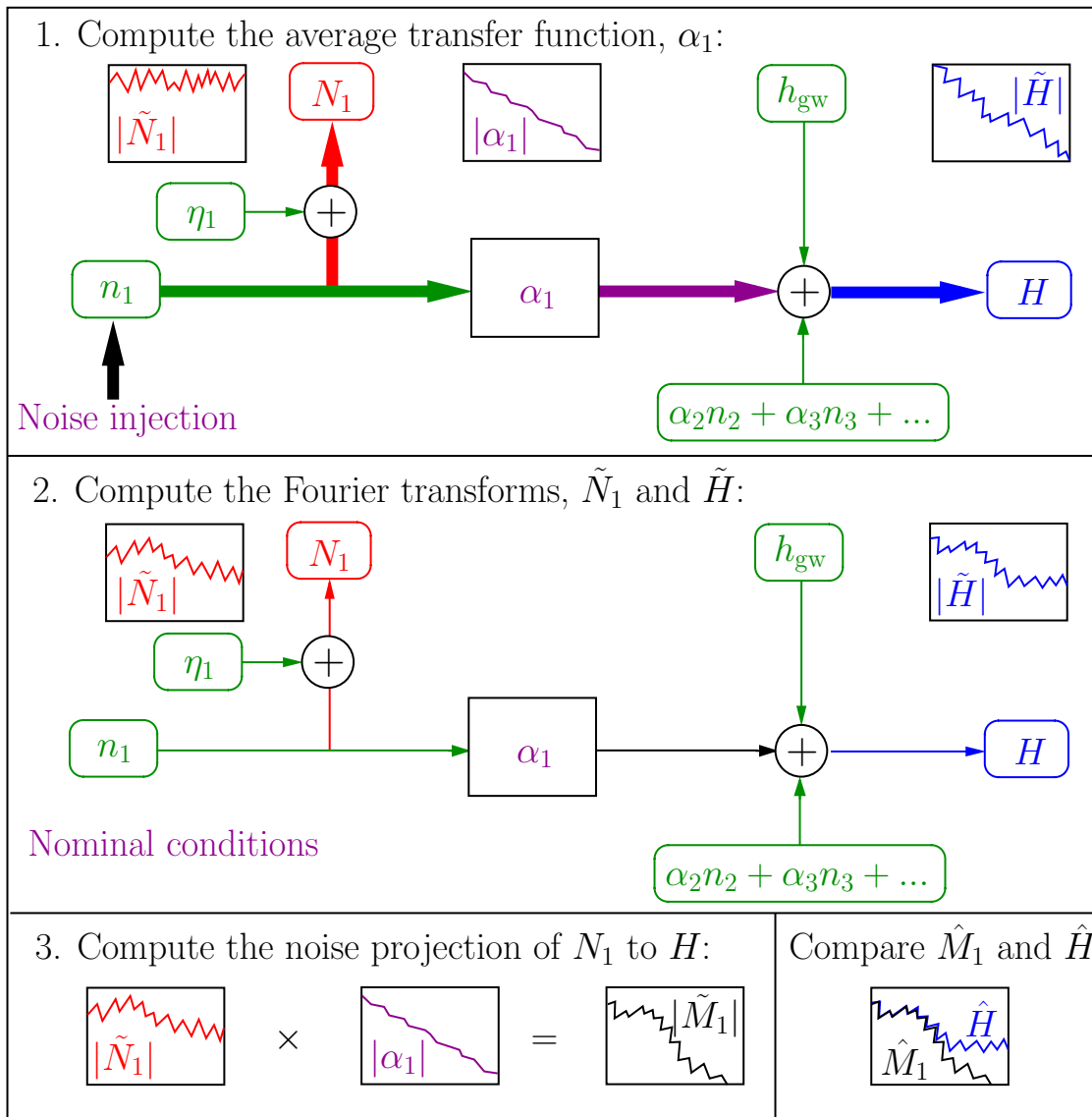
Figure 2.2.: Diagram of individual steps of the noise projection procedure. For steps 1-3, absolute values of example transfer functions and DFTs are shown. The bottom-right box shows a comparison of the projection and H. The thick lines in 1 represent noise dominance due to the noise that is injected to facilitate the transfer function measurement.

between N_j and H is dominated by correlations caused by the type of noise in question, and is large enough to allow computation of a well-defined transfer function with a small variance.

The complex response of the transfer function computed between N_j and H is,

$$\alpha_j = \left.\frac{\tilde{H}\tilde{N}_j^{\,*}}{\tilde{N}_j\tilde{N}_j^{\,*}}\right|_{n_j}, \tag{2.7}$$

where * denotes a complex conjugation, and $|_{n_j}$ indicates that both channels are dominated by n_j. Equation 2.7 is generally averaged over several time segments to reduce the variance[7]. This response will be referred to as simply the *transfer function* in the following discussion.

Alternatively, the transfer function can be calculated using a model, *e.g.,* a pendulum model for seismic noise coupling, or the frequency domain simulation FINESSE [FINESSE] for optical transfer functions. This may be necessary for determining α_i in situations where a suitable actuator for N_j does not exist. However, in most cases, measuring the transfer function while the system is in its nominal state is less prone to errors, since it does not depend, as does a model, on the accuracy with which parameters of the system are known. It is a good idea to compare the measured transfer function with that predicted by a model to check that the coupling is understood, and to refine the model. For example, fitting the measured transfer function to a parameterized model may lead to more accurate parameter estimates that can then be added to the model.

Computation of the transfer function can also be repeated for time segments during which different input signals were injected in order to determine the linearity of the coupling. For example, the transfer function can be measured in the presence of varying amplitudes of n_j, from just dominating both H and N_j, to dominating both by one or more orders of magnitude. In addition, single-frequency disturbances (sine-waves) can be applied, and the influence on other frequency bins in $\tilde{H}$ can be checked. If significant frequency nonlinearities exist, the measured linear transfer function represents a lower limit of the total coupling. Based on the degree of linearity of the coupling, one can decide whether to further pursue a linear noise projection measurement, or rather to use another experimental technique to identify the level of noise coupling. For the rest of this chapter, we will assume that the noise couplings are linear, *i.e.,* that a noise $\tilde{N}_i$ at a given frequency produces a noise $\alpha_i\tilde{N}_i$ in H at preciesely the same frequency. An example of the incorporation of some nonlinear effects in the transfer function of the ESD actuators will be give in Chapter 3.

---

[7]This assumes that the transfer function is relatively stable with time, which should be checked.

2. **Compute the Fourier transforms, $\tilde{H}$ and $\tilde{N}_j$:**
   After measuring the transfer function, the additional injected noise should be disconnected. The next step is to compute DFTs $\tilde{H}$ and $\tilde{N}_i$ during nominal detector conditions. These should be computed using simultaneous data segments to allow comparison of any common features that might appear later in the projections. During these measurements, it is useful to inject one or more *calibration lines*, or sine-wave disturbances of n_j that dominate the magnitude of both DFTs, to allow a check of the accuracy of the measured transfer function (see below and Chapter 4).

3. **Compute the noise projection of N_j to H:**
   Finally, combining the information gathered in steps 1 and 2, the noise present in N_j can be mapped by α_j to a new signal that represents the contribution of n_j to H. Again, this noise projection is given by,

$$\tilde{M}_j = \tilde{N}_j \alpha_j. \tag{2.8}$$

If an n_j calibration line was injected during the DFT measurements, its magnitude and phase should have the same values in both $\tilde{H}$ and $\tilde{M}_j$. The magnitude ratio and phase difference of these signals at the frequency of the calibration line are thus measures of the validity of the transfer function with respect to the real coupling, at that frequency. If the calibration line is injected continuously, repeated projections allow an assessment of the long-term stability of the transfer function, as described in Chapter 4.

In order to allow a graphical comparison of the Fourier transforms $\tilde{H}$ and $\tilde{M}_j$, it is useful to take their absolute values and normalize them to more convenient units. The normalization used is inconsequential, but should be the same for both signals, since the goal of noise projections is a relative comparison. Whenever spectra are shown in this work, averaged amplitude spectral densities (ASDs) [Heinzel02] are used, since most GW detector experimentalists use this normalization to measure noise. Here, the ASD of a channel is denoted by a carat, *e.g.,* the ASD of channel X as $\hat{X}$.

In realistic situations, more information about the system may be required to correctly apply the above procedure. In particular, control loops may complicate the measurements. In order to apply this procedure to signals associated with control loops, it is necessary to take the characteristics of the loops into account. In section 2.6, this will be demonstrated through application of the method to example control loops. In anticipation of that, the following section gives a brief overview of the control theory terminology and conventions used in the examples.

2.4. **Control theory**

Although a variety of control techniques exist, (*e.g.,* both feedback and feed-forward [Smith05] control are used within GEO 600), we consider the by far most commonly-used control type for laser-interferometric GW detectors, linear inverting feedback (LIF). This works by using a device called the *sensor* to measure the deviation of a given observable of the system of interest, the *plant*, from its operating point. The sensor output, here acalled the *error signal*, is passed through filters called the *servo* that transform it into a *feedback signal* of opposite sign. This is applied to a device, called the *actuator*, that acts on the system by changing the value of the observable in response to the feedback signal. Such a system thereby reduces the deviation of the observable from the operating point, in the steady-state.
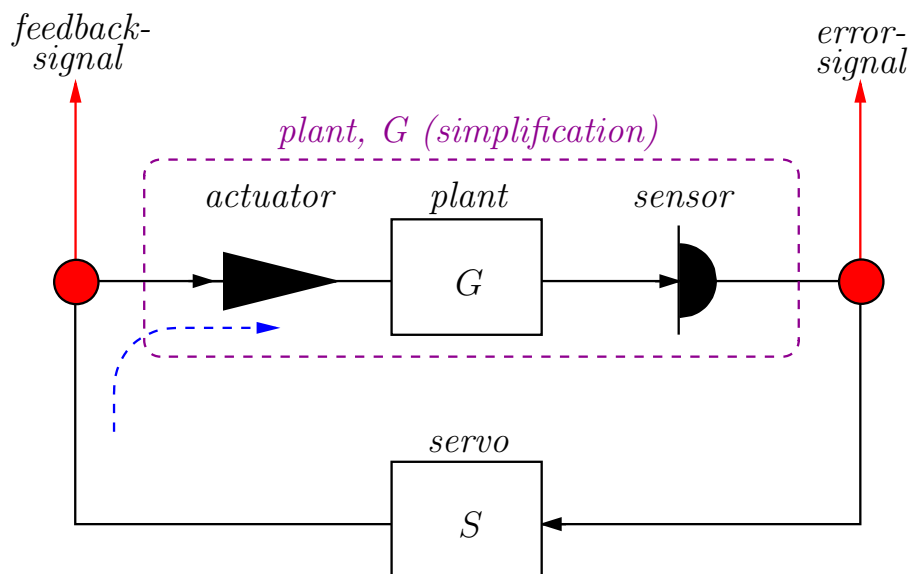
Figure 2.3.: Linear inverting feedback control loop. The actuator, plant, and sensor will be considered as one in this chapter, as indicated by the dotted box.

A simple LIF control loop is shown in Figure 2.3. In the examples that follow, since we are only concerned about signals that can be (easily) measured, the diagrams are simplified by considering the plant, to also include the the sensor and the actuator.

A LIF control loop that is nominally operating in the steady state is said to be a *closed-loop.* One that has a break in signal flow at some point, preventing feedback, is said to be an *open-loop.* The following will assume steady-state operation of the

control loops, and analysis in the frequency domain. Symbols representing different loop components, *e.g.*, G and S, will be taken to represent the complex transfer function responses of those components.
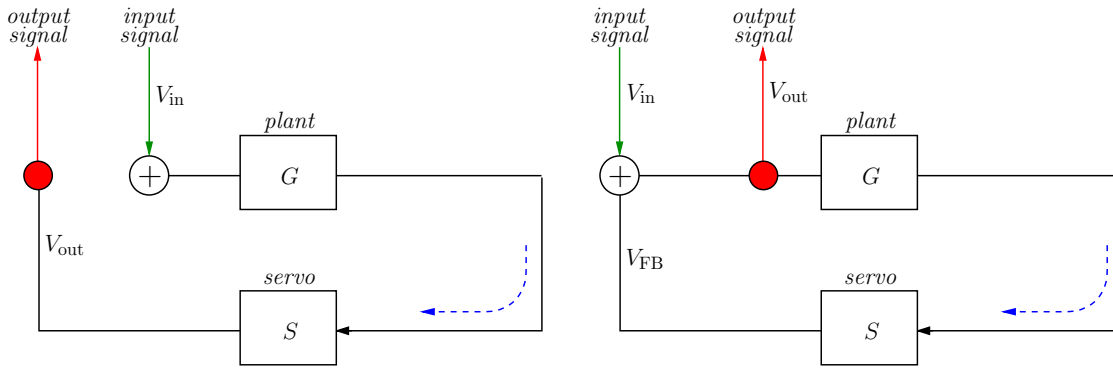
Figure 2.4.: Simple open- and closed-loops including measurement points that could be used to determine the open-loop gain and closed-loop transfer function.

The *open-loop gain* of a control loop, G_{ol}, is defined as the transfer function (response) that a signal experiences for one complete pass through the entire loop when it is open (*i.e.*, when there is no feedback). It consists of the complex multiple of the transfer functions of each of the components within the loop. In principle, this transfer function can be computed between a signal injected into the front of the open loop, and the output of the loop, as long as all components of the loop are located between these points. To demonstate this, consider the simple open-loop shown in the left diagram of Figure 2.4. Here, the output signal is,

$$V_{\text{out}} = V_{\text{in}}GS, \tag{2.9}$$

where V_{in} is the input signal, and G and S are the transfer functions of the plant and servo, respectively. Therefore, the transfer function measured from V_{in} to V_{out}, *i.e.*, the open-loop gain, is,

$$G_{\text{ol}} = GS. \tag{2.10}$$

In a closed-loop, a signal added at any point will be suppressed at the point directly after that by an amount called the *closed-loop transfer function*, or T_{cl}. To demonstrate this, consider the right diagram in Figure 2.4. The output signal is,

$$V_{\text{out}} = V_{\text{in}} + V_{\text{FB}}, \tag{2.11}$$
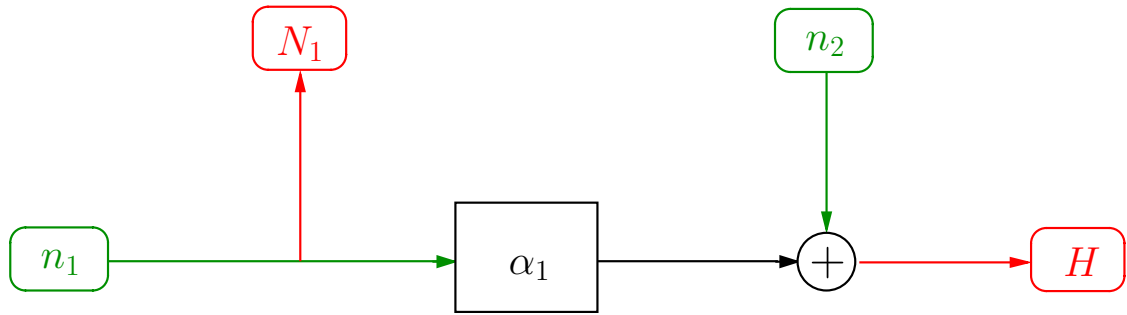
Figure 2.5.: Simple system for which an out-of-loop noise projection could be done.

where,

$$V_{\mathrm{FB}} = V_{\mathrm{out}} GS. \tag{2.12}$$

From these equations, it follows that,

$$V_{\mathrm{out}} = \frac{1}{1 - GS} V_{\mathrm{in}}. \tag{2.13}$$

Thus, the transfer function from the input signal to the output signal, *i.e.,* the closed-loop transfer function is,

$$T_{\mathrm{cl}} = \frac{1}{1 - GS} = \frac{1}{1 - G_{\mathrm{ol}}}. \tag{2.14}$$

Most control loops suppress disturbances only over a given bandwidth. A common way to characterize the bandwidth of these loops is by their *unity-gain frequency* (UGF), which is the Fourier frequency for which the open-loop gain is one. For more information about control theory see, [Freise].

2.5. Noise projection categories

Figure 2.5 shows a model system for which a noise projection could be done. Here the projection of N_1 to H is straightforward (requiring only accurate measurements of the noise channel and transfer function) following the procedure given in Section 2.3. In most real situations, the noise projection process is more complicated than this simple case. As already discussed, the validity of the projection relies upon the signals being measured are recorded properly, as true representations of the noise sources in question. Also, it is often necessary to take the details of one or
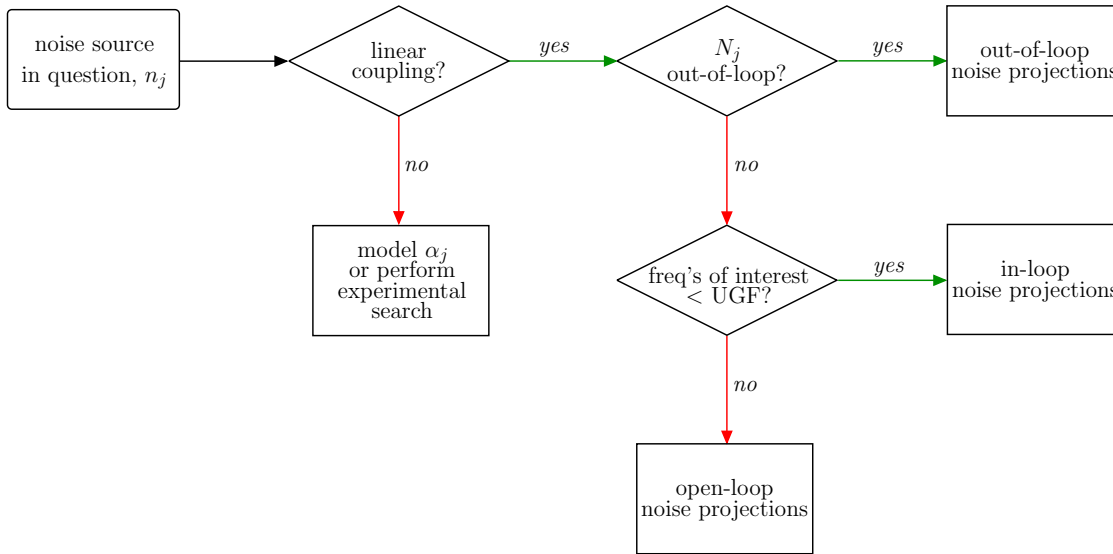
Figure 2.6.: Decision tree for selecting a noise analysis type based on the charac-
teristics of the system.

more control loops into account. This section briefly introduces some of the most
common noise projection categories. In the following we use the terms *in-loop* and
out-of-loop to describe measurement points that measure signals that are within, or
external to, the causal signal flow of a given control loop, respectively. The decision
process used to select one of the following types of noise projections is depicted in
Figure 2.6.

2.5.1. Out-of-loop projections

Channels that measure useful out-of-loop signals while the detector is in its nom-
inal state are ideal for noise projections since they can be measured continuously
without complications due to control loops (discussed below). In this case, the
situation is like that shown in Figure 2.5. The projection is conducted following
the procedure given in Section 2.3, and as long as N_j is a good representation
of n_j, and the coupling is linear, then $\tilde{M}_j$ accurately represents the level of this
noise in H. Out-of-loop channels exist where there is a reference that measures the
deviations of a given parameter independent of a control loop (*e.g.,* a photodiode
that measures the intensity fluctuations of the laser at a point after it has been
stabilized). However, it should be noted that during the course of commissioning,
once such a channel has been shown to measure a noise that couples significantly

to the detector output, it is often converted by the commissioners into an in-loop error signal and fed back to reduce the noise. Thus out-of-loop channels typically exist only if they do not measure a noise that couples significantly, or if no suitable control loop can be employed to reduce the noise that they measure.

2.5.2. In-loop projections

For a project as complicated as GEO 600, the level of a given noise source and/or its transfer function to H may depend significantly on the state of the entire system. Since most control loops associated with GEO 600 are closed in order to keep the detector in its nominal operating condition, it is desirable to measure $\tilde{H}$, $\tilde{N}_j$ and α_j, with these loops closed. However, the signal present in a noise channel associated with a feedback loop often consists of a mixture of several noise sources. For example, any noise that is added after the measurement point will be fed back and will pollute the measured signal. This mixing of noise sources due to loop gain sets a limit on the utility of in-loop measurements. In the next section we demonstrate that noise projections of in-loop noise channels within a single-path loop can only be interpreted with certainty for frequencies where the gain of that loop is less than unity. Although this imposes a severe limit on the utility of this method within control loops with high UGF, it should be noted that many of the control loops in gravitational-wave detectors are employed to reduce deviations (for example, seismically-driven mirror motions) that occur below the detection band of the instrument, and thus have loop gain less than unity over much of this band.

2.5.3. Open-loop projections

If no out-of-loop channels of the type described above exist for a given noise, and if the in-loop channels do not provide useful information due to loop-gain limitations, it may still be possible to determine the level of noise coupling by making the DFT measurements on an open-loop (the transfer functions are still measured in-loop). Many noise sources within a given control loop can be isolated by breaking the signal flow at different locations, such that only the desired noise adds to the measured channel. In the open-loop, the measured signals are not influenced by loop gain. Thus it is necessary to multiply the DFTs by the closed-loop transfer function of the loop containing N_j in order to project the correct level of noise coupling. Thus an open-loop projection is calculated as,

$$\tilde{M}_{j\mathrm{ol}} = \alpha_j \tilde{\mathbf{N}}_j T_{\mathrm{cl}}. \tag{2.15}$$

The drawback of this type of measurement is that the entire system is not at its nominal state, and thus any noise that depends on the state of the system may appear at a different level, or not at all.

2.6. Examples and simulations

A few examples that illustrate how noise projections work when applied to realistic control loops are presented in this section. These are not intended to be exhaustive or general, but rather indicative of the main features and drawbacks of the method. Since the application of out-of-loop noise projections is straightforward, following the procedure described in the last section, the following focuses on in-loop noise projections and the limits imposed on them by loop gain. Since for these simulations, the level of the noise sources do not depend on the state of the entire system (as was argued to be the case for real instrumental signals above), open-loop projections are used to determine the true noise coupling levels with which to compare the results of the in-loop projections.

2.6.1. Single loop

As a first example, consider the single-path feedback loop shown in Figure 2.7. This consists of a plant, G, and a servo, S, and has two independent noise sources, n_1 and n_2 that are suggestively referred to as *feedback noise* and *detection noise* because of their locations. The channels, N_1 and H, represent the *feedback-point* and *error-point* of the loop, respectively. We are interested in determining the level with which feedback noise, or any noise added after H and before N_1, in this case n_1, couples to H by measuring the in-loop noise projection $\tilde{M}_1$.

Following equations 2.10 and 2.14, the open-loop gain and closed-loop transfer functions of this loop are,

$$G_{\mathrm{OL}} \quad = \quad GS, \tag{2.16}$$

$$T_{\mathrm{CL}} \quad = \quad \frac{1}{1 - GS}. \tag{2.17}$$

When the loop is closed, N_1 and H will measure linear combinations of the noise
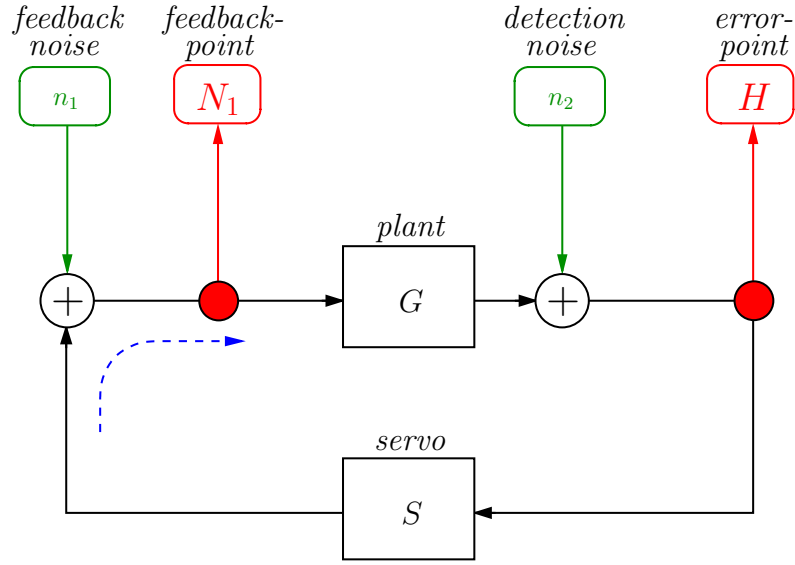
Figure 2.7.: Single-path feedback loop consisting of a plant and filter, two independent noise sources, and two measurement channels. Signals flow clockwise through the loop, as indicated by the dashed arrow.

sources n_1 and n_2. Their DFTs are given by,

$$\tilde{N}_1 = (\tilde{n}_1 + \tilde{n}_2 S)T_{\text{cl}}, \tag{2.18}$$
$$\tilde{H} = (\tilde{n}_1 G + \tilde{n}_2)T_{\text{cl}}. \tag{2.19}$$

The transfer function from N_1 to H is measured as described in 2.3, *i.e.,* while the system is dominated by n_1,

$$\alpha_1 = \left.\frac{\tilde{H}}{\tilde{N}_1}\right|_{n_1} = \frac{\tilde{n}_1 G T_{\text{cl}}}{\tilde{n}_1 T_{\text{cl}}} = G. \tag{2.20}$$

Before calculating the in-loop noise projection, let us determine the actual levels with which n_1 and n_2 couple to H by measuring their open-loop noise projections. The corresponding DFTs are measured with the loop broken in such a way that n_1 and n_2 are isolated into channels N_1 and H, respectively. Using the transfer function measured above, and the open-loop noise projection formula, (Equation 2.15) gives,

$$\tilde{M}_{1\text{ol}} = \tilde{N}_1|_{n_1} T_{\text{cl}} \alpha_1 = \tilde{n}_1 T_{\text{cl}} G, \tag{2.21}$$
$$\tilde{M}_{2\text{ol}} = \tilde{H}|_{n_2} T_{\text{cl}} \mathbb{I} = \tilde{n}_2 T_{\text{cl}}, \tag{2.22}$$

where $\mathbb{I}$ stands for the unity transfer function from H to itself. Note that both $\tilde{M}_1$

and $\tilde{M}_2$ include T_{cl}, since the DFTs were measured open-loop.

The in-loop projection of N_1 to H is calculated from the above information following Equation 2.8,

$$\tilde{M}_1 = \tilde{N}_1 \alpha_1 = (\tilde{n}_1 + \tilde{n}_2 S) T_{\mathrm{cl}} G. \tag{2.23}$$

This shows that $\tilde{M}_1$ is always an upper limit on the contribution of n_1 to H because it is polluted by n_2. More generally, the noise projection will be approximately correct for any Fourier frequency at which $\tilde{N}_1$ is dominated by a noise source added in the loop after H and before N_1, such as the feedback noise, n_1. On the other hand, for frequencies at which $\tilde{N}_1$ is dominated by a noise added after N_1 and before H, such as detection noise, n_2, the apparent projection will be an overestimate,

$$\tilde{M}_1|_{n_2} = \tilde{H}|_{n_2} G_{\mathrm{ol}}. \tag{2.24}$$

This expression can be used to set an upper limit on the contribution of noise added between points N_1 and H to the in-loop projection $\tilde{M}_1$,

$$\tilde{L}_1 = \tilde{H} G_{\mathrm{ol}}. \tag{2.25}$$

This is referred to as the *loop-noise upper limit*, and its normalized (by $\tilde{H}$) absolute value,

$$\bar{L}_1 = \left| \frac{\tilde{L}_1 \tilde{H}^*}{\tilde{H} \tilde{H}^*} \right| = |G_{\mathrm{ol}}| , \tag{2.26}$$

as the *normalized loop-noise upper limit*. For frequencies at which $\bar{L}_1$ is greater than unity (*i.e.,* below the UGF) $|\tilde{M}_1|$ exceeds $|\tilde{H}|$. Thus, for a single-path loop, definite information about the level of coupling of a given noise to the detector output cannot be obtained using in-loop noise projections below the UGF.

To better understand the performance of the in-loop projection described above, a simulation of the loop in Figure 2.7 was made. Uncorrelated white random noise was injected for both n_1 and n_2. The transfer functions of G and S were given a frequency dependence and gain such that the loop unity-gain frequency was at $140\,\mathrm{Hz}$, and each noise source dominated H over some frequency range. Transfer functions of G, H, and the open-loop gain of the full loop are shown in the left graph of Figure 2.8.

The right graph of Figure 2.8 shows several of the outputs of the simulation. These are normalized to amplitude spectral densities $\hat{H}$, $\hat{M}_1$, $\hat{M}_{1\mathrm{ol}}$, $\hat{M}_{2\mathrm{ol}}$, and $\hat{L}_1$. By comparing $\hat{M}_{1\mathrm{ol}}$ and $\hat{M}_1$, we can determine how accurately the in-loop projection
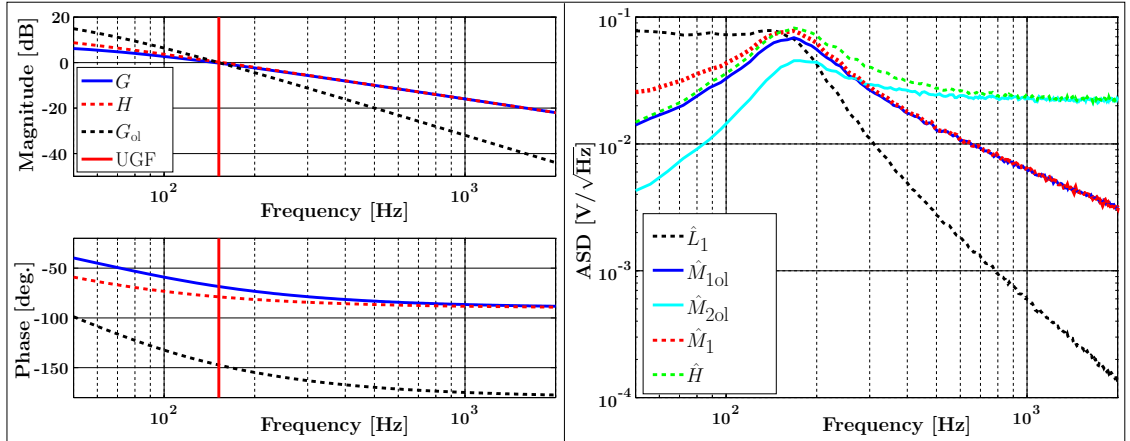
Figure 2.8.: Results of a simulation of a single-path feedback loop. Left: Transfer functions of G, H, and the open-loop gain. Right: Amplitude spectral densities of the noise projections, the detector output, and the loop-noise upper limit.

represents the coupling of n_1 to H. Above the UGF, the two agree well, and $\hat{M}_1$ is well above the loop-noise upper limit. For real measurements of the detector data, this would provide confidence of the validity of the projection even without the out-of-loop projection for comparison. Below the UGF, the projection is an overestimate of the actual contribution due to contamination of N_1 by n_2. This is allowed by $\bar{L}$, which is greater than unity below the UGF.

To summarize, within a single loop, an in-loop projection from N_1 to H is valid for frequencies at which a noise added after H and before N_1 dominates N_1. For frequencies at which this is not true, the projection can be an overestimate up to the limit set by $\tilde{L}_1$. Thus, dependable information can be gleaned only at frequencies above the UGF and for which the magnitude of $\tilde{M}_1$ is greater than that of $\tilde{L}_1$. If these conditions are not met for the noise source and frequencies of interest, the DFTs must be measured with the loop open.

2.6.2. Split-path loop

Consider the split-path loop shown in Figure 2.9. This consists of a plant, G, and two servos, S_1 and S_2, which are in separate paths called the *slow-* and *fast-path*, respectively. Noise sources are added at n_1, n_2, and n_3 and measurements are made through the channels N_1, N_2, and H. The desired outcome is an in-loop projection

of n_1 and n_2, the noise sources added in the two individual paths, to H. Although the following equations are general, note that in a typical split-path loop, the slow-path has higher gain than the fast-path at low frequency and lower gain at high frequency. The frequency at which the gains of the two paths are equal is called the *crossover frequency*, which is lower than the unity-gain frequency.
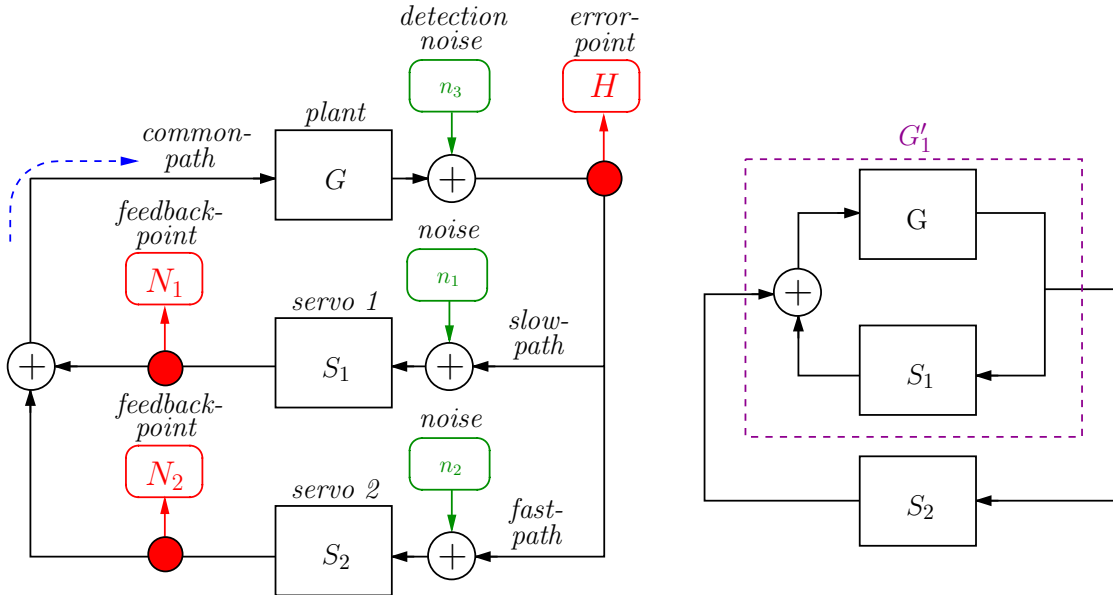
Figure 2.9.: Left: Split-path feedback loop consisting of a plant and two servos. Three independent noise sources are added and signals are recorded by three measurement channels. Signals flow clockwise, as indicated by the dashed arrow. Right: A rearrangement of the loop as a single-path loop consisting of the equivalent gain of the slow-path and the filter for the fast-path.

The open-loop gain of the entire loop and the slow- and fast-paths are,

$$G_{\text{ol}} = G(S_1 + S_2), \tag{2.27}$$
$$G_{\text{ol1}} = GS_1, \tag{2.28}$$
$$G_{\text{ol2}} = GS_2, \tag{2.29}$$

respectively. The closed-loop transfer function of the entire loop (measured in the common path) is

$$T_{\text{cl}} = \frac{1}{1 - G_{\text{ol}}} = \frac{1}{1 - G(S_1 + S_2)}. \tag{2.30}$$

In order to calculate the closed-loop transfer functions of the separate paths (*i.e.,* the amount of suppression a signal injected into one of these paths experiences at the point directly after injection), it is useful to form an equivalent single-path loop through simplification, as shown in the right diagram of figure 2.9. Here the slow-path and the plant form an equivalent gain,

$$G'_1 = \frac{G}{1 - GS_1}. \tag{2.31}$$

Similarly for the fast-path we get,

$$G'_2 = \frac{G}{1 - GS_2}. \tag{2.32}$$

It follows that the closed-loop transfer functions for the two split paths are,

$$T_{\mathrm{cl1}} = \frac{1}{1 - G'_2 S_1} = \frac{T_{\mathrm{cl}}}{1 - GS_2}, \tag{2.33}$$

$$T_{\mathrm{cl2}} = \frac{1}{1 - G'_1 S_2} = \frac{T_{\mathrm{cl}}}{1 - GS_1}. \tag{2.34}$$

The DFTs of the three channels, measured in the closed-loop, are each linear combinations of the three noise sources,

$$\tilde{H} = \tilde{n}_1 T_{\mathrm{cl1}} S_1 G'_2 + \tilde{n}_2 T_{\mathrm{cl2}} S_2 G'_1 + \tilde{n}_3 T_{\mathrm{CL}}, \tag{2.35}$$

$$\tilde{N}_1 = \tilde{n}_1 T_{\mathrm{cl1}} S_1 + \tilde{n}_2 T_{\mathrm{cl2}} S_2 G'_1 S_1 + \tilde{n}_3 T_{\mathrm{cl}} S_1, \tag{2.36}$$

$$\tilde{N}_2 = \tilde{n}_1 T_{\mathrm{cl1}} S_1 G'_2 S_2 + \tilde{n}_2 T_{\mathrm{cl2}} S_2 + \tilde{n}_3 T_{\mathrm{cl}} S_2. \tag{2.37}$$

Measurement of the noise-coupling transfer functions of N_1 and N_2 to H yield,

$$\alpha_1 = \left.\frac{\tilde{H}}{\tilde{N}_1}\right|_{n_1} = \frac{\tilde{n}_1 T_{\mathrm{cl1}} S_1 G'_2}{\tilde{n}_1 T_{\mathrm{cl1}} S_1} = G'_2, \tag{2.38}$$

$$\alpha_2 = \left.\frac{\tilde{H}}{\tilde{N}_2}\right|_{n_2} = \frac{\tilde{n}_2 T_{\mathrm{cl2}} S_2 G'_1}{\tilde{n}_2 T_{\mathrm{cl2}} S_2} = G'_1, \tag{2.39}$$

as one would expect from the simplified loop in Figure 2.9. The projections are found according to Equation 2.8 to be,

$$\tilde{M}_1 = \tilde{N}_1 \alpha_1, \tag{2.40}$$

$$\tilde{M}_2 = \tilde{N}_2 \alpha_2. \tag{2.41}$$

The projections of the two feedback-point channels for the cases in which their signals are dominated by noise added outside of the path in which they are situated

(*i.e.,* either in the common-path or in the fast-path if the channel is in the slow-path) are,

$$\tilde{M}_1|_{n_2} = \tilde{n}_2 T_{cl2} S_2 G_1' S_1 G_2' = \tilde{H}|_{n2} S_1 G_2', \tag{2.42}$$

$$\tilde{M}_1|_{n_3} = \tilde{n}_3 T_{cl} S_1 G_2' = \tilde{H}|_{n3} S_1 G_2', \tag{2.43}$$

$$\tilde{M}_2|_{n_1} = \tilde{n}_1 T_{cl1} S_1 G_2' S_2 G_1' = \tilde{H}|_{n1} S_2 G_1', \tag{2.44}$$

$$\tilde{M}_2|_{n_3} = \tilde{n}_3 T_{cl} S_2 G_1' = \tilde{H}|_{n3} S_2 G_1'. \tag{2.45}$$

Again, these can be used to set loop-noise upper limits on the projections. The normalized magnitude of these are,

$$\bar{L}_1 = |S_1 G_2'| = \left| \frac{GS_1}{1 - GS_2} \right|, \tag{2.46}$$

$$\bar{L}_2 = |S_2 G_1'| = \left| \frac{GS_2}{1 - GS_1} \right|. \tag{2.47}$$

As demonstrated in Equations 2.42-2.45, these upper limits hold for the case where N_x is not dominated by a noise added in the x-path. Split-path loops typically have high loop gain at the crossover frequency and much more gain in the fast-path at the UGF than in the slow-path. Applying these simplifying conditions to the above formulas shows the following:

- $\bar{L}_1$ is above unity below the crossover frequency, equals unity at the crossover frequency, and is less than unity for all frequencies above that.

- $\bar{L}_2$ is below unity below the crossover frequency, equals unity at the crossover frequency, is above unity between the crossover frequency and the UGF, equals unity at the UGF, and is below unity for all frequencies above that.

Figure 2.10 shows the results of a simulation for the control loop shown in Figure 2.9 with three uncorrelated white random noise sources and frequency-dependent gains for each path. The open-loop gain of the slow- and fast- paths and the entire loop are shown on the left. The crossover frequency is at $88\,\mathrm{Hz}$ and the unity gain frequency is at $310\,\mathrm{Hz}$. The right graph shows the results of the noise projections. Comparison of the loop-noise upper limits and $\hat{H}$ shows the behavior expected from the above calculations[8]. Comparison of the in-loop projections with the open-loop projections confirms that for frequencies at which the former are above the loop-noise upper limits, and for which these limits are less than $\hat{H}$, the in-loop noise projections are accurate representations of the actual noise coupling.

---

[8]$\hat{L}_2$ blows up between the crossover and the UGF because the phase contributes to form a zero in the denominator of Equation 2.47.
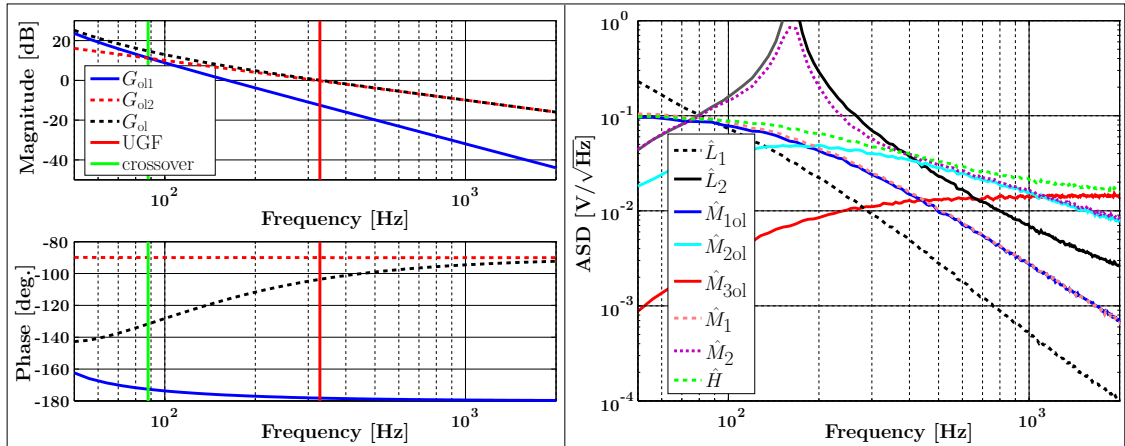
Figure 2.10.: Results of simulation of a split-path feedback loop. Left: Open loop gain of the slow- and fast-paths, and full loop. Right: Amplitude spectral densities of the noise projections, the detector output, and the loop-noise upper limits.

To summarize, in-loop noise projections performed on signals within the two separate paths of a split-path feedback loop are subject to two different loop-noise upper limits. These have the practical result of limiting the utility of in-loop projections in the slow- and fast-paths to above the crossover and unity-gain frequency, respectively. Again, if the frequencies of interest for the noise projections do not coincide with those allowed by these limitations, open-loop projections can still be done.

2.6.3. Coupled systems

Complex interferometric GW detectors such as GEO 600, often exhibit a significant amount of cross-coupling from one observable to another. For some situations, a direct cross-coupling to differential arm length motion due to the actuator is the dominant coupling mechanism. In these cases, the feedback signal of the loop can be taken as an out-of-loop measurement of the noise, and projected following the procedure given in 2.3. In others, the observable being controlled dominates the coupling to H. In these cases, since it is not possible to directly measure the observable, the use of any signal within the loop for in-loop noise projections could result in a erroneous estimate of the level with which the noise couples. In many cases information about the control loop can be used to determine a method to perform a noise projection. However, this is not general, and explanations of

individual examples extends beyond the scope of this work.

2.7. Summary

The fundamental principles of noise projection, a method used to determine the level with which noise sources couple to the detector output, were introduced in this chapter. The key point of the procedure given in 2.3 is the establishment of a causal transfer function by measurement. The method provided for doing this, *i.e.,* measurement in the presence of a dominant noise of the type one wishes to project, is more robust than establishing transfer functions based on ambient correlations or models. However, the method given here requires that the underlying transfer functions be linear (and stationary) in magnitude in order for noise projections to give the correct coupling level. This will be discussed in more detail in Chapter 4. In addition, for systems with significant frequency nonlinearities, the linear projections explained here will only serve as lower limits on the actual noise coupling. The incorporation of nonlinear effects in the noise projection procedure is beyond the scope of this work.

The procedure was tested using two example simulations, and found to be in agreement with calculation. For the examples presented, limits were set on the utility of in-loop noise projections for signals N_j that are recorded from within a control loop. These effectively limit projection of in-loop signals in single loops to frequencies above the UGF and for split-path loops for frequencies above the crossover and UGF for the slow- and fast-paths, respectively. Results of the application of noise projections to the real noise sources of GEO 600 are presented in the following chapter.

Chapter 3.

A noise analysis for GEO 600 using noise projections

3.1. Introduction

Noise analysis has played a crucial role in the commissioning of GEO 600 by providing information that has often led to improvement in the sensitivity of the detector. However, a review of this history is beyond the scope of this thesis. It can be followed in detail in many of the nearly 4000 pages of the GEO 600 Electronic Logbook [GEO 600 log]. This chapter describes aspects of the noise analysis done for GEO 600 near the start of the S5 data taking run. In particular, the linear noise projection method described in Chapter 2 is employed to create a snapshot of the coupling level of many noise sources to the detector output.

In order to clarify how the detector output signal is produced for S5, the following Section 3.2 gives a brief introduction to the calibration method currently in use. Section 3.3 briefly describes the setup and purpose of each subsystem that has been identified as important in terms of noise coupling to the detector output, and gives the noise projections related to these. These noise projections are compared to the theoretical sensitivity limit for GEO 600 with a 550 Hz signal-recycling cavity detuning throughout this chapter. Section 3.4 briefly discusses a few examples of other types of noise that have been found to couple to the detector output. In Section 3.5 the individual noise projections are compiled into a noise budget and compared to the actual detector output signal to determine how much of the total detector noise present near the start of S5 can be understood using linear noise projections.

3.2. S5 strain calibration

A thorough description of the calibration of the detector output to strain for times up to the S4 run can be found in [Hewitson04, Hewitson04b, Hewitson04c, Hewitson05]. The following briefly reviews some aspects of this, and focuses on the changes to the calibration method put in place before the S5 run.

As mentioned above, for S5 GEO 600 is, and will continue to be, operated as a DRMI with a signal recycling cavity detuning of roughly 550 Hz. In contrast to a power-recycled Michelson interferometer, a detuned dual-recycled MI has significant differential arm-length motion (DARM) signal present in both the in-phase P, and quadrature (*i.e.,* demodulated 90 degrees out of phase) Q, demodulations of the signal from the output photodiode for any demodulation phase chosen. The absolute demodulation phase of these signals is chosen such that both have significant DARM signal content over the GEO 600 measurement band, and as a compromise

between other technical factors, *e.g.,* to avoid demodulation phases for which the optical gain pole-zero model (see below) includes negative-frequency zeroes. The 'in-phase' error signal, P, is defined as the signal with the highest DARM signal content at DC. This makes it the more suitable of the two for use as the error signal input to the MID longitudinal control loop (MID loop), which keeps the MI at its operating point. This loop will be described in section 3.3.1. These two Michelson differential (MID) error signals are the main raw (uncalibrated) detector output signals of GEO 600.
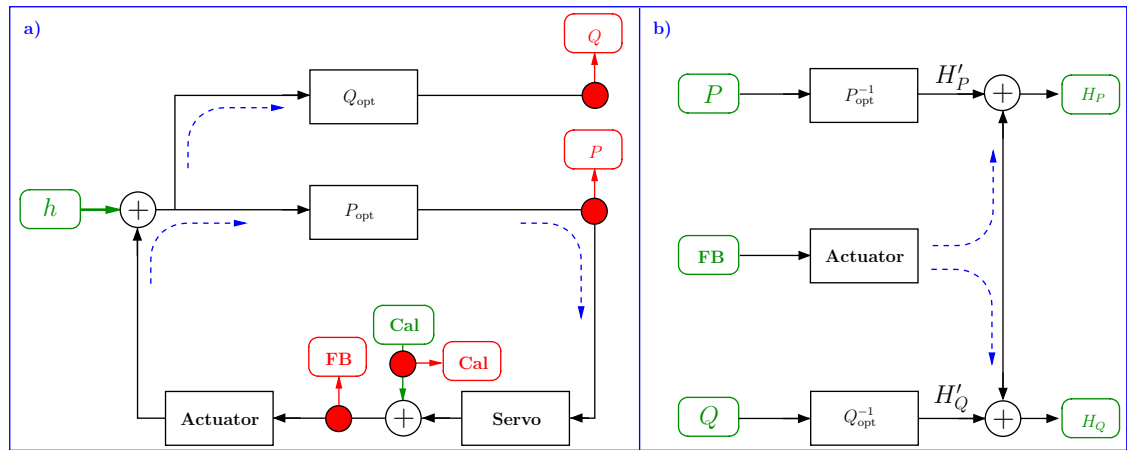
Figure 3.1.: Simplified diagrams for a) the conversion of strain h into detector outputs P and Q, and b) the reverse process, calibration of P and Q back into strain.

The calibration of the MID error signals is accomplished by using continuously injected periodic differential arm-length signals of known displacement, referred to as *calibration lines*, as references to convert the voltage present in the raw signals, P and Q, into units of strain. Figure 3.1a shows a schematic representation of the way that strain, h, that is imparted on the interferometer, is converted via the interferometer optical gains, P_{opt} and Q_{opt} (which for simplicity are assumed to also include the gain factor of the sensing electronics), into the raw detector outputs P and Q. Also shown is the MID loop, which controls the error signal P and thereby influences the actual strain in the interferometer. The calibration lines are injected into the feedback path of this loop, directly before the point where the servo feedback is measured[1]. In the figures in this chapter, red outputs, such

---

[1]There are three MID longitudinal feedback paths, namely drift control, the *slow path*, and the *fast path*. However, only the fast path has significant influence on the detector within the measurement band of GEO 600, as will be described in 3.3.1. Thus, for simplicity, only this path is considered here.

as those shown in Figure 3.1, represent measurement points for signals that are digitized by the DAQs and recorded as channels.

The S5 calibration process is depicted in Figure 3.1b. This consists of software that effectively reverses the flow of signals in Figure 3.1a in order to derive h from the channels P, Q, and the MID feedback. As for previous calibration schemes, the optical gains of the interferometer are determined by measuring the amplitudes and phases of the calibration lines in these signals and fitting these measurements to a parameterized model of the optical system. The resulting transfer function estimates of P_{opt} and Q_{opt} are inverted and then converted into filters and applied to P and Q. This produces $H_P{}'$ and $H_Q{}'$, which represent the strain in the controlled interferometer. Since this strain is influenced by the MID loop, it is necessary to remove the effects of this loop to determine h. For S5 this is done by filtering the measured feedback signal through a model of the actuator transfer function, and subtracting the result from $H_P{}'$ and $H_Q{}'$. The resulting signals, H_P and H_Q represent the effective strain input to the interferometer (in the absence of other types of noise, both would be equal to h). The subtraction of the feedback signal has the additional benefit of reducing the coupling of any noise added by the MID loop or the calibration signal electronics to the calibrated signals by a large factor[2].

In practice, the calibrated outputs H_P and H_Q contain not only strain signal, but also various types of noise. The fact that these signals are calibrated means that the strain signal in each must be the same, to within the accuracy of the calibration. This allows optimal combination methods to be employed. Maximum likelihood estimates are used to produce frequency-dependent filters that determine the relative weighting each signal should receive in order to produce an optimal combination. The result of the combination of the weighted signals has the best SNR for strain signal over the entire detection band [Hewitson05]. For S5, this is the final calibrated detector output signal, called H. The noise analysis described in this chapter will focus on measurements concerning H, since it is the most important signal for both commissioning and data analysis.

3.3. Instrumental noise contributions to H

Although the local environment is known to contribute noise to the detector output, the most significant noise encountered thus far in the commissioning of GEO 600

---

[2]The performance of the feedback noise subtraction depends on the relative accuracy of the calibration (*i.e.,* the accuracy of the filters used to model the optical responses of the interferometer, the actuator responses, and several electronic filters, etc) [Hewitson].

have been created within the instrument itself. The various subsystems of GEO 600 all contribute noise to the detector output at some level. This section focuses on the subsystems that have been identified as contributing significant levels of instrumental noise to the detector output. The setup of each will be briefly discussed, and noise projections for their associated channels to H for times during or relevant to S5 will be presented.

3.3.1. Michelson differential longitudinal loop

The MID loop is designed to measure differential length fluctuations of the arms of the MI, and control these over a bandwidth of roughly 100 Hz to keep the MI close to its 'dark fringe' operating point[3]. Operation close to the dark fringe is necessary to ensure linearity of the MID error signals, and important for reducing the coupling level of various noise sources (*e.g.,* laser intensity noise, see 3.3.4) to the detector output.

A simplified diagram of the MID loop is shown in Figure 3.2. A crystal oscillator (described below) produces a signal voltage at the RF (de)modulation frequency of the MI, $F_{\mathrm{MI}} \approx 14.9\,\mathrm{MHz}$. This is split into two paths, one going to an EOM and the other to the local oscillator (LO) inputs of the mixers for the output photodiode, PDO. The signal applied to the EOM imposes phase modulation sidebands at $\pm F_{\mathrm{MI}}$ on the carrier light at the input port of the DRMI. As described in 1.2.1, a fraction of these control sidebands shows up at the dark port due to the Schnupp arm length asymmetry. Demodulation of the signal from photodiode PDO, at F_{MI} gives the error signals P and Q. As mentioned above, since the demodulation phase is chosen such that P has the larger DARM signal at DC, it is used as the error signal for the servo.

After demodulation, the relatively large dynamic range of P is reduced by a filter, referred to as the *MID whitening filter*, in order to avoid adding noise to the signal as it is passed through the servo filters. The result is split into two servo paths[4]. The *slow path*, which dominates the loop gain from 0.2 Hz up to the crossover frequency at about 15 Hz, consists of the *slow servo*, a so called *MID de-whitening filter*, to undo the effects of the MID whitening filter, and the coil-magnet actuators that drive the intermediate masses of **MCe** and **MCn** differentially. The *fast path*

---

[3]An image of the 'dark fringe', or more specifically, the output laser beam intensity during a lock of the GEO 600 DRMI with a signal tuning of 550 Hz, is shown on the title page of this chapter.

[4]The third path, which is responsible for correcting slow drifts, is ignored here since it has a bandwidth of only 0.2 Hz
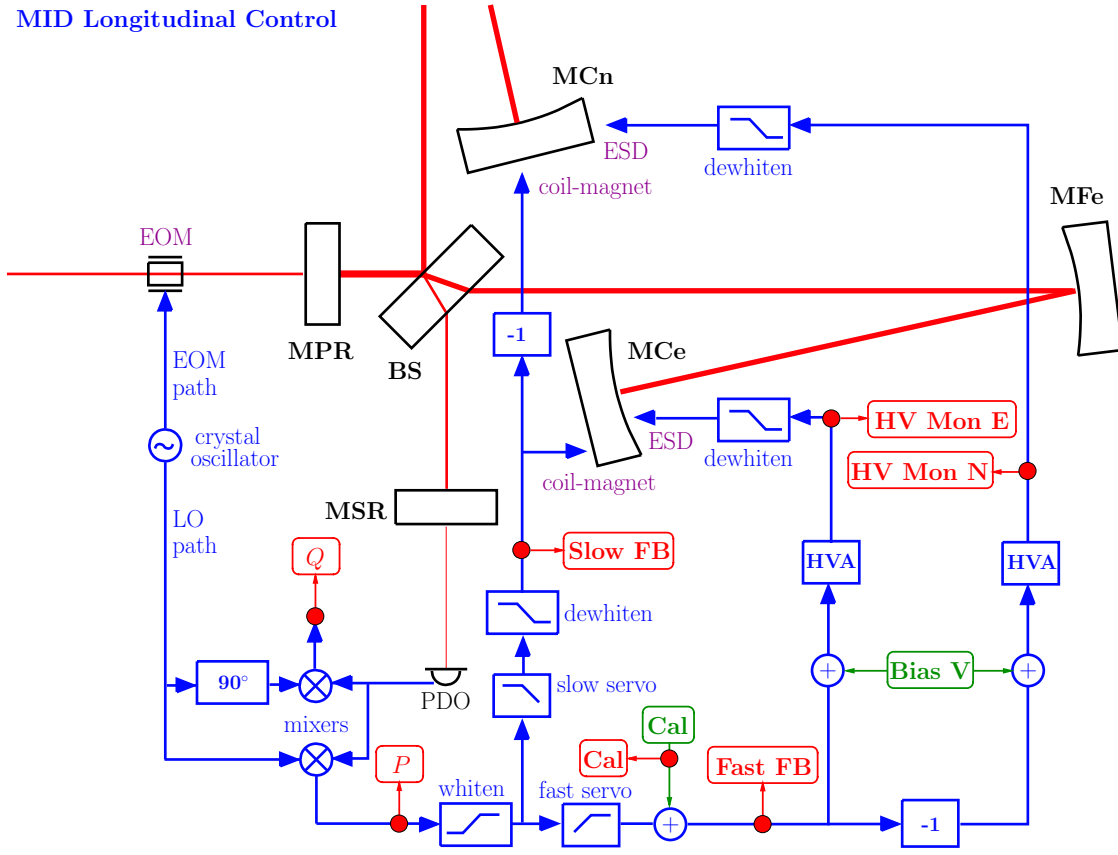
Figure 3.2.: Simplified layout of the Michelson differential longitudinal control loop.

dominates the loop gain above 15 Hz. It begins with the *fast servo*, the output of which is routed into two paths, one of which is inverted to allow differential feedback. These paths each contain a bias voltage adder, a high-voltage amplifier (HVA), and an MID de-whitening filter. The output signals of these filters are finally sent to the ESD actuators that act on the lowest stage of the near suspensions. The calibration lines for the strain calibration described in the previous section are added to the signals in the fast path, directly after the fast servo.

Several of the most important ways in which noise associated with the MID loop can couple into H are described below. Here, particular attention is given to individual noise sources in the MID loop because of its close association with H. The following subsections will focus only on the most important noise sources of the corresponding subsystem.

Detection noise

Noise that is added during the process of converting the light fields incident on the output photodiode into the error signals, P and Q, is referred to as detection noise. Since the MID detection process is quite complicated, involving quantum-noise limited light measurement, demodulation, *etc.*, there are several possible sources of detection noise. The most important ones are dark noise and shot noise.
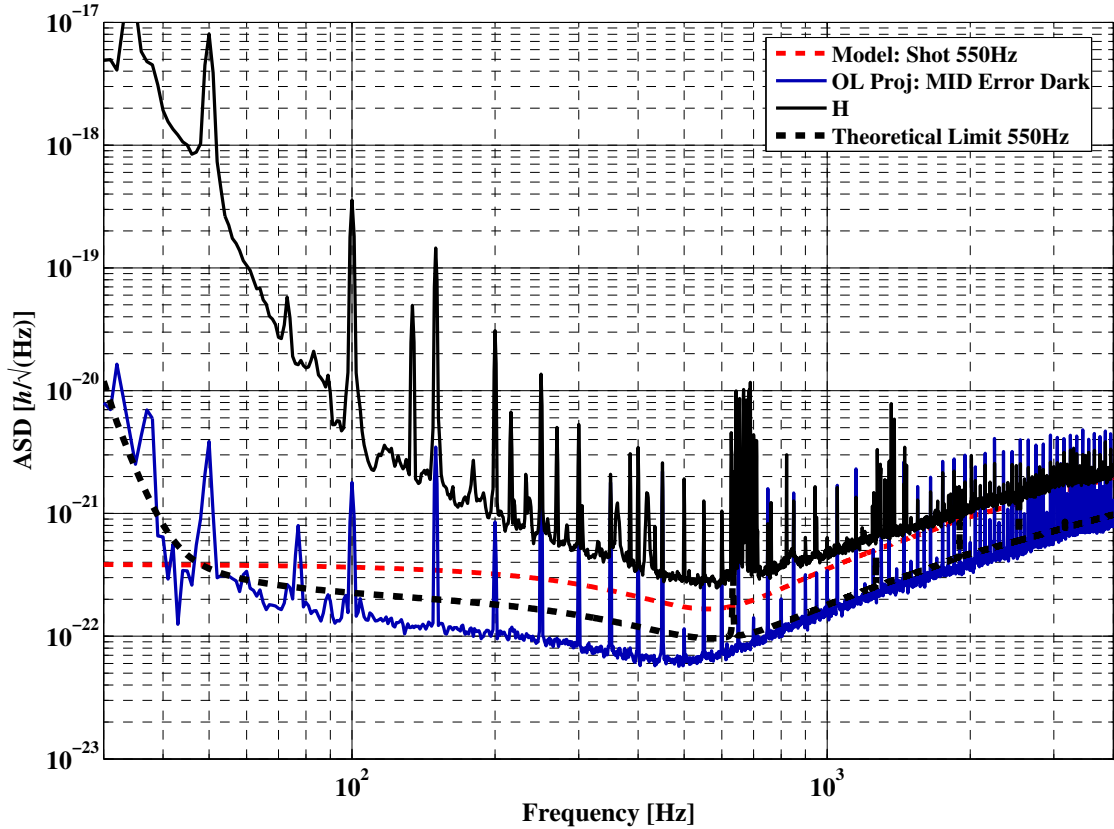
Figure 3.3.: Modeled shot noise contribution to H and an out-of-loop projection of the MID error signal dark noise.

Dark noise A lower limit on the total detection noise can be set by an open-loop noise projection of the noise present in the MID error signals when there is no light incident on PDO, the so called *dark noise*. This consists of PDO electronic noise (*e.g.,* Johnson noise of the impedence converting photo-current to voltage, amplifier noise, *etc.*), mixer noise, pickup on the cables and electronics between

PDO and the DAQs, and finally DAQs (digitization) noise. The noise projection of the dark noise of the MID error signals to H is shown in Figure 3.3. The noise level of this measurement is dominated by the electronic noise of PDO. Development of photodiodes taylored to the requirements of light sensing at various interferometer ports is a current subject of research within our group. For more information, see [Grote06].

Shot noise   One noise source that is not included in the dark noise lower limit is shot noise of the light incident on PDO. As discussed in 1.4.1, this sets a fundamental limit to the sensitivity with which strain can be measured with a given interferometer configuration and light power. The amplitude spectral density of shot noise photo-current produced by PDO when it is illuminated can be found using the formula (corresponding to Equation 1.7),

$$\tilde{S}_{\mathrm{I}}(f) = \sqrt{2e\bar{I}} \tag{3.1}$$

where e is the electron charge, and $\bar{I}$ is the average (DC) photo-current of PDO. This is converted to the voltage measured in P and Q by a frequency-dependent impedance (an L/C resonant circuit) [Grote06] and any other electronic gain or loss between the diode and the error signals. Additional factors due to the heterodyne detection method used must also be taken into account [Meers88].

The shot noise contribution to H that is shown in Figure 3.3 was computed using a FINESSE [FINESSE] model with the best known parameters of GEO 600 during the S5 run [Malec]. This modelled amplitude spectral density indicates that above about 700 Hz, the detector output is essentially limited by shot noise (*i.e.,* shot noise is smaller than H by less than a factor of $\sqrt{2}$ in amplitude). In addition, shot noise is a significantly contributing noise source above about 200 Hz, and is more than a factor of two higher than dark noise over the measurement band, by design.

The most clear way to reduce the sensitivity limit imposed on H by shot noise of the light at the dark port is to increase the carrier laser power in the DRMI. To accomplish this, it may be necessary to increase the injected laser power, and/or remove sources of optical loss in the DRMI. Work towards this end will likely take place within the next year.

Recording noise

As described in 3.2, H is derived in software from several channels, namely P, Q, the MID loop feedback signals, and the calibration signal. Each of these originates

as an analog voltage signal in its associated electronic device, and is converted to a digital signal by the data acquisition process depicted in Figure 3.4. Any noise that is added to these signals during this process (*e.g.,* electrical pickup on the cables and electronics, electronic noise of the whitening filters and digitization noise of the DAQs) is referred to as *recording noise*, and can contribute to limiting the sensitivity of H.
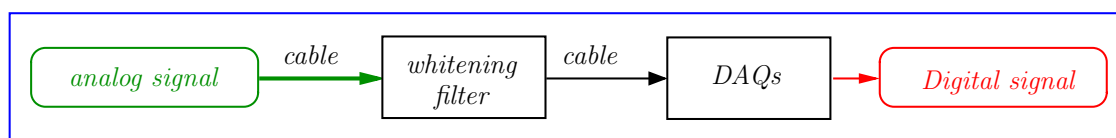

Figure 3.4.: Simplified diagram of the data acquisition process. The analog signal is sent via a cable to a whitening filter (which may consist of only an analog buffer stage) and then to the data acquisition system, where it is converted to a digital signal.

DAQs whitening filter noise: As will be discussed below, the dynamic range of the fast DAQs is finite. Therefore, to avoid adding noise in the recording process, analog signals with high dynamic range (greater than 6 orders of magnitude) must be filtered in such a way that they have a suitable SNR throughout the DAQ process. This is typically achieved using analog filters that reduce the dynamic range of the signal in question by filtering it by roughly the inverse of its spectrum. These are called *DAQs whitening filters*. The noise of the whitening filters for the channels discussed in this section have been checked to have negligible contribution to the channels used for noise projections for the frequencies of interest.

DAQs noise: The data acquisition system is used to convert the analog voltage signals produced by the instrument into digital signals for storage and analysis. Noise added to the signal after the point where it is physically connected to the DAQs input patch panel is referred to as *DAQs noise*. The most significant noise source common to all DAQs channels is the fundamental digitization noise resulting from the finite 16-bit amplitude resolution of the DAQs analog-to-digital converters (ADCs)[5] [Hewitson04]. For typical channel settings and an input range of 2 V peak-to-peak, this corresponds to about $3 \times 10^{-7} \mathrm{V}/\sqrt{\mathrm{Hz}}$.

---

[5]The ADCs are, in principle, able to provide 24-bit amplitude resolution. However, other noise sources present in the DAQs electronics reduce the achieved performance to about 17 effective bits. For that reason, the ADCs are now set to 16-bit mode, as a compromise between noise performance and data rate [Hewitson04].
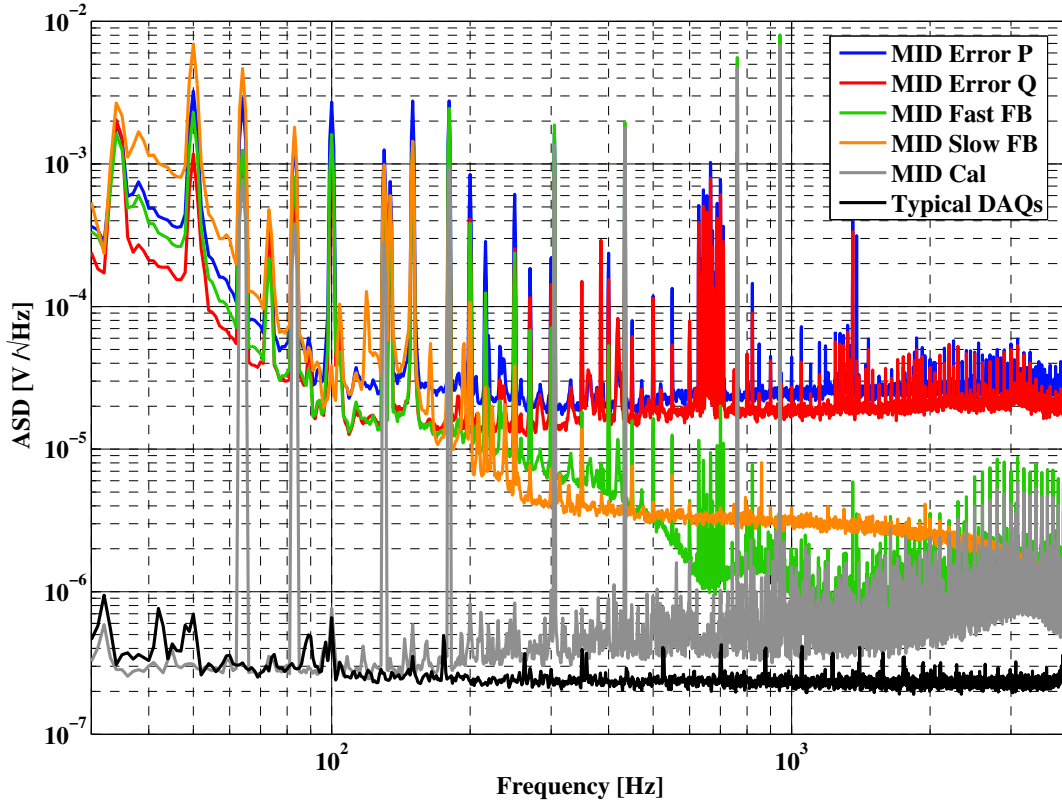
Figure 3.5.: Spectra of the typical level of DAQs noise measured in a channel, and the actual noise levels for the channels involved in the strain calibration process, as they are recorded in the DAQs.

In addition, signals recorded in the DAQs exhibit a non-negligible level of pickup from the environment and from other signals connected the DAQs, the latter through a process known as *cross-talk*. The susceptibility of a given channel to pickup has been shown to depend, among other variables, upon the output impedance of the device used to send the signal to the DAQs. For more information about the DAQs and its noise sources see [Hewitson04, Kötter, Kötter02].

Figure 3.5 shows a comparison between the DAQs noise for a typical channel, and the noise present in the DAQs channels that are involved in the calibration process. The error signals are both two orders of magnitude larger than DAQs noise over the entire detection band. The calibration lines in the calibration channel are well above DAQs noise. Both the fast and the slow

feedback signals are more than an order of magnitude above DAQs noise below about 300 Hz, which is sufficient since the noise in these signals does not couple significantly to H above that frequency, as will be shown below.

Feedback noise

As described above, P is the error signal input to the MID loop. It is filtered in the slow and fast paths (*i.e.,* the respective servo transfer functions are applied) before being passed to the actuators. In principle, with noiseless filters, the feedback signals would be coherent filtered versions of P. Any deviation from this due to noise that is added to the signal before it reaches the actuators is called *feedback noise.* Feedback noise couples into P and Q by creating unwanted DARM fluctuations via the actuators. However, feedback noise that is measured in the signals used to correct for the effects of the MID loop in the calibration process will be greatly reduced in H. To assure that all noise components added before the actuation are reduced, it is desirable to record the feedback signals as near as possible to the actuators, and to use these signals for the calibration. For the S5 run, the slow and fast feedback signals measured after their respective servo electronics are used. As shown in Figure 3.2, the output signals of the HVAs are the nearest measurements of the MID fast feedback to the ESD actuators. However, these have not yet been implemented in the calibration scheme, although this upgrade is planned for the future.

Fast path feedback noise Feedback noise from the electronics in the fast path of the MID loop has been one of the most persistent contributing noise sources in the history of GEO 600 commissioning. The contribution of noise from the servo electronics was largely alleviated (as described below) shortly before S5, when the calibration method was upgraded to allow subtraction of feedback noise from the detector outputs. However, since the fast feedback signal after the fast servo is used in the calibration, noise added after this point, *e.g.,* in the high-voltage amplifiers, will not be subtracted from H. Even if it was, reduction of the feedback noise would still be desirable, since any nonlinear effects (*e.g.,* sidebands, up-conversion) resulting from real DARM fluctuations are not reduced by noise subtraction, which is inherently linear.

With no noise subtraction, the transfer function from the fast feedback to H includes the Michelson de-whitening filter and the actuator response (essentially f^{-2} over the measurement band). Figure 3.6 shows open-loop projections of the MID fast servo feedback signal to H computed for a time before the feedback noise was subtracted in the calibration process (the large lines
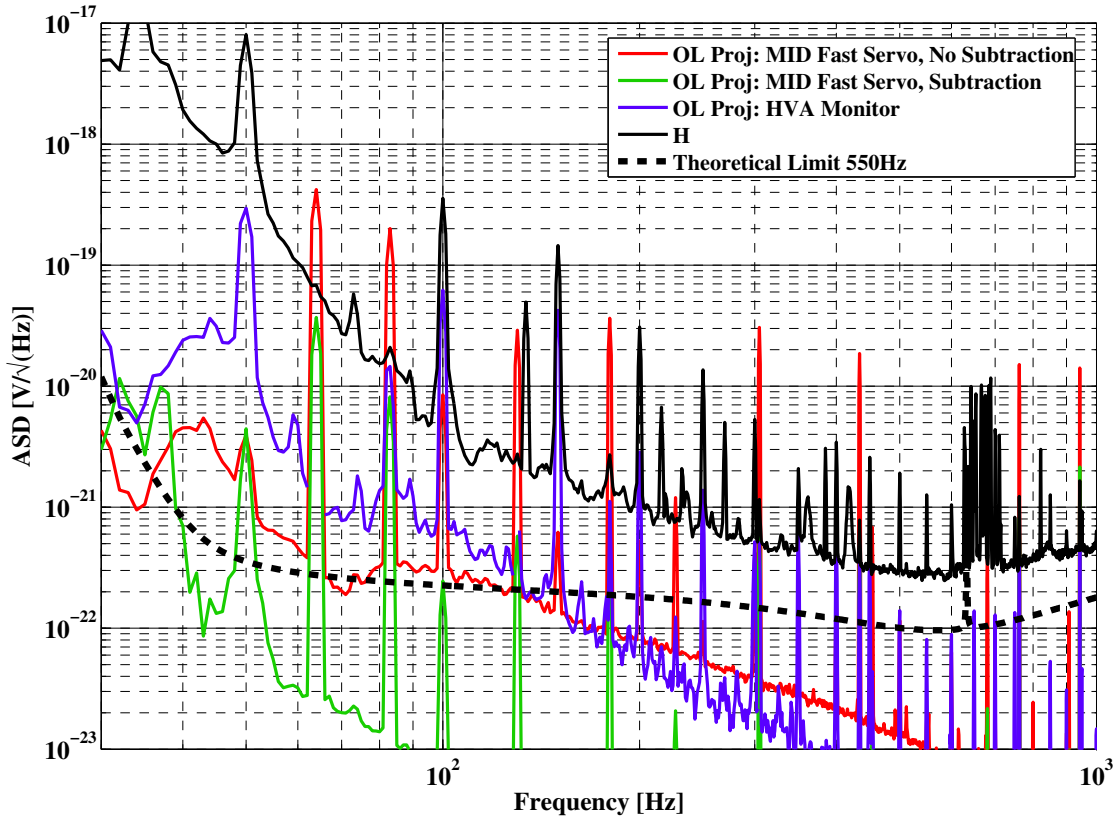
Figure 3.6.: Noise projections for the MID fast feedback signals to H.

that exceed H are calibration lines), and for a time during S5 using the calibration scheme described above. The servo noise coupling to H is reduced more than a factor of 10 at most frequencies. Also shown is an out-of-loop projection of the noise of the HVAs. This is not reduced by the calibration scheme since it appears after the measurement point for the fast servo feedback. A reduction of the contribution of noise of the HVAs to H will be necessary to reach the theoretical sensitivity limit. As described above, incorporating the HVA monitor signals in the calibration scheme could accomplish this. Another possible method would be to reduce the bias voltage applied to the ESDs. Additional consequences of doing this are described below.

Nonlinear noise from the electro-static drives: As described in Chapter 1, the ESDs are nonlinear actuators, responding with a force that is proportional to the square of the voltage applied to them. However, the Michelson servo electronics prepare a linear inverting feedback from the error signal. In order to apply this as a linear force, a large bias voltage is added to each signal before

it is amplified by the HVA and sent to the ESD, as was shown in Figure 3.2. The strength of the actuator, for small signals, is proportional to the bias voltage. Thus, one possible way to reduce the coupling of noise produced in the servo electronics and HVAs is to reduce the bias voltage. However, the smaller the bias, the larger the nonlinearities become. The following describes the relationship between the bias voltage and the nonlinearities introduced to the actuation.

Consider a time-domain feedback signal voltage consisting of a bias B, and a sine-wave of amplitude a at a given Fourier frequency, f_1,

$$U = a \sin \phi_1 + B, \tag{3.2}$$

where $\phi_1 = 2\pi f_1 t$ is used to be concise. Applying this to the actuator will result in a force on the mirror proportional to the square of the applied voltage,

$$
\begin{aligned}
F(U) \curvearrowleft U^2 &= a^2 \sin^2 \phi_1 + 2Ba \sin \phi_1 + B^2 \\
&= \frac{a^2}{2} - \frac{a^2}{2} \cos 2\phi_1 + 2Ba \sin \phi_1 + B^2.
\end{aligned} \tag{3.3}
$$

Here we see the production of nonlinear terms at the double-frequency $2f_1$. We can define the amplitude of the resulting signal at the double-frequency normalized by the amplitude at the signal frequency as the *up-conversion ratio*, which gives,

$$\frac{\mathrm{Amp}(2\phi_1)}{\mathrm{Amp}(\phi_1)} = \frac{a}{4B}. \tag{3.4}$$

If we now consider that the signal U is a control signal, and that reducing B linearly reduces the open-loop gain of the corresponding control loop, we find that we must increase the signal amplitude a in order to keep the same control bandwidth. Thus,

$$a \curvearrowleft \frac{1}{B} \ \therefore \ \frac{\mathrm{Amp}(2\phi_1)}{\mathrm{Amp}(\phi_1)} \curvearrowleft \frac{1}{B^2}. \tag{3.5}$$

Thus, for a control signal, double-frequency nonlinearities are proportional to the inverse square of the bias.

Now consider the same voltage signal, but with an additional component at Fourier frequency $2f_1$,

$$U = a \sin \phi_1 + b \sin \phi_2 + B. \tag{3.6}$$
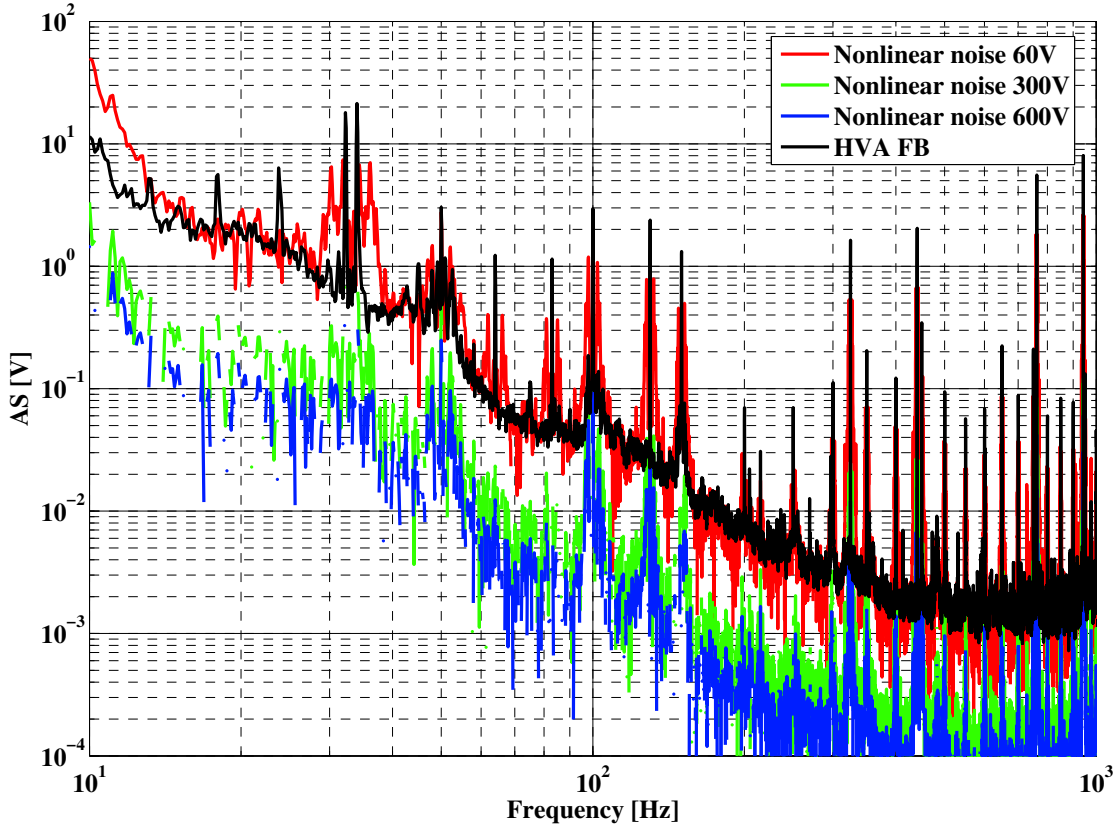
Figure 3.7.: Amplitude spectra of the MID feedback signal applied to the ESD, and the resulting level of nonlinear noise for three different bias voltages.

This produces a force on the mirror,

$$
\begin{aligned}
F(U) \backsim U^2 &= a^2 \sin^2 \phi_1 + b^2 \sin^2 \phi_2 + 2ab \sin \phi_1 \sin \phi_2 \\
&\quad + 2Ba \sin \phi_1 + 2Bb \sin \phi_2 + B^2 \\
&= \frac{a^2}{2} - \frac{a^2}{2} \cos 2\phi_1 + \frac{b^2}{2} - \frac{b^2}{2} \cos 2\phi_2 \\
&\quad + ab \cos \phi_1 \pm \phi_2 + 2Ba \sin \phi_1 + 2Bb \sin \phi_2 + B^2, \quad (3.7)
\end{aligned}
$$

which contains not only double-frequency up-conversion, but *beats* at frequencies $f_1 \pm f_2$. If we define a beat ratio as the summed amplitude at the beat frequencies normalized by the summed amplitude at the two signal frequencies, we find,

$$
\frac{\text{Amp}(\phi_1 \pm \phi_2)}{\text{Amp}(\phi_1) + \text{Amp}(\phi_2)} = \frac{2ab}{4B(a+b)} = \frac{ab}{2B(a+b)}. \tag{3.8}
$$

If we again consider U to be a control signal, for which decreasing B will linearly decrease the overall gain, and will have to be compensated by linearly increasing a and b. The result is that the beat ratio is also proportional to the inverse square of the bias,

$$a, b \backsim \frac{1}{B} \therefore \frac{\text{Amp}(\phi_1 \pm \phi_2)}{\text{Amp}(\phi_1) + \text{Amp}(\phi_2)} \backsim \frac{1}{B^2}. \tag{3.9}$$

Now consider the actual feedback signal applied to the ESDs. For this we use the signal measured after one of the HVAs. Figure 3.7 shows amplitude spectra of the linear inverting feedback signal applied to the ESD, compared to the nonlinear contributions that arise for the same feedback signal squared in the time domain, for bias voltages of 600, 300, and 60 V. This suggests that a reduction of bias voltage by even a factor of two would lead to the introduction of a significant amount of nonlinearities into the applied feedback[6].

Calibration signal noise: The calibration lines are produced in software and converted into an analog signal that is split into two paths, one going to the DAQs for recording as the calibration signal channel, and the other is added into the fast path after the servo filters, as shown in Figure 3.2. In order to avoid adding noise to the detector output, it is necessary that the calibration lines have a much greater SNR in the injected signal than in H. Out-of-loop projections of the injected calibration signal to H for S5, and a time before the implementation of feedback subtraction in the calibration scheme are shown in Figure 3.8. This shows not only that the calibration lines are supressed to a level near to the noise-floor of H, but also that the noise present at all other frequencies in the calibration signal now has an utterly negligible coupling to H.

Slow path feedback noise: Electronic noise added within the slow path couples to H via the transfer function of the intermediate mass drives of **MCe** and **MCn**. The magnitude of these accurately follows a f^{-4} slope over the detection band (see Figure 3.26 in 3.3.5), due to the response of each pendulum to forces applied by the magnet-coil actuators at the intermediate masses. This steep filtering combined with additional low-pass filtering within the slow servo relegates the coupling of any feedback noise to the detector output to the lower-frequency end of the measurement band. In addition, noise contributions of the slow servo are reduced by the MID whitening filter, as

---

[6]One possible way to improve both the noise performance of the MID actuation signal, and its linearity would be to implement a digital square-root processing of the signal before the HVA [Grote]. The feasibility of this improvement needs to be investigated.
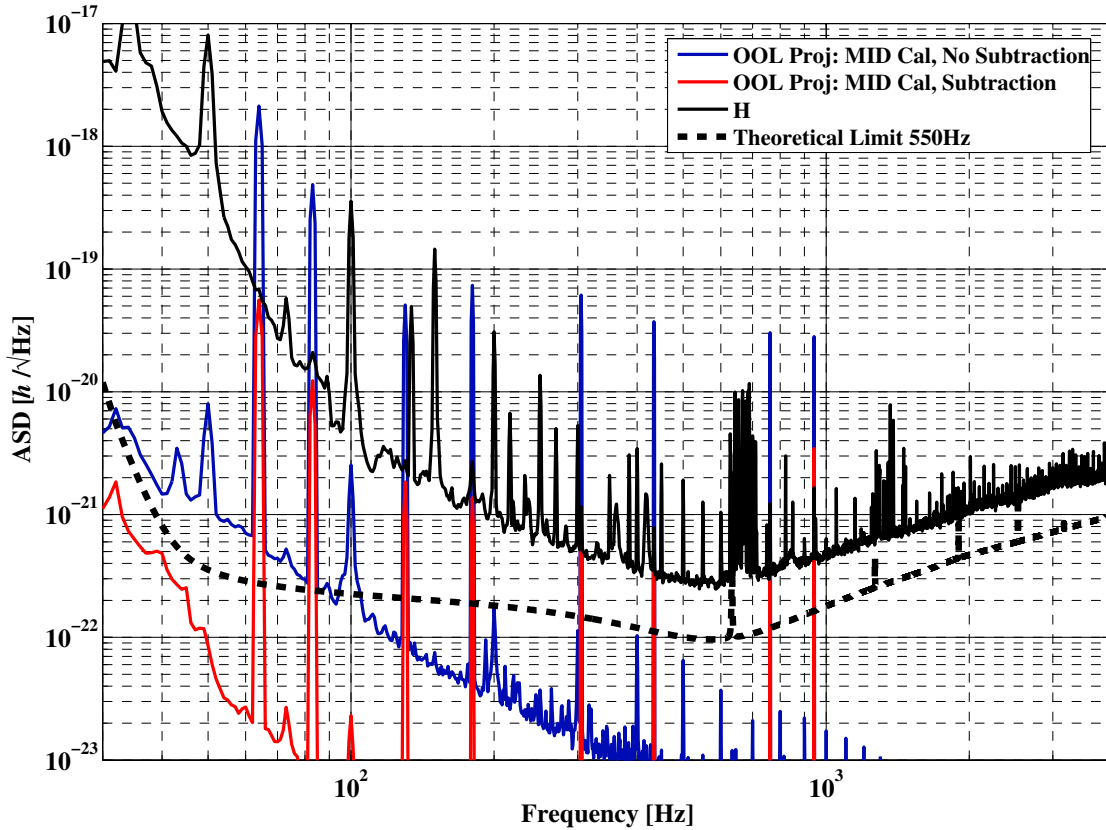
Figure 3.8.: Out-of-loop noise projection of the calibration signal to H for times before and after the recent upgrade to the calibration process. The calibration lines and noise are suppressed in H due to the feedback (which includes the calibration signal) subtraction done in the calibration scheme.

for the fast path. The Michelson de-whitening filter for the slow path is implemented directly after the slow servo, as shown in Figure 3.2. Also, feedback noise added in the slow servo is reduced by an additional factor in the calibration process.

Figure 3.9 shows in-loop[7] noise projections of the slow path feedback noise to H for S5, and for a time before S5 when feedback noise subtraction had not yet been implemented into the calibration scheme. Even with a steep low-pass filtering and noise subtraction an additional improvement in slow

---

[7]These in-loop noise projections are accurate since the crossover frequency for this loop is only 15 Hz, and the noise projection is above the loop-noise upper limit.
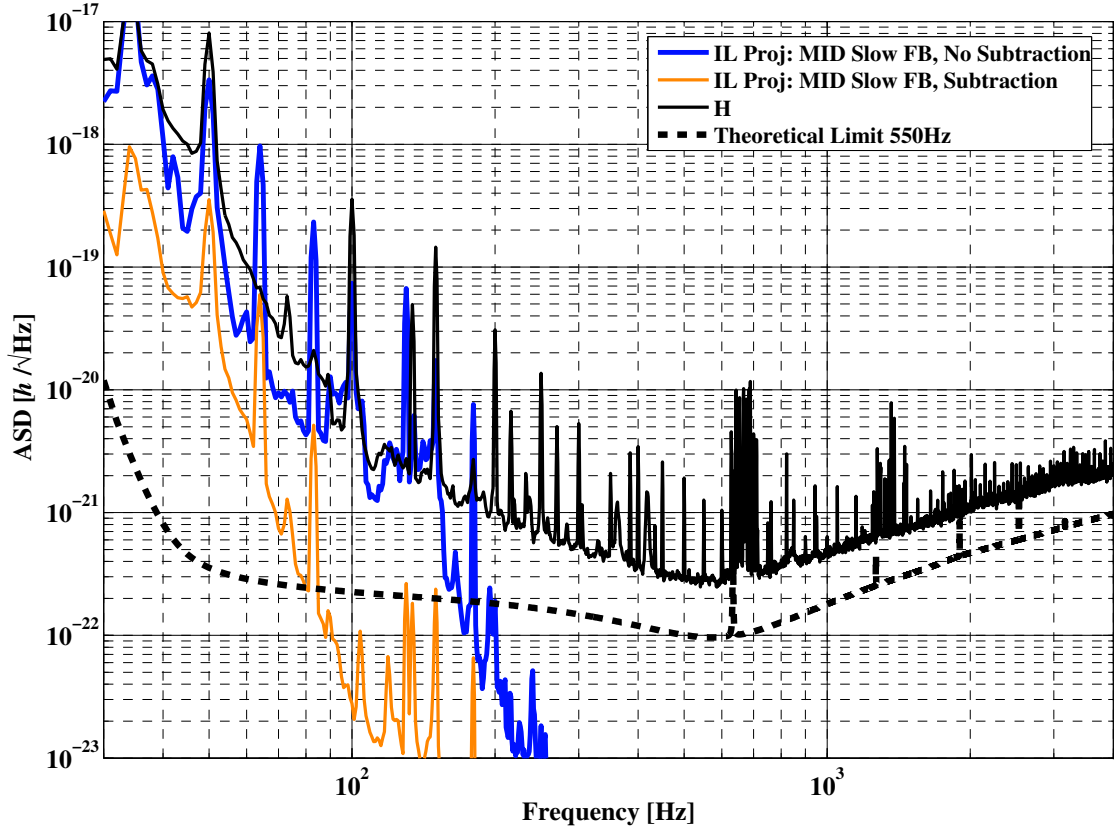
Figure 3.9.: Noise projection of the feedback noise of the MID slow servo to H for times before and after the recent upgrade to the calibration process.

path feedback noise is required in order to reach the sensitivity goal below 90 Hz.

(De)modulation signal noise

A voltage signal at the Michelson (de)modulation frequency, $F_{MI} \approx 14.9\,\text{MHz}$, is supplied by a low-noise custom-built commercial crystal oscillator with model name "Wenzel Streamline". The data sheet for this device is shown in Appendix C. The output signal from this oscillator is distributed to an EOM for the MID loop phase modulation, and to the local oscillator inputs of the mixers that demodulate the signals from PDO and QPDO (the latter being used for auto-alignment as described in section 3.3.5). After S4 the entire electronic setup for conditioning and distributing the (de)modulation signal was rebuilt using only high quality RF
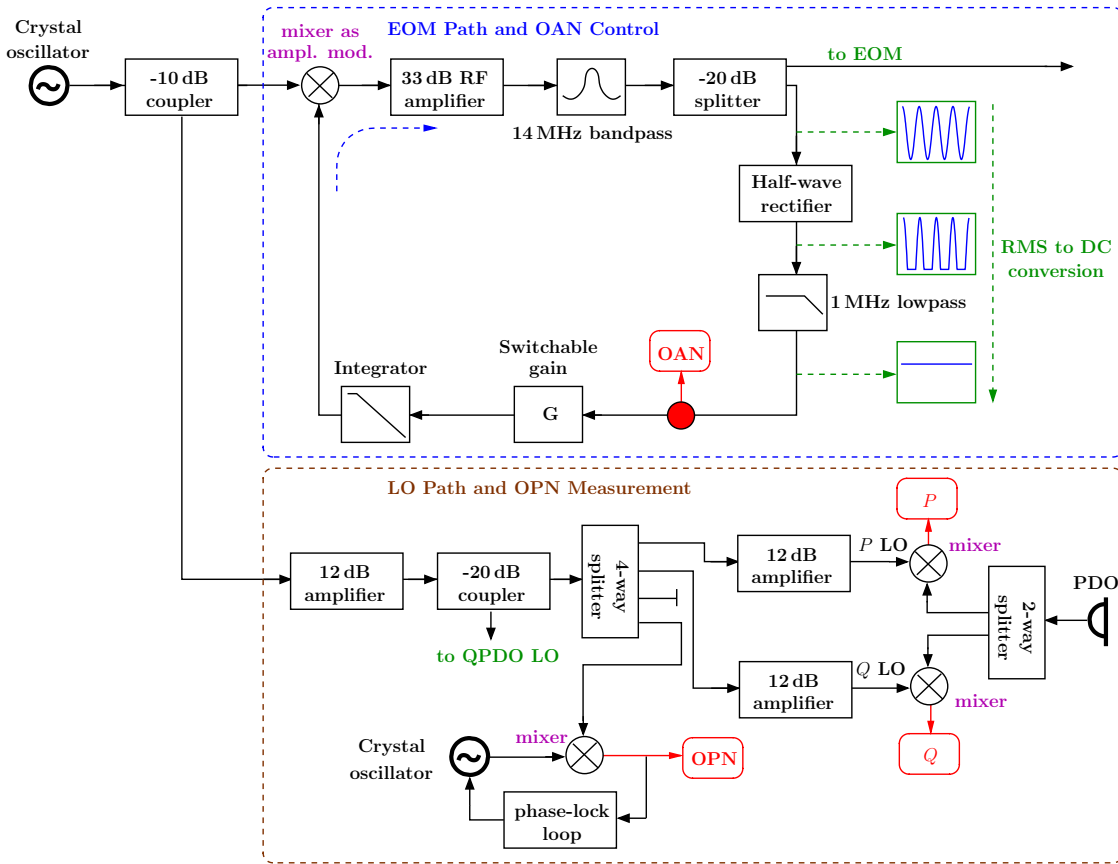
Figure 3.10.: Simplified layout of the RF electronics of the MI (de)modulation paths. The output of the main crystal oscillator signal is split into the EOM and LO paths. The amplitude of the signal in the EOM path is stabilized using a mixer as amplitude modulator, and the stabilized OAN is recorded. The phase noise of the signal in the LO path is measured by beating the signal against a second crystal oscillator, which is locked to the first using a phase-lock loop.

components in order to reduce noise on the signals in the LO and EOM paths. A simplified diagram of the current setup of the electronics associated with the Michelson (de)modulation signal is shown in Figure 3.10.

Noise in the amplitude and phase of the (de)modulation signals are known to couple to H. Both have been limiting noise sources over periods of time during GEO 600 commissioning, particularly before 2006, when lower-quality commercial signal generators were used prior to the installation of the crystal oscillator described above.
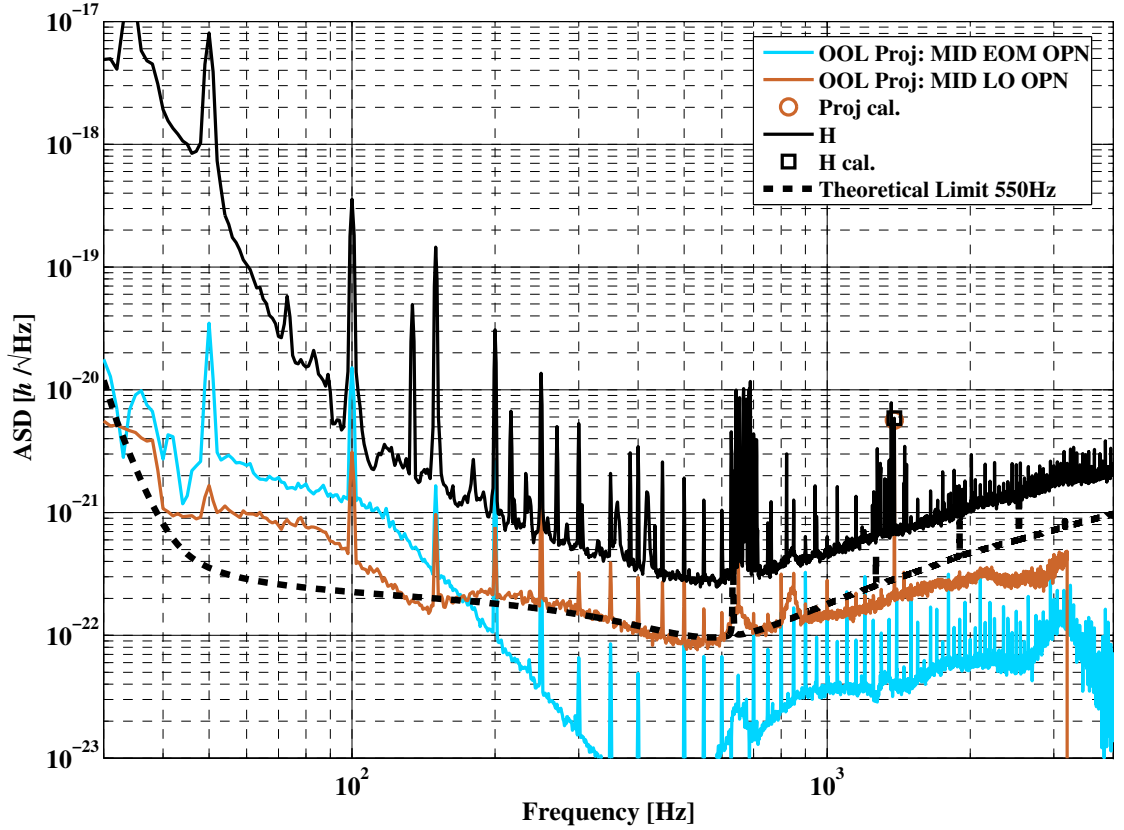
Figure 3.11.: Projection of MID oscillator phase noise in the EOM and LO paths to H.

Oscillator phase noise (OPN): Phase noise of the (de)modulation signal can couple to H through either the LO or EOM path. In the EOM path, OPN leads to the creation of (optical) noise sidebands on the MID loop control sidebands. These noise sidebands couple to H, for example, via asymmetries in the DRMI, such as the Schnupp asymmetry, which act to reduce the rejection of common-mode effects [Malec05].

Phase noise of the signal in the LO path can couple to H in (at least) two significant ways. First, phase noise sidebands on the LO of the MID mixers beat with those present on the RF signal from PDO, and the result appears in the error signals. Since the phase noise on the optical signal at the detector output is time-delayed and filtered with respect to that on the local oscillator signal, the beat of the two experiences very little common-mode cancellation, and the OPN translates (in a frequency-dependent way that is worse at

high frequencies [Grote]) into noise in P and Q. Second, through nonlinear mechanisms in the mixers, the off-phase signals in each of the mixers can create a strong coupling for OPN of the LO to their demodulated outputs, as described below.

In principle, an improved common-mode OPN rejection could be achieved by using a frequency-halved version of the optical signal at $2F_{\mathrm{MI}}$, the so-called, *2F signal*, which is detected at PDO, for the MID loop mixer local oscillators. Initial test have been performed to test the performance of this $2F$ LO. However, so far poor signal generation due to noise added in the sensing and frequency dividing stages, has not allowed for a demonstration of a significant reduction of the contribution of OPN to H (although a small reduction at some Fourier frequencies was seen). Even so, the fact that the OPN contribution to H was also not significantly increased in these tests is encouraging. Further work in this area is expected to take place after S5.

As shown in Figure 3.10, the oscillator phase noise of F_{MI} is measured out-of-loop by using a mixer to beat a signal split off from the MID loop LO path against the output of an auxiliary crystal oscillator of the same type and frequency. In order to measure purely phase noise, the phase of the auxiliary oscillator is locked to that of the MID loop LO signal with a low-bandwidth phase-lock loop. In addition, prior to S5, these OPN sensing electronics were used to sample the phase noise of the signal in the EOM path. Figure 3.11 shows a comparison of out-of-loop noise projections of the oscillator phase noise in the EOM path, and in the common LO path, to H. These show that the LO path is the dominant coupling path over most of the detection band. Although OPN is currently not (directly) limiting the sensitivity GEO 600, a broadband reduction of the level with which it couples to H will be needed to reach the sensitivity goal.

Figure 3.12 shows the transfer functions from oscillator phase noise to the three calibrated detector output signals. These show that the dominant coupling path for OPN to H is through the off-phase signal in the mixer for demodulating the P quadrature. Here a large DC signal in the Q quadrature mixes OPN of the LO strongly into the P quadrature,

$$\phi_P = \langle Q \rangle \phi_{\mathrm{OPN}}, \tag{3.10}$$

where ϕ_P is the phase noise contribution to P, ϕ_{OPN} is the OPN of the LO signal, and $\langle Q \rangle$ is the time-averaged (DC) signal in Q, as explained in [Flaminio06].

In principle, the level of this coupling can be reduced by controlling the DC
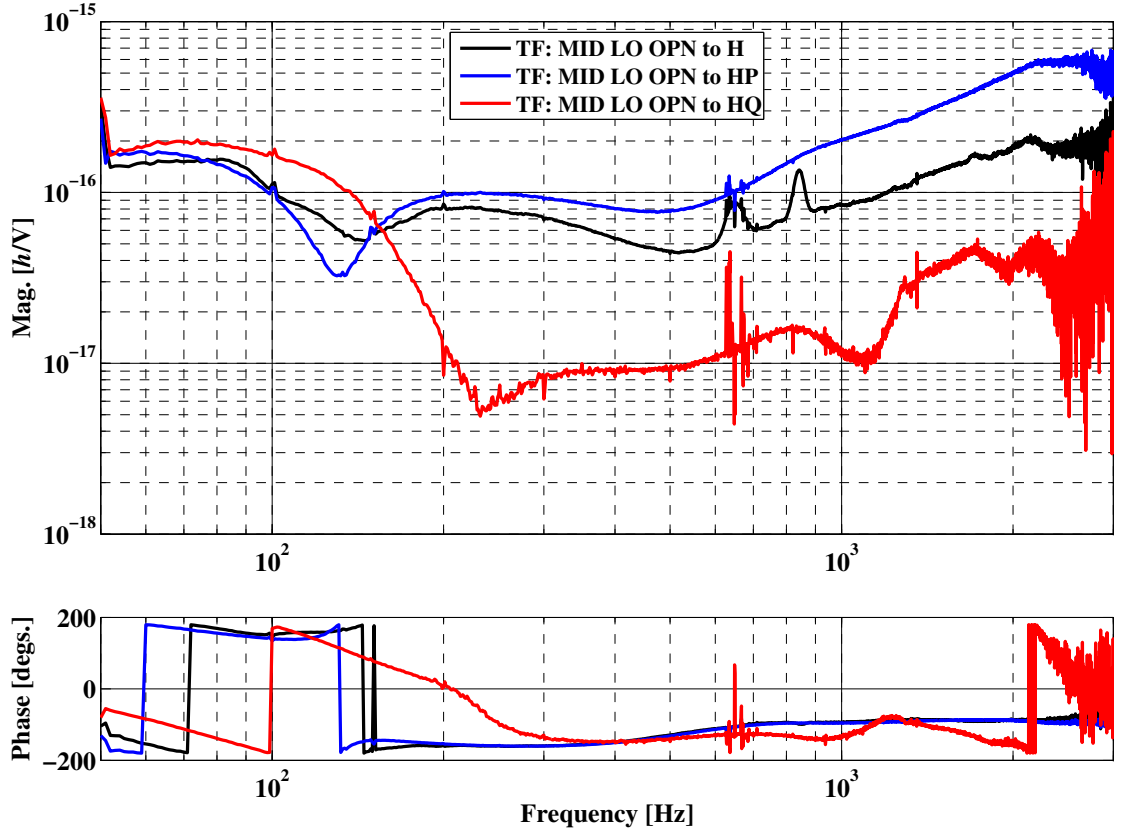
Figure 3.12.: Transfer functions from the phase noise of the MID loop local oscillators to H, H_P, and H_Q.

signal in Q using a low-bandwidth control loop to cancel the RF signal at the photodiode, a process referred to as *Q correction*. This upgrade has already been implemented in PDO, however it has not yet been sufficiently tested, and is thus not active during S5.

Oscillator amplitude noise (OAN): In contrast to the phase noise of F_{MI}, the amplitude noise couples most strongly through the EOM path. OAN of the LO path is negligible because the local oscillators of the mixers for P and Q are driven to saturation, which strongly suppresses the coupling of OAN of the LO to their outputs. The amplitude noise on F_{MI} in the EOM path is eventually imparted on the carrier and control sidebands, and couples to the detector output via asymmetries in the DRMI, as explained in [Malec05]. The measured transfer functions from amplitude noise on F_{MI} to H, H_P, and H_Q are shown in Figure 3.13. It is interesting to observe that the transfer
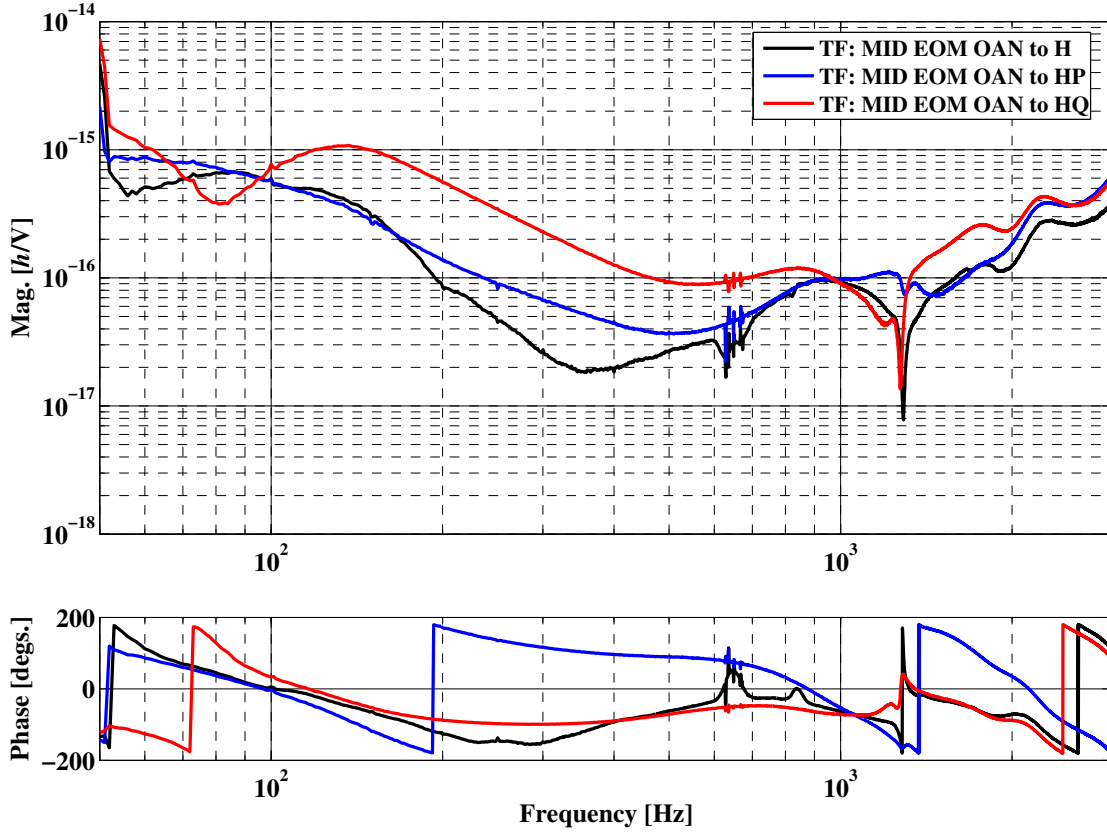
Figure 3.13.: Transfer functions from oscillator amplitude noise on F_{MI} in the EOM path to H, H_P, and H_Q.

function to H is lower at most frequencies than those to H_P and H_Q. This is due to the combining filters used to produce an optimal H.

In order to reduce the influence of OAN on H, the modulation signal amplitude fluctuations are measured and suppressed. Figure 3.10 shows the RF amplitude stabilization loop used for this purpose. Here a fraction of the modulation signal in the EOM path is converted to DC using a half-wave rectifier and low pass filter. The resulting signal, which represents the amplitude noise of the modulation signal, is then stabilized to a DC reference using a mixer as an amplitude modulation actuator. Currently there is no out-of-loop measurement of OAN after the suppression loop. The loop was judged to be beneficial by its influence on H. An out-of-loop projection of the free-running AON, and an in-loop projection of the stabilized OAN, are shown in Figure 3.14. The in-loop projection appears to be sufficiently below the
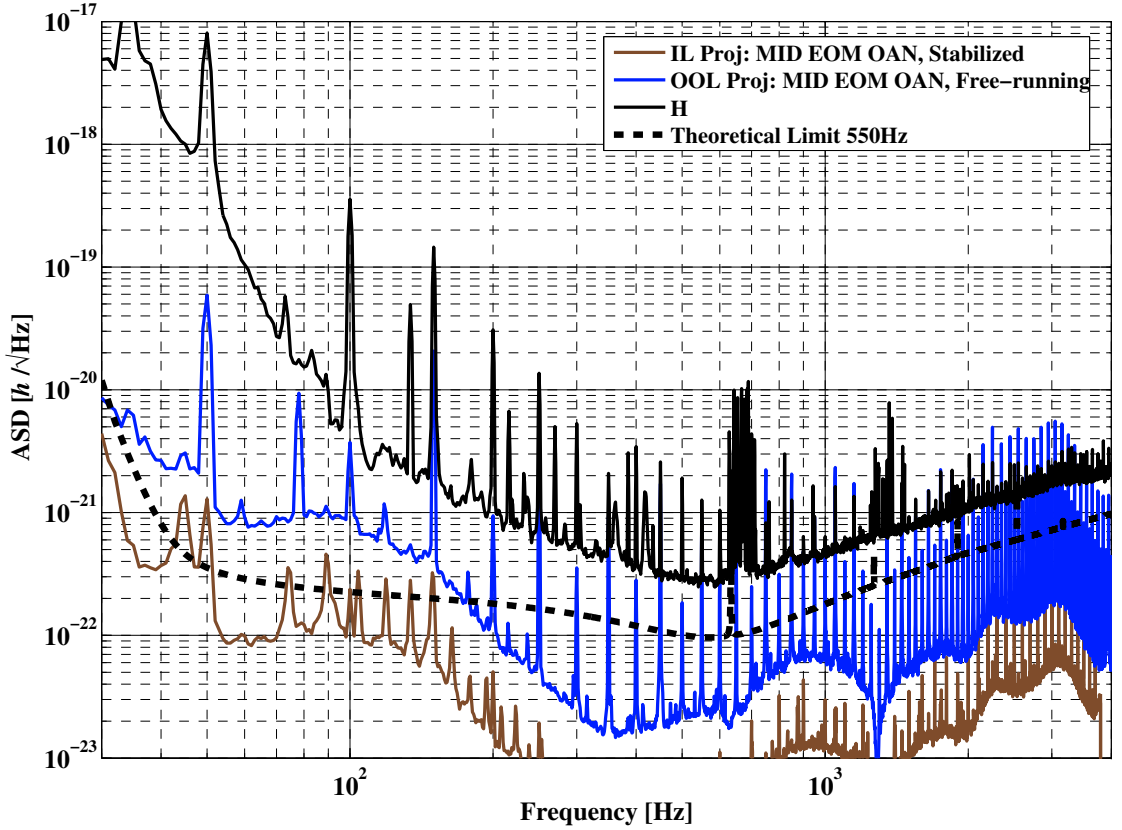
Figure 3.14.: Projection of oscillator amplitude noise on the signal in the EOM path of the MID loop to H.

sensitivity goal, however an out-of-loop measurement after the stabilization loop is needed to check the accuracy of this estimate.

3.3.2. Signal recycling longitudinal loop

In order to allow stable operation of the DRMI with a constant tuning of the signal-recycling cavity, and to reduce the coupling of various noise sources to the detector output, the length of the SRC must be accurately controlled. The signal-recycling longitudinal control loop (SR loop) that is responsible for accomplishing this is shown in Figure 3.15. The SR loop error signal is generated by imposing phase modulation sidebands at $\pm F_{\text{SR}} \approx 9\,\text{MHz}$ on the carrier light before MPR using an EOM, then demodulating the light reflected from the anti-reflective (AR) coating of the East face of the beamsplitter at F_{SR}. It represents the deviations in
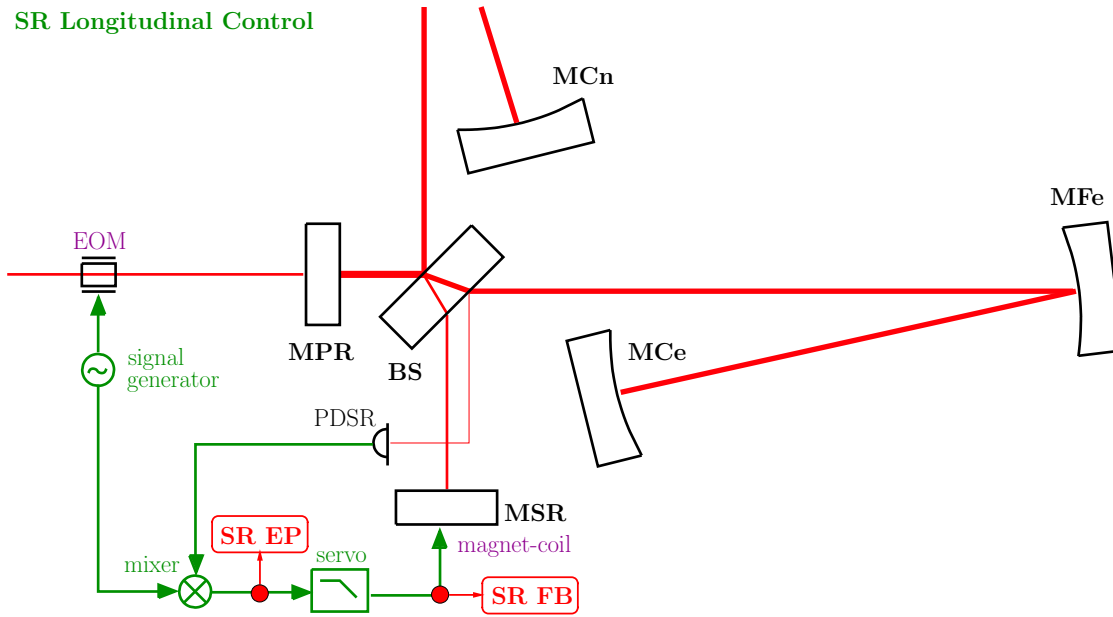
Figure 3.15.: Simplified diagram of the signal-recycling cavity longitudinal control loop.

length of the SRC with respect to the length required for the desired tuning, which is set by the exact value of F_{SR}. For more information about the signal-recycling longitudinal control see [Grote04b, Grote03]. This error signal is filtered by a single-path[8] servo consisting of a combination of analog and digital filters that prepare a feedback signal suitable for application to the coil-magnet actuators located at the mirror level of the signal-recycling double-triple pendulum suspension.

The signal-recycling loop has a unity gain frequency of roughly 25 Hz. Above this frequency, the feedback applied by the servo causes additional motion of the signal-recycling mirror. This is expected to couple to H via amplitude modulation of the sidebands at the dark port. In this case, the apparent strain produced by motions of MSR should be smaller than the same for one of the test mass mirrors by (roughly) the ratio of light fields on the mirrors [Strain]. For these measurements, there was roughly 2.1 kW on **MCe** and 4.7 W on MSR, giving an amplitude ratio of about 21, which translates into a coupling ratio of 42, since a far mirror displacement produces twice the apparent apparent displacement due to folded arms. The transfer functions from signal-recycling feedback to H_P, H_Q, and H are shown in Figure 3.16. These roughly follow the f^{-2} actuator/pendulum response expected

---

[8]The SR loop has a low-bandwidth drift control path similar to that the MID loop. This path is ignored in the following.
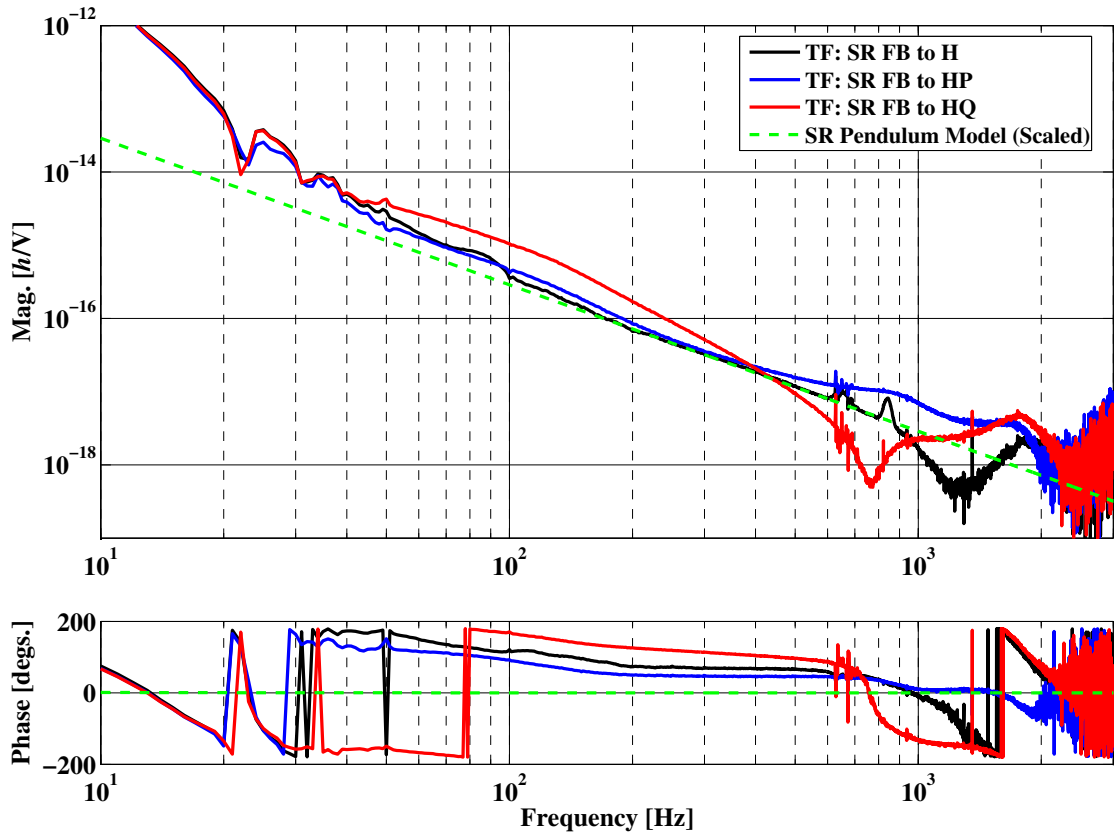
Figure 3.16.: Transfer functions from the longitudinal feedback signal applied to the signal recycling mirror to H, H_P, and H_Q.

from the above coupling mechanism, however a number of complicated resonant features are also apparent in each transfer function. The features are likely caused by audio sidebands about the various control sidebands, which experience different degrees of resonance within the different cavities of the DRMI and then combine with differents amplitudes and phases in the detector output [Malec05]. Many of the transfer functions shown in this chapter are similarly complicated to the ones shown in Figure 3.16. Research is currently underway to develop a more thorough understanding of the transfer functions presented in this work.

The level of the signal-recycling feedback noise that couples to H has been one of the major obstacles encountered thus far in commissioning; it has been a directly limiting noise source over several extended time periods. For the given laser power, the error signal is limited by shot noise of the light on PDSR at Fourier frequencies above about 50 Hz. In order to reduce the amount of this noise that is
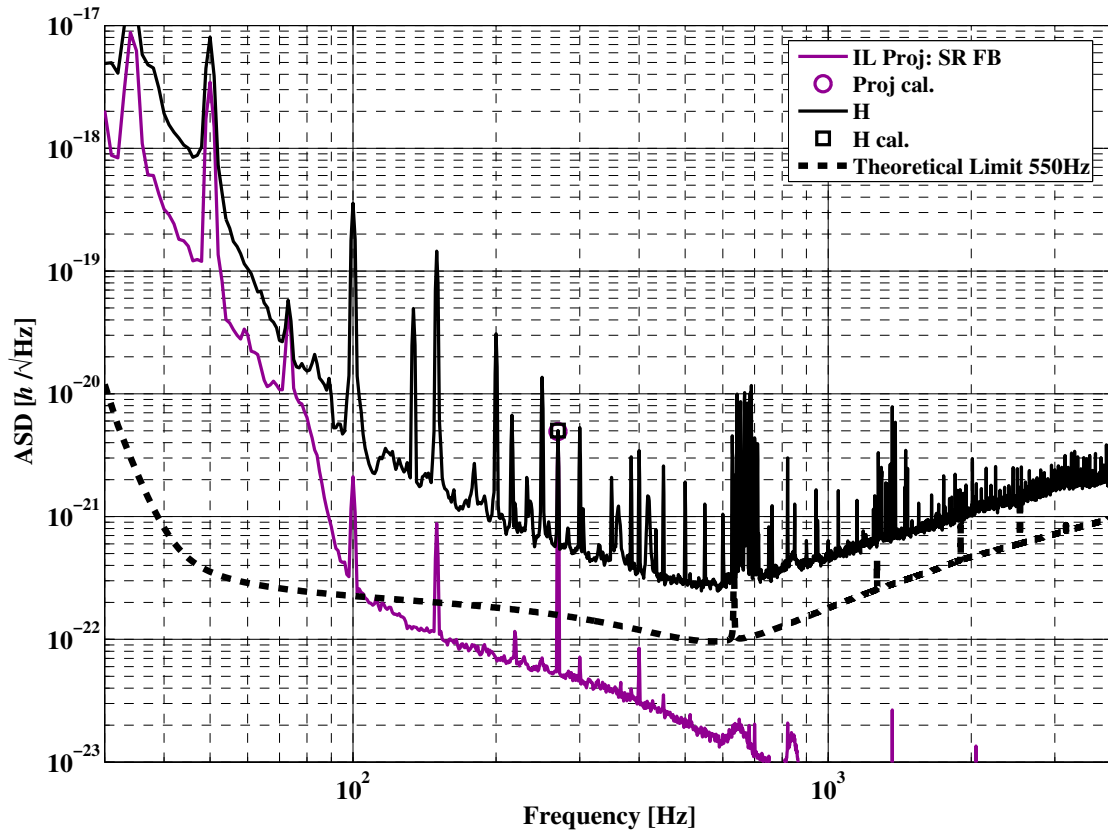
Figure 3.17.: Projection of the signal recycling loop feedback signal to H.

coupled into H in the detection band, a very steep digital filter was implemented into the servo before the S5 data-taking run. An in-loop projection of the signal-recycling feedback to H with this low-pass filter in place is shown in Figure 3.17. Although the signal recycling feedback is currently not a significantly contributing noise source over most of the detection band, its noise level is not sufficiently low to allow the sensitivity goal below about 100 Hz. Investigation of improved low-pass filters [Hewitson, Strain], and alternative error signals with better SNR [Grote] is underway, although a clear solution does not yet exist.

3.3.3. Power recycling longitudinal loop

The power-recycling longitudinal control loop (PR loop) is responsible for stabilizing the carrier frequency of the laser to the length of the power-recycling cavity (using the Pound-Drever-Hall technique [Drever83]). This loop is shown in Fig-
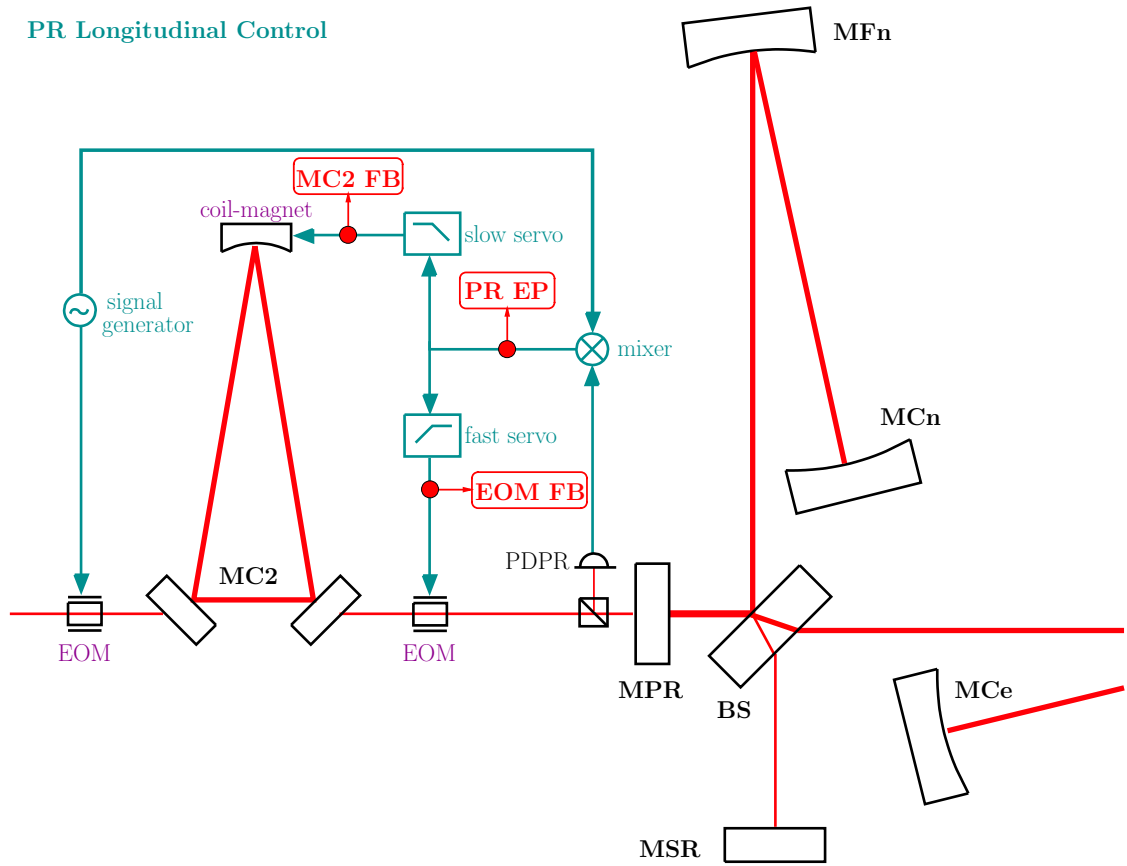
Figure 3.18.: Simplified diagram of the power-recycling cavity longitudinal control loop.

ure 3.18, and described in detail in [Freise, Grote03]. Phase sidebands at $F_{PR} \approx 40\,\text{MHz}$ are imparted on the light after MC1, and passed resonantly through MC2. These sidebands are anti-resonant in the PRC, allowing the cavity to be reflection locked. The error signal for the PR loop is produced by demodulating, at F_{PR}, the portion of the light present to the west of the PR mirror that flows towards the laser. This is directed to PDPR by a polarizing beamsplitter (associated with a Faraday isolator). The error signal represents the frequency fluctuations of the laser carrier with respect to the uncontrolled common-mode length of the power-recycling cavity.

The PR loop consists chiefly of analog electronics, which are split into a slow path and fast path. The full loop has a crossover frequency of roughly 300 Hz and a unity-gain frequency of about 25 kHz. The slow servo prepares an actuation signal that is sent to the coil-magnet actuators of MC2, controlling its length, and thereby

the laser frequency, at low Fourier frequencies. The fast servo high-passes the error signal and filters it for application to an EOM for fast frequency correction.
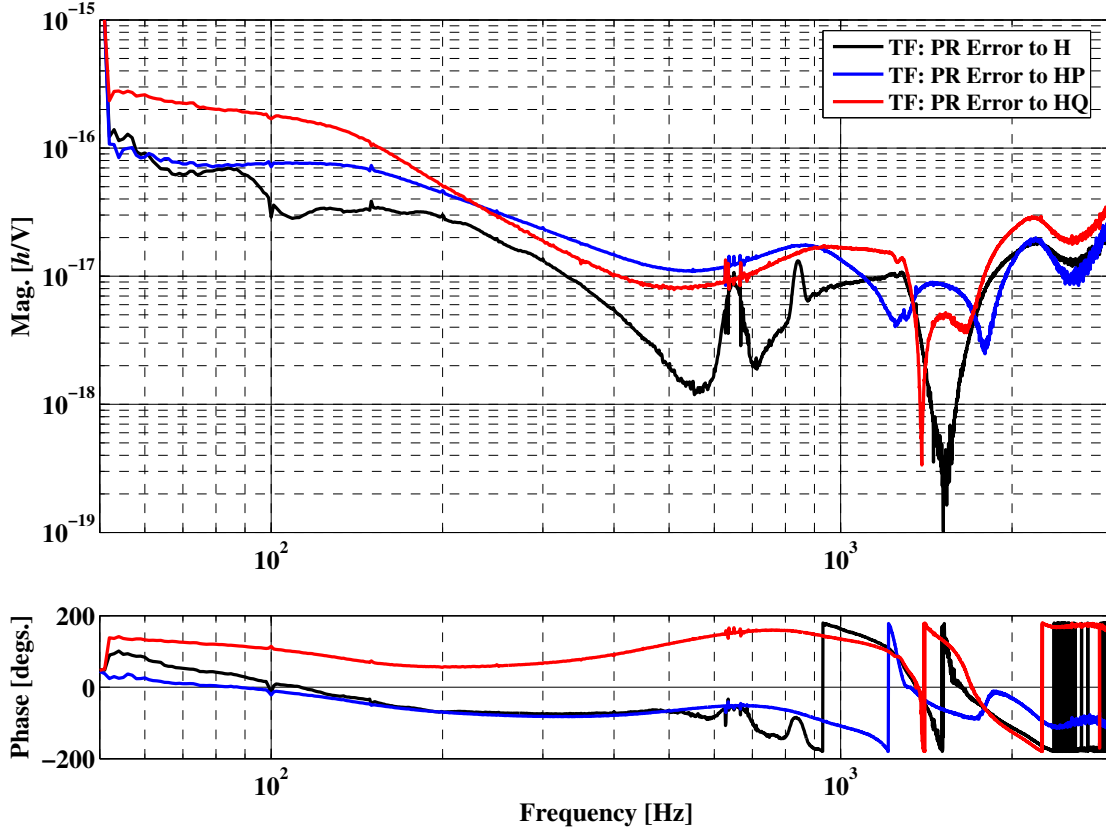
Figure 3.19.: Transfer functions from the power-recycling error signal to H, H_P, and H_Q.

Noise analysis experiments prior to S5 led to the conclusion that the dominant coupling path of noise associated with the PR loop to H is not feedback noise added in the servo electronics, but rather unsuppressed frequency noise of the laser carrier, which is present in the PR loop error signal.

Based on this finding, a different method than that presented in 2.3 was used to determine the transfer functions to H. Instead of injecting a dominant noise for the transfer function as near as possible to the actuators, noise was instead injected directly after the error point. In this state, a transfer function was measured from the error signal to the detector outputs. The results are shown in Figure 3.19. Because the loop gain is much greater than unity for essentially the entire detection band, the noise injected directly after the error point is entirely imparted on the
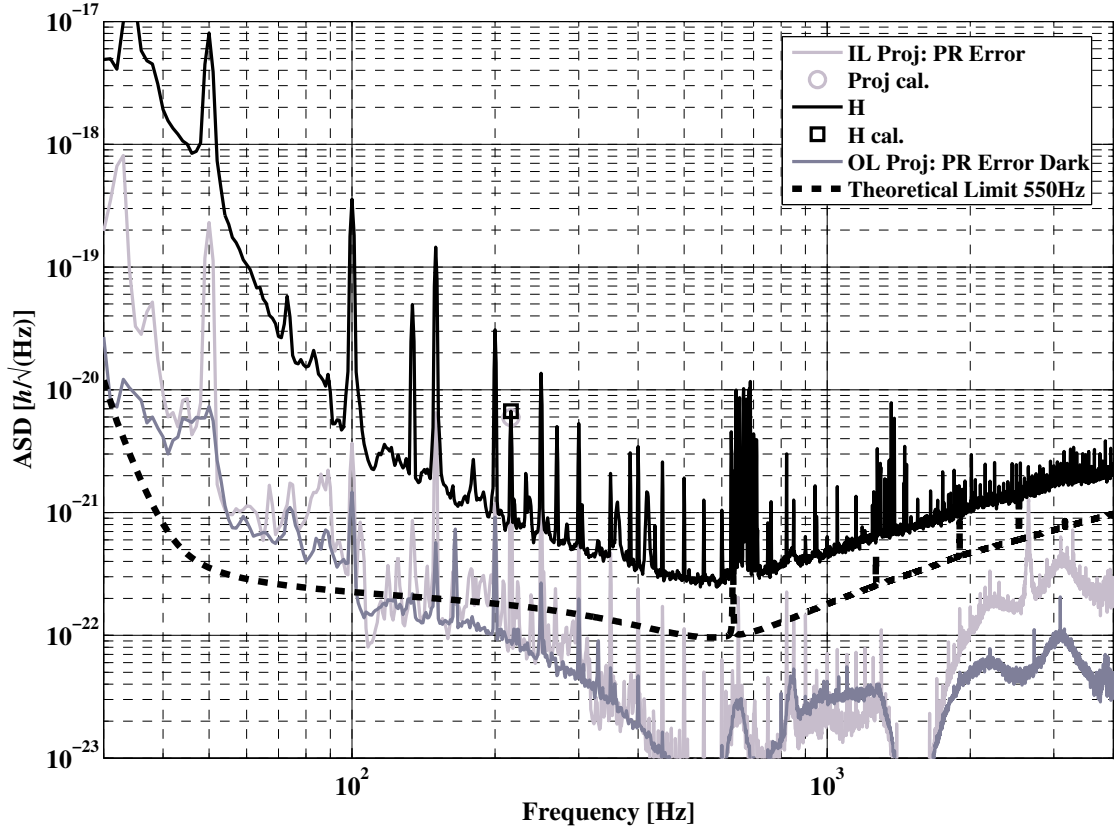
Figure 3.20.: In-loop and dark open-loop projections of the power recycling cavity longitudinal error signal to H.

laser frequency noise in the DRMI, and is at the same time measured in the error signal. This transfer function allows an in-loop projection of the error signal under nominal conditions, assuming that it is dominated by residual frequency noise. This noise projection method was confirmed to be accurate for predicting the level of noise in H during times of excess frequency noise. In addition, since for high loop gain, any sensing noise of the error signal will also be imparted on the frequency noise, it is useful to make an open-loop projection of the dark noise of the error signal for comparison. These noise projections are shown in Figure 3.20.
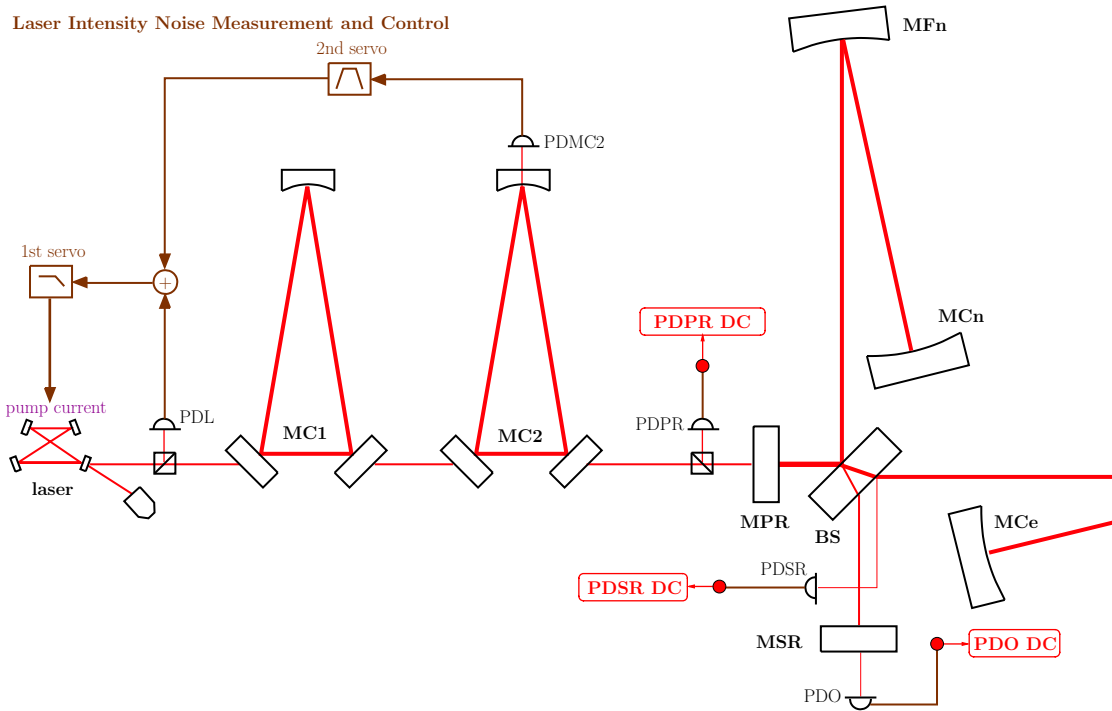
Figure 3.21.: Simplified diagram of the location of the photodiodes used to measure laser intensity noise, and the control loop used to suppress it.

3.3.4. Laser intensity noise

Laser intensity noise[9] (LIN) can couple to the detector output in a variety of ways. Calculations by Winkler [Winkler02] show that radiation pressure within the DRMI, particularly at the beamsplitter, can play a role. In addition, amplitude fluctuations of the laser carrier can couple to H via asymmetries present in the DRMI that result in a non-negligible amount of carrier light at PDO during nominal operation. Besides this, laser intensity noise will also be imparted on the various control sidebands, which can also contribute to H in complicated ways [Malec05].

Figure 3.21 shows the most important photodiodes used to measure laser intensity noise at various points, and the servos that are used to stabilize it.

Intensity noise of the laser light can be caused by a variety of processes. The most significant of these is the intensity noise of the free-running slave laser. This noise

---

[9]The noise referred to here could more accurately be described as noise of the optical power of the laser. The term "intensity noise" is commonly-used to describe this, even though intensity refers to power per unit area.

is detected by PDL, a photodiode on the laser bench, that is illuminated by a beam split off from the main beam shortly before it enters MC1. The resulting signal is actively stabilized in the first intensity stabilization loop, using the current of one of the slave laser pump diodes as actuator.

As mentioned in 1.3.2, the relatively high finesse ($\mathcal{F} \simeq 2000$) modecleaners convert beam geometry and pointing fluctuations of the incoming beam into intensity noise at their outputs. This effect leads to a significantly increased level of LIN after the modecleaners, with respect to the injected stabilized light. Thus it is necessary to further stabilize the laser intensity to a reference after the modecleaners. To achieve this, PDMC2 is used to monitor intensity fluctuations of a beam transmitted by one of the mirrors of MC2. The resulting signal is band-passed by the second loop servo and added to the error signal of the first loop. For a thorough description of the setup and performance of both stabilization loops, as well as measurements of the achieved relative intensity noise, see [Heurs].

After the modecleaners, three sensitive photodiodes measure intensity fluctuations at different ports of the DRMI. The light at the input port that is reflected from and transmitted towards the laser by the power-recycling mirror is detected at PDPR. LIN of the light picked off from the east arm by the anti-reflective coating of the east arm of the beamsplitter is detected at PDSR. Finally, intensity fluctuations at the output port are measured using PDO. For S5, all of these measurements are out-of-loop, since they occur after the PDMC2, the measurement point for the error signal of the second LIN stabilization loop.

Figure 3.22 shows measured transfer functions of the propagation of LIN from the laser input to the modecleaners, to the various measurement points described above. For this measurement, a dominant LIN was injected via the slave laser pump current actuator, and LIN stabilization was deactivated. The transfer function to PDMC2 consists of two single real poles, the modecleaner cavity poles, at around 8 kHz. That to the east arm, measured by PDSR, consists of the modecleaner cavity poles, and an additional single pole at around 17.5 Hz, the power-recycling cavity pole. Finally, the transfer function of the LIN to the output port PDO has roughly the same shape as that to the east arm, but with several additional resonant features, again due to the complicated interplay between LIN around control sidebands, and the resonant conditions in the DRMI.

Figure 3.23 shows the transfer functions from laser intensity noise measured at the dark port to H. The shapes of these transfer functions qualitatively exclude a significantly strong coupling via radiation pressure at the beamsplitter since they do not have a magnitude response close to f^{-2} over any frequency band. Instead, the complicated shape can be attributed to an interplay of competing effects, as
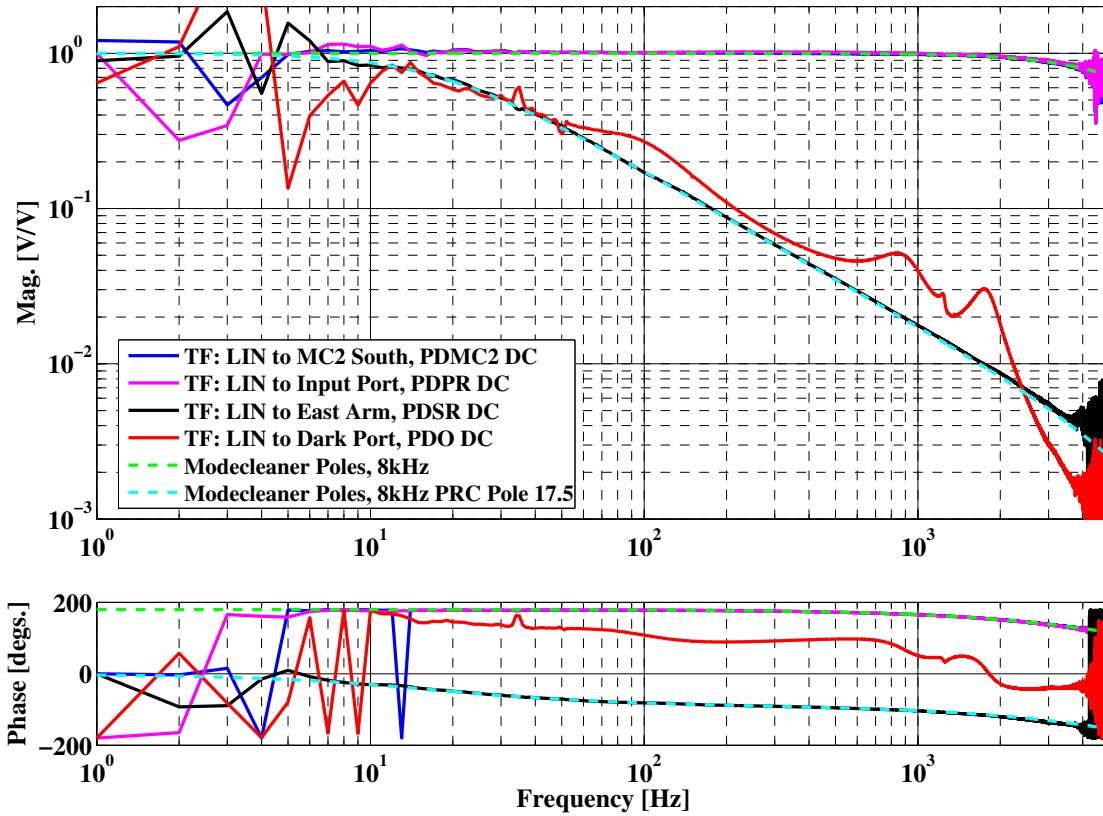
Figure 3.22.: Transfer function of laser intensity noise to various ports of the interferometer

described in [Malec05].

Out-of-loop noise projections of LIN at the input and output ports of the DRMI to H are shown in Figure 3.24. The noise projection for the east arm power measured by PDSR is not shown because the baseline noise of the signal was contaminated by resonant features which are apparently created by clipping of the beam somewhere along its path. The noise projections show that below about 200 Hz, laser intensity noise couples into H with a level that is too high to allow GEO 600 to reach the sensitivity goal. However, a further intensity stabilization can in principle be achieved either by increasing the gain of the existing stabilization, or by using another signal, for example that from PDPR, as an error signal for a third LIN stabilization loop.

In addition to intensity fluctuations of the laser carrier causing intensity fluctuations on the control sidebands, LIN on the control modulation signals translates into
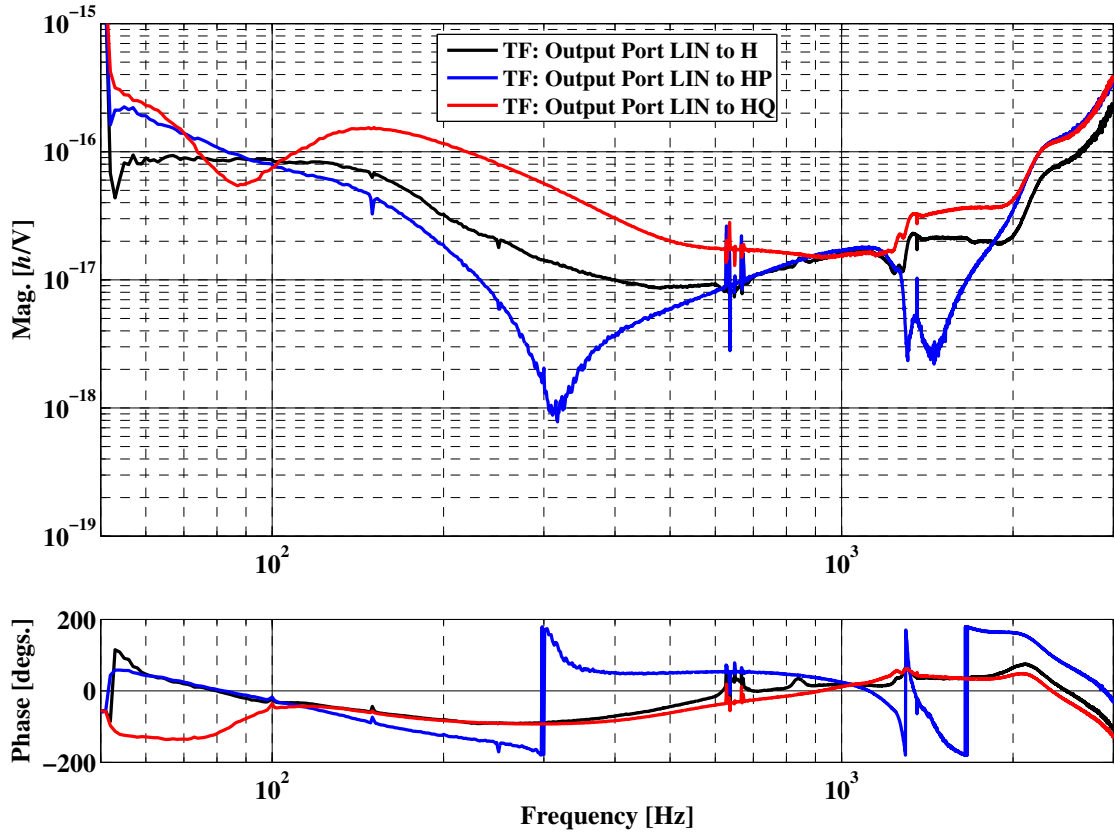
Figure 3.23.: Transfer function of laser intensity at the output port to H.

additional LIN on the carrier and sidebands via the modulation. This can also contribute noise to the detector output, as was discussed for the MID modulation above in 3.3.1.

3.3.5. MID automatic alignment loop

The Michelson differential automatic alignment loop (MID AA loop) is used to superimpose the axes of the beams from the East and North arms at the dark port. It is the most critical of all GEO 600 AA systems both in terms of detector stability and noise performance [Grote03]. In order to maintain longitudinal lock and allow maximum sensitivity, the angle between the interfering beams from the two arms at the dark port should be kept to within 1×10^{-8} rad [Grote04]. To achieve the required gain at the frequencies of the pendulum alignment modes, the MID AA loop has the highest bandwidth of any alignment loop, about 6 Hz. Although this
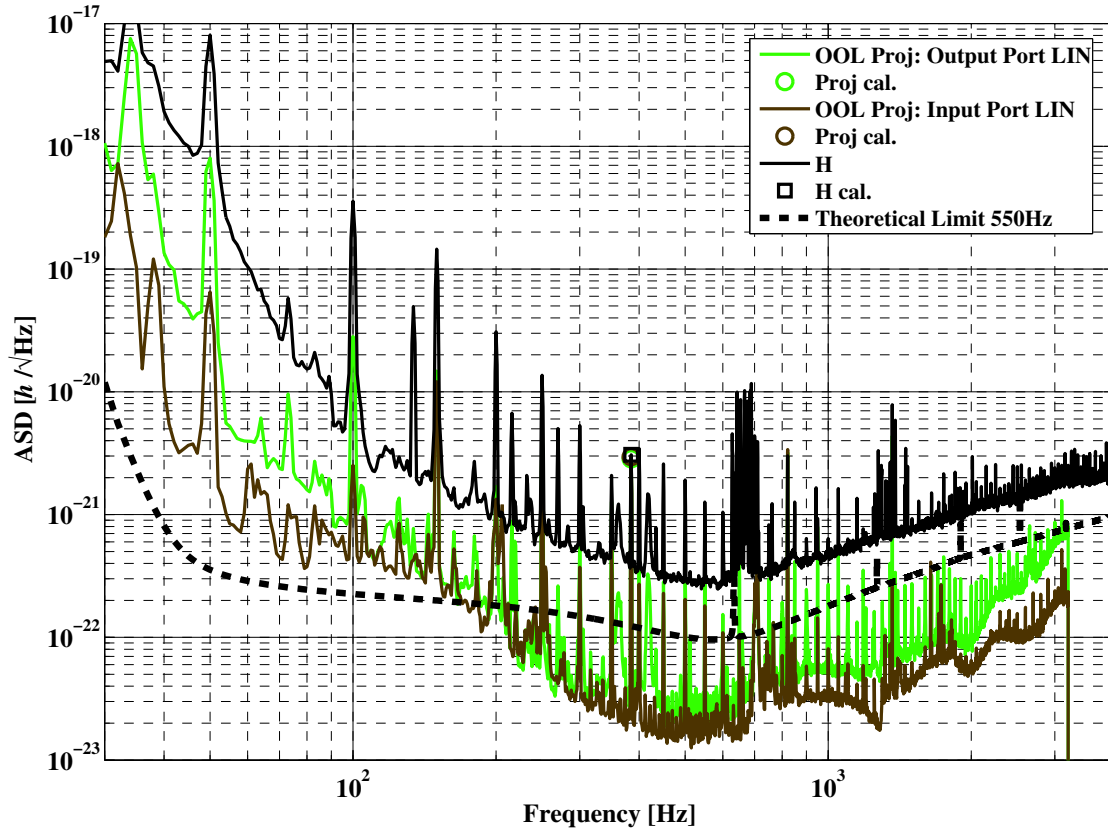
Figure 3.24.: Out-of-loop noise projections of laser intensity noise at the input and output ports of the DRMI to H.

bandwidth is below the detection band of GEO 600, alignment error signals are typically relatively noisy in comparison with length control signals. Therefore a strong filtering of noise by the servo and pendulum are required to allow the very steeply-sloped noise falloff required to achieve the theoretical sensitivity limit at 50 Hz.

Figure 3.25 shows a simplified diagram of the MID AA loop for one degree of freedom (rotation or tilt). The same modulation signal used for the MID loop, at F_{MI}, is used for the MID AA loop. The output beam at the dark port is centered (after the photodetector used for the MID loop) on the output quadrant photodiode, QPDO, with high bandwidth ($\approx 1\,\mathrm{kHz}$) by a galvanometer scanner [Grote03, Grote04c]. The MID AA loop error signal is generated by demodulating the signals from this quadrant photodiode at F_{MI} and making linear combinations of the signals from the individual quadrants, as explained in [Grote03]. It is filtered by a servo con-
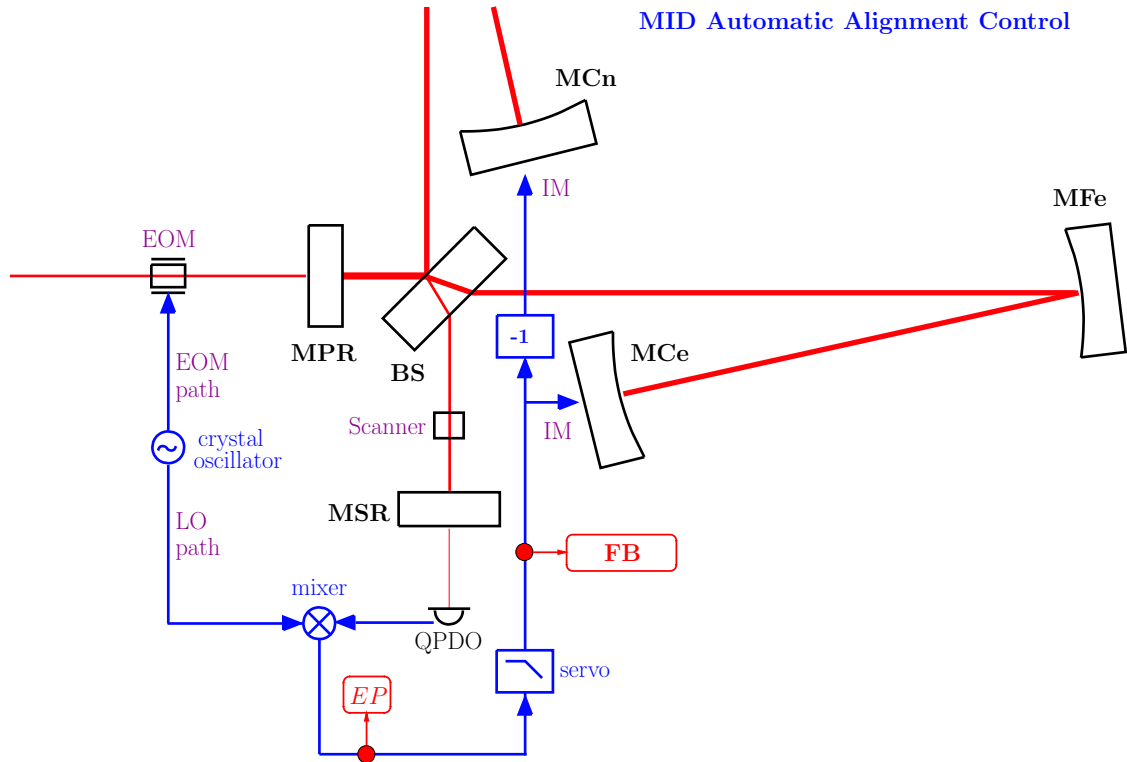
Figure 3.25.: Simplified diagram of the control loop for one (either) of the degrees of freedom of the Michelson differential automatic. A galvonometer scanner is used to center the output beam on the quadrant photodetector.

sisting of analog and digital filters that produce feedback signals that are sent to the magnet-coil actuators for the correct degree of freedom.

Figure 3.26 shows the transfer functions from the two MID AA feedback signals to H. These accurately exhibit an f^{-4} slope, which is the expected longitudinal mirror response to a longitudinal force added at the intermediate mass. The most likely cause of the relatively large coupling of alignment feedback to longitudinal mirror motion is an imbalance in the individual coils of the actuators, which causes an inherent longitudinal force for any applied rotation or tilt signal [Grote]. In principle, this effect can be compensated by a frequency-dependent orthogonalization of the longitudinal and alignment degrees of freedom of the intermediate mass drives. Another possible coupling mechanism is angle-to-length coupling caused by the rotation or tilt of the solid body of the mirror, in conjunction with a miscentering of the beam. For this mechanism, a given misalignment fluctuation will create a
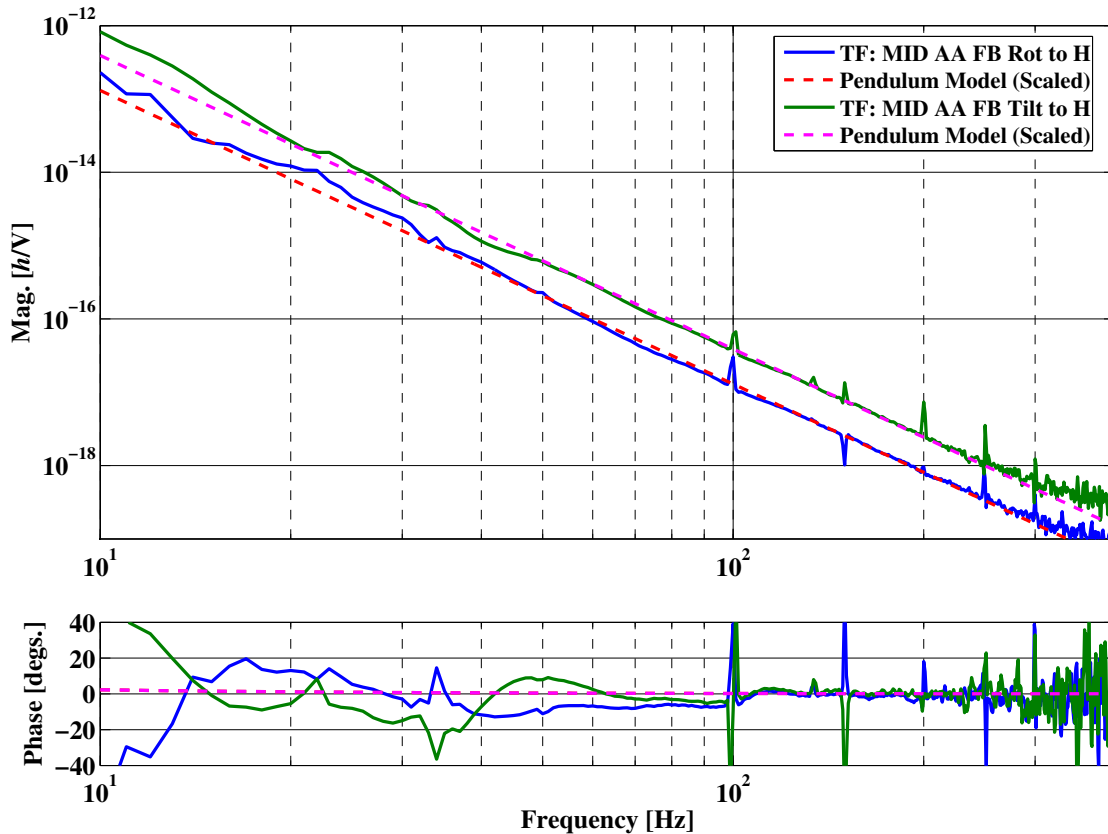
Figure 3.26.: Transfer functions of Michelson differential auto-alignment feedback signals to H, shown together with a model of the transfer function from a longitudinal force applied to the intermediate mass to longitudinal mirror motion.

larger (apparent) displacement of the mirror surface for a larger miscentering of the beam on the surface. The effects of this coupling in GEO 600 might be alleviated by a more accurate beam centering. In addition to these, imbalanced force due to *e.g.,* magnet variation, coil-magnet alignment, and asymmetry of the suspensions may play a strong role in the coupling.

Figure 3.27 shows in-loop noise projections of the tilt and rotation feedback signals to H. This shows that currently, noise contributed by the MID AA loop is dominantly limiting the detector sensitivity below about 80 Hz. Reduction of this noise is therefore a primary goal for the future. A software subtraction of this noise from H is discussed in Chapter 4.
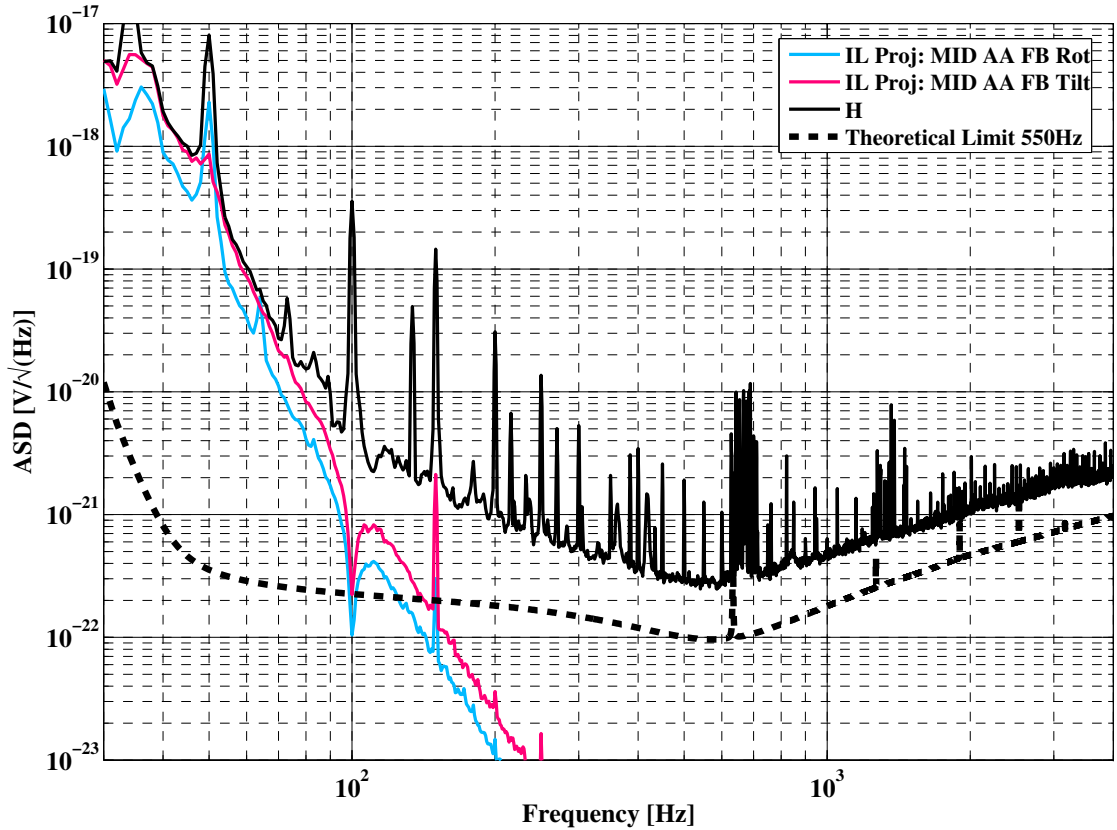
Figure 3.27.: In-loop noise projections of the Michelson differential automatic alignment feedback signals to H.

3.4. Additional noise contributions to H

In addition to the noise caused by the instrumental subsystems described above, noise analysis has been done for a variety of other noise sources, including environmental noise. A few notable examples are described below. The noise projection procedure has been applied with generally less success for all non-instrumental noise sources studied thus far. This is likely due to the fact that many of these, particularly environmental noise, do not have a single well-defined coupling path, and/or do not couple linearly. However, since the coupling of environmental noise to H has become more significant as the detector sensitivity has increased, it is expected that noise analysis of these noise will play a crucial role in the future success of commissioning.

3.4.1. Acoustic noise

As can be seen on the GEO 600 optical layout in A, although all of the main optics and cavity beams are located in vacuum, many auxiliary beams and their related optics and all photodiodes are mounted on optical benches located outside the vacuum system. This increases the susceptibility of the signals extracted from these beams to acoustic noise[10]. In fact, several features in the current spectrum of H have already been associated with acoustics. For example, the feature centered around 360 Hz, visible in spectra of H in this chapter, has been identified as an acoustically-driven resonance of a component located on the optical bench on which PDO is mounted.

So far, the coupling of acoustic noise to H has been observed to be largely non-linear. This has prevented the successful application of noise projections. Other sorts of analysis, chiefly enhanced acoustic noise measurements, have been performed instead.

The coupling of acoustic noise to H can be reduced by using higher quality and larger optics for the sensitive external beam paths, through acoustic mitigation of these paths, *etc.* The ambient acoustic noise level may also be reduced by improved isolation of the sources or other forms of mitigation. Work in this vein has already been done at GEO 600 and is expected to continue in the future.

3.4.2. Scattered light

Much of the commissioning work done over the last few years has involved identification and removal of scattered light components. In most cases observed so far, the coupling of scattered light to H was strongly non-linear. For this reason, the noise projection procedure was not well-suited for identifying these noise sources. However, a powerful and simple method was developed to identify the optical components that cause scattered light noise using transmissive filters, as explained in [Hild06]. Using this method, for example, back-scattered light from the optical bench supporting PDSR was identified as a limiting noise source over two separate extended time periods. This prompted a major re-design of the optical scheme that directs the beam to PDSR, including higher quality optical components, and a simplified optical path. Despite the work done so far, the noise in H over the frequency range of roughly 100 to 600 Hz still exhibits properties characteristic of

---

[10]Since the vacuum tanks can also transmit acoustic noise, slight clipping of beams within the vacuum system can also lead to increases coupling of acoustic noise.

scattered light, indicating that it is still a significantly contributing noise source. Research is currently underway to understand the scattered light noise coupling to the detector output [Hild].

3.4.3. Beam pointing
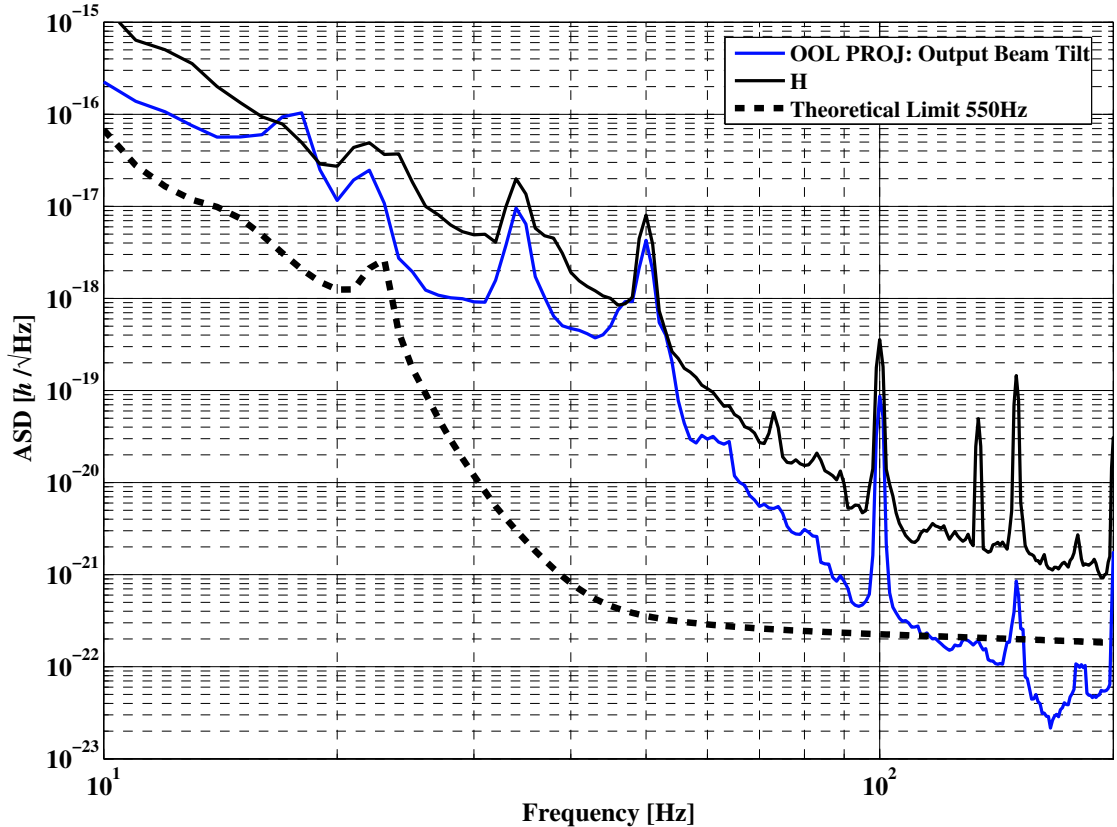
Figure 3.28.: Out-of-loop noise projection of tilt fluctuations of the output beam to H.

Movement of the beams that are used for detection of various signals can couple to H via a variety of mechanisms. These include scattered light, beam clipping, and non-uniformities of optics and photodiodes, *etc.* Prior to S5, measurements were made in order to estimate the coupling of pointing noise of the beam exiting the output port of the DRMI and incident on PDO to H. The axis of the beam was modulated in tilt using a suspended directing mirror (namely BDO2, which can be located in A), such that the beam moved vertically on PDO. This tilt motion was

detected by a position-sensitive device, located close to PDO. The output of this device was used to compute a transfer function to H. An out-of-loop projection of the ambient tilt of the output beam, again measured using the position-sensitive device, is shown in Figure 3.28. This indicates that the linear coupling of the output beam tilt to H is not a directly limiting noise source currently, but is above the sensitivity limit below about 100 Hz. A stabilization of the axis of the output beam, or a reduction of the coupling, perhaps with improved optics, may be required to reach the sensitivity goal.

3.4.4. Electrical pickup and magnetic fields
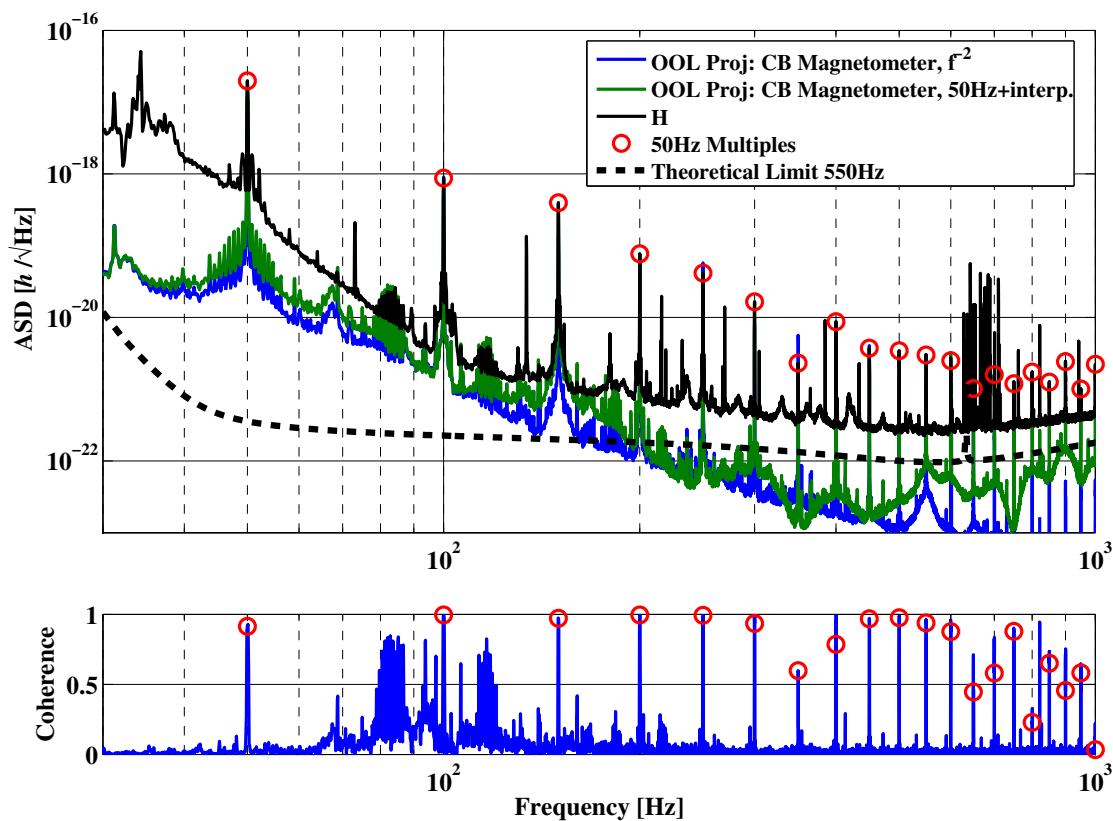
Figure 3.29.: Two types of out-of-loop "noise projections" of magnetic field fluctuations in the central building to H.

Among the most immediately apparent features of the detector output spectrum are the lines at multiples of 50 Hz[11]. These are features of the German mains power

---

[11] Also immediately apparent are the groups of large lines centered around 650 and 1300 Hz.

system, which is based on 50 Hz AC current. The multiples of the fundamental frequency originate from distortions of the waveform caused by the nonlinear loads of electrical devices [Lück]. In turn, these lines couple into virtually every electronic device through the mains power, ground loops, electromagnetic radiation, or electrical and magnetic fields, *etc.*

Figure 3.29 shows a high frequency resolution spectrum of H with every 50 Hz line marked. In addition, two types of "noise projections" of the magnetic field fluctuations measured by a magnetometer located in the central building are shown. The first of these is made by using each multiple of 50 Hz as a "calibration line" with which to estimate the transfer function, at that frequency, from magnetic fields to H. A full transfer function is then formed by interpolating the values between each point estimate. The second assumes an f^{-2} transfer function that could result from coupling via a mirror suspension that has magnets at its ultimate level (*e.g.,* the signal-recycling mirror). The overall gain of this transfer function is set such that H and the noise projection agree at 100 Hz. The subplot of the figure shows the measured coherence between the magnetometer and H. Although these estimates are obviously very inaccurate, they indicate that magnetic field fluctuations are conceivably a significant source of noise in H, and are worthy of further investigation.

3.5. The full technical noise budget

The most important noise projections measured near the start of S5 are shown overlaid in Figure 3.30. Also shown is the total of these noise projections, which is calculated by assuming all of the noise sources to be uncorrelated[12] and summing the individual noise projections in quadrature. This figure represents the known noise budget near the start of S5. Comparison with H shows that feedback control noise, particularly those of the MID AA loop limit the sensitivity below about 100 Hz. The higher frequency end of the spectrum, above about 600 kHz, is limited chiefly by shot noise, but is also influenced by a combination of MID loop dark noise and oscillator phase noise. The gap between H and the sum of the projections over the intermediate frequency range indicates that a large portion of the noise present in H at those frequencies is not explained by the noise projections. As mentioned above, the behavior of this noise indicates components that originate from nonlinear

---

These are the violin modes of the fused silica fibers of the quasi-monolithic triple pendulum suspensions. The properties of these fibers and their violin modes are characterized in detail in [Goßler]

[12]The coherence between the noise projections shown here is in general very small
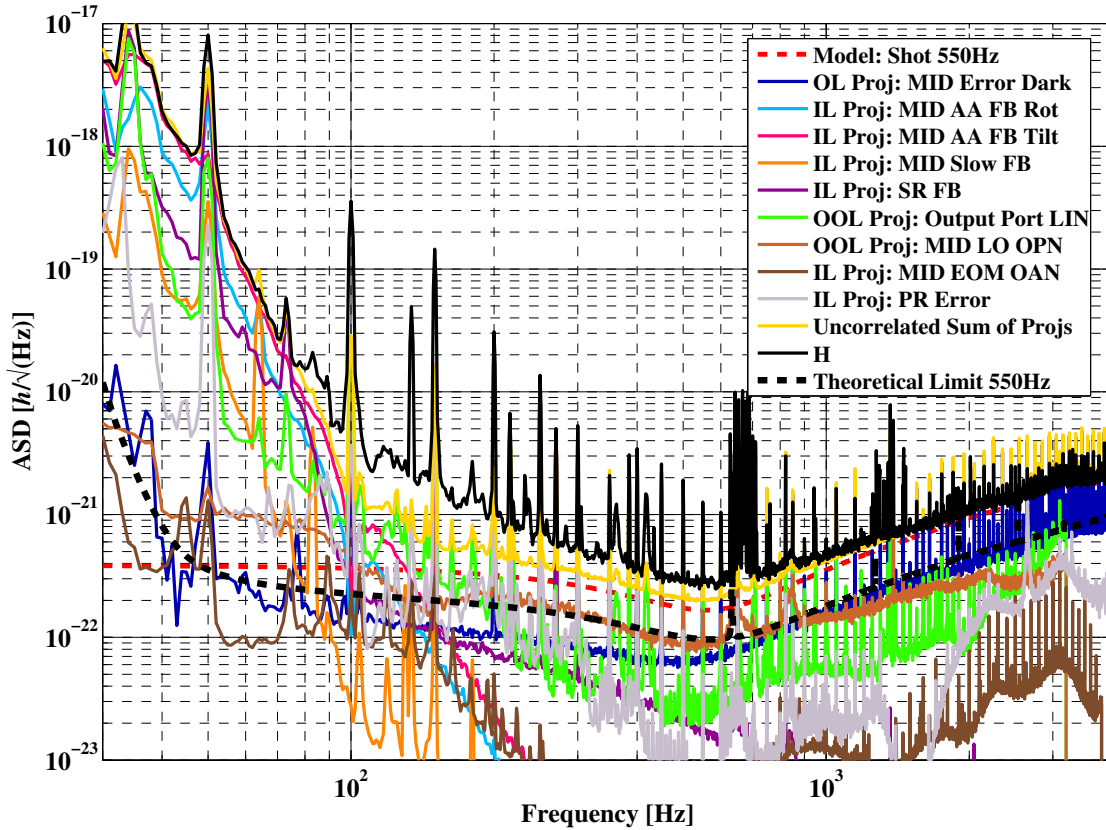
Figure 3.30.: A typical noise budget from a time near the start of S5, showing the most important noise projections to H. Also shown is the uncorrelated sum of the individual noise projections.

processes such as scattered light.

3.6. Summary

Linear noise projections of instrumental signals to H have played a critical role in the commissioning of GEO 600 by identifying the level with which instrumental noise couples to the detector output, and thereby often leading to its reduction and removal. In this chapter, noise projections relevant to S5 have been used to identify much of the limit to the current sensitivity. Despite this, the spectrum of H still has significant unidentified components. Some of the unidentified noise is believed to originate from environmental sources with nonlinear couplings. These are not

easily characterized using the noise projection method described in Chapter 2, and therefore have to be investigated using other noise analysis methods.

Chapter 4.

Automated noise budget, noise subtraction, and vetoes for false gravitational-wave events
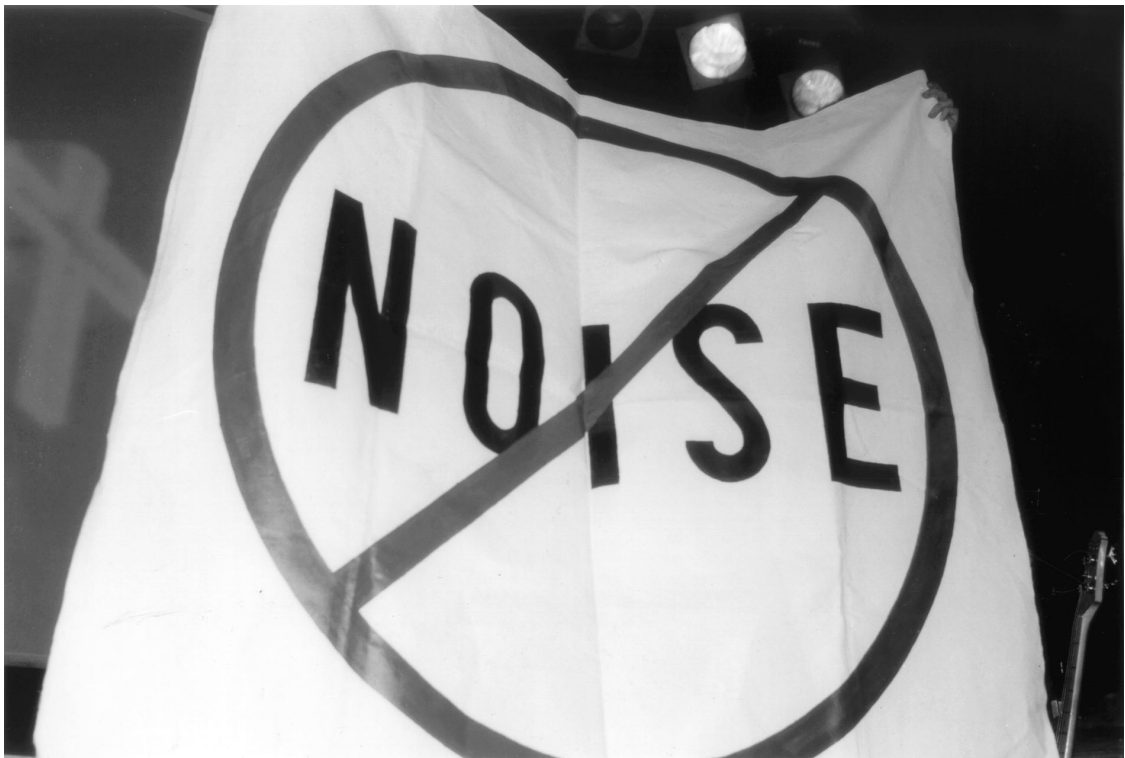
4.1. Introduction

In the previous two chapters, the procedure for noise projection and results of its application were presented. In this chapter, three general extensions to the noise projection method are introduced, and the initial results of tests relating to the implementation of each for the S5 run are presented.

4.2. Automated noise budget

The noise projections described in the previous chapters represented snapshots of the coupling of given noise sources to the detector output for particular stretches of time. Such information may be sufficient to allow the commissioners to identify the most important noise sources close to the time of measurement. However, noise levels and transfer functions are often dynamic (variations on the order of tens of percent are common under nominal conditions, but sometimes the variations are much larger). For this reason it is desirable to perform noise projections continuously in order to have an accurate measurement of the complete noise budget at all times. Automation of the noise projection procedure given in Chapter 2 requires the ability to compute both the Fourier transforms of the noise channels and detector output and the associated transfer functions at any arbitrary time during nominal detector operation. Possible ways of accomplishing this are discussed below.

If the above were accomplished, a noise budget could be obtained for any time, including during a data-taking run. One possible application of this information would be to make a real-time automatic noise budget monitor. This could be a set of amplitude spectral densities for H and each noise projection, like those shown in Figure 3.30, but with a constant update rate of, *e.g.,* 10 s. Automation of the noise budget is necessary for the two extensions described in the following sections.

4.2.1. Computing the Fourier transforms

Automated computation of the Fourier transforms for noise channels that are measured out-of-loop or in-loop is straightforward, since these signals are continuously available during nominal detector operation. However, this is not true for any noise channel that is measured in an open-loop (since loops are closed in nominal conditions). For open-loop noise projections, it may be possible to establish that the

noise source does not vary significantly with time, such that rare measurements of it are sufficient to estimate its value. Alternatively, if the noise is known to depend on another observable, it may be possible to predict its level using a model and another recorded signal (*e.g.,* predict shot noise level using a measurement of the DC laser power).

4.2.2. Computing the transfer functions

In the noise projection procedure given in Section 2.3, computation of the transfer function from N_j to H was carried out for a period during which a dominating noise of type n_j was injected. It is not practical to measure a transfer function for each noise channel continuously following this procedure, because adding dominant signals to the system reduces the sensitivity of the detector[1]. Instead, a less intrusive technique must be used to estimate the transfer function for arbitrary times.

Observation of the behavior of the transfer function with time can help dictate which technique to use. If a given transfer function is shown to be relatively stable on short timescales, and to vary only slowly, rare measurements of it are enough to estimate its value. For example, a dominant noise could be injected over the frequency band of interest for $100\,\mathrm{s}$ once per week, and the transfer function computed from that data could be used for the noise projections from that time up to the next measurement period. If a transfer function is shown to vary primarily by a frequency independent coefficient, rare measurements of the transfer function in combination with continuous measurement of this coefficient would allow estimation of the transfer function. Semi-continuous measurement of the coefficient can be accomplished in a minimally intrusive way by injecting a calibration line at a single Fourier frequency, and measuring the ratio of its amplitude in N_j and H for times long enough that the SNR of the line in H is sufficient to allow the desired accuracy of the coefficient estimation. Finally, transfer functions that vary in a frequency-dependent way are the most difficult to estimate semi-continuously. One method for accomplishing this is using calibration lines at several Fourier frequencies and then measuring the transfer function semi-continuously at those frequencies and fitting the results to a parameterized model as is done in the GEO 600 calibration process [Hewitson04c, Hewitson04b]. This, however requires a well-understood model for the transfer function.

---

[1]It is theoretically possible to inject pseudo-random noise at various points and subtract it from the detector output using the measured transfer functions, but this is technically difficult and requires that the system behaves perfectly linearly.

4.2.3. Initial tests
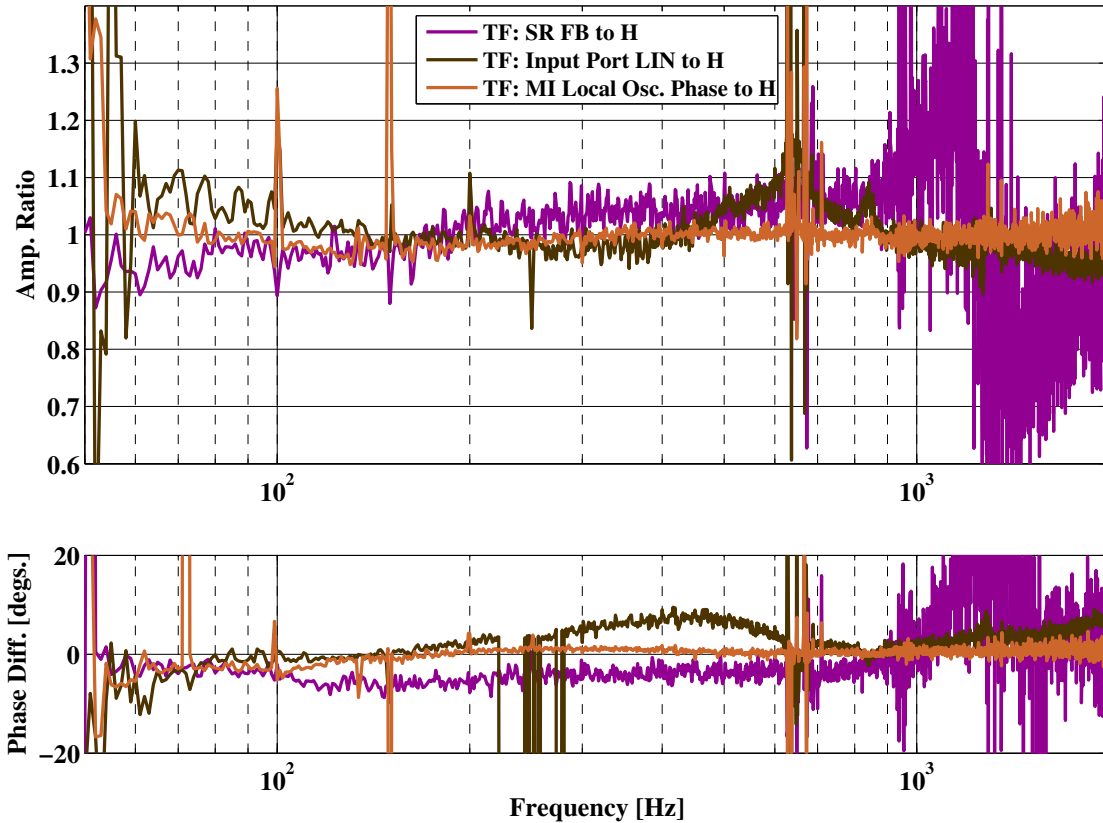
Figure 4.1.: Amplitude ratios and phase differences of several transfer functions from noise channels to H measured on two separate days (a Tuesday and Thursday of the same week) near the start of S5.

The transfer functions used for noise projections in GEO 600 are typically computed with 100 averages from 100 s of data taken during a period of time when a dominating band-limited random noise of type n_j was injected. In order to judge how stable these measurements are on day time scales, the transfer functions for several noise sources were computed twice, using periods of data with noise injected separated by roughly two days, near the start of S5. Amplitude ratios and phase differences of the transfer functions from these two times for several noise channels to H are shown in Figure 4.1. These measurements are within 10% in amplitude and 10 degrees in phase from roughly 60 to 2000 Hz (except for the transfer function for signal-recycling feedback, which was not accurately measured above about 1 kHz). This agreement was typical of the other noise transfer functions that were

checked by this method for the frequency ranges over which their associated noise source exhibited significant (*i.e.,* easy to measure) coupling to H.
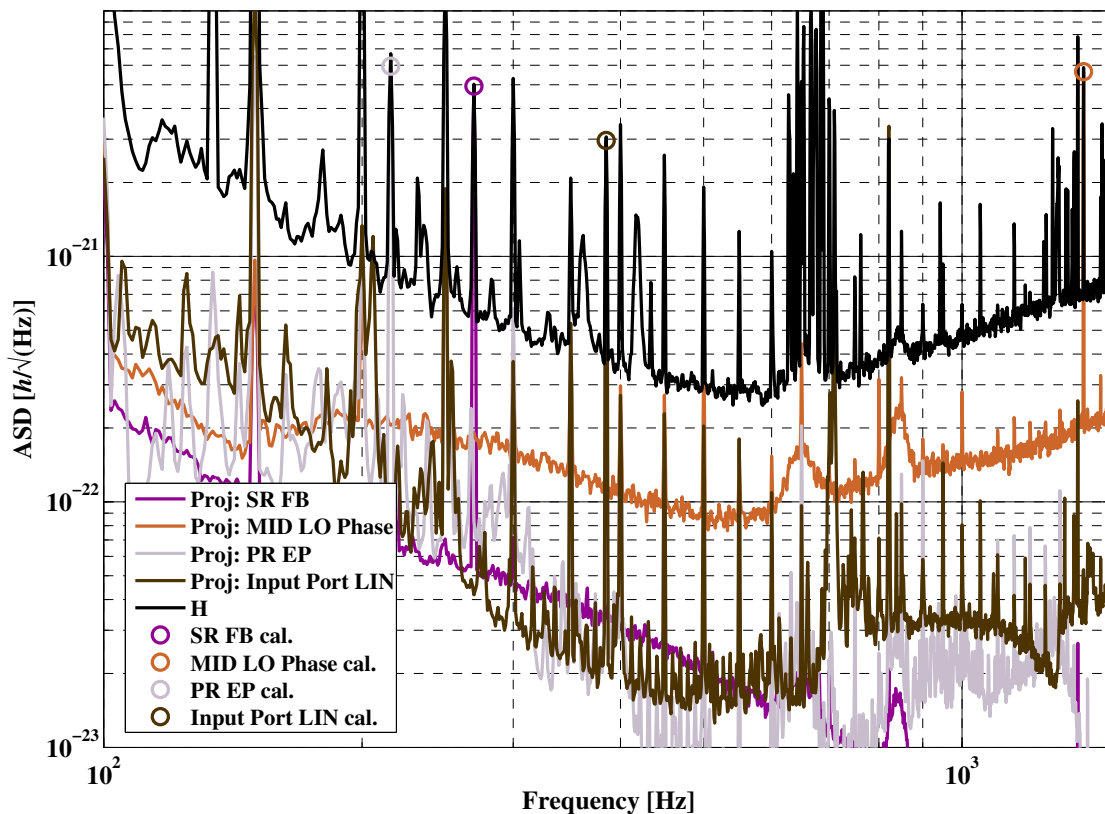
Figure 4.2.: Noise calibration lines (marked with circles) as they typically appear in ASDs (here produced from $100\,\mathrm{s}$ of data with 100 averages) of H and several projected noise channels during S5.

To allow the tracking of faster changes in the transfer functions, noise calibration lines that dominated both the noise channel and the detector output at a given Fourier frequency (in spectra longer than $1\,\mathrm{s}$) were injected for several noise sources. Figure 4.2 shows these calibration lines as they appear in typical (averaged $1\,\mathrm{s}$) ASDs of several of the noise projections and in H. The relative agreement between the amplitude of the calibration line in the associated noise projection and in H indicates the accuracy of the transfer function used for the projection with respect to the actual coupling. These calibration lines will be injected continuously throughout S5.

In order to estimate the accuracy of the transfer functions at the calibration line frequencies up to the time of writing, the amplitude ratios and phase differences
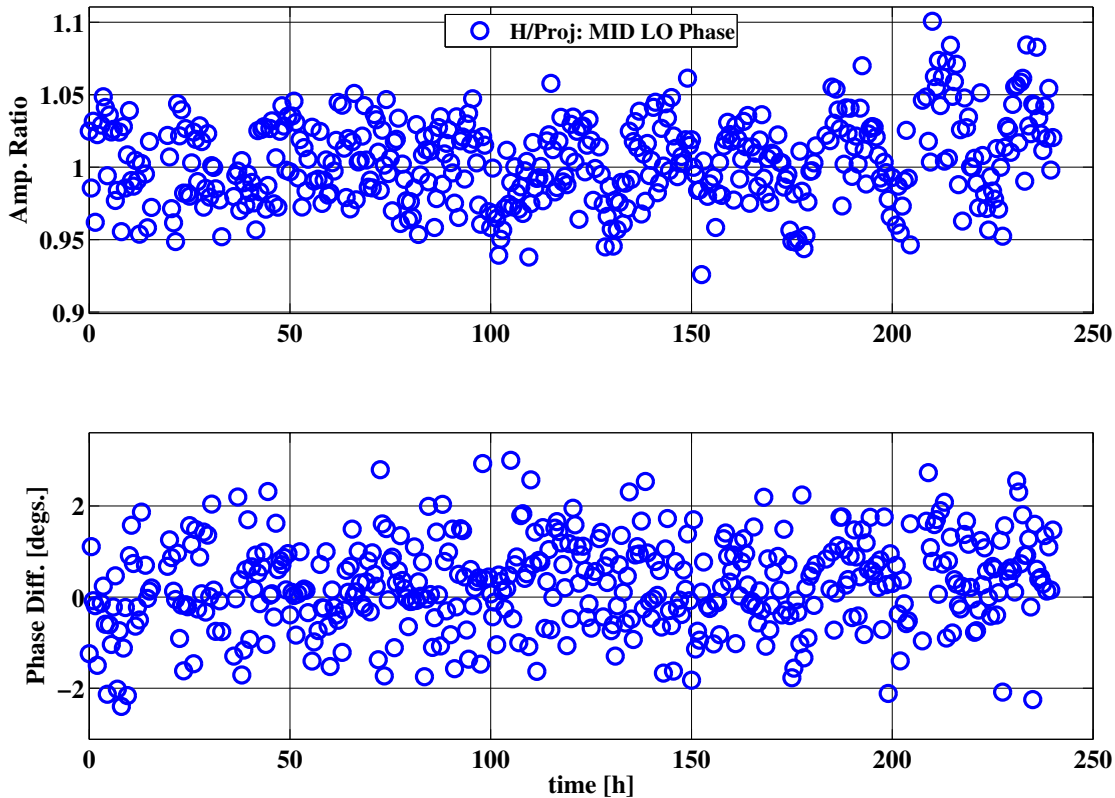
Figure 4.3.: Amplitude ratios and phase differences of H and the noise projection of the phase noise of the MI local oscillator, sampled at the calibration line frequency for 32 seconds twice per hour for ten days near the start of S5. Both y-axis scales are $\pm$ three standard deviations.

of the noise projections and H at those frequencies were computed and plotted versus time. Figure 4.3 shows a time series of 480 measurements of this for the projection of phase noise of the MI local oscillator to H over a ten day period. For these measurements, a 32 second long unaveraged Fourier transform of each signal was produced once each half hour, from which the phase and amplitude at the calibration line frequency were extracted. The SNR of the calibration line in H was typically close to 50 for each measurement. Figure 4.4 shows a histogram of the same data. These measurements show that this transfer function is relatively stable over time scales of several days at the frequency of the calibration line. Statistics for the same measurements performed on several noise projections are shown in Table 4.1. Most of the transfer functions checked by this method over these ten days were accurate to within about 10% in magnitude and 10 degrees of phase at the Fourier frequency of the calibration line. This level of accuracy is sufficient for
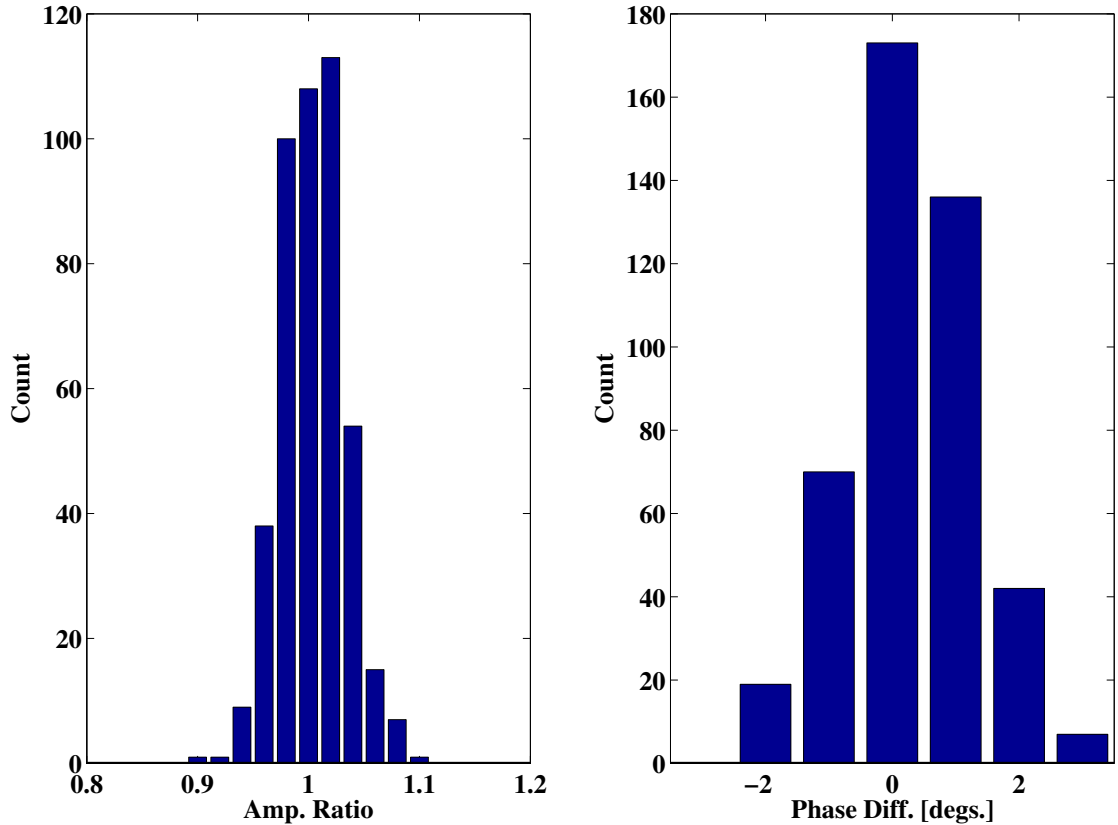
Figure 4.4.: Histograms of the amplitude ratios and phase differences of H and the MID oscillator phase noise projection for the ten day period.

most purposes involving several second long averaged transfer functions. Thus for S5 it appears reasonable to produce an automated noise budget using fixed transfer functions measured roughly once per week.

4.3. Technical-noise subtraction

As mentioned in Chapter 2, a potentially more sensitive detector output signal can be obtained by subtracting the noise budget, or individual noise projections from

Noise channel	Freq. [Hz]		Mean	Median	Stand. dev.
PR EP	216	Amp. Rat.	0.926	0.923	0.031
		Phase Diff.	-0.211°	-0.133°	1.189°
Input Port Power	385	Amp. Rat.	1.008	1.009	0.037
		Phase Diff.	11.2150°	12.312°	4.600°
Output Port Power	385	Amp. Rat.	0.972	0.973	0.039
		Phase Diff.	10.972°	12.039°	4.559°
MI Local Osc. Phase	1385	Amp. Rat.	1.005	1.003	0.035
		Phase Diff.	0.2440°	0.2398°	1.122°
SR FB	270	Amp. Rat.	1.023	1.020	0.042
		Phase Diff.	-5.663°	-5.614°	2.566°

Table 4.1.: Statistics for the amplitude ratios and phase differences of H and several noise projections over ten days of S5.

the detector output[2],

$$\tilde{H}' = \tilde{H} - \sum_j \tilde{M}_j = \tilde{h}_{\text{gw}} + \sum_i \alpha_i \tilde{n}_i - \sum_j \alpha_j \tilde{N}_j. \tag{4.1}$$

The degree to which the influence of a given noise source can be subtracted from the detector output depends on how well the noise channel represents the noise source (*i.e.,* $\tilde{N}_j \simeq \tilde{n}_j$, without additional noise), and the accuracy of the transfer function used to project the noise.

To illustrate the latter point, consider the subtraction of two perfectly coherent signals, one directly sampled from a given noise source, and the other sampled after the same noise is passed through a noiseless transfer function. The original signal is filtered through a filter designed to match the transfer function and then subtracted. The normalized error of the remainder at a given Fourier frequency is [Smith05],

$$\bar{\delta} = \sqrt{\left(\frac{A_{\text{o}}}{A_{\text{f}}}\right)^2 - 2\frac{A_{\text{o}}}{A_{\text{f}}}\cos(\phi) + 1}, \tag{4.2}$$

where $A_{\text{o}}/A_{\text{f}}$ is the ratio of the amplitudes of the original and filtered signals, and ϕ is the phase difference between the two signals. These are determined by the

---

[2]Here it is assumed that the noise channels have negligible sensitivity to gravitational waves (*i.e.,* differential motions of the arms of the Michelson interferometer). If this is not the case, noise subtraction cannot be done without being taken into account by the detector output calibration scheme.

accuracy of the filter used with respect to the transfer function through which the noise passes. Surface and contour plots of the dependence of this error on the amplitude ratio and phase difference of the filter and transfer function are shown in Figure 4.5. These show that to suppress the influence of a given noise on the detector output by a factor of, for example, ten requires that the filter used to project the noise accurately represents the underlying transfer function to within roughly 10% in amplitude and 5 degrees in phase.
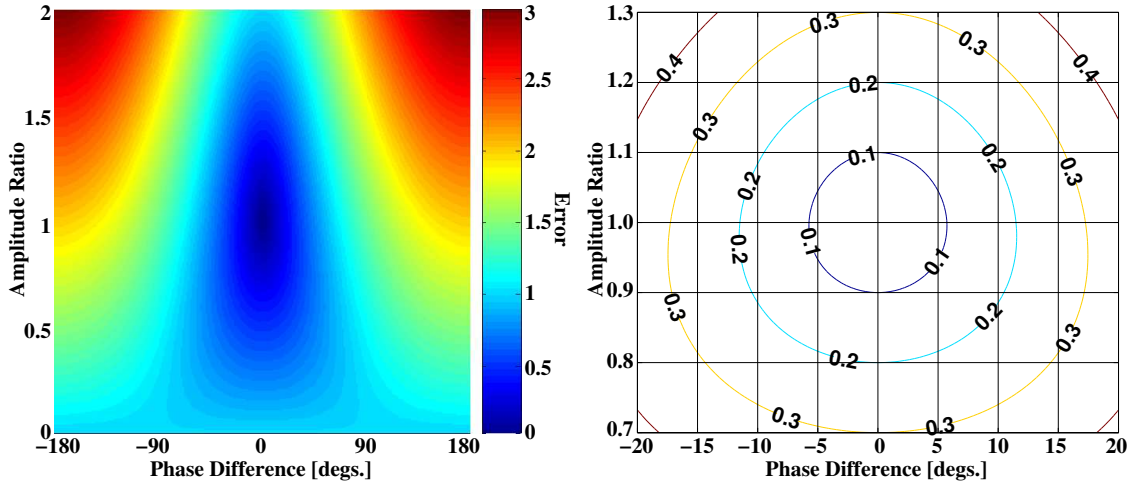
Figure 4.5.: Color depth-plot and contour plot of the normalized error of the subtraction of two correlated signals, as a function of the amplitude ratio and phase difference of the filter used and the real transfer function, at a given Fourier frequency.

4.3.1. Initial tests

In order to maintain a time-domain calibrated detector output signal, it is desirable to accomplish continuous noise subtraction for GEO 600 in the time-domain. The production of time-domain filters with the accuracy required for noise subtraction requires either verified long-term stability of the transfer functions or estimation of their time evolution and real-time adaptive filtering, as done in the GEO 600 calibration process [Hewitson04]. In Section 4.2 it was stated that for the first 10 days of S5, the 100 second long averaged transfer functions that are used for most noise projections are accurate to within about 10% in magnitude and 10 degrees in phase at the frequencies with which their coupling level is significant. This should be sufficient to allow a factor of several reduction of the influence of their associated noise sources on the detector output.
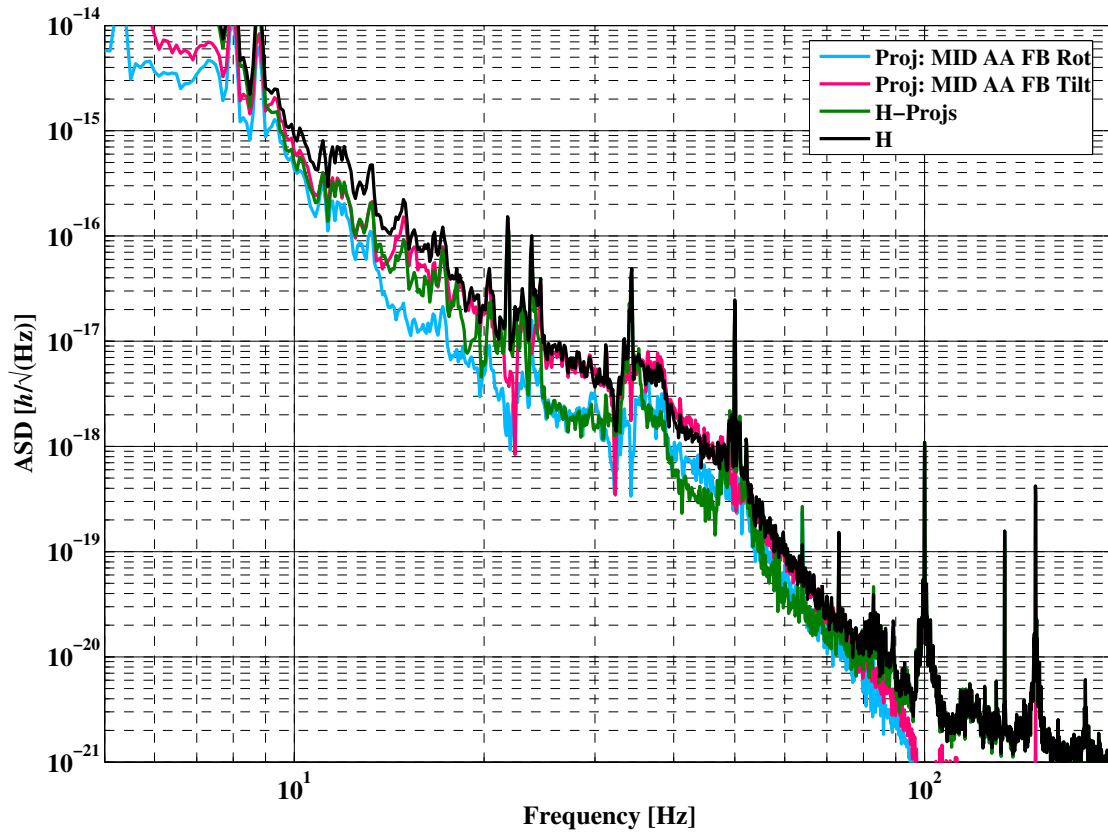
Figure 4.6.: Amplitude spectral densities of H, projected MID AA feedback signals, and the remainder of a time-domain software subtraction of MID AA feedback noise from H.

As was shown in the previous chapter, the sensitivity at the lower frequency end of the GEO 600 detection band is limited by feedback noise added by the MID automatic alignment loops. As a test of noise subtraction, a time-domain filter was built to match the frequency response of the measured transfer function for these feedback paths over the frequency range of interest (roughly 10 to 100 Hz). The two MID AA feedback channels were then filtered through this, and the result was subtracted from H. Figure 4.6 shows a comparison of typical ASDs of H, the projected MID AA feedback signals, and the remainder of the subtraction of the projections from H. A clear improvement in the sensitivity of the detector output can be seen. The ratio of H and the remainder is shown in Figure 4.7. Using this method the detector output signal sensitivity can be increased by roughly a factor of 2-3 over most of the band from 10-70 Hz. The improvement in sensitivity is limited partially by the accuracy of the transfer function, and partially by the
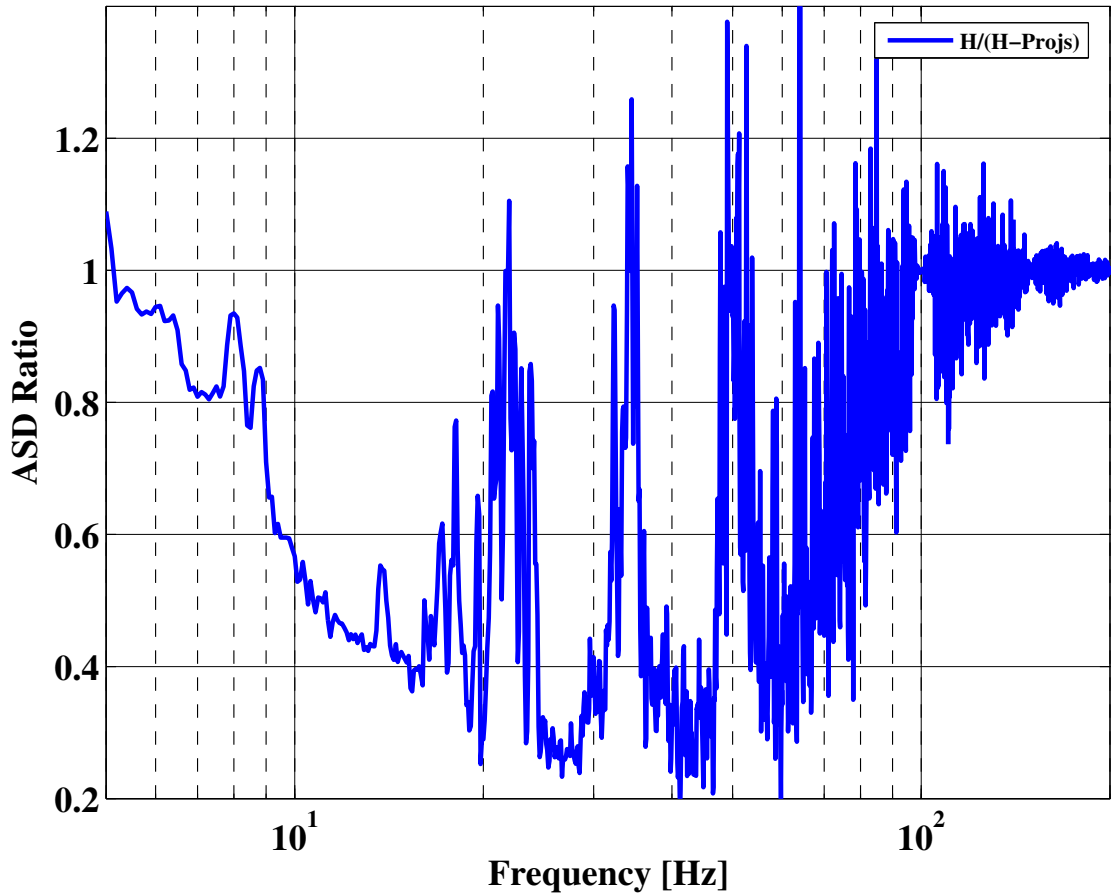
Figure 4.7.: Ratio of amplitude spectral densities of H and the remainder of a time-domain software subtraction of MID AA feedback noise from H that were shown in Figure 4.6.

influences of other noise sources over that frequency range (*e.g.,* feedback to the signal-recycling mirror, see Figure 3.30).

For S5 it is not possible to subtract the entire noise budget from the detector output in the time-domain. Several of the most important noise projections are measured open-loop or calculated (*e.g.,* shot and dark noise), and thus no correlated time-domain data is available for subtraction.

4.4. Vetoes for false gravitational-wave events

The noise projection method can also be extended to help reduce the detrimental influence of technical noise on the analysis of the detector output data for gravitational-wave information. Candidate gravitational wave events that appear both in a noise projection and in the detector output can be identified as originating from instrumental or environmental noise, and vetoed. Such vetoes are extremely important in several gravitational wave searches, in particular the search for unmodeled, short-duration gravitational wave bursts.

A very simple example of a veto strategy based on noise projections is as follows. Consider a search for gravitational-wave burst events that uses an event-trigger generator (ETG) to scan the detector output data and produce a list of candidate events, each parameterized by their time of occurrence, central Fourier frequency, and amplitude. Now consider that each of the noise projections is scanned by the same ETG, resulting in a likewise parameterized list of events. The parameters of these projected technical-noise events can be compared with those of the detector output events. If they are deemed to be coincident, *i.e.,* to fall within time, frequency and amplitude windows set by an assessment of the errors of the transfer functions and the ETG parameter estimation, they can be vetoed.

In practice, the above method can be improved upon with a more sophisticated method, as described in [Ajith06]. Since the timescales for burst events are short ($\ll 1$ s), the performance of any veto method based on noise projections depends strongly on the stability of the transfer functions on these timescales. The development of a robust veto for candidate GW events caused by technical noise for S5 and beyond is a subject of continuing and intense research within our group.

4.4.1. Initial tests

In order to check the performance of veto methods based on noise projections, burst-like events were injected into several noise paths. The projected noise channels were then compared to H for time periods containing injections. Figure 4.8 shows an ASD of H and the noise projection for the MID oscillator phase noise for one second during which a burst event was injected. Here the injected event dominates the oscillator phase noise and H from about 800 to 1200 Hz. An assessment of the veto efficiency of several possible veto strategies based on the data from these hardware injections is ongoing.

As mentioned above, any veto strategy that aims at using the phenomenological
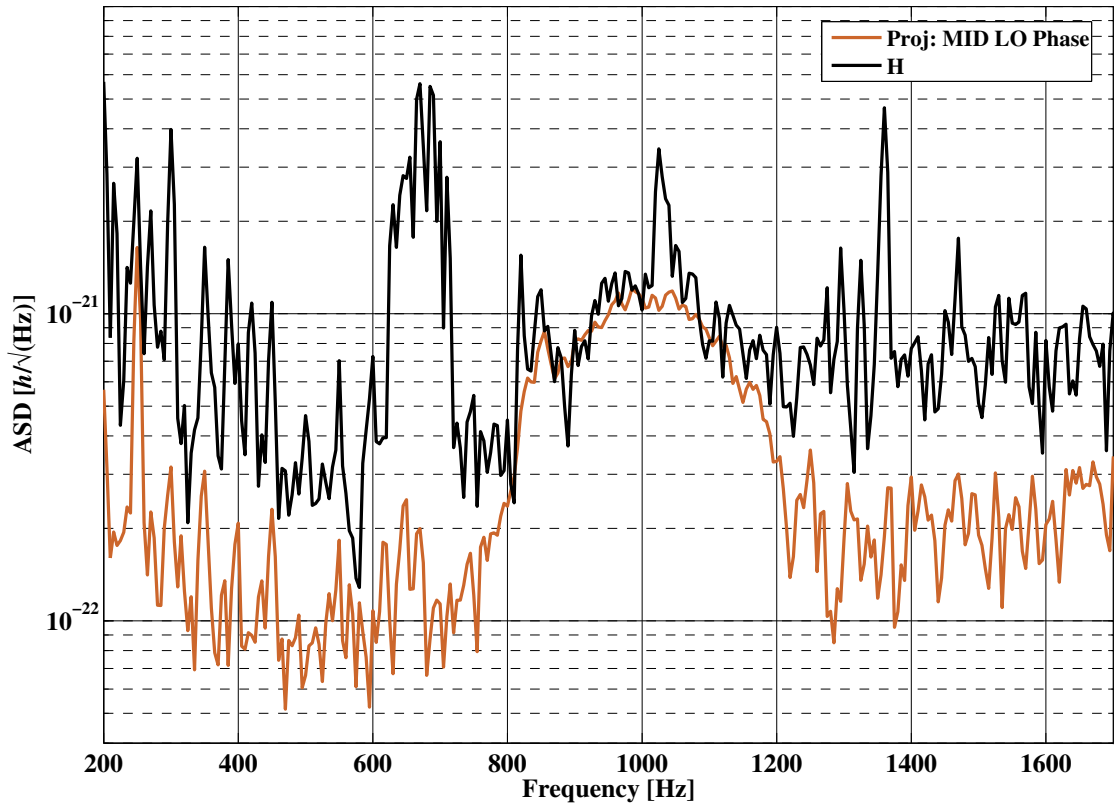
Figure 4.8.: Short (1 second with 5 averages) ASD of H and the projected phase noise of the Michelson local oscillator for a time with an injected phase noise burst-like event.

data produced by noise projections to veto burst events will rely on the real transfer functions being relatively stable on short timescales. For that reason, an experiment was done to check the stability of the transfer functions for the noise channels considered as candidate veto channels for S5 [Ajith06b]. For each noise source, a dominant noise was injected for 100 s, and an averaged transfer function to H was computed for this entire time stretch, (as for those transfer functions presented in Chapter 3). Then, short transfer functions were computed for each 1/16 s segment of the same data stretch, and the amplitude ratio and phase difference of each short transfer function with respect to the averaged transfer function over the full stretch were computed. Figure 4.9 shows the outcome of this for the transfer function from MID oscillator phase noise to H. For this data stretch and noise channel, amplitude variations of more than $\pm 20\%$ are visible. This is considerably larger than the average variations on longer timescales described above. Similar effects have been observed in several of the other transfer functions. Unless these

fast variations can be reduced or tracked, they may reduce the efficiency[3] of a veto strategy based on noise projections for S5.

Magnitude Ratio

Phase Difference [degs.]
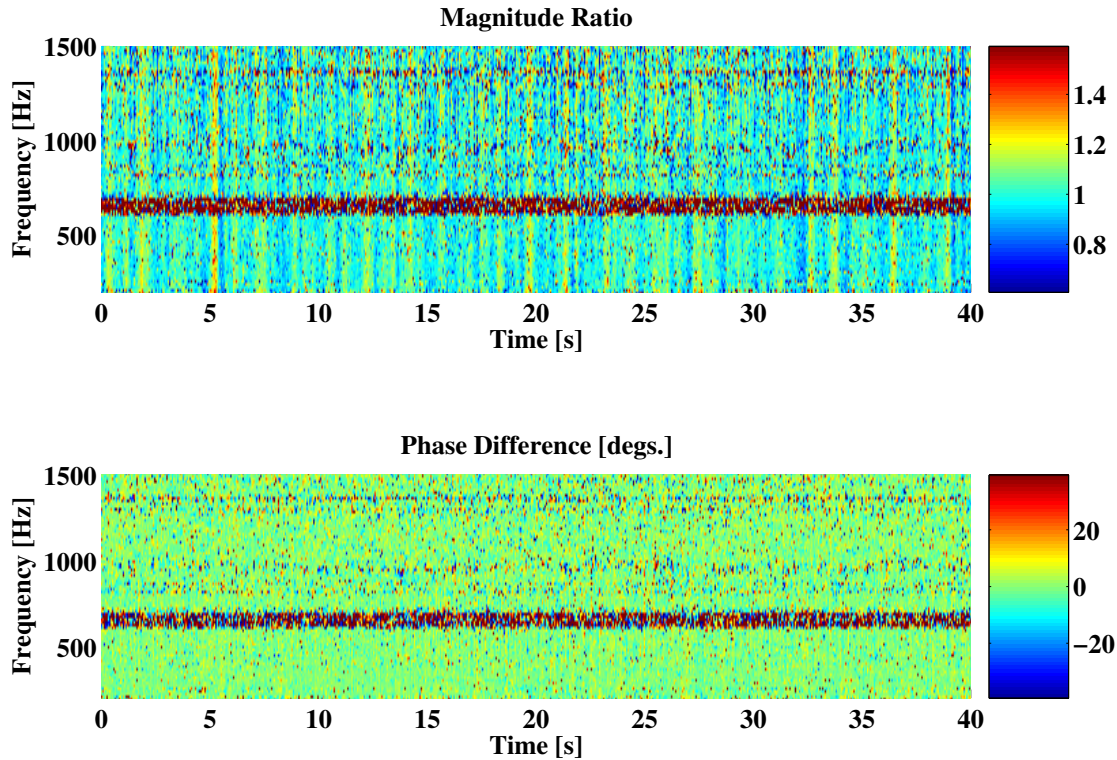
Figure 4.9.: Time-frequency map of the amplitude ratio and phase difference of short measurements of the transfer function from oscillator phase noise to H, with respect to the averaged transfer function calculated for a 100 s time stretch. The color-bar units are those given in the title of each subplot.

4.5. Summary

Several extensions to the noise projection method were described in this chapter, along with first results of the ongoing work to implement each of these within the GEO 600 detector characterization system.

---

[3]The mechanism by which large errors in the transfer functions reduce the efficiency of the veto is by allowing more chance coincidences, or *false alarms*, to be counted among the actual coincidences.

Through continuous calculation of the Fourier transforms and tracking of the time evolution of the transfer functions, many of the noise projections that form the noise budget can be produced automatically. This allows computation of the level with which various noise sources couple to the detector output at arbitrary times, including during a data-taking run, when the detector hardware is inaccessible. It was shown that for the first ten days of S5, the several-second averaged transfer functions used for noise projections are typically accurate to within 10% in magnitude and 10 degrees of phase at the Fourier frequencies at which they have been probed.

Subtraction of the technical noise projections from the detector output was introduced as a technique to obtain a more sensitive detector output. It was shown for data taken during the early part of S5, by subtracting two noise projections from H up to a factor of 3 improvement in sensitivity between 10 and 70 Hz can be achieved.

Finally, using the noise projection technique it is possible to veto candidate gravitational wave events based on phenomenological evidence that they actually originate from technical noise. Initial tests of this using burst-like signal injections are promising, and work is ongoing within our group to use these data to evaluate the efficiency of different veto strategies. However, the stability of the transfer functions on burst timescales appears to be significantly worse than for longer timescales for some noise projections. This may reduce the efficiency of some vetoes.

Appendix A.

Optical layout

The official GEO 600 optical layout is produced using OPTOCAD [OPTOCAD] and maintained by Roland Schilling. The following diagrams are from the most up-to-date version, 1.48.

GEO 600 optical layout
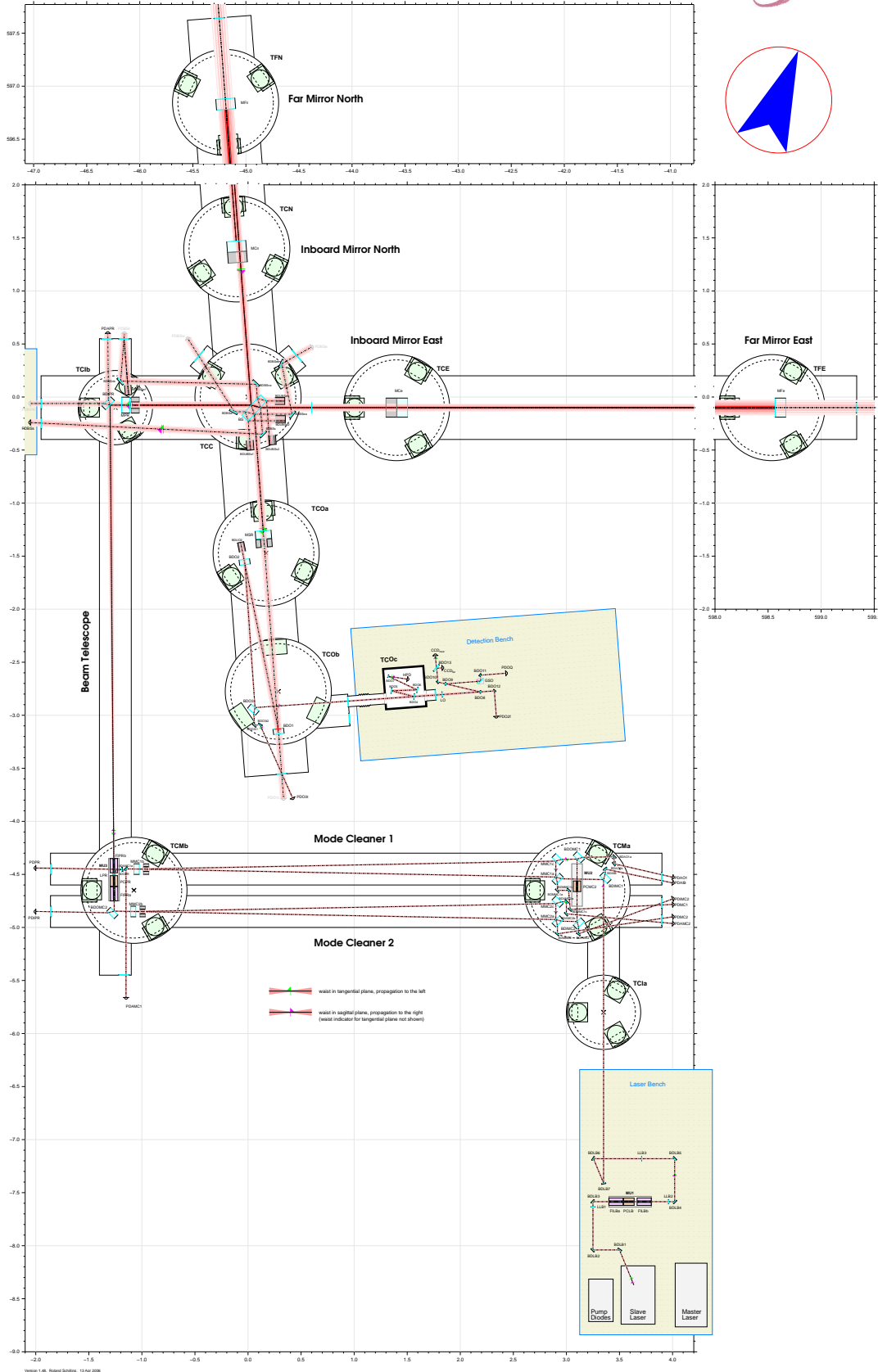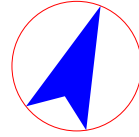
Figure A.1.: Full optical layout of GEO 600.
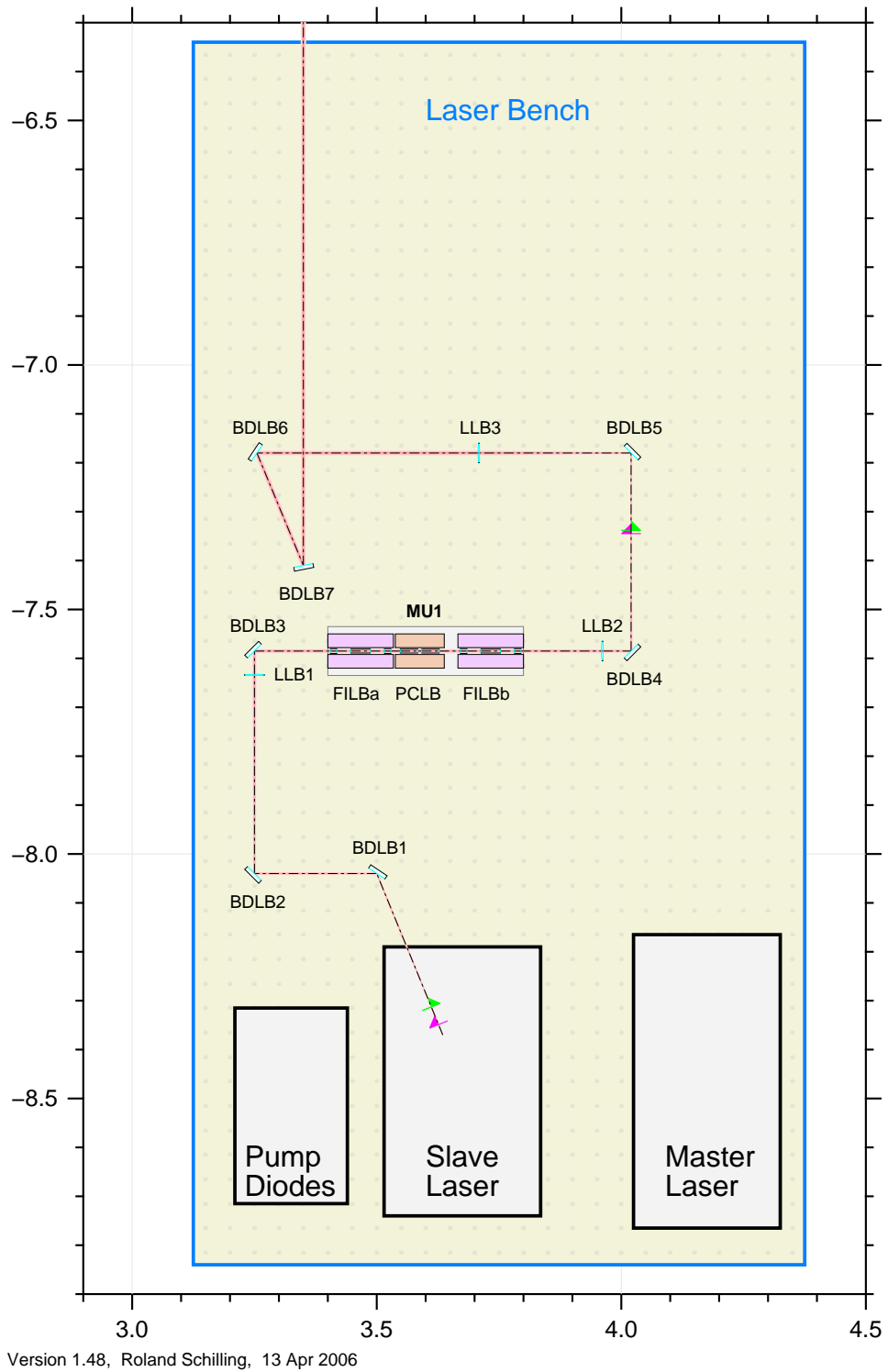
Figure A.2.: Optical layout of the laser bench.
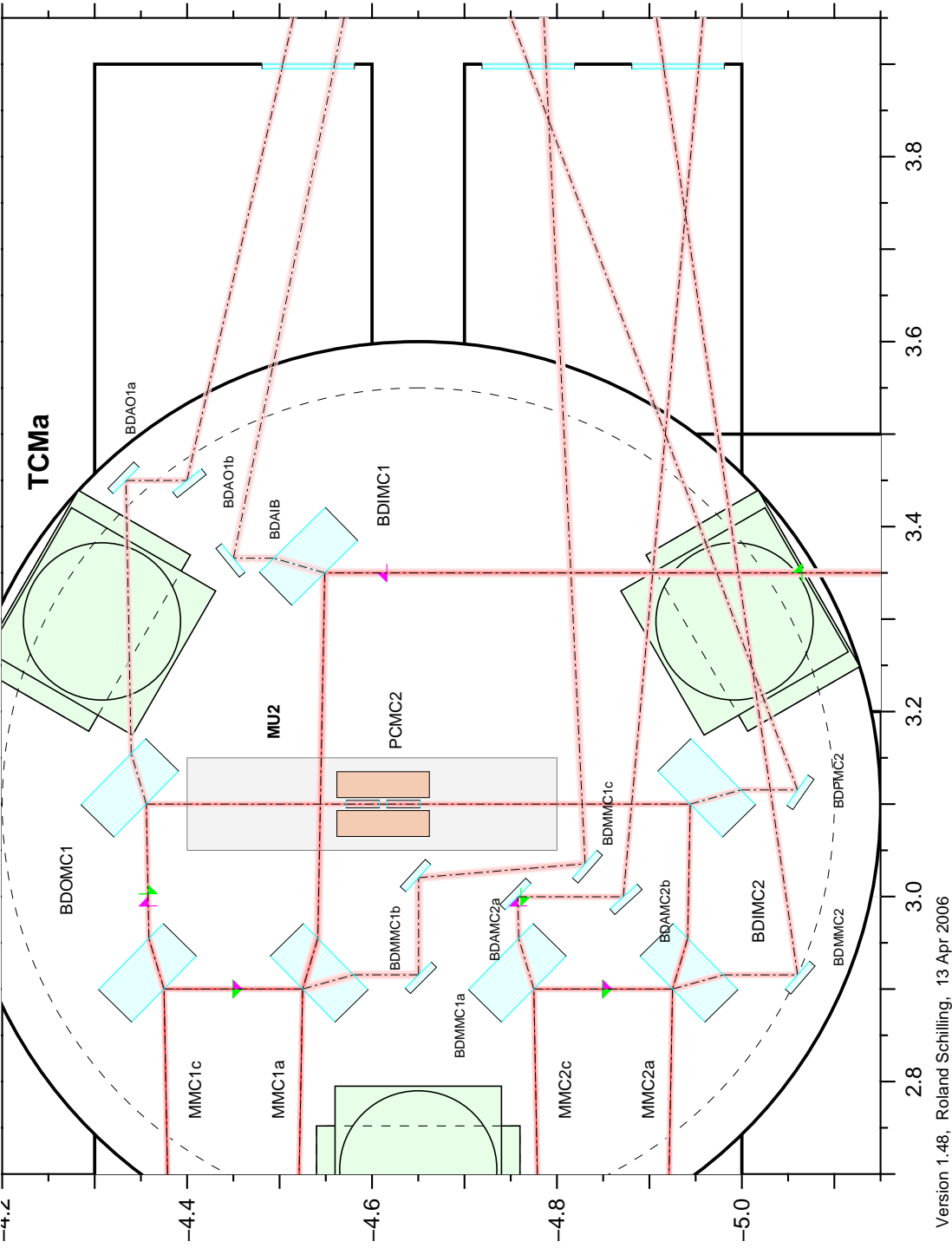
Figure A.3.: Optical layout of the modecleaner vacuum tank TCMa.
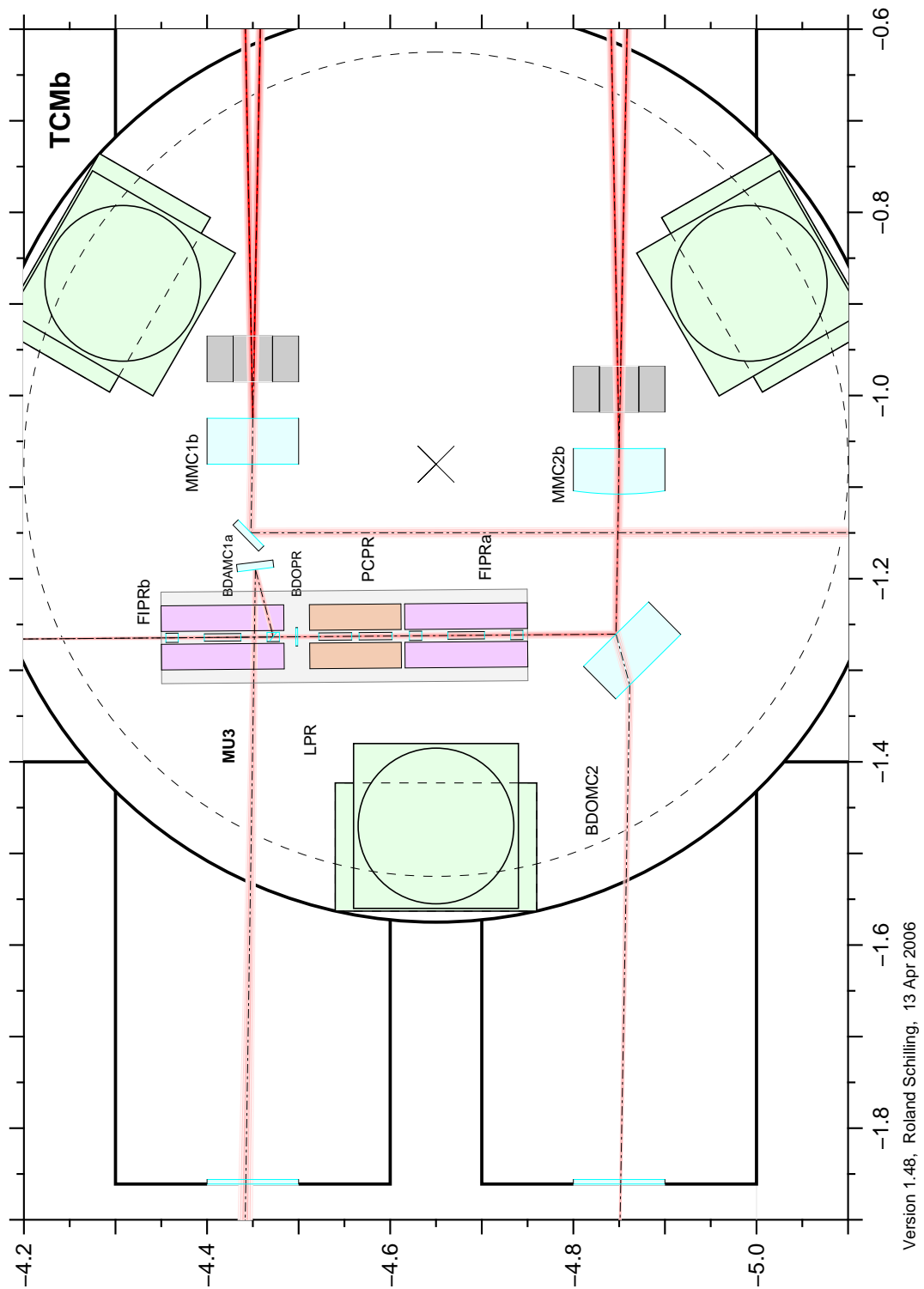
Figure A.4.: Optical layout of the modecleaner vacuum tank TCMb.
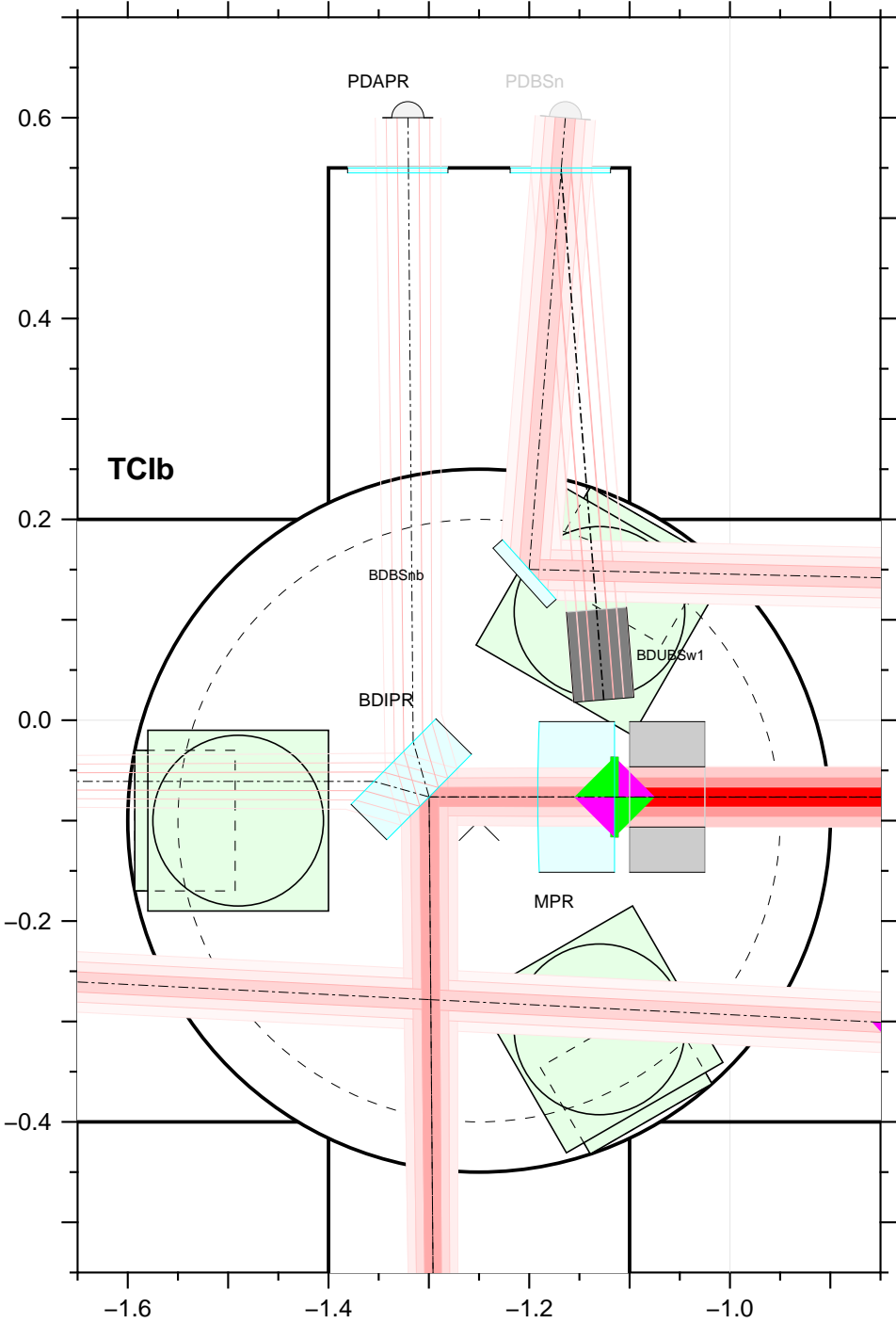
Figure A.5.: Optical layout of the vacuum tank containing the power-recycling mirror.
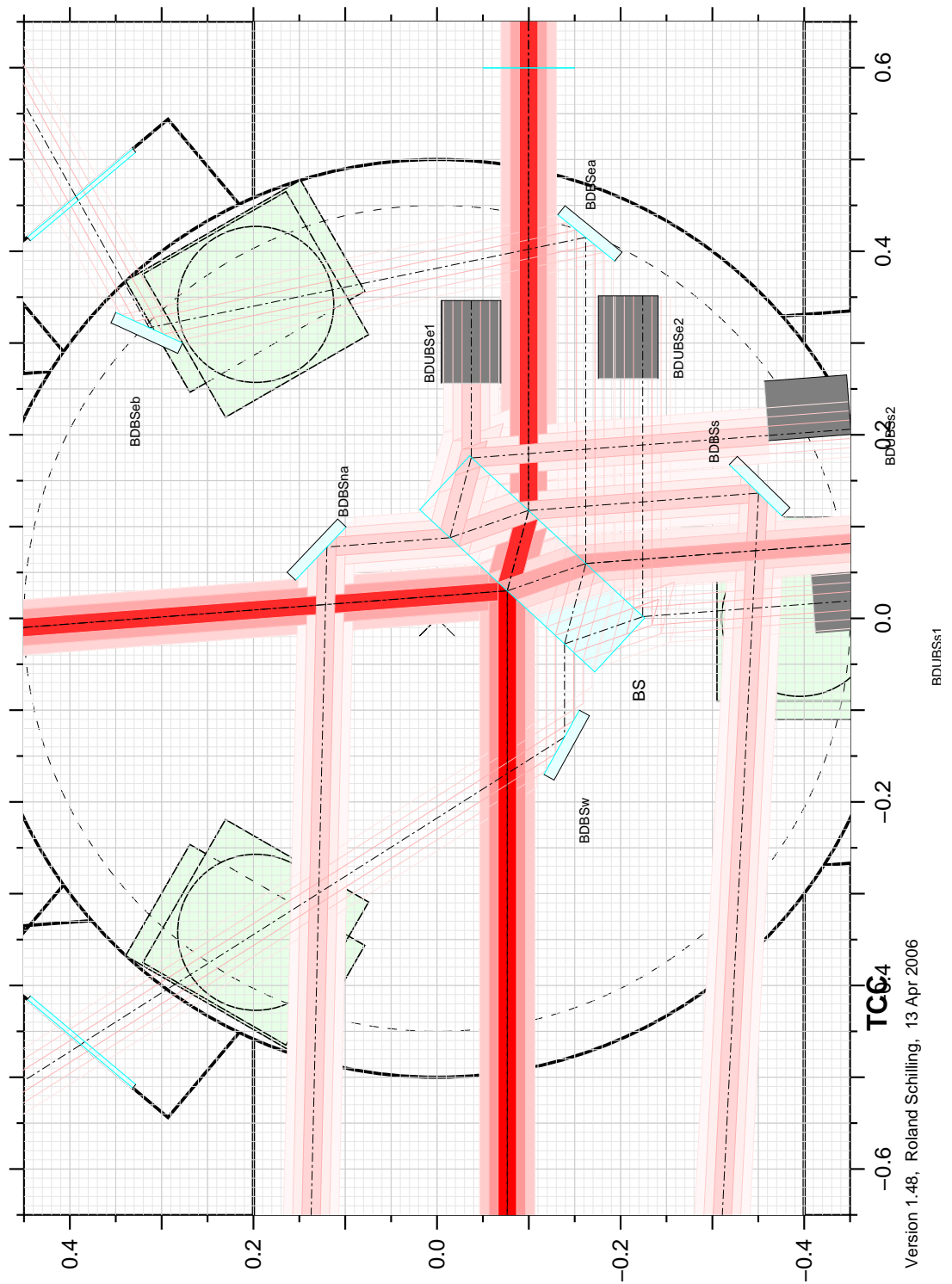
Figure A.6.: Optical layout of the vacuum tank containing the beamsplitter.
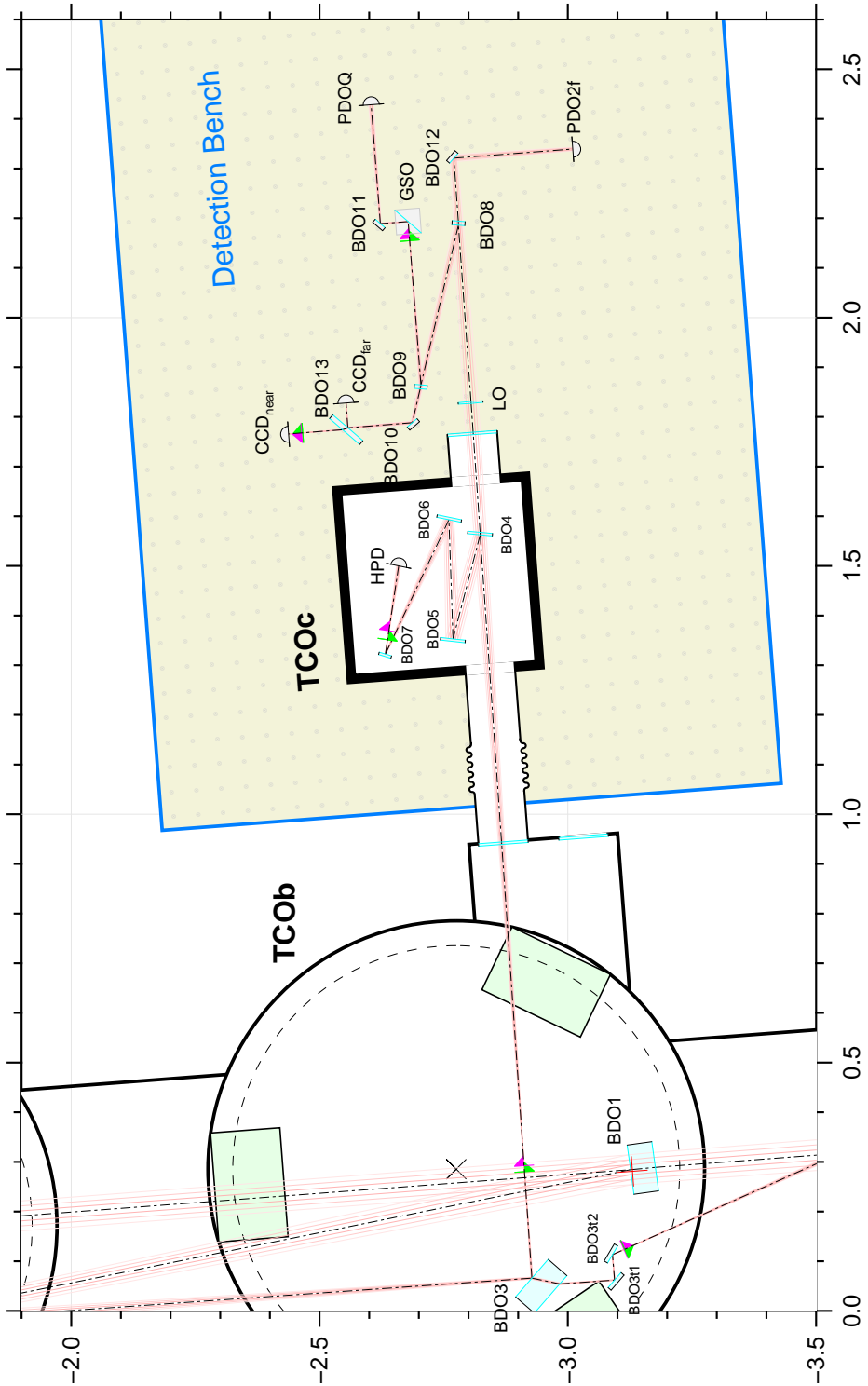
Figure A.7.: Optical layout of the output detection bench.

Appendix B.

Timetable

The following is a condensed list of GEO 600 milestones. See the timetable in [Grote03] for times up to the start of this list.

Aug 23 – September 9, 2002 GEO 600 participates in S1, the first LSC science data-taking run, as a power-recycled Michelson interferometer.

November 15, 2002 First lock of the dual-recycled Michelson interferometer (with a large signal-recycling cavity detuning).

December 23, 2002 Monolithic suspension of the core optics of the Michelson interferometer finished.

November 5 – 12, 2003 S3 I, the first part of GEO 600 participation in S3, and the first science data every recorded by a dual-recycled long-baseline laser-interferometric GW detector.

December 30, 2003 – January 13, 2004 GEO 600 rejoins S3 for a second period, called S3 II, with an improved sensitivity and duty cycle.

February 22 – March 24, 2005 GEO 600 participates in S4.

September 5, 2005 Completed installation of power-recycling mirror with 1000ppm transmission.

January 20 – May 1, 2006 GEO 600 takes data for S5 during nights and weekends, and continues to commission during the daytime.

May 2, 2006 Start of full-time (24/7) participation in S5.

Appendix C.

Crystal oscillator for the MID loop

A low-noise crystal oscillator is used to produce the MID (de)modulation signal, as described in Section 3.3.1. The data sheet provided to GEO 600 by the manufacturer is shown here. Similar models with output frequencies close to those currently used to control the signal-recycling and power-recycling cavities were also purchased, but have not been installed since they have not been shown to be necessary for the noise requirements of those loops.
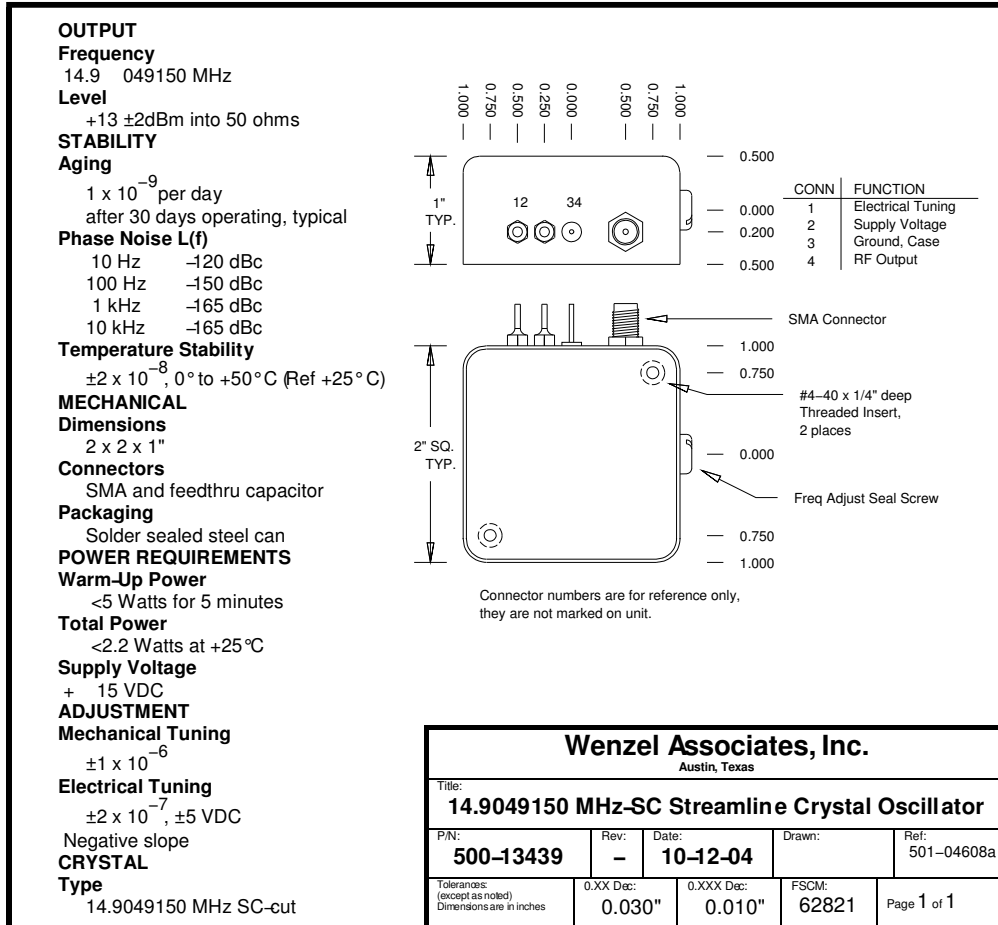
Figure C.1.: Data sheet for the "Wenzel Streamline", a low-noise crystal oscillator used to generate a voltage signal at the Michelson (de)modulation frequency, $F_{\mathrm{MI}} \approx 14.9\,\mathrm{MHz}$.

Bibliography

[Acernese] F. Acernese *et al*, "The status of VIRGO", *Class. Quantum Grav.* **23** S63-S69, (2006).
`http://stacks.iop.org/0264-9381/23/S63` 5

[Adhikari] R. Adhikari, "Sensitivity and Noise analysis of 4 km Laser Interfermetric Gravitational Wave Antennae", PhD Thesis, Massachusetts Institute of Technology, (2004).
`www.ligo.caltech.edu/docs/P/P040032-00.pdf` 17, 42

[Ajith06] P. Ajith, M. Hewitson, J.R. Smith and K.A. Strain, "Robust vetoes for gravitational-wave burst triggers using known instrumental couplings", *Class. Quantum Grav.* **23** 5825-5837, (2006).
`http://stacks.iop.org/CQG/23/5825` 118

[Ajith06b] P. Ajith, personal communication. 119

[ALLEGRO] `http://sam.phys.lsu.edu/` 4

[Allen] B. Allen, W. Hua, A. Ottewill, "Automatic cross-talk removal from multi-channel data", (1999).
`http://arxiv.org/abs/gr-qc/9909083` 42, 45

[Ando] M. Ando *et al*, "Current status of TAMA", *Class. Quantum Grav.* **19** 1409-1419, 2002.
`http://www.iop.org/EJ/abstract/0264-9381/19/7/324/` 5

[Astone] P. Astone *et al*, "Status report on the EXPLORER and NAUTILUS detectors and the present science run", *Class. Quantum Grav.* **23** S57-S62, (2006).
`http://stacks.iop.org/0264-9381/23/S57` 4

[AURIGA] `http://www.auriga.lnl.infn.it/` 4

[Braginsky] V.B. Braginsky and S.P. Vyatchanin, "Frequency fluctuations of non-linear origin in self-sustained optical oscillators", *Phys. Lett. A* **279** 154-162, (2002).

`http://dx.doi.org/10.1016/S0375-9601(00)00824-0` 27

[Buonanno] A. Buonanno and Y. Chen, "Optical noise correlations and beating the standard quantum limit in advanced gravitational-wave detectors", *Class. Quantum Grav.* **18** L95-L101, (2001).
`http://stacks.iop.org/0264-9381/18/L95` 15, 22

[Callen] H.B. Callen and R.F. Greene, "On a Theorem of Irreversible Thermodynamics", *Phys. Rev.* **86** 702-710, (1952).
`http://link.aps.org/abstract/PR/v86/p702` 25

[Caves] C.M. Caves, "Quantum-mechanical noise in an interferometer", *Phys. Rev.* **23** 1693-1708, (1981).
`http://link.aps.org/abstract/PRD/v23/p1693` 15, 22

[Cerdonio] M. Cerdonio, M. Bonaldi, D. Carlesso, E. Cavallini, S. Caruso, A. Columbo, P. Falferi, G. Fontana, P.L. Fortini, R. Mezzena, A. Ortolan, G.A. Prodi, L. Taffarello, G. Vedovato, S. Vitale and J.P. Zendri, "The ultra-cryogenic gravitational-wave detector AURIGA", *Class. Quantum Grav.* **14** 1497-1494, (1996).
`http://stacks.iop.org/0264-9381/14/1491` 4

[Crooks] D.R.M. Crooks, "Mechanical Loss and its Significance in the Test Mass Mirrors of Gravitational Wave Detectors", PhD Thesis, University of Glasgow, (2003). 10

[Crooks04] D.R.M. Crooks, *et al*, "Experimental measurements of coating mechanical loss factors", *Class. Quantum Grav.* **21** S1059-S1065, (2004).
`http://stacks.iop.org/0264-9381/21/S1059` 26

[DeWaard] A. De Waard,Y. Benzaim, G. Frossati, L. Gottardi, H. Van der Mark, J. Flokstra, M. Podt, M. Bassan, Y. Minenkov, A. Moleti, A. Rocchi, V. Fafone and G.V. Pallottino, "MiniGRAIL progress report 2004", *Class. Quantum Grav.* **22** S215-S219, (2004).
`http://stacks.iop.org/0264-9381/22/S215` 4

[Drever] R.W.P. Drever, J. Hough, A.J. Munley, S.A. Lee, R. Spero, S.E. Whitcomb, H. Ward, G.M. Ford, M. Hereld, N.A. Robertson, I. Kerr, J.R. Pugh, G.P. Newton, B. Meers, E.D. Brooks and Y. Gursel, "Gravitational wave detectors using laser interferometers and optical cavities: Ideas, principles and prospects", in Meystre P, and Scully M O, eds., *Proceedings of the NATO Advanced Study Institute on Quantum optics and Experimental General Relativity (Quantum optics, experimental gravitation and measurement theory)*, 503-514,

Plenum Press, New York, (1983). 11

[Drever83] R.W.P. Drever, J.L. Hall, F.V. Kowalski, J. Hough, G.M. Ford, A.J. Munley and H.Ward, "Laser Phase and Frequency Stabilization Using an Optical Resonator", *Appl. Phys.* **B 31** 97-105, (1983). 88

[EXPLORER] http://www.roma1.infn.it/rog/explorer/ 4

[Finesse] A. Freise, "Finesse: Frequency domain interferometer simulation software", internal note, (2002).
The program is currently available at:
`http://www.rzg.mpg.de/~adf`. 23, 47, 70

[Flaminio] R. Flaminio, R. Gouaty and E. Tournefier, "Search for noise sources in C1 and C2 Sensitivities", internal document of VIRGO, (2004).
`http://wwwlapp.in2p3.fr/virgo/notes/Notes2004/`
`VIR-NOT-LAP-1390-277.pdf` 42

[Flaminio06] R. Flaminio, R. Gouaty and E. Tournefier, "Analysis of the sensitivity of the recycled interferometer during C5, C6 and C7 runs", internal document of VIRGO, (2006).
`http://wwwlapp.in2p3.fr/virgo/notes/Notes2006/`
`VIR-NOT-LAP-1390-313.pdf` 82

[Freise] A. Freise, "The Next Generation of Interferometry: Multi-Frequency Optical Modelling, Control Concepts and Implementation", PhD thesis, University of Hannover, (2003).
`http://www.amps.uni-hannover.de/dissertationen/freise_diss.pdf` 9, 13, 17, 18, 23, 51, 89

[GEO 600] `http://www.geo600.uni-hannover.de/`. 6

[GEO HF] B. Willke, *et al*, "The GEO HF project", *Class. Quantum Grav.***23** S207-S214, (2006).
`http://stacks.iop.org/CQG/23/S207` 15, 22

[GEO 600 log] `http://lns01.aei.mpg.de/geo600/geologbook.nsf`(password protected). 64

[Goßler] S. Goßler, "The suspension systems of the interferometric gravitational-wave detector GEO 600", PhD thesis, University of Hannover, (2005).
`http://www.amps.uni-hannover.de/dissertationen/gossler_diss.pdf`
18, 19, 20, 26, 27, 103

[Goßler04] S. Goßler *et al*, *Rev. Sci. Instrum.* **74** 3787-3795, (2003).
`dx.doi.org/10.1063/1.1589160` 18

[Goßler04b] S. Goßler, G. Cagnoli, D.R.M. Crooks, H. Lück, S. Rowan, J.R. Smith, K.A. Strain, J. Hough, K. Danzmann, "Damping and tuning of the fiber violin modes in monolithic silica suspensions", *Class. Quantum Grav.* **21** S923-S933, (2004).
`http://stacks.iop.org/CQG/21/S923` 20, 26

[Grote] H. Grote, personal communication. 18, 77, 82, 88, 97

[Grote03] H. Grote, "Making it Work: Second Generation Interferometry in GEO 600!", PhD thesis, University of Hannover, (2003). 9, 13, 20, 21, 86, 89, 95, 96, 131

[Grote04] H. Grote, G. Heinzel, A. Freise, S. Goßler, B. Willke, H. Lück, H. Ward, M.M. Casey, K.A. Strain, D.I. Robertson, J. Hough and K. Danzmann, "Alignment control of GEO 600", *Class. Quantum Grav.* **21** S441-S449, (2004).
`http://stacks.iop.org/0264-9381/21/S441` 21, 95

[Grote04b] H. Grote, A. Freise, M. Malec, G. Heinzel, B. Willke, H. Lück, K.A. Strain, J. Hough and K. Danzmann, "Dual recycling for GEO 600", *Class. Quantum Grav.* **21** S473-S480, (2004).
`http://stacks.iop.org/0264-9381/21/S473` 30, 86

[Grote04c] H. Grote, G. Heinzel, A. Freise, S. Goßler, B. Willke, H. Lück, H. Ward, M.M. Casey, K.A. Strain, D. Robertson, J. Hough and K. Danzmann, "Automatic Beam Alignment for the Mode-Cleaner Cavities of GEO 600", *Appl. Opt.* **43** 1938-1945, (2004).
`http://www.opticsinfobase.org/abstract.cfm?URI=ao-43-9-1938` 96

[Grote06] H. Grote, "High-power low-noise multiple-resonant photodetector for interferometric gravitational wave detectors", manuscript in preparation, (2006). 25, 70

[Gwo] D.H. Gwo, "Ultraprecision bonding for cryogenic fused-silica optics", *Proc. SPIE-Intl. Soc. Opt. Eng.* **3435** 136-142, (1998).
`dx.doi.org/10.1117/12.323731` 20

[Harms] J. Harms, "Quantum Noise in the Laser-Interferometer Gravitational-Wave Detector GEO 600", Diploma thesis, University of Hannover, (2002).
`http://www.amps.uni-hannover.de/diplomarbeiten/dipl.harms.ps.zip` 23

[Heinzel] G. Heinzel *et al*, "Experimental Demonstration of a Suspended Dual Recycling Interferometer for Gravitational Wave Detection", *Phys. Rev. Lett.***81** 5493-5496, (1998).
http://link.aps.org/abstract/PRL/v81/p5493

[Heinzel02] G. Heinzel, A. Rüdiger and R. Schilling, "Spectrum and spectral density estimation by the Discrete Fourier Transform (DFT), including a comprehensive list of window functions and some new flat-top windows", Internal Note of the Albert Einstein Institute, (2002). 6, 43, 48

[Heng] I.S. Heng, E. Daw, J. Giaime, W.O. Hamilton, M.P. Mchugh and W.W. Johnson, "Allegro: noise performance and the ongoing search for gravitational waves", *Class. Quantum Grav.***19** 1889-1895, (2002).
http://www.iop.org/EJ/abstract/0264-9381/19/7/389 4

[Heurs] M. Heurs, "Gravitational waves in a new light – Novel stabilisation schemese for solid-state lasers", PhD thesis, University of Hannover, (2004).
http://www.amps.uni-hannover.de/dissertationen/heurs_diss.pdf 16, 93

[Hewitson] M. Hewitson, personal communication. 66, 88

[Hewitson03] M. Hewitson, H. Grote, G. Heinzel, K.A. Strain, H. Ward and U. Weiland, "Calibration of the power-recycled gravitational wave detector, GEO600" *Rev. Sci. Instrum.* **74** 4184-4190, (2003).
dx.doi.org/10.1063/1.1597959 30

[Hewitson04] M. Hewitson, "On aspects of characterising and calibrating the interferometric gravitational wave detector, GEO 600", PhD thesis, University of Glasgow, (2004). 10, 32, 43, 64, 71, 72, 115

[Hewitson04b] M. Hewitson, S. Babak, R. Balasubramanian, K. Danzmann, H. Grote, G. Heinzel, J. Hough, M.A. Papa, J.R. Smith, K.A. Strain, H. Ward, B. Willke and G. Woan, "Calibration of the dual-recycled GEO 600 detector for the S3 science run", *Class. Quantum Grav.* **21** S1711-S1722, (2004).
http://www.iop.org/EJ/abstract/CQG/21/20/014/ 32, 64, 109

[Hewitson04c] M. Hewitson, G. Heinzel, J.R. Smith, K.A. Strain, H. Ward, "Principles of calibrating the dual-recycled GEO 600", *Rev. Sci. Instrum.* textbf75 4702-4709, (2004).
dx.doi.org/10.1063/1.1804831 32, 64, 109

[Hewitson05] M. Hewitson, H. Grote, S. Hild, H. Lück, P. Ajith, J.R. Smith,

K.A. Strain, B. Willke and G. Woan, "Optimal time-domain combination of the two calibrated output quadratures of GEO600", *Class. Quantum Grav.* **22** 4253-4261, (2005).
http://stacks.iop.org/CQG/22/4253 35, 64, 66

[Hild] S. Hild, personal communication. 101

[Hild06] S. Hild, H. Grote, J.R. Smith, M. Hewitson, "Towards gravitational wave astronomy: Commissioning and characterization of GEO600", *J. Phys.: Conf. Ser.* **32** 66-73, (2006).
http://stacks.iop.org/JPCS/32/66 35, 36, 100

[Hild06b] S. Hild, H. Lück, W. Winkler, K.A. Strain, H. Grote, J.R. Smith, M. Malec, M. Hewitson, B. Willke, J. Hough and K. Danzmann, "Measurement of a low absorptive sample of OH-reduced fused silica", accepted by *Applied Optics*, (2006). 23

[Hild06c] S. Hild (for the LIGO Scientific Collaboration), "The Status of GEO600", accepted by *Class. Quantum Grav.*, (2006). 12

[Kawabe] K. Kawabe, L. Matone and J. Betzwieser, "Excess Noise Mechanism in LIGO Output Mode Cleaner", internal document of LIGO, (2004).
http://www.ligo.caltech.edu/docs/T/T040158-00.pdf 18

[Kötter02] K. Kötter, *et al*, "Data acquisition and detector characterization of GEO600", *Class. Quantum Grav.***19** 1399-1407, (2002).
http://stacks.iop.org/0264-9381/19/1399 43, 72

[Kötter] K. Kötter, "Data Acquisition and Data Analysis for the Gravitational-Wave Detector GEO 600", PhD thesis, University of Hannover, (2003).
http://www.amps.uni-hannover.de/dissertationen/koetter_diss.pdf 43, 72

[Levin] Y. Levin, "Internal thermal noise in the LIGO test masses: A direct approach", *Phys. Rev.* **57** 659-663, (1998).
http://link.aps.org/abstract/PRD/v57/p659 25, 26

[LIGO] http://www.ligo.caltech.edu/. 5

[LSC04] The LIGO Scientific Collaborration, "Detector Description and Performance for the First Coincidence Observations Between LIGO and GEO", *Nucl. Instrum. Meth., A* **517** 154-179, (2004).
http://www.arxiv.org/abs/gr-qc/0308043 30

[LSC05] The LIGO Scientific Collaborration, "Upper Limits on Gravitational Wave Bursts in LIGO's Second Science Run", *Phys. Rev.***72** 062001, (2005)
`http://link.aps.org/abstract/PRD/v72/e062001` 2

[LSC05b] The LIGO Scientific Collaborration,"Search for Gravitational Waves from Galactic and Extra-galactic Binary Neutron Stars" *Phys. Rev.* **72** 082001, (2005).
`http://link.aps.org/abstract/PRD/v72/e082001` 2

[LSC05c] The LIGO Scientific Collaborration, "Search for Gravitational Waves from Primordial Black Hole Binary Coalescences in the Galactic Halo", *Phys. Rev.* **72** 082002, (2005).
`http://link.aps.org/abstract/PRD/v72/e082002` 2

[LSC05d] The LIGO Scientific Collaborration, "Upper Limits on a Stochastic Background of Gravitational Waves", *Phys. Rev. Lett.* **95** 221101, (2005).
`http://link.aps.org/abstract/PRL/v95/e221101` 2

[LSC05e] The LIGO Scientific Collaborration, "Limits on Gravitational-Wave Emission from Selected Pulsars Using LIGO Data", *Phys. Rev. Lett.***94** 181103, (2005).
`http://link.aps.org/abstract/PRL/v94/e181103` 2

[Lück] H. Lück, personal communication. 18, 103

[Lück04] H. Lück, A. Freise, S. Goßler, S. Hild, K. Kawabe and K. Danzmann, "Thermal correction of the radii of curvature of mirrors for GEO 600", *Class. Quantum Grav.***21** S985-S989, (2004).
`http://stacks.iop.org/0264-9381/21/S985`

[Lück06] H. Lück, *et al*"Status of the GEO600 detector" 2006 *Class. Quantum Grav.***23** S71-S78.
`http://stacks.iop.org/CQG/23/S71` 6, 35

[Malec] M. Malec, personal communication. 70

[Malec05] M. Malec, "Commissioning of advanced, dual-recycled gravitational-wave detectors: simulations of complex optical systems guided by the phasor picture", PhD thesis, University of Hannover, (2005).
`http://www.amps.uni-hannover.de/dissertationen/malec_diss.pdf` 9, 17, 23, 81, 83, 87, 92, 94

[Meers] B.J. Meers, "Recycling in laser-interferometric gravitational-wave detectors", *Phys. Rev. DD* **38** 2317, (1988).

`http://link.aps.org/abstract/PRD/v38/p2317` 13

[Meers88] B.J. Meers and K.A. Strain, "Modulation, signal, and quantum noise in interferometers", *Phys. Rev. DD* **38** 2317, (1988).
`http://link.aps.org/abstract/PRA/v44/p4693` 23, 70

[MiniGRAIL] `http://www.minigrail.nl/`. 4

[Miyakawa] Miyakawa O, *et al* "Measurement of Optical Response of a Detuned Resonant Sideband Extraction Interferometer", to be published. 23

[Mizuno] J. Mizuno, "Comparison of optical configurations for laser-interferometric gravitational-wave detectors", PhD thesis, University of Hannover, (1995). 12, 16, 22

[Mossavi] K. Mossavi, M. Hewitson, S. Hild, F. Seifert, U. Weiland, J.R. Smith, H. Lück, H. Grote, B. Willke, K. Danzmann, "A photon pressure calibrator for the GEO600 gravitational wave detector", *Phys. Lett. A* **353** 1-3, (2006).
`http://dx.doi.org/10.1016/j.physleta.2005.12.053` 16

[NAUTILUS] `http://www.roma1.infn.it/rog/nautilus/`. 4

[OptoCad] R. Schilling, "OptoCad, A Fortran 95 module for tracing Gaussian beams through an optical set-up, Version 0.74", internal document of GEO 600, 2002. 123

[Penn] S.D. Penn *et al*, "Mechanical loss in tantala/silica dielectric mirror coatings", *Class. Quantum Grav.* **20** 2917-2928, (2003).
`stacks.iop.org/cq/20/2917` 26

[Penn05] S.D. Penn *et al*, "Frequency and surface dependence of the mechanical loss in fused silica", to be published, (2005). 26

[Saulson] P.R. Saulson, "Thermal noise in mechanical experiments", *Phys. Rev. D* **42** 2437-2445, (1990).
`http://link.aps.org/abstract/PRD/v42/p2437` 25

[Schnabel] R. Schnabel, J. Harms, K.A. Strain and K. Danzmann, "Squeezed light for the interferometric detection of high-frequency gravitational waves", *Class. Quantum Grav.* **21** S1045-S1051, (2004).
`http://stacks.iop.org/0264-9381/21/S1045` 15, 22

[Schnier] D. Schnier, J. Mizuno, G. Heinzel, H. Lück, A. Rüdiger, R. Schilling, M. Schrempel, W. Winkler and K. Danzmann, "Power-Recycling in the Garch-

ing 30-m prototype interferometer for gravitational-wave detection", *Phys. Lett. A* **225** 210-216, (1997).
`http://dx.doi.org/10.1016/S0375-9601(96)00893-6` 11

[Shoemaker] D. Shoemaker, R. Schilling, L. Schnupp, W. Winkler, K. Maishberger, A. Rüdiger, "Noise behavior of the Garching 30-meter prototype gravitational-wave detector", *Phys. Rev. D***38** 423-432, (1988).
`http://link.aps.org/abstract/PRD/v38/p423` 9

[Sigg] D. Sigg (for the LIGO Science Collaboration), "Status of the LIGO detectors", *Class. Quantum Grav.* **23** S51-S56, (2006).
`stacks.iop.org/0264-9381/23/S51` 5

[Smith] J.R. Smith, G.M. Harry, J.C. Betzwieser, A.M. Gretarsson, D.A. Guild, S.E. Kittelberger, M.J. Mortonson, S.D. Penn and P.R. Saulson, "Mechanical loss associated with silicate bonding of fused silica", *Class. Quantum Grav.***20** 5039, (2003).
`http://www.iop.org/EJ/abstract/CQG/20/23/007/` 20

[Smith04] J.R. Smith, G. Cagnoli, D.R.M. Crooks, M.M. Fejer, S. Goßler, H. Lück, S. Rowan, J. Hough and K. Danzmann, "Mechanical quality factor measurements of monolithically suspended fused silica test masses of the GEO 600 gravitational wave detector", *Class. Quantum Grav.* **21** S1091-S1098, (2004).
`http://stacks.iop.org/CQG/21/S1091` 10, 20, 25, 26

[Smith04b] J.R. Smith, *et al*, "Commissioning, characterization, and operation of the dual-recycled GEO 600", *Class. Quantum Grav.***21** S1737-S1745, (2004).
`http://www.iop.org/EJ/abstract/CQG/21/20/016/` 31

[Smith05] J.R. Smith, H. Grote, M. Hewitson, S. Hild, H. Lück, M. Parsons, K.A. Strain and B. Willke, "Feedforward correction of mirror misalignment fluctuations for the GEO 600 gravitational wave detector", *Class. Quantum Grav.***22** S3093-S3104, (2005).
`http://stacks.iop.org/CQG/22/3093` 27, 30, 49, 114

[Smith06] J.R. Smith, *et al*, "Noise projections for GEO 600 during S4", manuscript in preparation. 35

[Sneddon] P.H. Sneddon, S. Bull, G. Cagnoli, D.R.M. Crooks, E.J. Elliffe, J.E. Faller, M.M. Fejer, J. Hough and S. Rowan, "The intrinsic mechanical loss factor of hydroxy-catalysis bonds for use in the mirror suspensions of gravitational wave detectors", *Class. Quantum Grav.***20** 5025, (2003).
`http://stacks.iop.org/0264-9381/20/5025` 20

[Strain] K.A. Strain, personal communication. 86, 88

[Strain91] K.A. Strain and B.J. Meers, "Experimental demonstration of dual re-
cycling for interferometric gravitational-wave detectors", *Phys. Rev. Lett.***66**
1391-1394, (1991).
`http://link.aps.org/abstract/PRL/v66/p1391`

[Strain02] K.A. Strain, "Electrostatic drives for GEO 600", Internal document of
GEO 600, (2002). 21

[TAMA] `http://tamago.mtk.nao.ac.jp/`. 5

[Tatsumi] D. Tatsumi, personal communication. 42

[Taylor79] J.H. Taylor, L.A. Fowler, and P.M. McCulloch, "Measurements of gen-
eral relativistic effects in the binary pulsar PSR1913 + 16", *Nature* **277** 437-
440, (1979).
`dx.doi.org/10.1038/277437a0` 2

[Valbruch] H. Vahlbruch, S. Chelkowski, B. Hage, A. Franzen, K. Danzmann and
R. Schnabel, "Demonstration of a squeezed-light-enhanced power- and signal-
recycled Michelson interferometer", *Phys. Rev. Lett.* **95** 211102, (2006)
`http://link.aps.org/abstract/PRL/v95/e211102` 22

[Vahlbruch06] H. Vahlbruch, S. Chelkowski, B. Hage, A. Franzen, K. Danzmann
and R. Schnabel, "Coherent Control of Vacuum Squeezing in the Gravitational-
Wave Detection Band", *Phys. Rev. Lett.* **97** 011101, (2006).
`http://link.aps.org/abstract/PRL/v97/e011101` 22

[VIRGO] `http://wwwcascina.virgo.infn.it/` 5

[Willems] P. Willems, V. Sannibale, J. Weel and V. Mitrofanov, "Investigations of
the dynamics and mechanical dissipation of a fused silica suspension", *Phys.
Lett.A* **297** 37-48, (2002).
`http://dx.doi.org/10.1016/S0375-9601(02)00380-8`

[Willke] B. Willke, *et al*, "The status of GEO 600", *Class. Quantum Grav.* **21** S417-
S423, (2004).
`http://stacks.iop.org/CQG/21/S417` 30

[Winkler] W. Winkler, "Eine optische VerzÃ¶gerungsleitung fÃ¼r ein Breitband-
Gravitationswellenexperiment", PhD Thesis, Max Planck Institute for Quan-
tum Optics, Garching, (1983). 9

[Winkler91] W. Winkler *et al* "Heating by optical absorption and the performance of interferometric gravitational wave detectors", *Phys. Rev. A* **44** 7022-7036, (1991).
http://prola.aps.org/abstract/PRA/v44/i11/p7022_1

[Winkler02] W. Winkler, "Fluctuating light pressure in recycled interferometers", internal document of GEO 600, (2002). 16, 92

[Winkler06] W. Winkler, *et al* "The GEO600 core optics", manuscript in preparation, (2006). 23, 26

Acknowledgements

I have been extremely lucky to have had the opportunity to do graduate work within the very inspiring atmosphere at the Hannover Albert Einstein Institute. For that I thank Professor Karsten Danzmann, who through tireless effort has put together one of the top institutes for Gravitational research in the world.

Over the past four years I spent much of my time "on-site" at the GEO 600 detector in Ruthe. During this time, the detector was transformed from a newly-built and flaky machine, to a very stable and sensitive device, which can almost be called an observatory. The people who worked (almost) daily at the site to accomplish this monumental feat are Harald Lück, Benno Willke, Hartmut Grote, Martin Hewitson, Stefan Hild, and during visits, Ken Strain. I am very grateful to have been able to spend this time working with such a great team of people in Ruthe. All of them have my utmost respect. The work presented in this thesis could not have been done without the support they gave me and their contributions to the GEO 600 project.

It has also been my pleasure to work with many other people associated with GEO 600. These include Ajith Parameswaran, Andreas Freise, Michaela Malec, Uta Weiland, Karsten Kötter and Kasem Mossavi. I have also enjoyed working with various members of the AEI Hannover, AEI Golm, Glasgow, Garching, Birmingham and Cardiff groups.

During the first year of my graduate studies, I worked nearly every day with Stefan Goßler, or Dr. Gobler, as he is now known in Australia. I thank him for teaching me that no matter how hard it seems to hunt noise in a GW detector, it is never as hard as hanging a GEO 600 monolithic suspension.

I would also like to thank the members of the ILIAS working group 1 for European GW detector commissioning for very interesting discussions and meetings that have benefeited both GEO 600 and VIRGO.

I am very gracious to Stefan Hild, Martin Hewitson, Hartmut Grote, Benno Willke, Ajith Parameswaran, Ken Strain, and Stefan Goßler for reading drafts of chapters of this thesis, and giving me useful comments. Thanks also to Felicitas Wiese and Stefan Hild for helping me to translate the *Zusammenfassung*. The LaTeX template used for this thesis was based on files provided to me by Andreas Freise and Martin Hewitson. Thanks.

Finally I want to thank the most special people in my life, my parents, Connie and Patrick Mahoney, and my fiancee, Felicitas Wiese for their unwavering support.

Curriculum vitae

Joshua R. Smith
Krambuden 9
38300 Wolfenbüttel
Deutschland

Born: August 26th, 1980 in Glens Falls, NY, USA
Marital Status: unmarried

Education

- June 2002 – present: Ph.D. student, *Albert-Einstein-Institut* (AEI) and *Universität Hannover* (UH).

- May 2002: B.Sc. Physics, Syracuse University (SU); 3.3 GPA.

- September 1998 – May 2002: Undergraduate, SU.

- June 1998: Regents Diploma, Indian lake Central School (ILCS).

- September 1985 – June 1998: Kindergarten, Elementary School, Middle School and High School, (ILCS).

Research Experience

- June 2002 – present: Graduate Researcher, GEO 600, AEI and UH.

- September 1999 – May 2002: Research Assistant, Experimental Relativity Group, SU.

- June – August 2001: Student Assistant, GEO 600.

- June – August 2000: Caltech Summer Undergraduate Research Fellow, LIGO Livingston Observatory.

- January – March 1999: Research Assistant, Center For Really Neat Research,

SU

Teaching Experience

- October 2003 – February 2005: Design and direction of *Fortgeschrittenes Praktikum 1* undergraduate laboratory, "Measuring the mechanical energy dissipation of a pendulum", UH.

- January 1999 – December 2000: Undergraduate Teaching Assistant for introductory-level physics, SU.

Publications

2006

- "Linear projection of technical noise for interferometric gravitational-wave detectors", J.R. Smith, P. Ajith, H. Grote, M. Hewitson, S. Hild, H. Lück, K.A. Strain, B. Willke, J. Hough and K. Danzmann, *Class. Quantum Grav.* **23** 527-537, (2006).
  `http://stacks.iop.org/CQG/23/527`

- "Measurement of a low-absorption sample of OH-reduced fused silica", S. Hild, H. Lück, W. Winkler, K. Strain, H. Grote, J. Smith, M. Malec, M. Hewitson, B. Willke, J. Hough and K. Danzmann, *Appl. Opt.* **45** 7269-7272 (2006).
  `http://www.opticsinfobase.org/abstract.cfm?URI=ao-45-28-7269`

- "Robust vetoes for gravitational-wave burst triggers using known instrumental couplings", P. Ajith, M. Hewitson, J.R. Smith, K.A. Strain, *Class. Quantum Grav.* **23** 5825-5837, (2006).
  `http://stacks.iop.org/CQG/23/5825`

- "The status of GEO 600", S. Hild for the LIGO scientific collaboration, *Class. Quantum Grav.* **23** S643-S651 (2006).
  `http://stacks.iop.org/CQG/23/5825`

- "A photon pressure calibrator for the GEO600 gravitational wave detector", K. Mossavi, M. Hewitson, S. Hild, F. Seifert, U. Weiland, J.R. Smith, H. Lück, H. Grote, B. Willke, K. Danzmann, *Phys. Lett. A* **353** 1-3, (2006).
  `http://dx.doi.org/10.1016/j.physleta.2005.12.053`

- "Towards gravitational wave astronomy: Commissioning and characterization of GEO600", S. Hild, H. Grote, J.R. Smith, M. Hewitson, *J. Phys.: Conf. Ser.* **32** 66-73, (2006).
  `http://stacks.iop.org/JPCS/32/66`

- "Status of the GEO600 detector", H. Lück, P. Ajith, B. Allen, P. Aufmuth,

C. Aulbert, S. Babak, R. Balasubramanian, B.W. Barr, S. Berukoff,
A. Bunkowski, G. Cagnoli, C.A. Cantley, M.M. Casey, S. Chelkowski,
Y. Chen, D. Churches, T. Cokelaer, C.N. Colacino, D.R.M. Crooks,
C. Cutler, K. Danzmann, R.J. Dupuis, E. Elliffe, C. Fallnich, A. Franzen,
A. Freise, I. Gholami, S. Goßler, A. Grant, H. Grote, S. Grunewald,
J. Harms, B. Hage, G. Heinzel, I.S. Heng, A. Hepstonstall, M. Heurs,
M. Hewitson, S. Hild, J. Hough, Y. Itoh, G. Jones, R. Jones, S.H. Huttner,
K. Kötter, B. Krishnan, P. Kwee, M. Luna, B. Machenschalk, M. Malec,
R.A. Mercer, T. Meier, C. Messenger, S. Mohanty, K. Mossavi,
S. Mukherjee, P. Murray, G.P. Newton, M.A. Papa, M. Perreur-Lloyd,
M. Pitkin, M.V. Plissi, R. Prix, V. Quetschke, V. Re, T. Regimbau,
H. Rehbein, S. Reid, L. Ribichini, D.I. Robertson, N.A. Robertson,
C. Robinson, J.D. Romano, S. Rowan, A. Rüdiger, B.S. Sathyaprakash,
R. Schilling, R. Schnabel, B.F. Schutz, F. Seifert, A.M. Sintes, J.R. Smith,
P.H. Sneddon, K.A. Strain, I. Taylor, R. Taylor, A. Thüring, C. Ungarelli,
H. Vahlbruch, A. Vecchio, J. Veitch, H. Ward, U. Weiland, H. Welling,
L. Wen, P. Williams, B. Willke, W. Winkler, G. Woan, R. Zhu, *Class.
Quantum Grav.* **23** S71-S78, (2006).
`http://stacks.iop.org/CQG/23/S71`

- "The GEO HF project", B. Willke, P. Ajith, B. Allen, P. Aufmuth,
C. Aulbert, S. Babak, R. Balasubramanian, B.W. Barr, S. Berukoff,
A. Bunkowski, G. Cagnoli, C.A. Cantley, M.M. Casey, S. Chelkowski,
Y. Chen, D. Churches, T. Cokelaer, C.N. Colacino, D.R.M. Crooks,
C. Cutler, K. Danzmann, R.J. Dupuis, E. Elliffe, C. Fallnich, A. Franzen,
A. Freise, I. Gholami, S. Goßler, A. Grant, H. Grote, S. Grunewald,
J. Harms, B. Hage, G. Heinzel, I.S. Heng, A. Hepstonstall, M. Heurs,
M. Hewitson, S. Hild, J. Hough, Y. Itoh, G. Jones, R. Jones, S.H. Huttner,
K. Kötter, B. Krishnan, P. Kwee, H. Lück, M. Luna, B. Machenschalk,
M. Malec, R.A. Mercer, T. Meier, C. Messenger, S. Mohanty, K. Mossavi,
S. Mukherjee, P. Murray, G.P. Newton, M.A. Papa, M. Perreur-Lloyd,
M. Pitkin, M.V. Plissi, R. Prix, V. Quetschke, V. Re, T. Regimbau,
H. Rehbein, S. Reid, L. Ribichini, D.I. Robertson, N.A. Robertson,
C. Robinson, J.D. Romano, S. Rowan, A. Rüdiger, B.S. Sathyaprakash,
R. Schilling, R. Schnabel, B.F. Schutz, F. Seifert, A.M. Sintes, J.R. Smith,
P.H. Sneddon, K.A. Strain, I. Taylor, R. Taylor, A. Thüring, C. Ungarelli,
H. Vahlbruch, A. Vecchio, J. Veitch, H. Ward, U. Weiland, H. Welling,
L. Wen, P. Williams, W. Winkler, G. Woan, R. Zhu, *Class. Quantum Grav.*
23 S207-S214, (2006).
`http://stacks.iop.org/CQG/23/S207`

2005

- "Feedforward correction of mirror misalignment fluctuations for the GEO 600 gravitational wave detector", J.R. Smith, H. Grote, M. Hewitson, S. Hild, H. Lück, M. Parsons, K.A. Strain and B. Willke, *Class. Quantum Grav.* **22** 3093-3104, (2005).
  `http://stacks.iop.org/CQG/22/3093`

- "Optimal time-domain combination of the two calibrated output quadratures of GEO600", M. Hewitson, H. Grote, S. Hild, H. Lück, P. Ajith, J.R. Smith, K.A. Strain, B. Willke and G. Woan, *Class. Quantum Grav.* **22** 4253-4261, (2005).
  `http://stacks.iop.org/CQG/22/4253`

- "Preparing GEO 600 for gravitational wave astronomy: a status report", M. Hewitson for the LIGO Scientific Collaboration, *Class. Quantum Grav.* **22** S891-S900, (2005).
  `http://stacks.iop.org/CQG/22/S891`

- "Results from the first burst hardware injections performed on GEO 600", R. Balasubramanian, H. Grote, I.S. Heng, M. Hewitson, H. Lück, J.R. Smith, K.A. Strain, H. Ward and B. Willke, *Class. Quantum Grav.* **22** 3015-3028, (2005).
  `http://stacks.iop.org/CQG/22/3015`

- "The status of GEO 600", H. Grote, B. Allen, P. Aufmuth, C. Aulbert, S. Babak, R. Balasubramanian, B.W. Barr, S. Berukoff, A. Bunkowski, G. Cagnoli, C.A. Cantley, M.M. Casey, S. Chelkowski, D. Churches, T. Cokelaer, C.N. Colacino, D.R.M. Crooks, C. Cutler, K. Danzmann, R. Davies, R.J. Dupuis, E. Elliffe, C. Fallnich, A. Franzen, A. Freise, S. Goßler, A. Grant, S. Grunewald, J. Harms, G. Heinzel, I.S. Heng, A. Hepstonstall, M. Heurs, M. Hewitson, S. Hild, J. Hough, Y. Itoh, R. Jones, S.H. Huttner, K. Kawabe, C. Killow, K. Kötter, B. Krishnan, V. Leonhardt, H. Lück, B. Machenschalk, M. Malec, R.A. Mercer, C. Messenger, S. Mohanty, K. Mossavi, S. Mukherjee, P. Murray, S. Nagano, G.P. Newton, M.A. Papa, M. Perreur-Lloyd, M. Pitkin, M.V. Plissi, V. Quetschke, V. Re, S. Reid, L. Ribichini, D.I. Robertson, N.A. Robertson, J.D. Romano, S. Rowan, A. Rüdiger, B.S. Sathyaprakash, R. Schilling, R. Schnabel, B.F. Schutz, F. Seifert, A.M. Sintes, J.R. Smith, P.H. Sneddon, K.A. Strain, I. Taylor, R. Taylor, A. Thüring, C. Ungarelli, H. Vahlbruch, A. Vecchio, J. Veitch, H. Ward, U. Weiland, H. Welling, P. Williams, B. Willke, W. Winkler, G. Woan and I. Zawischa, *Class.*

Quantum Grav. **22** S193-S198, (2005).
`http://stacks.iop.org/CQG/22/S193`

- "The status of GEO 600", K.A. Strain, B. Allen, P. Aufmuth, C. Aulbert,
  S. Babak, R. Balasubramanian, B.W. Barr, S. Berukoff, A. Bunkowski,
  G. Cagnoli, C.A. Cantley, M.M. Casey, S. Chelkowski, D. Churches,
  T. Cokelaer, C.N. Colacino, D.R.M. Crooks, C. Cutler, K. Danzmann,
  R. Davies, R.J. Dupuis, E. Elliffe, C. Fallnich, A. Franzen, A. Freise,
  S. Goßler, A. Grant, H. Grote, S. Grunewald, J. Harms, G. Heinzel, I. Heng,
  A. Hepstonstall, M. Heurs, M. Hewitson, S. Hild, J. Hough, Y. Itoh,
  R. Jones, S.H. Huttner, K. Kawabe, C. Killow, K. Kötter, B. Krishnan,
  V. Leonhardt, H. Lück, B. Machenschalk, M. Malec, R.A. Mercer,
  C. Messenger, S. Mohanty, K. Mossavi, S. Mukherjee, P. Murray, S. Nagano,
  G.P. Newton, M.A. Papa, M. Perreur-Lloyd, M. Pitkin, M.V. Plissi,
  V. Quetschke, V. Re, S. Reid, L. Ribichini, D.I. Robertson, N.A. Robertson,
  J.D. Romano, S. Rowan, A. Rüdiger, B.S. Sathyaprakash, R. Schilling,
  R. Schnabel, B.F. Schutz, F. Seifert, A.M. Sintes, J.R. Smith,
  P.H. Sneddon, I. Taylor, R. Taylor, A. Thüring, C. Ungarelli, H. Vahlbruch,
  A. Vecchio, J. Veitch, H. Ward, U. Weiland, H. Welling, P. Williams,
  B. Willke, W. Winkler, G. Woan and I. Zawischa, *Proceedings of the SPIE
  5500* 25-36, (2004).

- "Upper Limits on a Stochastic Background of Gravitational Waves", The
  LIGO Scientific Collaborration, *Phys. Rev. Lett.* **95** 221101, (2005).
  `http://link.aps.org/abstract/PRL/v95/e221101`

- "Search for Gravitational Waves Associated with the Gamma Ray Burst
  GRB030329 Using the LIGO Detectors", The LIGO Scientific
  Collaborration, *Phys. Rev.* **72** 042002, (2005).
  `http://link.aps.org/abstract/PRD/v72/e042002`

- "First All-sky Upper Limits from LIGO on the Strength of Periodic
  Gravitational Waves Using the Hough Transform", The LIGO Scientific
  Collaborration,*Phys. Rev.* **72** 102004, (2005).
  `http://link.aps.org/abstract/PRD/v72/e102004`

- "Limits on Gravitational-Wave Emission from Selected Pulsars Using LIGO
  Data", The LIGO Scientific Collaborration, *Phys. Rev. Lett.* **94** 181103,
  (2005).
  `http://link.aps.org/abstract/PRL/v94/e181103`

- "Search for Gravitational Waves from Galactic and Extra-galactic Binary

Neutron Stars", The LIGO Scientific Collaborration, *Phys. Rev.* **72** 082001, (2005).
`http://link.aps.org/abstract/PRD/v72/e082001`

- "Search for Gravitational Waves from Primordial Black Hole Binary Coalescences in the Galactic Halo", The LIGO Scientific Collaborration, *Phys. Rev.* **72** 082002, (2005).
`http://link.aps.org/abstract/PRD/v72/e082002`

- "Upper Limits on Gravitational Wave Bursts in LIGO's Second Science Run", The LIGO Scientific Collaborration, *Phys. Rev.* **72** 062001, (2005).
`http://link.aps.org/abstract/PRD/v72/e062001`

2004

- "Commissioning, characterization, and operation of the dual-recycled GEO 600", J.R. Smith, B. Allen, P. Aufmuth, C. Aulbert, S. Babak, R. Balasubramanian, B.W. Barr, S. Berukoff, A. Bunkowski, G. Cagnoli, C.A. Cantley, M.M. Casey, S. Chelkowski, D. Churches, T. Cokelaer, C.N. Colacino, D.R.M. Crooks, C. Cutler, K. Danzmann, R. Davies, R.J. Dupuis, E. Elliffe, C. Fallnich, A. Franzen, A. Freise, S. Goßler, A. Grant, H. Grote, S. Grunewald, J. Harms, G. Heinzel, I.S. Heng, A. Hepstonstall, M. Heurs, M. Hewitson, S. Hild, J. Hough, Y. Itoh, R. Jones, S.H. Huttner, K. Kawabe, C. Killow, K. Kötter, B. Krishnan, V. Leonhardt, H. Lück, B. Machenschalk, M. Malec, R.A. Mercer, C. Messenger, S. Mohanty, K. Mossavi, S. Mukherjee, P. Murray, S. Nagano, G.P. Newton, M.A. Papa, M. Perreur-Lloyd, M. Pitkin, M.V. Plissi, V. Quetschke, V. Re, S. Reid, L. Ribichini, D.I. Robertson, N.A. Robertson, J.D. Romano, S. Rowan, A. Rüdiger, B.S. Sathyaprakash, R. Schilling, R. Schnabel, B.F. Schutz, F. Seifert, A.M. Sintes, P.H. Sneddon, K.A. Strain, I. Taylor, R. Taylor, A. Thüring, C. Ungarelli, H. Vahlbruch, A. Vecchio, J. Veitch, H. Ward, U. Weiland, H. Welling, P. Williams, B. Willke, W. Winkler, G. Woan and I. Zawischa, *Class. Quantum Grav.* **21** S1737-S1745, (2004).
`http://www.iop.org/EJ/abstract/0264-9381/21/20/016/`

- "Mechanical quality factor measurements of monolithically suspended fused silica test masses of the GEO 600 gravitational wave detector", J.R. Smith, G. Cagnoli, D.R.M. Crooks, M.M. Fejer, S. Goßler, H. Lück, S. Rowan, J. Hough and K. Danzmann, *Class. Quantum Grav.* **21** S1091-S1098, (2004).
`http://stacks.iop.org/0264-9381/21/S1091`

- "Principles of calibrating the dual-recycled GEO 600", M. Hewitson, G. Heinzel, J.R. Smith, K.A. Strain, and H. Ward, *Rev. Sci. Instrum.*75 4702-4709, (2004).
  `http://dx.doi.org/10.1063/1.1804831`

- "Calibration of the dual-recycled GEO 600 detector for the S3 science run", M. Hewitson, S. Babak, R. Balasubramanian, K. Danzmann, H. Grote, G. Heinzel, J. Hough, M.A. Papa, J.R. Smith, K.A. Strain, H. Ward, B. Willke and G. Woan, *Class. Quantum Grav.*21 S1711-S1722, (2004).
  `http://www.iop.org/EJ/abstract/0264-9381/21/20/014/`

- "Damping and tuning of the fiber violin modes in monolithic silica suspensions", S. Goßler, G. Cagnoli, D.R.M. Crooks, H. Lück, S. Rowan, J.R. Smith, K.A. Strain, J. Hough and K. Danzmann *Class. Quantum Grav.*21 S923-S933, (2004).
  `http://stacks.iop.org/0264-9381/21/S923`

- "Status of GEO 600", B. Willke, P. Aufmuth, C. Aulbert, S. Babak, R. Balasubramanian, B.W. Barr, S. Berukoff, G. Cagnoli, C.A. Cantley, M.M. Casey, S. Chelkowski, D. Churches, C.N. Colacino, D.R.M. Crooks, C. Cutler, K. Danzmann, R. Davies, R.J. Dupuis, E. Elliffe, C. Fallnich, A. Freise, S. Goßler, A. Grant, H. Grote, S. Grunewald, J. Harms, G. Heinzel, I.S. Heng, A. Hepstonstall, M. Heurs, M. Hewitson, S. Hild, J. Hough, R. Ingley, Y. Itoh, O. Jennrich, R. Jones, S.H. Hutter, K. Kawabe, C. Killow, K. Kötter, B. Krishnan, V. Leonhardt, H. Lück, B. Machenschalk, M. Malec, R.A. Mercer, C. Messenger, S. Mohanty, K. Mossavi, S. Mukherjee, S. Nagano, G.P. Newton, M.A. Papa, M. Perreur-Lloyd, M. Pitkin, M.V. Plissi, V. Quetschke, V. Re, S. Reid, L. Ribichini, D.I. Robertson, N.A. Robertson, S. Rowan, A. Rüdiger, B.S. Sathyaprakash, R. Schilling, R. Schnabel, B.F. Schutz, F. Seifert, A.M. Sintes, J.R. Smith, P.H. Sneddon, K.A. Strain, I. Taylor, C.I. Torrie, C. Ungarelli, A. Vecchio, H. Ward, U. Weiland, H. Welling, P. Williams, W. Winkler, G. Woan and I. Zawischa, *Class. Quantum Grav.*21 S417-S423, (2004).
  `http://stacks.iop.org/CQG/21/S417`

- "Detector Description and Performance for the First Coincidence Observations Between LIGO and GEO", the LIGO Scientific Collaborration, *Nucl. Instrum. Methodsin Physics Research A* **517** 154-179, (2004).
  `http://www.arxiv.org/abs/gr-qc/0308043`

- "Setting upper limits on the strength of periodic gravitational waves from

PSR J1939+2134 using the first science data from the GEO 600 and LIGO detectors", the LIGO Scientific Collaborration, *Phys. Rev.***69** 082004, (2004).
`http://link.aps.org/abstract/PRD/v69/e082004`

- "Upper limits on the strength of periodic gravitational waves from PSR J1939+2134", the LIGO Scientific Collaborration, *Class. Quantum Grav.***21** S671-S676, (2004).
  `http://www.iop.org/EJ/abstract/0264-9381/21/5/042/`

- "First upper limits from LIGO on gravitational wave bursts", the LIGO Scientific Collaborration, *Phys. Rev.***69** 102001, (2004).
  `http://link.aps.org/abstract/PRD/v69/e102001`

- "First upper limits from LIGO on gravitational wave bursts", A.J. Weinstein for the LIGO Scientific Collaborration, *Class. Quantum Grav.***21** S677-S684, (2004).
  `http://stacks.iop.org/0264-9381/21/S677`

- "Analysis of LIGO data for gravitational waves from binary neutron stars", the LIGO Scientific Collaborration, *Phys. Rev.***69** 122001, (2004).
  `http://link.aps.org/abstract/PRD/v69/e122001`

- "Analysis of first LIGO science data for stochastic gravitational waves", the LIGO Scientific Collaborration, *Phys. Rev.***69** 122004, (2004).
  `http://link.aps.org/abstract/PRD/v69/e122004`

2003

- "Mechanical loss associated with silicate bonding of fused silica", J.R. Smith, G.M. Harry, J.C. Betzwieser, A.M. Gretarsson, D.A. Guild, S.E. Kittelberger, M.J. Mortonson, S.D. Penn and P.R. Saulson, *Class. Quantum Grav.***20** 5039-5047, (2003).
  `http://www.iop.org/EJ/abstract/0264-9381/20/23/007/`
  Nominated for inclusion in the *Class. Quantum Grav.*Research Highlights of 2003/2004, see
  `http://www.iop.org/EJ/journal/-page=extra.High0304/CQG`

- "A report on the status of the GEO 600 gravitational wave detector", M. Hewitson, P. Aufmuth, C. Aulbert, S. Babak, R. Balasubramanian, B.W. Barr, S. Berukoff, G. Cagnoli, C.A. Cantley, M.M. Casey, S. Chelkowski, D. Churches, C.N. Colacino, D.R.M. Crooks, C. Cutler, K. Danzmann, R. Davies, R. Dupuis, E. Elliffe, C. Fallnich, A. Freise, S. Goßler, A. Grant, H. Grote, S. Grunewald, J. Harms, G. Heinzel, S. Heng,

A. Hepstonstall, M. Heurs, J. Hough, Y. Itoh, O. Jennrich, R. Jones, S. Hutter, K. Kawabe, C. Killow, K. Kötter, B. Krishnan, V. Leonhardt, H. Lück, B. Machenschalk, M. Malec, K. Mossavi, S. Mohanty, S. Mukherjee, S. Nagano, G.P. Newton, M.A. Papa, M. Perreur-Lloyd, M. Pitkin, M.V. Plissi, V. Quetschke, S. Reid, L. Ribichini, D.I. Robertson, N.A. Robertson, S. Rowan, A. Rüdiger, B.S. Sathyaprakash, R. Schilling, R. Schnabel, B.F. Schutz, F. Seifert, A.M. Sintes, J. Smith, P. Sneddon, K.A. Strain, I. Taylor, C.I. Torrie, A. Vecchio, H. Ward, U. Weiland, H. Welling, H. Welling, P. Williams, B. Willke, W. Winkler, G. Woan and I. Zawischa, *Class. Quantum Grav.***20** S581-S591, (2003).
`http://stacks.iop.org/CQG/20/S581`

- "Detector characterization in GEO 600", A.M. Sintes, P. Aufmuth, C. Aulbert, S. Babak, R. Balasubramanian, B.W. Barr, S. Berukoff, G. Cagnoli, C.A. Cantley, M.M. Casey, S. Chelkowski, D. Churches, C.N. Colacino, D.R.M. Crooks, C. Cutler, K. Danzmann, R. Davies, R. Dupuis, E. Elliffe, C. Fallnich, A. Freise, S. Goßler, A. Grant, H. Grote, S. Grunewald, J. Harms, G. Heinzel, S. Heng, A. Hepstonstall, M. Heurs, M. Hewitson, J. Hough, Y. Itoh, O. Jennrich, R. Jones, S. Hutter, K. Kawabe, C. Killow, K. Kötter, B. Krishnan, V. Leonhardt, H. Lück, B. Machenschalk, M. Malec, K. Mossavi, S. Mohanty, S. Mukherjee, S. Nagano, G.P. Newton, M.A. Papa, M. Perreur-Lloyd, M. Pitkin, M.V. Plissi, V. Quetschke, S. Reid, L. Ribichini, D.I. Robertson, N.A. Robertson, S. Rowan, A. Rüdiger, B.S. Sathyaprakash, R. Schilling, R. Schnabel, B.F. Schutz, F. Seifert, J. Smith, P. Sneddon, K.A. Strain, I. Taylor, C.I. Torrie, A. Vecchio, H. Ward, U. Weiland, H. Welling, H. Welling, P. Williams, B. Willke, W. Winkler, G. Woan and I. Zawischa, *Class. Quantum Grav.***20** S581-S591, (2003).
`http://stacks.iop.org/CQG/20/S731`

2001

- "High quality factor measured in fused silica", S.D. Penn, G.M. Harry, A.M. Gretarsson, S.E. Kittelberger, P.R. Saulson, J.J. Schiller, J.R. Smith, S.O. Swords, *Rev. Sci. Instrum.***72** 3670-3673, (2001).
`http://arxiv.org/abs/gr-qc/0009035`